CHARACTERIZATION OF A PRECISION PULSAR TIMING GRAVITATIONAL WAVE DETECTOR

A Dissertation

Presented to the Faculty of the Graduate School

of Cornell University

in Partial Fulfillment of the Requirements for the Degree of

Doctor of Philosophy

by

Michael Timothy Lam

August 2016

CHARACTERIZATION OF A PRECISION PULSAR TIMING GRAVITATIONAL WAVE DETECTOR

Michael Timothy Lam, Ph.D.

Cornell University 2016

We aim to construct a Galactic-scale detector comprised of an array of pulsars distributed across the sky in an effort to detect low-frequency (nanohertz) gravitational waves. Even without a detection, observations of pulsar timing arrays have allowed us to begin to place impactful astrophysical constraints on dynamical processes occurring during galaxy mergers. Understanding the detector is necessary for improving our sensitivity to gravitational waves and making a detection. Therefore, our goal is to characterize the entire propagation path through the pulsar timing array detector. To do so, we must understand: what intrinsic noise processes occur at the pulsar, what effects the interstellar medium has on pulsed radio emission, and what errors we introduce when measuring the incident electromagnetic radiation at our observatories.

In this work, we observed of one of the most spin-stable objects known for 24 hours to understand the fundamental limits of precision pulsar timing. We investigated the effect of non-simultaneous, multi-frequency sampling of pulsar dispersion measures on timing and analyzed the cause of deterministic and stochastic temporal variations seen in dispersion measure time series. We analyzed errors in pulse arrival times and determined the white noise budget for pulsars on the timescale of a single observation. Finally, we measured the excess noise beyond the white noise model in pulsar timing residuals and incorporated our results into a global model over all pulsar populations to improve excess noise scaling relations.

BIOGRAPHICAL SKETCH

Michael Timothy Lam was born on December 22, 1989, the first child of John Lam and Cindy Sherling. He was born in New York City and raised mostly in the culturally diverse township of Flushing, to which he fondly remembers the many people and restaurants. During his early years, he grew up in a 15-story apartment building and played with many of the other children of the complex. When he was five, he had the difficult process of learning to deal with a brother, Eric Lam, though they would end up being great companions for years afterwards. Shortly thereafter, his parents would end up divorcing, living two-and-a-half city blocks apart for many years. After his parents' divorce, his father ended up re-marrying, and his stepmother Kitty Law has been a constant source of guidance in his life. When he was nine, he had a much easier time of learning how to deal with a second brother from an early age, Christopher Sherling, whose is equally as great of a companion. He has been constantly in awe of both of his brothers' hard work and passion throughout their educations and beyond.

From a very early age, he wanted to be an astronomer, largely in part to his shared love of science fiction from his parents. He learned to love reading and has always considered himself to be a good student in school. He attended Stuyvesant High School in Manhattan where he learned not only how to commute through the city and function on little sleep but how to pursue his interests in math and science. It was there that he started running competitively, an endeavor he would continue for years later.

At the age of five, his parents took him to their college reunion at Colgate University, where he met Professor Thomas Balonek and two undergraduate students at the Foggy Bottom Observatory. He attended the same event at the age of 10 and 15, and finally applied and was accepted to Colgate in the fall of 2007. He

worked with Professor Balonek for his first summer of research, learning how to operate the Observatory's telescope and collect many nights of data of quasars. During his sophomore year, Professor Jeffrey Bary encouraged him to apply for a Research Experience for Undergraduates at the National Radio Astronomy Observatory after he expressed his interest in studying compact objects. He worked with Paul Demorest in Charlottesville, VA, which was his first exposure to pulsar timing close to the formation of NANOGrav, and ended up traveling to both the Green Bank Telescope for practice observing and Arecibo Observatory for a summer school in radio astronomy, for the first and certainly not the last times.

Before his senior year, he continued work with advisor, Thomas Balonek, developing and then using a program for his senior research project in time series analysis of quasar variability. Besides astronomy, he also studied computer science, being advised by Alexander Nakhimovsky and delighted by the professors and challenges from the separate field of study, especially enjoying the theoretical courses taught by Philip Mulry. He graduated magna cum laude with a Bachelor of Arts in Astronomy and Computer Science in 2011. During his time at Colgate, he continued to run competitively, proudly improving under the careful guidance of his coaches. While he would do it many times after, his first 100 mile week was one of the hardest.

In the fall of 2011, he began his graduate student career at Cornell University. He was interested in furthering his interests in statistics and time series analysis with his interest in pulsars and soon began to work with Jim Cordes' group and the North American Nanohertz Observatory for Gravitational Waves (NANOGrav) collaboration. He is excited to begin the next stage of his career at West Virginia University, working with Maura McLaughlin and the NANOGrav Physics Frontier Center as they continue the pursuit of gravitational wave astronomy.

I dedicate this work Thomas Balonek and Jeffrey Bary for all of their support, and to all of those who believed in me when I did not believe in myself.

ACKNOWLEDGMENTS

No discussion of who to acknowledge for support in the creation of this work should begin with anyone other than Jim Cordes. I knew Jim by name only even before my first day at Cornell and he has been the best mentor I could have asked for. He has been someone who truly lived up to the title of "advisor" and looked out for my academic, professional, and personal well-being. Even though I have not always been the most clear communicator in discussing a problem, he was very patient and very helpful. He has been an excellent teacher and I will never see a blackboard in the same way. I hope that one day my pile of notes will be half as tall as his. Though he was often busy, he was always willing to find time for me. I looked forward to the weeks when Jim was around and would stop by daily to discuss research; I have yet to meet someone else with such passion and enthusiasm and I am very grateful to have similar interests to him. I am indebted to him and honored to have been prepared for my journey by him.

Along with Jim, I must acknowledge Jim's right-hand man, Shami Chatterjee, someone I also consider a great mentor and friend. He was always willing to sit down and help me as I struggled through a problem and always willing to help me clean up my paper, proposal, and job application drafts; while I considered myself a decent writer when I came in, I consider myself a better science writer and communicator because of him. He provided me guidance in working with undergraduates, collaborators, and myself.

I would also like to mention other members of Jim's research group. Dusty Madison's vast experience and knowledge have always impressed and inspired me and while I know he thinks I do more work than he does, I can only strive to be the kind of researcher he has become. Tim Dolch was constantly juggling his work and his life while at Cornell with flying colors and I am grateful for his patience

with my impatience; I miss our late-night conversations and am proud to have had the chance to work on such a large project with him. Laura Spitler was busy finishing her time in the group when I was just starting but I will never forget her early advice to me when I visited as a prospective student and beyond. Robert Wharton brought fresh discussion (along with humor) of separate projects to the table that have always excited my interested; I am awed at his work ethic and I always strived to work harder because of him. Adam Brazier's humor in life and curiosity at my work has always been welcome and it has been my distinct pleasure to have worked with him on NANOGrav's cyber-infrastructure efforts at the final stages of my graduate career.

Beyond the Cordes group there have been many graduate students I have interacted with, learned from, and been inspired by over the years, and I believe I have been very privileged that they were all a part of my life. I have considered Mike Jones my partner-in-crime, both the source of shenanigans and the voice of reason when they were needed. Tyler Pauly has been a friend who could distract me and make me laugh while being serious when both of those were needed. Eva-Maria Mueller was my officemate for the longest stretch of time at Cornell and I am grateful that she somehow put up with me. Joyce Byun was a voice of reality and balance. Amit Vishwas and Luke Leisman were welcome sights for a daily session of post-run talk. And I'd like to say a very big thank you to everyone else who made my time at Cornell special.

Within the NANOGrav community, I have to thank Paul Demorest as my first pulsar timing advisor during my undergraduate career, where I discovered that this was the kind of science I wanted to study, and for his constant help with research by e-mail and with late-night observing by phone over the years. Similarly, I have to thank Scott Ransom and Ryan Lynch for helping me out when

I feared the worst had happened at our telescopes. Dan Stinebring and Joe Lazio provided very insightful discussions and were constantly interested in my work and made me truly feel like a collaborator. The same goes for Maura McLaughlin, who also encouraged me to travel abroad to the Max Planck Institute for Radio Astronomy in Germany and I look forward to working with in the coming years at West Virginia University. Emmanuel Fonseca has been a welcome sight in the trenches with me and I have enjoyed both the work and the fun. And, over several meetings at International Pulsar Timing Array conferences and during my brief time working in Germany, I have to thank Nicolas Caballero for his friendship and wisdom, and for continuing to share my pains and joys from across the ocean.

Most know that I keep sane by being a part of the local running community. There are countless individuals I have been privileged to run with and race against and I have been very proud of all of their successes. I must mention Julie Quinn and Alex Looi, who have been with me from the very start, for putting up with my nonsense and pushing me to be the best I could be. In addition to spending my free time running, I had the distinct pleasure of joining the reddit AskScience team in the middle of my career. They allowed me to take my passion for outreach and education and really share it with the world. They have stimulated my broader scientific curiosity, have shown enormous interest in my research, have allowed me to vent when I have needed it, and tried their damnedest to keep me from finishing this document. I would also like to acknowledge the creators of the video game FTL, who provided me with countless hours of stress relief at times when I probably should have been working.

My research was made possible by the NSF PIRE program award number 0968296, the NSF Physics Frontier Center award number 1430284, and the NASA New York Space Grant award number NNX15AK07H. And I must thank Jill Tar-

bell for all of her assistance in handling my financial and logistical support over the years.

Last but certainly not least, I must thank my family in all of their support. I am often very busy but they rarely are too busy for me. They have been with me every step of the ride.

TABLE OF CONTENTS

LIST OF TABLES

LIST OF FIGURES

CHAPTER 1

INTRODUCTION

The discovery of pulsars has provided us with precision tools for investigating Galactic dynamics, as probes of core collapse supernovae, as instruments to explore ultra-dense matter equations of state, and as tests of gravity. In this chapter, we will provide an introduction to gravitational waves (GWs), pulsars, pulsar timing, and GW experiments with pulsar timing arrays (PTAs).

1.1 The Gravitational Wave Universe

Colloquially known as "ripples" in spacetime, GWs are propagating metric perturbations that cause subtle changes in the distances between objects. Observations of GWs offer a new window to viewing the Universe beyond traditional electromagnetic-based astronomy. Just as we build many different kinds of telescopes to observe different frequencies of light across the electromagnetic spectrum, different classes of GW observatories spanning the separate GW spectrum frequency bands will enable us to probe particular sources and underlying physics.

The primary sources of GWs are compact objects, such as black holes, typically in binaries. PTAs observe in the low-frequency GW band and can be used to observe supermassive black hole binaries at the very centers of distant merging galaxies (Detweiler 1979; Hellings & Downs 1983; Romani 1989; Foster & Backer 1990), observations that allow us to understand dynamical processes during mergers that are not possible with electromagnetic telescopes. Other possible sources observable by PTAs include cosmic strings (Starobinskiĭ 1979; Sanidas et al. 2013) and primordial GWs from the inflationary epoch (Grishchuk 2005).

1.2 A Primer on Gravitational Waves

Just over a century ago, Einstein (1915b) developed his landmark theory of general relativity (GR), which describes the effect that mass and energy have on both space and time. Gravity is explained by the geometric curvature of spacetime, with objects following curved paths rather than experiencing an instantaneous central force as described by Newtonian theory. GR has yielded explanations for observed phenomena in disagreement with the Newtonian framework. Early in its development, it explained the anomalous advance of Mercury's perihelion precession of Mercury beyond the predictions from Newtonian mechanics (Le Verrier 1859; Einstein 1916). Apparent shifts in the position of a star due to the bending of light around the Sun observed by Eddington during the 1919 solar eclipse quickly verified Einstein's predictions and cemented the place of the theory in history (Dyson et al. 1920; Einstein 1915a).

The mathematics of GR are represented with the Einstein field equations, a set of 16 (10 unique) differential equations succinctly represented as

$$G_{\mu\nu} \equiv R_{\mu\nu} - \frac{1}{2} R g_{\mu\nu} = \frac{8\pi G}{c^4} T_{\mu\nu}, \tag{1.1}$$

where the left hand side describes the geometric curvature of spacetime and the right hand side describes the local source energy and momentum distribution multiplied by fundamental constants. Here, $G_{\mu\nu}$ is the Einstein tensor, containing terms that include the metric tensor $g_{\mu\nu}$ which determines the spacetime interval between two points, and functions of derivatives of the metric in both the Ricci tensor $R_{\mu\nu}$ and the Ricci scalar curvature R. The stress-energy tensor $T_{\mu\nu}$ contains terms for the density and flux of both energy and momentum. In normal spacetime, all tensors in Eq. 1.1 are symmetric 4×4 tensors, e.g., the indices $\mu, \nu \in \{0, 1, 2, 3\}$ are four arbitrary coordinates, one in time and three in space.

In the linearized gravity regime, we can write the Einstein field equations as

$$\Box \bar{h}_{\mu\nu} = -\frac{16\pi G}{c^4} T_{\mu\nu}, \tag{1.2}$$

where $\Box \bar{h}_{\mu\nu}$ represents the GW propagation with the usual wave operator. For more details, see the appendix to this chapter. We can use Eq. 1.2 to derive useful scaling relations for two orbiting point masses emitting GWs. Given two masses M orbiting at a separation R with a characteristic timescale (period) T and observed at a distance D, it can be shown (by dimensional analysis or again see the appendix for this derivation) that the GW strain is approximately

$$h \sim \frac{G}{Dc^4}\frac{MR^2}{T^2} \sim \frac{G}{Dc^4} MR^2 f^2 \sim \frac{G}{4\pi^2 Dc^4} MR^2 \Omega^2, \tag{1.3}$$

where f is the frequency of emission (Ω is the angular orbital frequency). In the Newtonian limit, we use the Keplerian orbital frequency to relate $\Omega^2 \sim GM/R^3$ and thus we arrive at

$$\begin{aligned} h &\sim \frac{(GM)^2}{4\pi^2 c^4 DR} \\ &\approx 6 \times 10^{-16} \left(\frac{M}{10^8 M_\odot}\right)^2 \left(\frac{\mathrm{Mpc}}{D}\right) \left(\frac{\mathrm{mpc}}{R}\right), \end{aligned} \tag{1.4}$$

where the mpc separation is roughly when the energy loss of the system is dominated by GW emission. The GW frequency is given by

$$\begin{aligned} f &\sim \frac{1}{2\pi}\left(\frac{GM}{R^3}\right)^{1/2} \\ &\approx 100 \text{ nHz } \left(\frac{M}{10^8 M_\odot}\right)^{1/2} \left(\frac{\mathrm{mpc}}{R}\right)^{3/2}. \end{aligned} \tag{1.5}$$

Fiducial values are for expected supermassive black hole binaries in merging galaxies in local galaxy clusters that are in the final stages of the GW-dominated inspiral.

We can relate the GW strain to the timing precision required from a pulsar. Relating the GW to the fractional change in distance ($h \sim \Delta L/L$), for a given h,

we need to keep track of the position of a pulsar to well within ΔL. We thus have

$$\begin{aligned} \Delta L &\sim hL \sim hcT \\ &\approx 9.5 \text{ m} \left(\frac{h}{10^{-16}}\right) \left(\frac{T}{10 \text{ yr}}\right), \end{aligned} \tag{1.6}$$

where $L \sim cT$ is the length from the light/GW travel time. The timing precision is then trivially found to be

$$\begin{aligned} \Delta t &\sim \frac{\Delta L}{c} \sim hT \\ &\approx 32 \text{ ns} \left(\frac{h}{10^{-16}}\right) \left(\frac{T}{10 \text{ yr}}\right). \end{aligned} \tag{1.7}$$

Therefore, we require timing precision at the nanosecond level from pulsars in order to measure the effects of passing GWs.

1.3 The Discovery of Pulsars

Baade & Zwicky (1934) first described the theoretical possibility of a neutron star, a small, dense object composed primarily of neutrons originating as a stellar remnant from a supernova; such an object could support itself from gravitational collapse beyond the Chandrasekhar (1931) limit. The idea of neutron stars remained a theoretical curiosity through the middle of the 20th century, it took many decades before their existence could be observationally confirmed. The field of pulsar astronomy came into existence in 1967, when graduate student Jocelyn Bell (Burnell) detected a celestial pulsed signal at a radio frequency of 81.5 MHz at the Mullard Radio Astronomy Observatory near Cambridge, UK (Hewish et al. 1968). Temporarily named LGM-1 for "little green men" in reference to a possible though unlikely transmission from an extraterrestrial intelligence, the radio source was quickly theorized to be associated with a rapidly rotating neutron star (Gold

1968; Pacini 1968; Gold 1969). Confirmation came with the discovery of regular pulsations from the Crab Nebula supernova remnant and the measurement of a steady slow down in its spin rate (Staelin & Reifenstein 1968; Comella et al. 1969; Richards & Comella 1969).

While all neutron stars are extraordinary objects, it was the discovery of the subclass of recycled, millisecond pulsars (MSPs) that truly allowed for precision timing experiments. Backer et al. (1982) discovered B1937+21, with a period of 1.558 ms, at Arecibo Observatory, an order of magnitude smaller than the period of the young Crab pulsar. It remains one of the fastest spinning pulsars known, as well as one of the most precisely timed. Since then, several hundred MSPs have been discovered, and their extreme spin stability has opened the door to a wide range of tests of fundamental physics previously discussed.

1.4 Basic Properties of Pulsars

The most fundamental observables of pulsars are the spin period P and period derivative $\dot{P}$. Different populations of pulsars fill different areas of this phase space. Figure 1.1 shows the phase space in the form of the $P - \dot{P}$ diagram with data taken from Manchester et al. (2005)[1] and Olausen & Kaspi (2014)[2]. The region in the center contains canonical pulsars (CPs), those with moderate (~ 1 s) periods and radio emission powered by rotation. CPs start their lives in the top left of the figure, at low P and high $\dot{P}$, and travel toward the bottom right (longer but more slowly changing periods); the solid lines denote characteristic ages of the pulsar assuming rotational energy is converted entirely into magnetic dipole

[1] `http://www.atnf.csiro.au/research/pulsar/psrcat`
[2] `http://www.physics.mcgill.ca/~pulsar/magnetar/main.html`

radiation and the magnetic field strength is constant. When CPs move to the lower right, the emission mechanism shuts off and they cross the pulsar "death line" into the shaded "graveyard" region. Note that the region is ill-defined and is a function of the emission mechanism itself. Once they cross into the region, the "dead" objects cease being observable radio pulsars. For neutron stars with a main-sequence binary companion, when the companion begins to evolve off the main sequence and increase in size, mass transfer can occur onto the neutron star. The process of accretion will spin up neutron stars to millisecond periods and reactivate the emission mechanism. Once fully "recycled" in this manner, MSPs can become extremely spin stable, have a small period derivative, and act as extremely accurate and precise clocks. Magnetars, whose primary energy reservoir is in their magnetic fields, are shown in the top right.

Dispersion in the ionized interstellar medium results from a frequency-dependent refractive index, resulting in pulses being delayed as a function of radio frequency ν, with lower frequency emission traveling slower than higher frequency emission. The dispersive delay from infinite frequency is $\Delta t \propto \mathrm{DM}/\nu^2$, where DM is the dispersion measure, equal to $\int_0^L n_e dl$, the integral of the electron density along the line of sight. Figure 1.2 shows the dispersive delay as a function of frequency for PSR J1713+0747 and the effect of proper de-dispersion. DM is another fundamental observable of pulsars observed at multiple radio frequencies, although precision estimation of DM is non-trivial (see Chapter 3 and Cordes et al. 2016).

Precise time-tagging of pulses from pulsars is performed by standard signal processing methods tied to accurate timekeeping. Individual pulse shapes appear very different but average together into a stable pulse profile. Such a waveform is used as a template in matched filtering of new pulse profile data, a procedure that

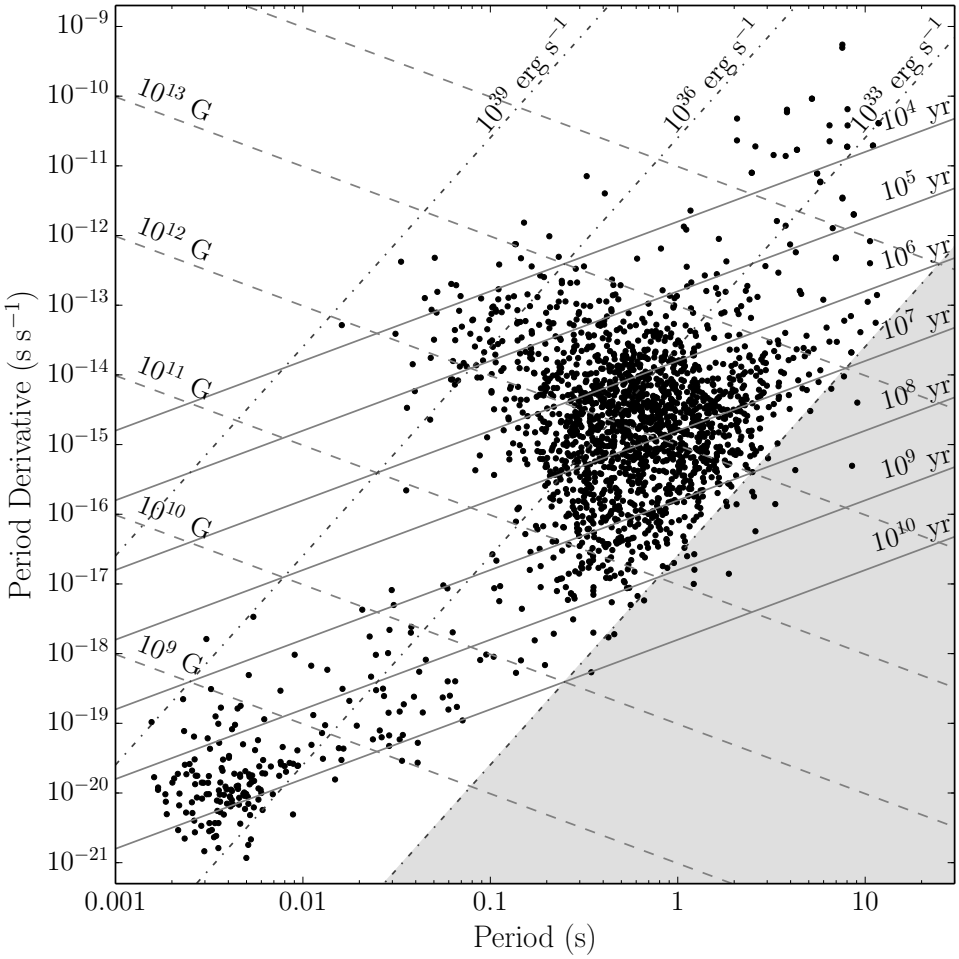

Figure 1.1: $P - \dot{P}$ diagram. The central region shows canonical pulsars while the top right shows magnetars and the bottom left shows millisecond pulsars. Lines of constant characteristic age (solid), surface magnetic field (dashed), and spin-down luminosity (the loss rate of rotational energy given the assumption of complete conversion of rotational energy into radiation; dashed-dotted) are overplotted. The shaded gray region is the pulsar graveyard, with the boundary at the "death line". Data are taken from Manchester et al. (2005) and Olausen & Kaspi (2014).

finds the optimal pulse time of arrival (TOA) assuming that the observed pulse at an epoch is a noisy version of the template. In general, bright pulsars with sharp features in their template shapes and short periods will perform better as precision clocks. Since signal-to-noise ratios (S/Ns) for single pulses from typical MSPs are relatively low, many pulses are averaged together in a process known as

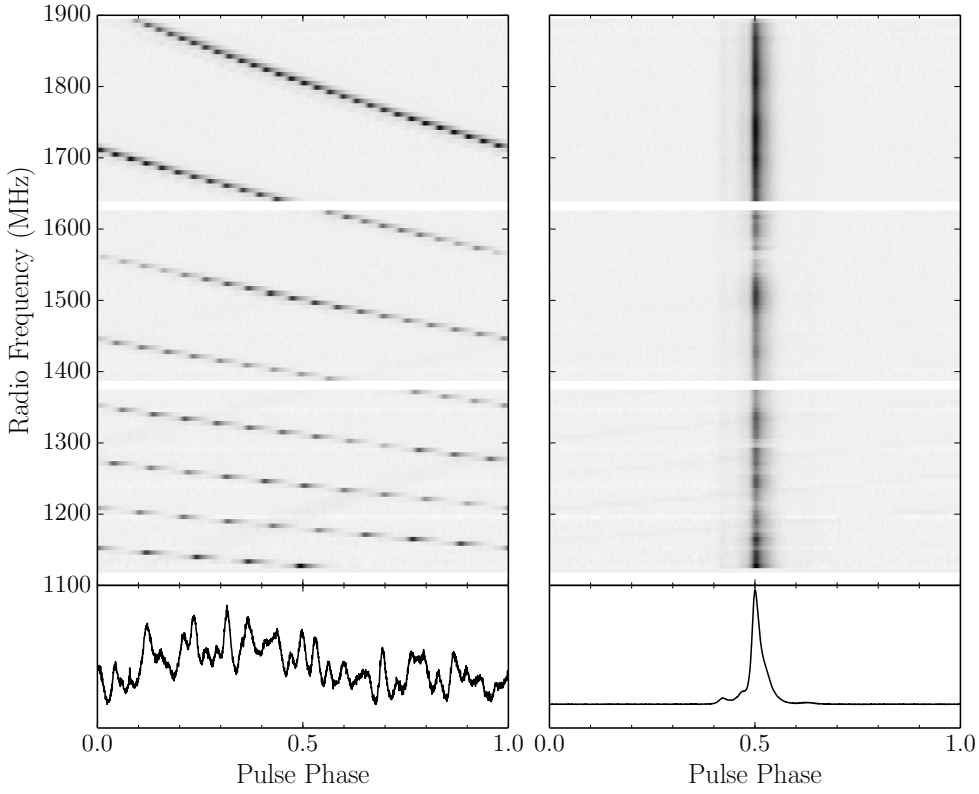

Figure 1.2: Example of dispersion in pulses with data taken from the Green Bank Telescope for the 24-hour global campaign on PSR J1713+0747. The panels on the left show dispersed pulses (with wraps in phase due to pulse folding) while the panels on the right show de-dispersed and aligned pulses. The pulses have been coherently de-dispersed within each of the 6.25 MHz frequency channels. The two horizontal gaps are pre-masked radio frequency interference from a Global Positioning System satellite (signal at $\sim$ 1620 MHz and its reflection lower in the band). Top: Radio pulses as a function of frequency and pulse phase. Bottom: Pulses summed over all frequencies.

folding. The procedure assumes a well-known initial timing model for the pulsar such that smearing of the pulse across frequency is minimized. See Chapter 5 for more details on the topics discussed here.

Precision pulsar timing relies on our ability to accurately track each rotation of the pulsar over a baseline of many years. Using both the TOAs and an initial

timing model, we can update and introduce new parameter estimates that describe the kinematics of the pulsar-observatory system. In addition to the timing model parameters, we obtain timing residuals from the fit, defined as the difference between the data (pulse TOAs) and the timing model. Residuals allow models to be updated over time. They also contain useful information about the noise processes and allow us to properly characterize the noise model separately from the timing model. Residuals often show noise inconsistent with errors from the template fitting of a finite S/N pulse alone.

1.5 Tests of Gravity with Pulsars

1.5.1 Measurements of Post-Newtonian Gravity

High-precision pulsar timing experiments have allowed for a number of extremely stringent constraints on GR. One common method of placing constraints is in the Parameterized Post-Newtonian (PPN) formalism, where various order post-Newtonian corrections to classical gravity quantify physically-motivated deviations from GR. See Will (2014) for an overview of the 10 PPN parameters. Pulsar timing has provided some of the strongest constraints on a number of the PPN parameters.

The three α parameters measure if there exist preferred-frame effects. The current best limit on $\alpha_1 = 4 \times 10^{-5}$, which causes a polarization of the pulsar's eccentricity vector, comes from PSR J1738+0333 (Shao & Wex 2012). Non-zero α_2 causes spin precession and alters the pulsar's observed orbital inclination. The non-detection of precession in the pulse profile shapes of two pulsars led to a limit of $\alpha_2 < 1.6 \times 10^{-9}$ at the 95% confidence level (Shao et al. 2013). The

parameter α_3, which measures violations of total momentum conservation, is the most stringent PPN constraint, with a value 4×10^{-20} from a set of measured anomalous eccentricities in MSP binary orbits (Stairs et al. 2005).

A similar analysis of stable pulse profile shapes as with α_2 allowed a limit on ξ, representing anisotropies within gravitational interactions, equal to $\xi < 3.9 \times 10^{-9}$ also at the 95% level (Shao & Wex 2013). Both α_3 and ζ_2 measure violations of total momentum conservation in the form of self-acceleration of a binary center of mass. Since α_3 is so strongly constrained, its contribution to the self-acceleration is negligible, allowing the upper limit on ζ_2 to be measured at the 4×10^{-5} level (Will 1992).

Other constraining tests of gravity have been possible with pulsar timing. As an example, Zhu et al. (2015) placed constraints on temporal changes in the gravitational constant G close to the limit from Lunar Laser Ranging (Hofmann et al. 2010) and over a significantly longer baseline. Tests of Strong Equivalence Principle violations in the strong-field limit were set by the circularity of binary systems in the Galactic potential, with the parameter $\Delta < 5.6 \times 10^{-3}$ (Stairs et al. 2005).

1.5.2 Indirect evidence of GWs

Observational evidence for the existence of GWs first came from pulsar timing experiments. Hulse & Taylor (1975) discovered the first double neutron star system, B1913+16, at Arecibo, which eventually led to the 1993 Nobel Prize in Physics. A tight binary with an orbital period of 7.75 hours, the system is losing angular momentum by radiating away energy that is not detected in the electromagnetic spectrum. The loss is inferred to be in the form of GWs, with the period becoming

smaller and the size of the orbit shrinking by about 1 cm per year (Weisberg et al. 2010). The decay of the period matched the prediction from GR, with the observed-to-predicted rate of decay ratio equal to 0.96 ± 0.09, without taking into account an additional kinematic correction to the observed rate from the Galactic potential (Taylor & Weisberg 1982). Later work continued to refine the ratio, with the value of the ratio now measured to be 0.997 ± 0.002, a much more stringent constraint on GR (Taylor & Weisberg 1989; Weisberg et al. 2010).

1.5.3 Pulsar Timing Arrays

The concept of a pulsar timing array experiment for the detection of GWs dates back to the realization that Doppler tracking of several spacecraft within the solar system simultaneously could allow for a detection of GWs (Estabrook & Wahlquist 1975). It was soon realized that regular, pulsed emission could be used in the detection of low-frequency GWs as the time interval between pulses changed (Sazhin 1978; Detweiler 1979). Correlations between arrival times of pulses from an array of pulsars could be used to detect GWs of order nanohertz frequencies from merging supermassive black hole binaries (see Eqs. 1.4, 1.5; Hellings & Downs 1983; Romani 1989; Foster & Backer 1990).

Currently, three pulsar timing array experiments are underway, run by the North American Nanohertz Observatory for Gravitational Waves (NANOGrav; McLaughlin 2013), the European Pulsar Timing Array (EPTA; Kramer & Champion 2013), and the Parkes Pulsar Timing Array (PPTA; Hobbs 2013; Manchester et al. 2013). All three collaborations combine their data in a global effort called the International Pulsar Timing Array (IPTA; Hobbs et al. 2010; Manchester & IPTA 2013).

Pulsar timing will result in the direct detection of low-frequency GWs in the near future. The first direct detection of GWs in the hertz-kilohertz band has recently come from the Laser Interferometer Gravitational-Wave Observatory (LIGO; Abbott et al. 2016). They announced the detection of GWs coming from merging stellar mass black holes (more massive than previously predicted) with a signal strong enough to be visible by eye among the noise. Besides these two types of experiments, the Laser Interferometer Space Antenna (LISA) is a future space-based LIGO analog designed primarily to observe microhertz-hertz GWs from massive black hole binaries and extreme mass ratio inspirals (massive black holes with small compact object companions). In addition, very-low-frequency GWs ($sim10^{-16}$ Hz range) currently are being probed by cosmic microwave background experiments. All four bands will need to be observed in order to detect sources across the full GW spectrum.

LIGO has demonstrated the need for a complete understanding of the detector and the contributing noise sources in order to properly attribute an observed signal to a GW source. During the initial LIGO run, the characterization of the noise model demonstrated their understanding of both the instrumental systematics and their low sensitivity during that phase of the project; they indeed detected no astrophysical signal at that time. Upgrades to the facility have lowered the noise floor, with current sensitivity allowing them to make the first few detections (see also Abbott et al. 2016b). Further improvements will allow LIGO to become an extremely sensitive GW instrument. Similarly, we require an understanding of the noise sources within the PTA, as the signal propagates from the pulsar through the interstellar medium to the telescope, so that we can confidently detect and then regularly observe GWs.

1.6 Characterization of Pulsar Timing Arrays

This dissertation describes efforts to understand a PTA as a Galactic-scale detector. We want to first characterize our detector and eventually improve it, for both the initial detection of GWs and long-term observations using PTAs. This work focuses on all aspects of pulse propagation through the detector. In Chapter 2, we discuss a multi-telescope campaign that observed one of the best-timed pulsars. We describe the timing errors that result from non-simultaneous multi-frequency observations and the resultant mis-estimation of the pulse dispersion measure (DM) in Chapter 3. We next investigate causes of DM variations from a variety of effects in Chapter 4, including linear trends, periodic or quasi-periodic changes, and stochastic variations. In Chapter 5, we develop a white noise budget for pulse TOAs on short ($\lesssim$ 1 hour) timescales, characterizing the timing precision of the NANOGrav MSPs. In Chapter 6, we investigate the timing noise excess beyond the white noise model and update scaling relations of the excess noise as a function of fundamental pulsar observables, moving us towards a comprehensive noise model for the NANOGrav MSPs. In Chapter 7, we present future avenues for research into the further characterization and calibration of our pulsar timing GW detector. Finally, in chapter 8, we summarize our conclusions. We also include a number of appendices at the end as reference material. Appendix A documents the PyPulse program, a set of software tools developed primarily for handling of pulse profile data purely in Python. Appendix B documents Quicklook, a program built with PyPulse for the rapid data processing and inspection of pulse profiles and their related data products.

1.7 Appendix

Here we will derive the result of Eqs. 1.2 and 1.3. First, we will consider GR for isolated systems, which can be approximated in two limits. Consider some source of gravity of mass $\sim \mathcal{M}$ and size $\sim \mathcal{R}$ that is varying on a timescale $\sim \mathcal{T}$. We define the dimensionless parameters

$$\hat{c} = \frac{c\mathcal{T}}{\mathcal{R}}, \quad \hat{G} = \frac{G\mathcal{M}\mathcal{T}^2}{\mathcal{R}^3}, \tag{1.8}$$

in a system where we choose the units such that $\mathcal{M} \sim \mathcal{R} \sim \mathcal{T} \sim 1$ and $\hat{G} \sim G$, $\hat{c} \sim c$. We can estimate the strength of gravity with the dimensionful compactness parameter (the ratio of the gravitational binding energy to the rest energy) $\epsilon \sim E_g/\mathcal{M}c^2 \sim \Phi/c^2 \sim G\mathcal{M}/\mathcal{R}c^2 \sim \hat{G}/\hat{c}^2$, where Φ is the gravitational potential. In the low-speed limit $\epsilon \sim (v/c)^2 \ll 1$ ($\hat{G}$ fixed), it is useful to expand Φ in powers of $1/\hat{c}$. The $\mathcal{O}(1)$ term yields the Newtonian limit for gravity while the $\mathcal{O}(1/\hat{c}^2)$ term yields what is known as post-1-Newtonian gravity, with higher order terms yielding higher post-Newtonian corrections. However, in the low source gravity limit when when $\hat{G}$ is small ($\mathcal{O}(\hat{G})$, $\hat{c}$ fixed), we obtain the linearized gravity formalism useful for describing GWs. In the $\hat{G} \to 0$ limit, we recover the equations of motion for special relativity. Both limits are useful for simply describing a wide range of different phenomena.

GWs are derived from plane-wave solutions in the linearized gravity framework. For clarity, we define our coordinates such that $x^\mu = (ct, x, y, z)$ and the Minkowski metric is $\eta_{\mu\nu} = \text{diag}(-1, 1, 1, 1)$. We can approximate the metric in the weak-field limit as flat, Minkowski spacetime with a small perturbation metric added,

$$g_{\mu\nu} = \eta_{\mu\nu} + h_{\mu\nu} + \mathcal{O}([h_{\mu\nu}]^2), \quad |h_{\mu\nu}| \ll 1. \tag{1.9}$$

We will ignore all higher-order (non-linear) terms of $h_{\mu\nu}$. It is convenient to define

the trace-reversed metric perturbation as

$$\bar{h}_{\mu\nu} \equiv h_{\mu\nu} - \frac{1}{2} h \eta_{\mu\nu} \tag{1.10}$$

while choosing the Lorenz gauge such that $\partial^{\mu} \bar{h}_{\mu\nu} = 0$. We note that $h = \eta^{\mu\nu} h_{\mu\nu}$ and therefore $\bar{h} = -h$ and is in "trace-reversed" form. With our choice of gauge, the linearized Einstein field equations are then, after combining Eqs. 1.1 and 1.10, we arrive at Eq. 1.2, which we again write as

$$\Box \bar{h}_{\mu\nu} = -\frac{16\pi G}{c^4} T_{\mu\nu}. \tag{1.11}$$

In vacuum far away from any source, the right hand side is zero and we arrive at the usual form of the wave equation, $\Box \bar{h}_{\mu\nu} = 0$. Given the vacuum assumption, we can write the metric perturbation in the transverse-traceless (TT) gauge, such that it is purely spatial ($h^{\mathrm{TT}}_{0\nu} = 0$), transverse to the direction of motion ($\partial^{\mu} h^{\mathrm{TT}}_{\mu\nu} = 0$), and traceless ($\eta^{\mu\nu} h^{\mathrm{TT}}_{\mu\nu} = h^{\mathrm{TT}} = 0$). We note that the trace-reversed metric perturbation, again assuming the vacuum solution, will equal the original metric perturbation in the transeverse-traceless gauge ($\bar{h}^{\mathrm{TT}}_{\mu\nu} = h^{\mathrm{TT}}_{\mu\nu}$) and so we will drop the "bar" for convenience.

We can write the usual *ansatz* for the wave equation solution as

$$h^{\mathrm{TT}}_{\mu\nu} = \mathrm{Re}\Big[C_{\mu\nu} e^{i k_{\lambda} x^{\lambda}}\Big] = \mathrm{Re}\Big[C_{\mu\nu} e^{i(kz - \omega t)}\Big], \tag{1.12}$$

where $C_{\mu\nu}$ is a constant, symmetric "amplitude" metric, $k^{\lambda} = (\omega/c, k^1, k^2, k^3) = (\omega/c, 0, 0, k)$ is the wave vector pointing in the z-direction, ω is the wave (angular) frequency. The usual dispersion relation $\omega = kc$ is satisfied because the wave vector is null ($k_{\lambda} k^{\lambda} = 0$) in the vacuum solution. Under the condition that the perturbation is transverse, we have in general that

$$\partial^{\mu} h^{\mathrm{TT}}_{\mu\nu} = i C_{\mu\nu} k^{\mu} e^{i k_{\lambda} x^{\lambda}} = 0, \tag{1.13}$$

which implies $k^\mu C_{\mu\nu} = 0$. Like $h^{\mathrm{TT}}_{\mu\nu}$, by definition $C_{\mu\nu}$ must be purely spatial and thus $C_{0\nu} = 0$, and combining both conditions on $C_{\mu\nu}$, we find that $C_{3\nu} = 0$ and the tensor's only nonzero components are where $\mu, \nu \in \{1, 2\}$. The matrix form can be written as

$$C_{\mu\nu} = \begin{pmatrix} 0 & 0 & 0 & 0 \\ 0 & C_{11} & C_{12} & 0 \\ 0 & C_{12} & -C_{11} & 0 \\ 0 & 0 & 0 & 0 \end{pmatrix} \equiv \begin{pmatrix} 0 & 0 & 0 & 0 \\ 0 & h_+ & h_\times & 0 \\ 0 & h_\times & -h_+ & 0 \\ 0 & 0 & 0 & 0 \end{pmatrix}, \tag{1.14}$$

where we have utilized the fact that $C_{\mu\nu}$ must be traceless and symmetric. On the right, we have renamed the coefficients to describe the "plus" (+) and "cross" (×) polarization modes of the wave.

We will now derive the scaling relations for a binary system emitting GWs as shown by Eq. 1.3. Consider two masses m_1, m_2 orbiting in a binary far away from the observer at a distance D. Analogously to electromagnetism, we can use a multipole formulation to describe the nature of gravitational radiation. Note that such a formulation treats gravity as a vector (spin-one) field rather than a tensor (spin-two) field; however, it is useful to obtain the approximate scaling relations. The mass monopole, equivalent to the electric monopole, will simply equal $\sum_i m_i$ and does not produce radiation because it is conserved. The mass dipole, equivalent to the electric dipole, will be $\sum_i m_i r_i$ and will also produce no radiation. The first time-derivative will be $\sum_i m_i \dot{r}_i$, which is the constant momentum and therefore cannot produce radiation either. Now we must also consider the equivalent to magnetic dipole radiation. The magnetic moment $\boldsymbol{\mu} \sim \mathbf{r} \times \mathbf{j} \sim \mathbf{r} \times (\rho \mathbf{v})$, where $\mathbf{r}$ is the position vector and $\mathbf{j}$ is the electric current density equal to the charge density ρ times the velocity vector $\mathbf{v}$. Thus, the analogous expression to the magnetic momentum is the angular momentum of the system. Since the second time-derivative

of the magnetic moment is what generates magnetic-dipole radiation, we focus on the second time-derivative of the angular momentum, which is zero and therefore no gravitational dipole radiation can be generated.

The next order term is the gravitational quadrupole, again analogous to the electric quadrupole. The power radiated for such a quadrupole is $L \sim \langle \dddot{\mathcal{I}}^2 \rangle$, where $I_{jk} \sim \sum_i m_i r_{ij} r_{ik}$ is the second moment of the mass distribution, $\mathcal{I}_{jk}$ is the trace-free part of I_{jk}, and the average occurs over many characteristic periods of the source.

Recall the two masses orbiting each other and assume $m_1 \sim m_2 \sim M$. The amplitude of the gravitational field far from the source (and transverse) will be $h \propto I/D \sim MR^2/D$ (analogous to the electric radiation field $E \sim qa/D$). We require two time derivatives of the I_{jk} so that in geometrized units (where $G = c = 1$ and mass, length, and time are in equivalent units), the strain is dimensionless. By dimensional analysis, we include the prefactor G/c^4, and

$$h_{jk} \sim \frac{G}{Dc^4} \ddot{I}_{jk}. \tag{1.15}$$

For reference, the full form of the quadrupole formula can be solved with the use of Green's functions and Eq. 1.2, and includes $\ddot{I}_{jk}$ evaluated at the retarded time $t - r/c$ and another factor of 2 out front. We can continue with the approximation and show that Eq. 1.15 can be written as

$$h \sim \frac{G}{Dc^4} \frac{MR^2}{T^2}, \tag{1.16}$$

which yields the result given by Eq. 1.3. See chapter 36 of Misner et al. (1973) and chapter 7 of Carroll (2004) for more information regarding the choices made in our approximations.

BIBLIOGRAPHY

Abbott, B. P., Abbott, R., Abbott, T. D., et al. 2016, Physical Review Letters, 116, 061102

Abbott, B. P., Abbott, R., Abbott, T. D., et al. 2016, Physical Review Letters, 116, 241103

Baade, W., & Zwicky, F. 1934, Proceedings of the National Academy of Science, 20, 259

Backer, D. C., Kulkarni, S. R., Heiles, C., Davis, M. M., & Goss, W. M. 1982, Nature, 300, 615

Carroll, S. M. 2004, Spacetime and geometry / Sean Carroll. San Francisco, CA, USA: Addison Wesley, ISBN 0-8053-8732-3, 2004, XIV + 513 pp.,

Chandrasekhar, S. 1931, ApJ, 74, 81

Comella, J. M., Craft, H. D., Lovelace, R. V. E., & Sutton, J. M. 1969, Nature, 221, 453

Cordes, J. M., Shannon, R. M., & Stinebring, D. R. 2016, ApJ, 817, 16

Detweiler, S. 1979, ApJ, 234, 1100

Dyson, F. W., Eddington, A. S., & Davidson, C. 1920, Philosophical Transactions of the Royal Society of London Series A, 220, 291

Einstein, A. 1915, Sitzungsber. preuss.Akad. Wiss., vol. 47, No.2, pp. 831-839, 1915, 47, 831 Explanation of the Perihelion Motion of Mercury from the General Theory of Relativity

Einstein, A. 1915, Sitzungsberichte der Königlich Preußischen Akademie der Wissenschaften (Berlin), Seite 844-847.

Einstein, A. 1916, Naturwissenschaften, 4, 481

Estabrook, F. B., & Wahlquist, H. D. 1975, General Relativity and Gravitation, 6, 439

Foster, R. S., & Backer, D. C. 1990, ApJ, 361, 300

Gold, T. 1968, Nature, 218, 731

Gold, T. 1969, Nature, 221, 25

Grishchuk, L. P. 2005, Physics Uspekhi, 48, 1235

Hellings, R. W., & Downs, G. S. 1983, ApJL, 265, L39

Hewish, A., Bell, S. J., Pilkington, J. D. H., Scott, P. F., & Collins, R. A. 1968, Nature, 217, 709

Hobbs, G. 2013, Classical and Quantum Gravity, 30, 224007

Hobbs, G., Archibald, A., Arzoumanian, Z., et al. 2010, Classical and Quantum Gravity, 27, 084013

Hofmann, F., Müller, J., & Biskupek, L. 2010, A&A, 522, L5

Hulse, R. A., & Taylor, J. H. 1975, ApJL, 195, L51

Kramer, M., & Champion, D. J. 2013, Classical and Quantum Gravity, 30, 224009

Le Verrier, U. J. 1859, Annales de l'Observatoire de Paris, 5, 1

Manchester, R. N., Hobbs, G. B., Teoh, A., & Hobbs, M. 2005, AJ, 129, 1993

Manchester, R. N., Hobbs, G., Bailes, M., et al. 2013, PASA, 30, e017

Manchester, R. N., & IPTA 2013, Classical and Quantum Gravity, 30, 224010

McLaughlin, M. A. 2013, Classical and Quantum Gravity, 30, 224008

Misner, C. W., Thorne, K. S., & Wheeler, J. A. 1973, San Francisco: W.H. Freeman and Co., 1973,

Olausen, S. A., & Kaspi, V. M. 2014, ApJS, 212, 6

Pacini, F. 1968, Nature, 219, 145

Richards, D. W., & Comella, J. M. 1969, Nature, 222, 551

Romani, R. W. 1989, NATO Advanced Science Institutes (ASI) Series C, 262, 113

Sanidas, S. A., Battye, R. A., & Stappers, B. W. 2013, ApJ, 764, 108

Sazhin, M. V. 1978, SvA, 22, 36

Shao, L., & Wex, N. 2012, Classical and Quantum Gravity, 29, 215018

Shao, L., & Wex, N. 2013, Classical and Quantum Gravity, 30, 165020

Shao, L., Caballero, R. N., Kramer, M., et al. 2013, Classical and Quantum Gravity, 30, 165019

Staelin, D. H., & Reifenstein, E. C., III 1968, Science, 162, 1481

Stairs, I. H., Faulkner, A. J., Lyne, A. G., et al. 2005, ApJ, 632, 1060

Starobinskiĭ, A. A. 1979, Soviet Journal of Experimental and Theoretical Physics Letters, 30, 682

Taylor, J. H., & Weisberg, J. M. 1982, ApJ, 253, 908

Taylor, J. H., & Weisberg, J. M. 1989, ApJ, 345, 434

Weisberg, J. M., Nice, D. J., & Taylor, J. H. 2010, ApJ, 722, 1030

Will, C. M. 1992, ApJL, 393, L59

Will, C. M. 2014, Living Reviews in Relativity, 17, 4

Zhu, W. W., Stairs, I. H., Demorest, P. B., et al. 2015, ApJ, 809, 41

CHAPTER 2

A 24 HR GLOBAL CAMPAIGN TO ASSESS PRECISION TIMING OF THE MILLISECOND PULSAR J1713+0747

The radio millisecond pulsar J1713+0747 is regarded as one of the highest-precision clocks in the sky, and is regularly timed for the purpose of detecting gravitational waves. The International Pulsar Timing Array collaboration undertook a 24-hour global observation of PSR J1713+0747 in an effort to better quantify sources of timing noise in this pulsar, particularly on intermediate (1 – 24 hr) timescales. We observed the pulsar continuously over 24 hr with the Arecibo, Effelsberg, GMRT, Green Bank, LOFAR, Lovell, Nançay, Parkes, and WSRT radio telescopes. The combined pulse times-of-arrival presented here provide an estimate of what sources of timing noise, excluding DM variations, would be present as compared to an idealized $\sqrt{N}$ improvement in timing precision, where N is the number of pulses analyzed. In the case of this particular pulsar, we find that intrinsic pulse phase jitter dominates arrival time precision when the S/N of single pulses exceeds unity, as measured using the eight telescopes that observed at L-band/1.4 GHz. We present first results of specific phenomena probed on the unusually long timescale (for a single continuous observing session) of tens of hours, in particular interstellar scintillation, and discuss the degree to which scintillation and profile evolution affect precision timing. This paper presents the data set as a basis for future, deeper studies.

Published: Dolch, T., Lam, M. T., et al., 2014, ApJ, 794, 21

2.1 Introduction

The International Pulsar Timing Array[1] (IPTA; Hobbs et al. 2010, Manchester & IPTA 2013) is a gravitational wave (GW) detector currently consisting of ~ 50 pulsars distributed across the sky, monitored regularly by up to seven telescopes around the world: the Arecibo Observatory in the US, the Effelsberg radio telescope in Germany, the NRAO Green Bank Telescope (GBT) in the US, the Lovell radio telescope at Jodrell Bank Observatory in the UK, the Nançay radio telescope in France, the Parkes telescope in Australia, and the Westerbork Synthesis Radio Telescope (WSRT) in the Netherlands. Some of the pulsars in the IPTA have been precision-timed for a decade or more. These observations are performed by the European Pulsar Timing Array (EPTA; Kramer & Champion 2013), the North American Nanohertz Observatory for Gravitational Waves (NANOGrav; McLaughlin 2013), and the Parkes Pulsar Timing Array (PPTA; Hobbs 2013, Manchester et al. 2013). The three collaborations combine their data as the IPTA.

Pulsar timing compares times-of-arrival (TOAs) to those predicted from a model that describes the pulsar's rotation, its binary motion, the interstellar medium (ISM) between us and the pulsar, and the Earth's motion in the Solar System. The measured TOAs are typically derived from pulsar profiles that have been averaged over the observation duration; and referenced against a high-precision frequency standard at the observatories (typically hydrogen masers); which in turn is referenced to an international timing standard (Lorimer et al. 2004). If the resulting differences between measured and modelled TOAs (the so-called "timing residuals") deviate significantly from zero, this indicates astrophysical processes that are either not (or not completely) accounted for by the timing model. One

[1] `http://ipta.phys.wvu.edu`

possibility for such a process is long-period GWs perturbing the spacing between pulses as they propagate from a pulsar to the Earth. Obtaining accurate enough timing residuals to detect these GWs requires repeated measurements over many years. Sensitivity to GWs increases as observation duration grows, and the longest observation spans, as well as the red spectrum of the expected GWs, mean that the array is most sensitive at a frequency of about 10 yr (Sesana 2013). Individual TOAs are obtained by measuring the offset of emission beamed across the line-of-sight (LOS) at a given time from a template profile shape. Pulses can be averaged over a subintegration time, also known as "folding" according to a best-known pulse period. The template profile is high-S/N and often averaged from long-term observations. From the radiometer equation relevant for pulsars in Lorimer et al. (2004) we have:

$$\mathrm{S/N} \propto \frac{G\sqrt{t_{\mathrm{int}}\Delta f}}{T_{\mathrm{sys}}} \tag{2.1}$$

in which S/N represents the integrated pulse S/N, G the telescope gain, t_{int} the pulse subintegration time, Δf the bandwidth, and T_{sys} the telescope's system temperature. Thus subintegration time, bandwidth, and gain are all important observational parameters, with G/T_{sys} most significantly impacting the reduction of radiometer noise, assuming we are comparing sensitivities for the same slice in frequency, and given that the telescopes are all equipped with receivers having state-of-the-art T_{sys} levels. (Throughout this paper, pulse S/N will refer to the ratio of the peak pulse amplitude to the standard deviation of the mean-subtracted off-pulse amplitudes.)

Pulsar timing arrays (PTAs) aim to detect perturbations due to GWs (Sazhin 1978, Foster & Backer 1990) in TOAs from millisecond pulsars (MSPs) on the order of 100 ns (Jenet et al. 2004) after the TOAs are corrected for many other effects. These include terrestrial clock calibration, solar system ephemeris, vari-

ations in dispersion measure (DM; proportional to the integrated LOS electron column density), proper motion, and position errors, all in the presence of noise due to other GWs at the source pulsars themselves. While the modeling uncertainties due to all the effects just listed are significant, GWs should perturb TOAs in a correlated way across the sky as a function of angle-of-separation between pulsars (Hellings & Downs 1983). This correlation makes the detection criterion less sensitive to any systematic errors in the TOAs or in the timing model for any one pulsar. Detectable strains (spatial strains due to GWs; h) are expected to be on the order of $h \sim 10^{-15}$ at nHz frequencies (Sesana 2013). Plausible sources producing GW strains in the PTA frequency range include: a stochastic background of GWs (Detweiler 1979, Hellings & Downs 1983) due to merging supermassive black hole binaries (SMBHBs), continuous wave sources from individual SMBHBs in $z < 1.5$ galaxies (Sesana et al. 2009), bursts on timescales of months from SMBHBs in highly elliptical orbits (Finn & Lommen 2010), cosmic strings (Starobinskiĭ 1979, Sanidas et al. 2013), phase transitions in the early universe (Caprini et al. 2010), and relic GWs from the era of inflation (Grishchuk 2005). Additionally, PTAs make possible the detection of GW bursts-with-memory, signals that are anticipated from events such as the final merger of SMBHBs and potentially from exotic phenomena at extremely high redshift (van Haasteren & Levin 2010, Cordes & Jenet 2012, Madison et al. 2014).

Through the IPTA consortium, all three PTAs (NANOGrav, the EPTA, and the PPTA) share timing data from their seven different observatories. The seven telescopes have different receivers, backend instruments, sensitivities, and radio frequency interference (RFI) environments, and have been observing their selected sets of pulsars for a range of epochs. Each telescope also has a history of regularly improving instrumentation, and thus TOAs obtained at later times are often of a

much higher quality than those from earlier times. This trend is helpful for timing precision, but a wider bandwidth may require a more complicated frequency-dependent pulse profile model, due to frequency-dependent pulse shapes (Liu et al. 2014, Pennucci et al. 2014). Differences amongst PTAs include the number of standard observing frequencies and the methods for modeling DM variations. Fortunately, many of these difficulties in data combination are not insurmountable, and tremendous progress has already been made (see Manchester & IPTA 2013). The benefits of such a combination are many, and include an improved cadence, cross checks, better frequency coverage, and more pulsars correlated across the sky.

Apart from the need to combine data from many telescopes, there is also the need to better understand what might intrinsically limit timing quality. PSR J1713+0747 (Foster et al. 1993) is regularly observed by all IPTA telescopes, and provides much of the sensitivity for GW upper limit calculation (Arzoumanian et al. 2014) with a timing stability of ~ 100 ns on timescales of five years or more (Verbiest et al. 2009). In contrast, the first MSP discovered, PSR B1937+21, is well known to be extremely stable on the order of weeks to months, but its residuals show a significant red noise power spectrum visible on timescales of years (Kaspi et al. 1994). As we design larger telescopes and observing programs, it is imperative that we know the fundamental limits of timing precision, i.e. at what point additional gain, observing time, or bandwidth will not increase our timing precision.

Upper limit papers such as those by Shannon et al. (2013), van Haasteren et al. (2011), and Demorest et al. (2013) have all calculated GW limits based on TOAs over 5+ years. If the observation duration at a single epoch were increased from the typical subintegration time by a factor of X, the timing precision (in the

absence of other limiting effects) would be naively expected to improve by $\sqrt{X}$ as in Equation 1. This is simply due to the fact that the number of pulses collected would increase, if TOAs (in the absence of GWs) can be fitted to standard timing models such that the residuals are white noise, assuming there are no significant pulse shape changes between observation epochs.

Many properties of a pulsar along its particular LOS are not precisely predictable: DM variations, interstellar scintillation (ISS), scattering variations, and low-level glitches, to name a few. Glitches are not observed in PSR J1713+0747 or in MSPs in general (Espinoza et al. 2011), though they may be present at low amplitudes in many pulsars (see, however, Espinoza et al. 2014) and therefore may act as a limiting factor in searches for GWs; they may be especially problematic sources of noise in searches for GW bursts-with-memory. M28A is another exception (Cognard & Backer 2004), though admittedly this may be because it is particularly young for an MSP.

Pulse phase jitter, which is independent of radio frequency, is also a limiting factor for pulsar timing. Jitter, also known as pulse-to-pulse modulation, was first described in Cordes & Downs (1985) for canonical pulsars, established for PSR B1937+21 by Cordes et al. (1990), and more recently measured in PSR J1713+0747 in Shannon et al. (2014) and Shannon & Cordes (2012). The term refers to the distribution of arrival times of single pulses about the the peak of the averaged template pulse, which have slight offsets in pulse phase. Neither increasing telescope size nor bandwidth eliminates the presence of TOA jitter errors, jitter being both broadband and independent of pulse profile S/N. Generally, the only way to reduce jitter-induced white noise in most pulsars is to increase the observation duration (Cordes et al. 2004), though there are exceptions; see

Osłowski et al. (2013) and Osłowski et al. (2011) for an example of a jitter mitigation technique on PSR J0437−4715.

Table 2.1. Observing Schedule and Parameters

Telescope	Obs. Mode	Start UT	End UT	Min. Subint. Length (s)	Cent. Freq. (MHz)	Bandwidth (MHz)	Min. Channel Width Possible (MHz)	Pulse Profile S/N[a] for Obs. Duration[b]	Time to Stated S/N (hr)[c]
Arecibo	Int[d]	23-JUN 03:17	23-JUN 04:44	-	1382	800	6.25	3138	1.45
Effelsberg	Fold[e]	22-JUN 18:26	23-JUN 03:40	10	1348	200	1.56	473	7.20
GBT	Int	22-JUN 00:56	23-JUN 10:15	-	1497	800	6.25	2200	8.95
GMRT	CF[f]	22-JUN 13:38	22-JUN 21:58	60	1387	33.3	1.04	80	7.63
Lovell	Fold	22-JUN 18:04	23-JUN 05:34	10	1532	400	0.25	404	9.85
Nançay	Fold	22-JUN 22:33	22-JUN 23:30	60	1524	512	16	125	0.95
Parkes	Fold[g]	22-JUN 10:20	22-JUN 16:20	60	1369	256	0.25	344	6.00
LOFAR	CF	22-JUN 18:11	23-JUN 03:00	5	148.9	78.1	0.195	8	8.82
Westerbork	CF	22-JUN 21:46	23-JUN 04:39	10	345[h]	80	8.75	27	4.95

[a]All S/N values are scaled to 512 phase bins. These S/N values are affected by both scintillation and observation length as well as the telescope parameters.
[b]The duration here refers to the duration of the folding portions of a telescope's observation run only.
[c]In addition to observation time, scintillation also significantly influenced these S/N values.
[d]Intensity recording mode (non-folding). Single pulses are the minimum subintegration time.
[e]Normal pulse folding mode, using coherent de-dispersion.
[f]Offline coherent filterbank mode. For these multi-antenna telescopes acting as a phased array, folding and coherent de-dispersion is applied offline.
[g]The Parkes DFB3/4 backend, one of three backends used in parallel, does not apply coherent de-dispersion online.
[h]Observations alternated between 345 MHz and 1398 MHz as center frequencies. Refer to Figure 1 and Table 2 for details.

These considerations motivate observations of PSR J1713+0747 for 24 continuous hours, using nine radio telescopes: the seven IPTA telescopes along with LOFAR (LOw Frequency ARray, van Haarlem et al. 2013, Stappers et al. 2011) in the Netherlands and the GMRT (Giant Meterwave Radio Telescope) in India. See Table 1 for details of the allotted frequencies for each telescope. The duration of 24 hr was chosen because MSP timing has been explored at the hour and week timescales, but not in the intermediate regime. The inclusion of LOFAR provided an ultra-low frequency (110 – 190 MHz) component to the observation, sampling a frequency range that features prominent effects from the interstellar medium. Observing at L-band/1.4 GHz is ideal for studying the timing properties of this particular pulsar, being reasonably bright given its flux spectrum with a power-law of slope of –1.7 (Kuzmin & Losovsky 2001), but not significantly affected by red noise in the timing residuals due to the ISM (Keith et al. 2013). The GMRT filled in the time coverage gap between Parkes and the European telescopes, enabling a continuous 24 hr of observing.

Another major science goal of the global PSR J1713+0747 observation relates to the LEAP project (Large European Array for Pulsars; Bassa et al. 2016, Kramer & Champion 2013), which uses the Effelsberg, Nançay, Lovell, WSRT, and Sardinia radio telescopes as a phased array, together as sensitive as Arecibo, with a comparable total collecting area ($3 \times 10^4\,\mathrm{m}^2$), but with a much greater observable declination range than Arecibo. As PTAs advance, this configuration may prove to be critical for the detection of GWs. The 24-hr global observation of PSR J1713+0747 helps the LEAP effort by adding three more telescopes – Arecibo itself, as well as the Green Bank Telescope and the GMRT. The present dataset therefore opens up the possibility of experimenting with a telescope having over twice the collecting area of Arecibo alone. The combined effort will be referred to

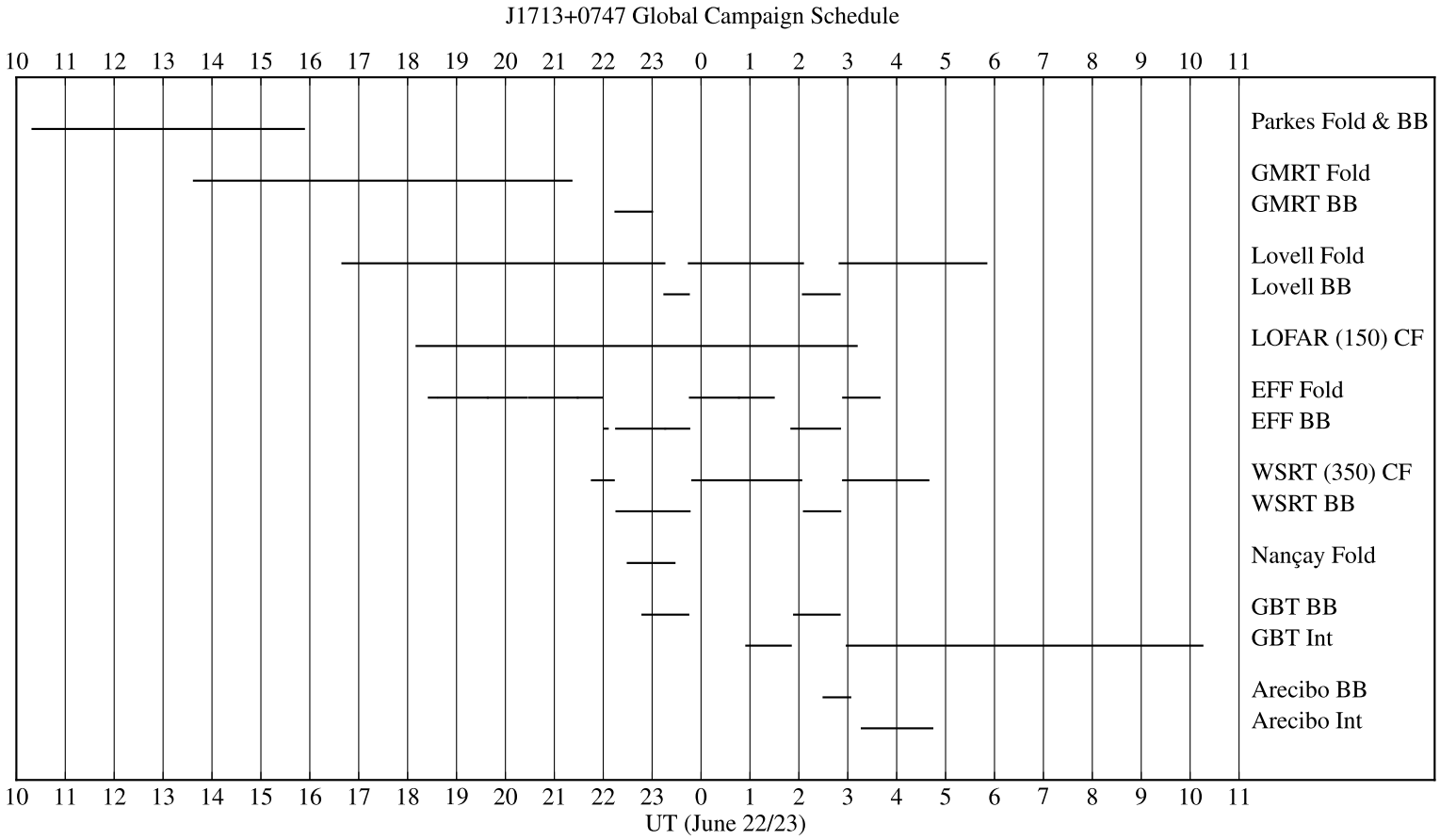

Figure 2.1: Timeline of the global observation of PSR J1713+0747, showing the various telescopes and observing modes. Here, "Fold" refers to ordinary pulse folding with coherent de-dispersion. "BB" refers to baseband mode at L-band/1.4 GHz, recording complex voltages without folding. "Int" refers to intensity integrations, also known as "coherent search mode", which is similar to baseband mode except recording an intensity rather than full voltage information. "CF" refers to the offline coherent filterbank mode used at LOFAR and WSRT, in which the telescope recorded a coherent sum (tied-array beam) of all the antennas, which was written out as complex voltages and then coherently de-dispersed and folded offline.

Table 2.2. Baseband Observing Parameters

Telescope	Obs. Mode	Start UT	End UT	Cent. Freq. (MHz)	Bandwidth (MHz)
Arecibo	BB[a]	23-JUN 02:30	23-JUN 03:00	1378	200
Effelsberg	BB	22-JUN 22:15	22-JUN 23:45	1396	128
	BB	23-JUN 02:05	23-JUN 02:50	1396	128
GBT	BB	22-JUN 22:15	22-JUN 23:15	1378	200
	BB	23-JUN 01:50	23-JUN 02:52	1378	200
GMRT	BB	22-JUN 22:24	23-JUN 00:00	1387	33.3
Lovell	BB	22-JUN 22:14	22-JUN 23:44	1396	128
	BB	23-JUN 01:47	23-JUN 02:56	1396	128
Parkes	BB	22-JUN 10:20	22-JUN 16:20	1369	256
Westerbork	BB	22-JUN 22:16	22-JUN 23:45	1398	128
	BB	23-JUN 02:05	23-JUN 02:51	1398	128

[a]Baseband voltage recording mode

in the present paper as GiantLEAP.

This dataset also represents a unique opportunity to measure clock offsets between telescopes and how they vary across overlapping time intervals. When combining TOAs from different telescopes (or when backends change on a single telescope) an offset or "jump" is needed. Such a jump can be due to delays in the backends themselves, such as cable delays, conspiring with factors that are difficult to quantify individually (see Lommen & Demorest 2013 and Kramer & Champion 2013 for further explanation). The jumps can then be quantified by fitting for one arbitrary timing offset per telescope/backend pair per frequency only in the overlapping region, such that the rms of the combined dataset is minimized. Simultaneous observations – the longer the better – provide an opportunity to measure such offsets and their drifts with high accuracy.

Timing stability on the ~ 24 hr timescale can also be quantified using the Allan variance of the residuals. The Allan variance was originally used to quantify the stability of atomic clocks (see Matsakis et al. 1997 for details). The present dataset allows us to evaluate the Allan variance for clock frequencies of 10^{-2} Hz all the way into frequencies corresponding to the five or even twenty year datasets (Zhu et al. 2015) that exist for PSR J1713+0747.

Yet another goal of the PSR J1713+0747 24-hour global campaign is to assess a noise floor. How does rms precision increase as longer timespans of data are analyzed? Does the improvement "bottom out" or continue indefinitely with the number of collected pulses on these timescales?

We intend the present paper to be a description of the data set itself as well as being an introduction to a series of papers, given the size of the dataset and the large number of science goals. Here we present some first science results, and intend to expand upon them and address other topics in later papers. In §2, we describe the observation and the resulting dataset in detail, supplemented by the Appendix. In §3, we explore a number of first results emerging from the all-telescope analysis. §4 shows some general first results on the timing error budget, and finally §5 mentions some future paper topics based on the data.

2.2 Description of the Data

The observations were conducted on 22 Jun 2013 (MJD 56465 – 56466) starting with the Parkes Telescope and progressing through the other eight telescopes for as much time as possible between rise and set. The observation timeline can be seen in Figure 1. The time of year was such that local midnight roughly corresponded

to the middle of each telescope's observation. PSR J1713+0747 was approximately 146° from the Sun, minimizing the possibility of any solar effects on the data (You et al. 2007).

As Figure 1 shows, there were different modes used amongst the telescopes – ordinary pulse folding, baseband mode, coherent filterbank mode (formed offline), and non-folded intensity integrations (also known as "coherent search mode"). For ordinary pulse folding, coherent de-dispersion is applied in real time (Hankins & Rickett 1975), correcting for pulse delays due to dispersion in the ISM across few-MHz channels (with the exception of the DFB backends at Parkes in which de-dispersion is applied after the fact – see Appendix). All the non-baseband data presented here have coherent de-dispersion applied. Observing in baseband mode affords a number of advantages. For the science goal of expanding LEAP with Arecibo and GBT, baseband recording is a requirement of any phased array formed offline. It also allows us to evaluate how cyclic spectroscopy (Demorest 2011, Walker et al. 2013, Stinebring 2013) might improve the quality of some of the dataset as a method of obtaining a significantly higher frequency resolution (Archibald et al. 2014), Jones et al. 2014, in preparation). The baseband sessions were driven by when the transit telescopes (Arecibo and Nançay) could observe the pulsar. Hence, the first baseband session was when the source transited at Nançay, when baseband data was obtained at GMRT, Lovell, Effelsberg, Westerbork, GBT and Nançay, while the second session was when the source transited at Arecibo, and baseband data was obtained with the Lovell, Effelsberg, Westerbork, GBT and Arecibo telescopes. Non-folded intensity integrating is similar to baseband mode, except that intensities rather than signed voltages are recorded, without phase information, resulting in a more manageable data size. Both baseband data and non-folded intensity recording yield single pulse information. Otherwise, single

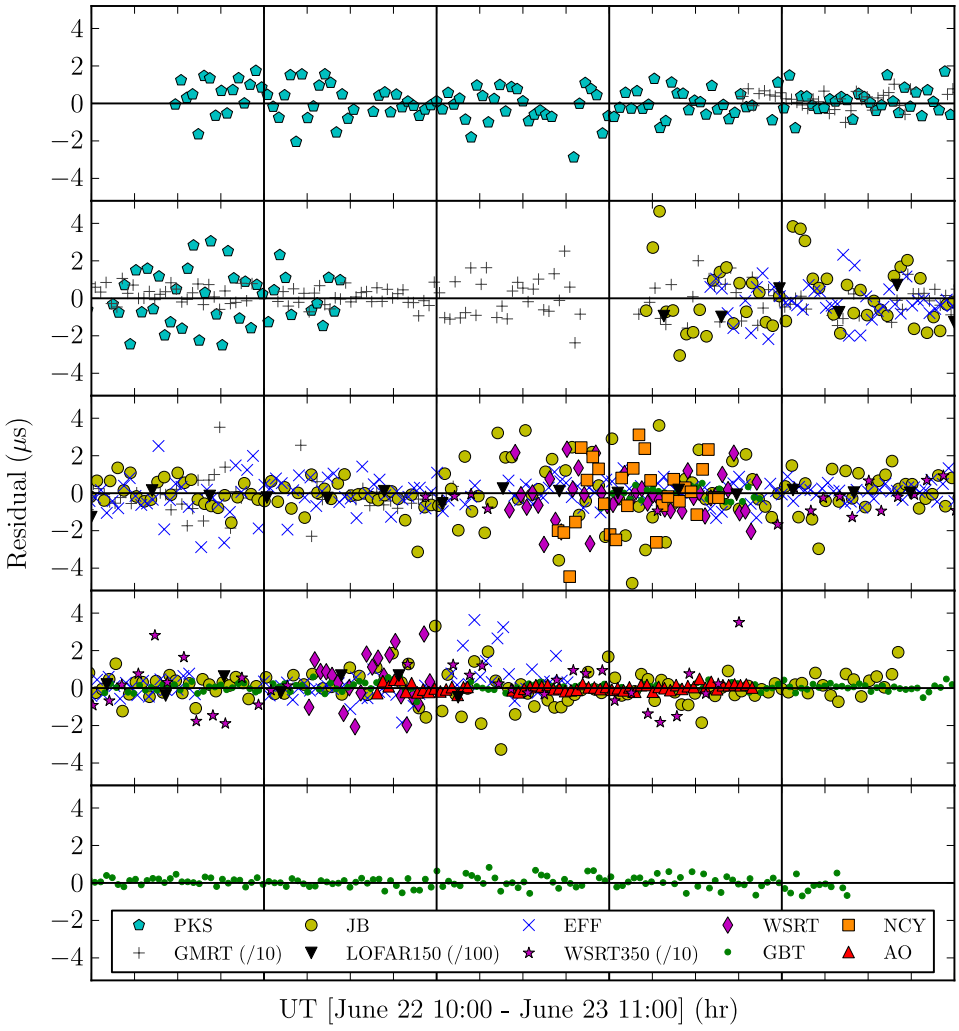

Figure 2.2: 24-Hour Timing Residuals: timing residuals for the nine telescopes as a function of time. Values shown are for L-band/1.4 GHz observations unless otherwise noted. Uncertainties on each residual are not shown here in order to maintain clarity. In all cases, the fitting error on individual residuals is on the order of the scatter of all residuals shown for a particular telescope. All residual values are for 120 s integrations, except LOFAR which is for 20 min. The increase in residual values in the third and fourth rows from the top is due to most telescopes having switched to the lower bandwidth baseband mode. Residual values from the GMRT, WSRT-350 MHz, and LOFAR-150 MHz are scaled down by factors of 10, 10, and 100 respectively in order to show all residuals in a single panel.

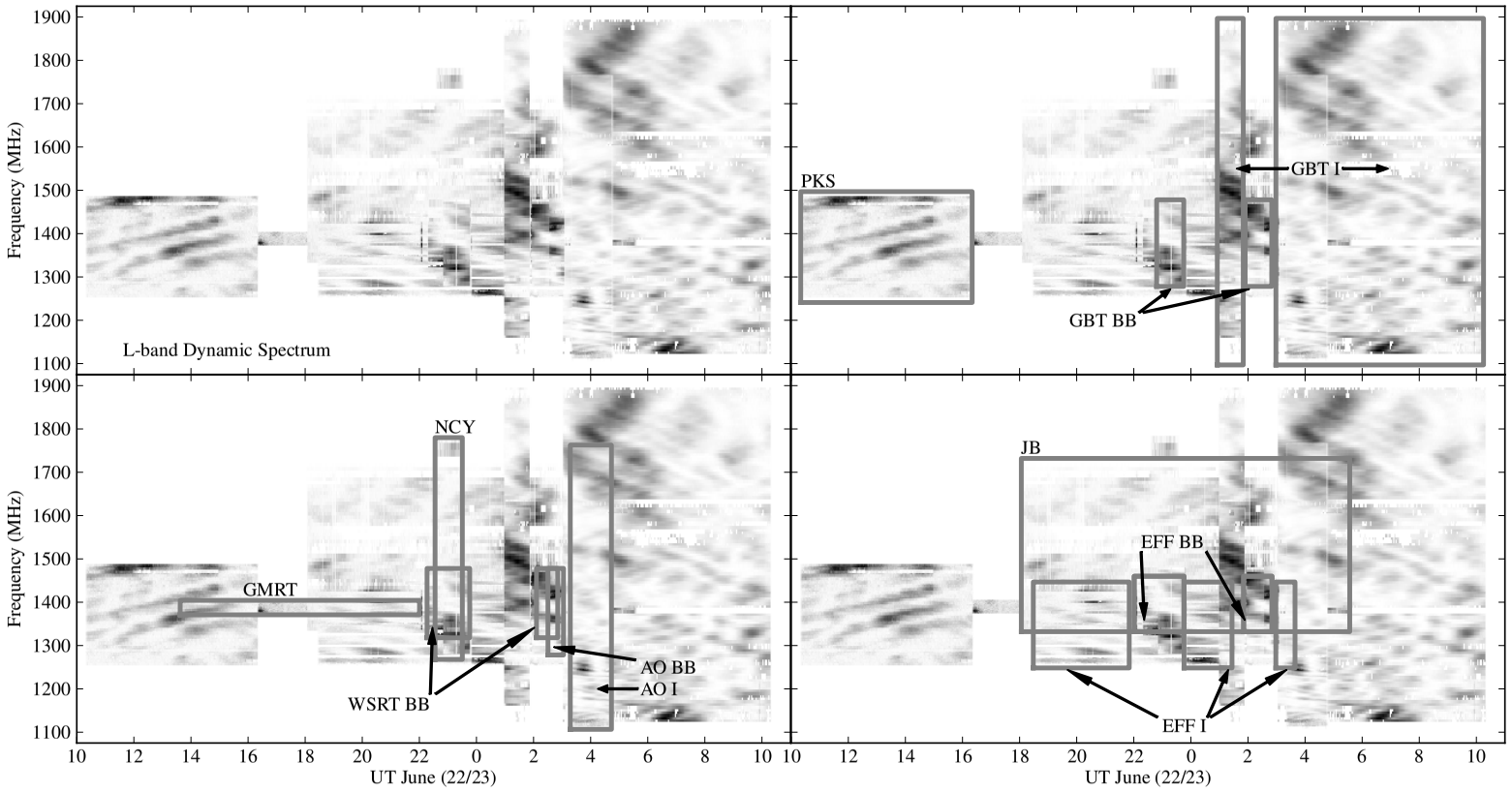

Figure 2.3: Dynamic Spectrum: L-band/1.4 GHz dynamic spectrum for 8 of the 9 telescopes (excluding LOFAR at 150 MHz and WSRT at 350 MHz). Note the narrowing of the scintillation bandwidth as a function of frequency, along with a decrease in scintillation timescale with decrease in frequency. Scintillation patterns are shown to overlap well between telescopes, thus establishing (in §3.3) a typical spatial scale for the scintillation pattern. A cross-hatched pattern is clear, which is usually only observable at low frequencies, but observable here because of the large bandwidth and 24-hr observation time. When observations overlap, the regions of the dynamic spectrum shown are from telescopes with the highest sensitivity per patch $dA = d\nu dt$.

pulses are not recoverable due to the folding process.

Baseband was not, in general, the default observing mode. Taking baseband data for the entire rise-to-set time at each telescope would be cumbersome in terms of data volume (which as it is approached 60 TB total largely due to the baseband component) and in some cases would also limit bandwidth. For example, in the case of the GUPPI/PUPPI backends (Green Bank / Puerto Rican Ultimate Pulsar Processing Instrument; DuPlain et al. 2008), baseband recording can only be conducted over 200 MHz of bandwidth, as opposed to the 800 MHz available for the folding and intensity integration modes. The overlapping baseband portion of the observation for GiantLEAP consisted of two baseband allotments (see Figure 1). Arecibo could only participate in one of these sessions due to the limited range in zenith angle. Parkes observed with baseband data taking in parallel for its entire observation duration.

Reduced profiles are in the PSRFITS format processed with the PSRCHIVE and DSPSR software packages (Hotan et al. 2004, van Straten et al. 2012), with final timing residuals determined by the TEMPO2 software package (Hobbs et al. 2006). Residuals are generated with a common TEMPO2 parameter file, after having produced TOAs with PSRCHIVE based on standard observatory-specific template pulse profiles, noise-reduced using PSRCHIVE when necessary. Different profiles are used because of local bandpass, frequency range, and calibration differences. We create TOAs from 120 s fiducial subintegrations in common between L-band/1.4 GHz telescopes. This choice of subintegration time was a compromise between, on the one hand, having a sufficient number of TOAs in order to probe timing precision on long timescales (see §3.1), and on the other, having a minimum TOA S/N of approximately 1 across all L-band/1.4 GHz telescopes (see §3.2 for an application

to measuring jitter). Further details about specific telescopes can be found in the Appendix and in Table 1, in which the S/N of each telescope's 120 s TOAs can be found, with baseband details in Table 2. As can be seen in Table 1, the possible minimum subintegration length is less than 120 s for most telescopes, providing flexibility for future studies. Slots in which the table is blank indicate intensity integrations, which can be integrated to any time greater than $2/\Delta\nu$, where $\Delta\nu$ is the channel width. WSRT, GMRT, and LOFAR, being multi-antenna telescopes, observed in a tied-array mode (formed online) which dumped complex voltage data to be coherently de-dispersed and folded using DSPSR. We refer to this as the "coherent filterbank" mode because a filterbank is formed offline, except for GMRT, for which we still refer to the modes used as folding and baseband, given the additional optimization employed (see Appendix for details).

We remove RFI automatically in post-processing using PSRCHIVE. The program defines an off-pulse window by iteratively smoothing the profile and finding the minimum. Using the maximum minus minimum intensity values defined in this window, we apply a median filter to identify RFI spikes and flag spikes at greater than $4\,\sigma$ from half the intensity difference. Any remaining particularly noisy frequency channels or time integrations are manually removed after visual inspection. At Lovell, RFI is excised in real time. For the other telescopes, post-facto algorithms are used – one that excises "rows" and "columns" of RFI in frequency and time, and another that excises RFI within the pulse profile itself according to bad phase bins.

The residuals shown in Figure 2 were generated by folding the respective data sets from each individual telescope with a parameter file that was created from 21 years of PSR J1713+0747 data (Zhu et al. 2015), all with the same Bureau

International des Poids et Mesures (BIPM) correction table to the global atomic timescale, TT(BIPM2012), with the 2013 extrapolation, and the Jet Propulsion Laboratory DE421 planetary ephemeris. The DM ($15.99113 \pm 0.00001\,\mathrm{pc\,cm^{-3}}$) is the only fitted astrophysical parameter determined from the present observation across all L-band/1.4 GHz telescopes simultaneously. Relative offsets were also fitted between telescopes. These are simply free parameters that align the residuals and do not represent absolute clock offsets, and are not shown here for this reason. The remainder of the parameters were held fixed at the Zhu et al. (2015) values (see Table 3 in the Appendix for further details). The timing residuals at other, higher subintegration times are computed from this base set of residuals. To test that residuals can be averaged down without a loss in modeled timing precision, we also generated a set of 10 s subintegration time TOAs with PSRCHIVE from the GBT, and found that simply averaging the 10 s residuals produced new residuals with rms values different from the 120 s TEMPO2 residuals at $\ll 1\,\sigma$. Therefore, we can create 10 s residuals, average them, and obtain nearly identical 120 s residuals to those resulting from 120 s TOAs.

The eight telescopes at L-band/1.4 GHz saw a changing spectrum due to interstellar scintillation, as shown in the dynamic spectrum, or plot of pulsar intensity vs. time and frequency, in Figure 3. Scintillation is due to the scattering and refraction of pulsed emission in the ionized ISM, and can significantly change the pulse profile S/N as can be seen in Table 1. Figure 3 shows that bright scintles contribute to the high S/N of telescopes after about 23-JUN 00:00. The image was created by fitting the telescopes' templates via matched filtering for a given telescope with a given profile $P(\nu, t)$ and reporting the amplitude with the off-pulse mean subtracted. Amplitudes are converted to corresponding intensities depending on each telescope's calibration data and then scaled to an identical color scaling

for Figure 3. Dynamic spectra from different telescopes were scaled empirically to match them in Figure 3, lacking absolute calibration for some telescopes, but using the noise diode calibrations employed (see Appendix for details). A cross-hatched pattern is clear. Such a pattern is usually only observable at low frequencies due to the small scintle size in frequency and time even for modest bandwidths (Rickett 1970). Note the narrowing of the scintillation bandwidth (Δ_ν, the typical scintle width in frequency) as a function of frequency, along with a decrease in scintillation timescale (Δ_t, the typical timescale for scintillation) with decrease in frequency. Scintillation patterns are shown to overlap well between telescopes, thus establishing a typical spatial scale of a waveform – see §3.3. In some cases there appear to be deviations between the scintillation patterns seen at different telescopes, but this always corresponds to times when the source was close to rising or setting at one of the telescopes involved.

Narrowband template fitting (Taylor 1992) assumes a relatively constant profile with frequency. In addition to distorting the pulse phase, merely averaging across frequency would result in drifting residuals with a non-white appearance (Craft 1970), due to the intrinsic profile evolution acting in combination with ISS. Profile shape changes with frequency are present in all canonical pulsars – see Hankins & Rickett (1986) for multifrequency observations on many pulsars, and Hassall et al. (2013) which uses observations from LOFAR and other telescopes. Similar shape changes have also been found in MSPs (Kramer et al. 1999), including PSR J1713+0747.

Figure 4 shows the presence of profile evolution with frequency in this observation's GBT data. Starting with 8 hrs of GBT data, we use the fiducial subintegration length of 120 s and a subband size of 50 MHz. We sum profiles in time to get

16 profiles as a function of observing frequency and phase, $P(\nu, \phi)$. These profiles are de-dispersed using the best fit, L-band/1.4 GHz DM. For each $P(\nu, \phi)$, we fit a NANOGrav standard template $T(\phi)$ to the data profile $P(\nu, \phi)$ to find the best-fit phase offset $\delta\phi(\nu)$ and amplitude $A(\nu)$. We create difference profiles by shifting and scaling $T(\phi)$ using the best fit phase offset $\delta\phi(\nu)$ and amplitude $A(\nu)$ for each frequency and then subtracting as $D(\nu, \phi) = P(\nu, \phi) - A(\nu)T(\phi - \delta\phi(\nu))$, where $D(\nu, \phi)$ are the difference profiles. These are plotted in the main panel of Figure 4. The right panel shows the timing offsets as a function of frequency, $\delta\phi(\nu)$, with the 1422 MHz profile set to zero offset because the template most closely resembles these data in the center of the band. These timing offsets will be dependent on the value of our measured DM, which in turn is dependent on the frequency dependent (FD) model parameters (Arzoumanian et al. 2015) used in TEMPO2. The FD parameters correspond to the coefficients of polynomials of the logarithm of radio frequency that show the TOA shift due to profile evolution. If the profile evolution within a subband is small and if the FD model parameters quantify the offsets well when each subband is independently used to create a set of timing residuals, then the weighted broadband residuals should be consistent with the white noise expected from scintillation. As Figure 2 shows for all the telescopes, the residuals are qualitatively white noise-like in character. The broadband weighting, then, appears to correctly take the profile evolution / scintillation interaction into account. The profile evolution shown with frequency in Figure 4 is likely to be intrinsic and not an instrumental artifact because the equivalent Arecibo plot (i.e. using a different receiver at a different telescope) is nearly identical across the same bandwidth. A more detailed analysis of the observed profile frequency evolution is a subject of future work.

We address this profile-evolution problem for all telescopes with bandwidths of

100 MHz or more (that is, all telescopes except the GMRT) by computing TOAs for multiple narrow frequency channels, using PSRCHIVE as described above. For the GBT and for Arecibo, the band is divided into 16 bins of 50 MHz each. The data from the other telescopes are split into subbands in similar fashion. We then obtain sets of narrowband timing residuals using the FD parameters in TEMPO2. The four best-fit FD parameters can be found in Table 3 in the Appendix, representing third-order polynomial coefficients starting with the lowest order first. We then perform a weighted mean of these values in order to obtain the broadband residuals. For all telescopes we use the FD parameters with TEMPO2 independently computed from (Zhu et al. 2015; provided as preliminary values prior to publication).

Intrinsic pulse profile evolution is thought to arise from varying offsets between the emission region and the surface of the neutron star, with higher frequency emission being produced closer to the surface (see Cordes 2013 for a more detailed discussion). If a profile at a high narrowband frequency differs significantly from a profile at a low narrowband frequency, then any frequency-dependent pulse shape changes will be highly covariant with the DM measurements at each epoch. Multi-frequency timing minimizes such covariances. The timing offsets due to intrinsic pulse shape changes with radio frequency are constant in time. Effects due to interstellar scintillation and scattering will depend on time, however. The former produces a varying S/N across the band due to scintillation that changes the relative weighting of each subband as part of the final TOA; the latter broadens the pulse, resulting in a scattering delay. (The L-band/1.4 GHz frequency is chosen, for the present dataset and for most standard timing observations, so that scatter broadening is minimal.)

2.3 Analysis of the Multi-Telescope Data

The following assumptions and terminology will be used throughout this section:

The rms of the timing residuals over the total time span is consistent with the errors expected from a finite S/N ratio and from single-pulse stochasticity that is intrinsic to the pulsar. From Cordes & Shannon (2010), finite S/Ns yield an approximate template fitting error of

$$\sigma_{\mathrm{S/N}} = \frac{W_{\mathrm{eff}}}{S(N_\phi)\sqrt{N_\phi}}, \tag{2.2}$$

where $S(N_\phi)$ is the S/N of the pulse profile (peak to rms off-pulse) that has N_ϕ phase bins and W_{eff} is the effective pulse width. Cordes & Shannon (2010) give an expression for W_{eff} that we use for PSR J1713+0747, yielding 0.54 ms.

Here, N_ϕ is included because for the GMRT, N_ϕ was 64, while for the other telescopes, N_ϕ was 512, and this difference has been noted in all relevant calculations. These values for N_ϕ are chosen such that N_ϕ is small enough to afford sub-μs timing precision at some telescopes, while at the same time, producing a $S(N_\phi)$ small enough such that the pulse peak measurement is reasonably accurate. When we use $\sigma_{\mathcal{R}}$, it will refer to the total residual rms, whether template fitting error, jitter, radiometer white noise, or white noise due to the ISM.

2.3.1 Timing Residual Precision vs. Integration Time

In Figure 5 we show the logarithmic change of the L-band/1.4 GHz TOA residual rms, a proxy for timing precision, as both a function of subintegration time T and of the corresponding number of pulses N. The time per TOA is plotted on the

abscissa, and the corresponding number of pulses for each residual subintegration time is also shown. The ordinate shows the rms of the residuals within the entire observation time of the telescope. For this reason, the data points for Arecibo do not extend to as long of a timescale as the other telescopes despite the high sensitivity. We start from TOAs from the base subintegration time of 120 s, and integrate down (i.e. to larger subintegrations) for each successive step. We show this function for five of the L-band/1.4 GHz telescopes, choosing the maximum integration time at each telescope which corresponds to at least eight subintegrations in order to ensure that small-number statistics (due to having only a few long-subintegration residuals) are not important. Nançay and WSRT are not shown because of their short, non-contiguous observing times. GMRT's residuals did not probe small values of N and are not shown. Error bars are $1\,\sigma$ and are simply the standard error of the scattered subintegration rms values in a block of TOAs. For reference, the expected $1/\sqrt{N}$ slope is plotted. Each successive data point is not independent of the data points in Figure 5 for small values of N. In all telescopes, there are no significant deviations from this simple improvement in timing rms with number of pulses collected. This is expected behavior for the backends used in this observation (see Stairs et al. 2002 that uses data from PSR B1534+12 as a demonstration that this kind of integrating-down behavior works efficiently for coherent de-dispersion machines in contrast to filterbank machines). For PSR J1713+0747, this means that on timescales of ~ 1 hr (the largest time which on this timescale we can make multiple samples with a minimum of eight TOAs), there is no significant evidence of an absolute noise floor.

The comparative sensitivity of the telescopes can be seen along with the fact that longer tracks produce smaller uncertainties in the residual rms $\sigma_{\mathcal{R}}$. Arecibo and GBT have up to eight times the bandwidth as some of the other telescopes and,

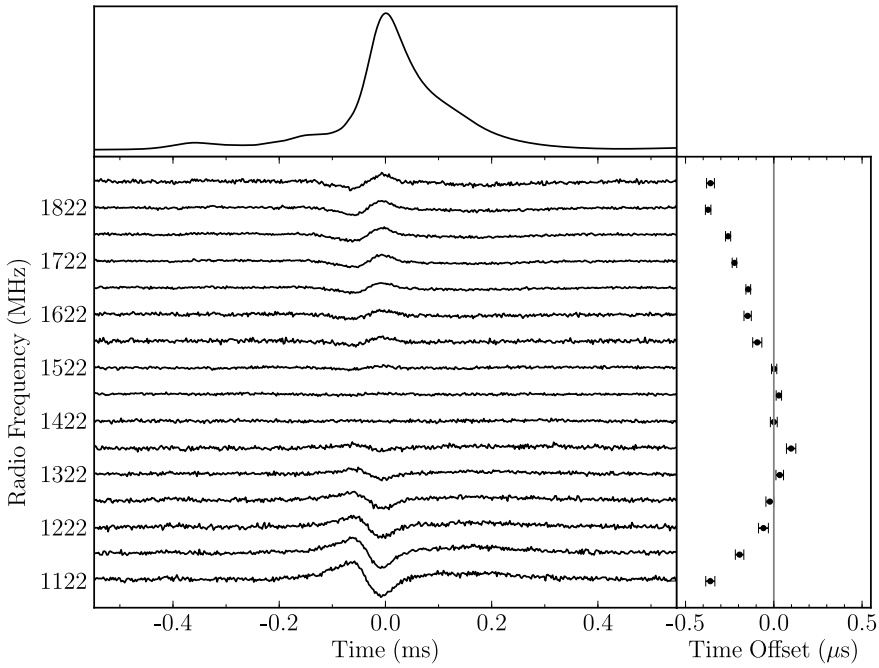

Figure 2.4: Differential offset times vs. frequency for the GBT. The top panel shows the standard NANOGrav template used for GUPPI at L-band/1.4 GHz. The main panel shows the difference profiles as a function of frequency, calculated by subtracting a best-fit template from the data profiles. The right panel shows the mean-subtracted, best-fit phase offsets for each data profile versus frequency. These offsets are a function of the FD (frequency dependent) polynomial parameters in TEMPO2 that model timing offsets due to pulse profile frequency evolution. The shape of the time offset vs. frequency curve is covariant with any residual dispersion delay across the band.

considering also the sensitivities, fall significantly beneath the others in terms of timing rms. Previous studies of PSR J1713+0747 (Shannon & Cordes 2012) have shown a tracking of this $1/\sqrt{N}$ for an N of 1 to 10^5, corresponding to subintegration times of 4.57 ms to 457 s.

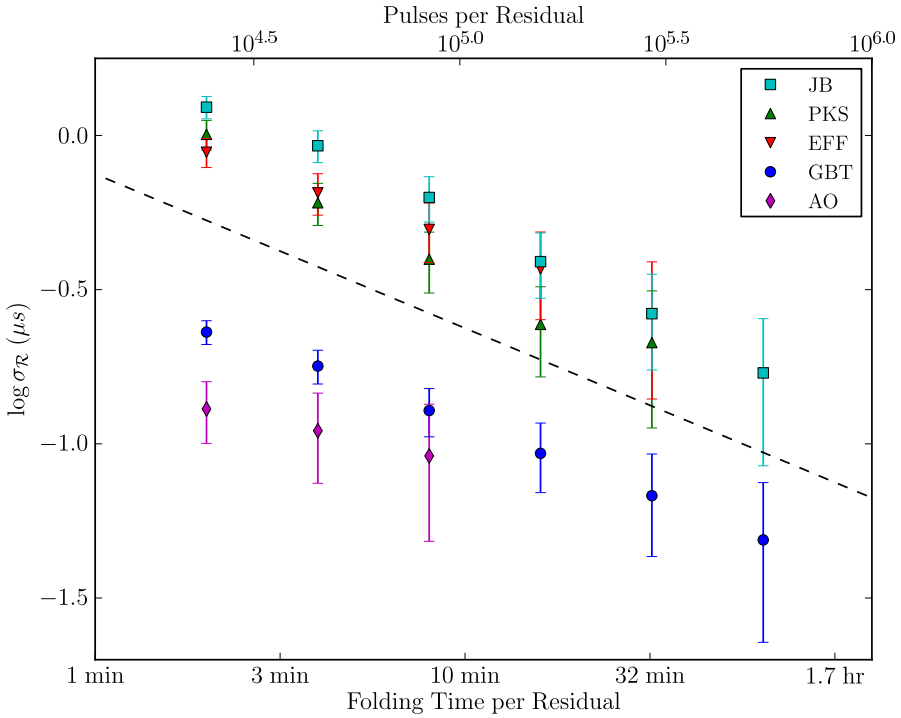

Figure 2.5: Improvement of L-band/1.4 GHz timing rms with number of collected pulses N. Both subintegration time per residual and number of pulses are shown in the abscissa for reference. Symbols, from top to bottom: teal squares, Lovell/JB; green upward triangles, Parkes; red downward triangles, Effelsberg; blue circles, GBT; magenta diamonds, Arecibo. Error bars are the standard error of the scattered rms values. The dashed lines show a $1/\sqrt{N}$ law for reference. The residuals are derived from telescopes with different bandwidths, and the resulting timing rms values are dependent both on collecting area and bandwidth.

2.3.2 Timing Residual Precision From Template Fitting and Pulse Jitter

Radiometer noise is always reduced by additional bandwidth but jitter noise, measurable in high S/N timing observations, is not improved because it is identical and correlated across frequency. Thus, the minimum expected rms in the broadband timing residuals is somewhat higher than what we would predict from merely reducing the narrowband timing rms by the increased bandwidth factor. The error from

jitter, given in Cordes & Shannon (2010), is $\sigma_{\rm J} \propto W_{\rm eff}/\sqrt{N}$. The noise value $\sigma_{\rm J}$ has no dependence on bandwidth or telescope sensitivity. Knowing how much the rms for an individual TOA would be composed of $\sigma_{\rm J}$ typically requires either directly measuring the jitter via single pulses, or measuring the correlated TOAs across frequency. Shannon & Cordes (2012) report a value of $26\,\mu$s for a single-pulse $\sigma_{\rm J}$ from PSR J1713+0747 also based on Arecibo observations, using both measurement methods. Shannon et al. (2014) have also measured PSR J1713+0747's single pulse phase jitter rms as $31.1 \pm 0.7\,\mu$s. Here, we show the presence of jitter in PSR J1713+0747 by demonstrating the non-dependence of a noise component on telescope sensitivity.

In order to directly measure the presence of jitter in Figure 6, we binned residuals from *all telescopes* into approximately eight bins/decade in S/N and then took the scatter of the arrival times within each bin, $\sigma_{\mathcal{R}}$. The subintegrations used were 120 s within frequency bins of ~ 50 MHz, and only residuals for which S/N > 1 were included.

We fit a curve given by the following equation, which comes from the assumption that the white noise timing residuals, $\sigma_{\mathcal{R}}$, are composed of two other white noise components added in quadrature:

$$\sigma_{\mathcal{R}} = \sqrt{\sigma_{\rm J}^2 + (\sigma_{S_0}(S_0/S))^2} \tag{2.3}$$

where S simply represents S/N, S_0 refers to a particular fiducial S/N, and σ_{S_0} is the timing rms due to template fitting. Using the fiducial 120 s TOAs, we find that $\sigma_{\rm J} = 0.17 \pm 0.02\,\mu$s, which implies a single pulse jitter of $27.0 \pm 3.3\,\mu$s, consistent with the measurement in Shannon & Cordes (2012) of $26\,\mu$s. This value is also consistent within $< 2\,\sigma$ of the more recent measurement of Shannon et al. (2014). The other fitted parameter, $\sigma_{\rm S_0=1}$, signifying the white noise value in the absence

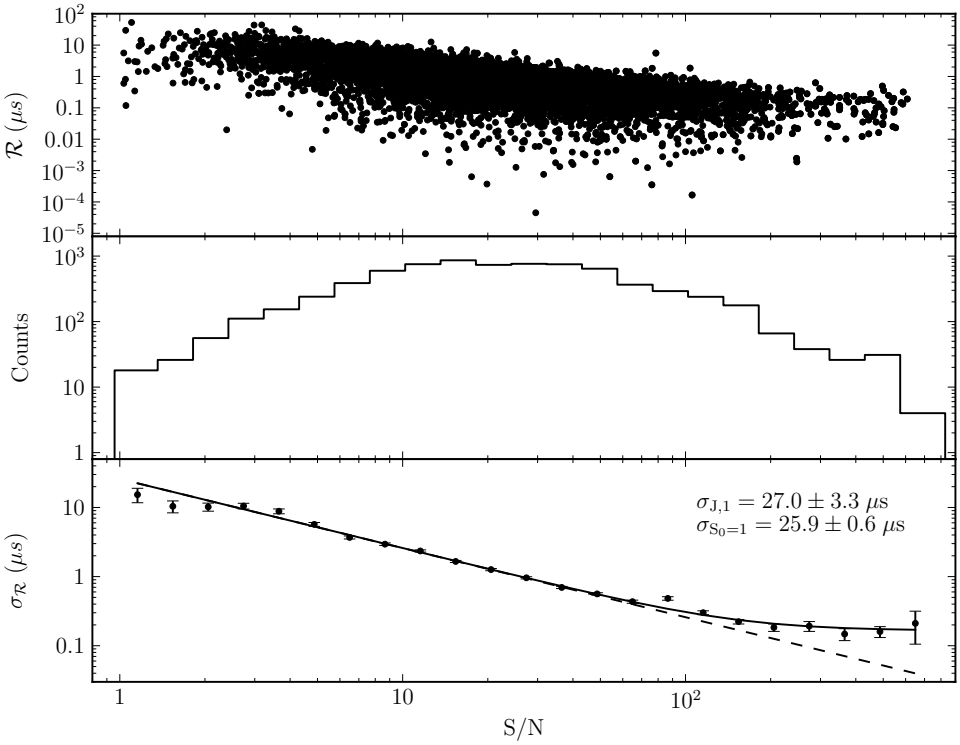

Figure 2.6: Improvement of residual rms with S/N, for ~ 50 MHz timing residuals. Shown in the top plot are the timing residual values as a function of S/N, using data from all telescopes. The middle plot shows the number of residuals in each bin. In the bottom plot, rms values on the residuals are shown using logarithmic bins with 8 bins/decade. We fit Equation 3 shown as the solid line fit, which yields a white noise in the timing residuals due to pulse phase jitter of $\sigma_{J,1} = 27.0 \pm 3.3\,\mu$s. Scaled to 120 s integrations, $\sigma_J = 0.17 \pm 0.02\,\mu$s. All residuals shown in the top panel of Figure 6 are for an integration/folding time of 120 s, removing residuals below an S/N of 1. The single pulse jitter timing rms is $\sigma_{J,1}$, and $\sigma_{S_0=1}$ is the timing rms in the absence of jitter for a S/N of 1. The dashed line represents the expected timing uncertainties in the absence of pulse phase jitter.

of jitter, was $25.9 \pm 0.6\,\mu$s.

The presence of jitter in PSR J1713+0747 does mean that for a telescope as sensitive as Arecibo, LEAP, or GiantLEAP, including the future Square Kilometer Array (SKA) or the Five-hundred-meter Aperture Spherical Telescope (FAST)

telescopes, both $\sigma_{\rm J}$ and the ordinary timing rms scale as $1/\sqrt{N}$ (Cordes et al. 2004, Cordes & Shannon 2010, Lazio 2013). The dominance of pulse phase jitter seen in the Arecibo portion of the present study may necessitate the use of such long tracks for all future highly-sensitive telescopes to further reduce $\sigma_{\mathcal{R}}$. This is seen in a particularly dramatic fashion over eight of the nine telescopes here. Even when using one telescope alone, GBT or Arecibo for instance, the fit to $\sigma_{\mathcal{R}}$ yields $\sigma_{\rm J,1}$ values of $21.6 \pm 4.1\,\mu$s (GBT) and $27.9 \pm 5.3\,\mu$s (Arecibo). The $\sim 1\,\sigma$ consistency of each single-telescope value with the all-telescope value implies that the jitter numbers reported are not telescope-dependent, and are intrinsic to the pulsar as expected.

Single pulse phase jitter causes a timing error $\propto 1/\sqrt{N}$ that is independent of S/N. The two contributions are equal for single-pulse $({\rm S/N})_1 \sim 1$ (Shannon & Cordes 2012). S/N > 1 single pulses should be present, given that a telescope is sensitive to jitter noise (Cordes & Shannon 2010).

A more detailed analysis is deferred to a separate publication. Single pulses can be extracted from any of the observations with baseband data or intensity integrations, which were taken at various times during the global campaign in all nine telescopes. However, it is interesting that fitting Equation 3 across the eight telescopes in Figure 6 allows a jitter measurement without probing into residuals with a subintegration time of $< 120\,$s, much less with single pulses. The residuals in the brightest bin, rescaled to subintegrations of a single period, correspond to a single pulse S/N of ~ 3.

2.3.3 Strong Correlation of Diffractive Scintillation Between Telescopes

Figure 3 shows that the frequency-time structure in the dynamic spectrum is qualitatively identical between simultaneous measurements from different telescopes, apart from low-elevation-angle observations and from masked episodes of RFI. This high correlation includes telescope pairs with the largest separations (up to 9000 km), Parkes and GMRT; GMRT with the European telescopes (Jodrell Bank, Effelsberg, and WSRT), between the GBT and the European telescopes, and between the GBT and Arecibo.

The observations are consistent with the expectation that the dynamic spectra for PSR J1713+0747 should be highly correlated between all terrestrial telescopes because of the low level of scattering along the line of sight. We estimate the spatial scale ℓ_d of the diffraction pattern from the parallax distance $d = 1.05 \pm 0.06\,\mathrm{kpc}$ (Chatterjee et al. 2009) and the scintillation bandwidth $\Delta\nu_d \approx 0.6 \pm 0.2\,\mathrm{MHz}$ at 0.43 GHz (Bogdanov et al. 2002) using Eq. 9 of Cordes & Rickett (1998),

$$\ell_d = \frac{1}{\nu}\left(\frac{cd\Delta\nu_d}{4\pi C_1}\right)^{1/2}, \tag{2.4}$$

where $C_1 = 1.16$ using a default, uniform Kolmogorov scattering medium. This yields $\ell_d \approx 5 \times 10^4\,\mathrm{km}$ at 0.43 GHz and scaling by $\nu^{1.2}$, the diffraction scale at 1.4 GHz is $\ell_d \approx 2 \times 10^4\,\mathrm{km}$, much larger than the Earth.

2.4 Initial Results on the Noise Budget of the Timing Residuals

In this section we briefly consider some aspects of PSR J1713+0747's noise budget, in other words, whether the S/N across telescopes corresponds to expectations from general considerations. A more detailed consideration of the noise budget will be found in a forthcoming paper.

Figure 7 (top panel) shows the grand average profile for the eight telescopes that observed at L-band/1.4 GHz. Low frequencies are shown in the lower panels. Profiles are summed across the full band from individual subbands' residual values, weighted by the off-pulse noise values, and folded according to the measured L-band/1.4 GHz value of DM. The resulting L-band/1.4 GHz profile has a S/N of $\sim$ 4000, where the signal value is taken as the amplitude at the maximum value of the summed pulse and the noise is taken from the off-pulse part of the combined profile. S/N values were calculated using the first 100 bins of the profile for the noise region. The profile was centered at maximum, with $N_\phi = 512$, before summation. See Table 1 for estimates of the degree to which each telescope contributes to the total pulse profile S/N. Low frequency profiles are also shown for reference, showing significant profile evolution with frequency. The pulsar is weak at low frequencies because it appears to turn over somewhere above the LOFAR band (Hassall et al. 2014 in preparation).

The minimum rms on timing residuals from the eight-telescope L-band/1.4 GHz profile can be estimated using Equation 2.2. Given an effective pulse width of 0.54 ms, that we have 512 phase bins, and that the 24-hr pulse profile S/N in the grand average profile was about 4000, this yields a template fitting error, $\sigma_{\mathrm{S/N}}$, of

about 3 ns. Given a 24-hr implied template fitting error of 3 ns and an implied 24-hr jitter timing error of $170/\sqrt{30}/\sqrt{24} = 6.3$ ns (rescaling from the 120 s jitter value given in §3.2 to a 24 hr value), we add these values in quadrature to arrive at an approximate timing uncertainty of 7 ns. Jitter and template fitting alone would then yield a timing residual error of 7 ns on a 24-hr TOA.

The uncertainty from our L-band/1.4 GHz DM measurement of 0.00001 pc cm^{-3} from §2 corresponds to 24 ns of smearing across the band. A better measurement of the DM on MJD 56465 – 56466 would require incorporation of the 150 MHz LOFAR data and the 350 MHz WSRT data, but taking into account a model of the pulse profile evolution with frequency that extends to these lowest two frequencies. Such a model is a topic of exploration for a future paper on interstellar electron density variations. Any discovered DM variations, along with an improved DM smearing value, would need to inform the noise floor assessment.

2.5 Further Work

The initial results presented will be important for the three PTAs and for the IPTA as a whole. For some telescopes, PSR J1713+0747 is timed (or is under consideration to be timed) for longer observation durations at each epoch, or at a higher observing cadence. Being amongst a small set of pulsars with the lowest timing residual rms values, it strongly influences the sensitivity of the entire IPTA, despite the necessity of calculating angular correlations in order to populate the Hellings and Downs diagram and detect a stochastic background of GWs (Hellings & Downs 1983). Increasing the observation duration for these pulsars helps the sensitivity of the IPTA to other types of GW source populations, such

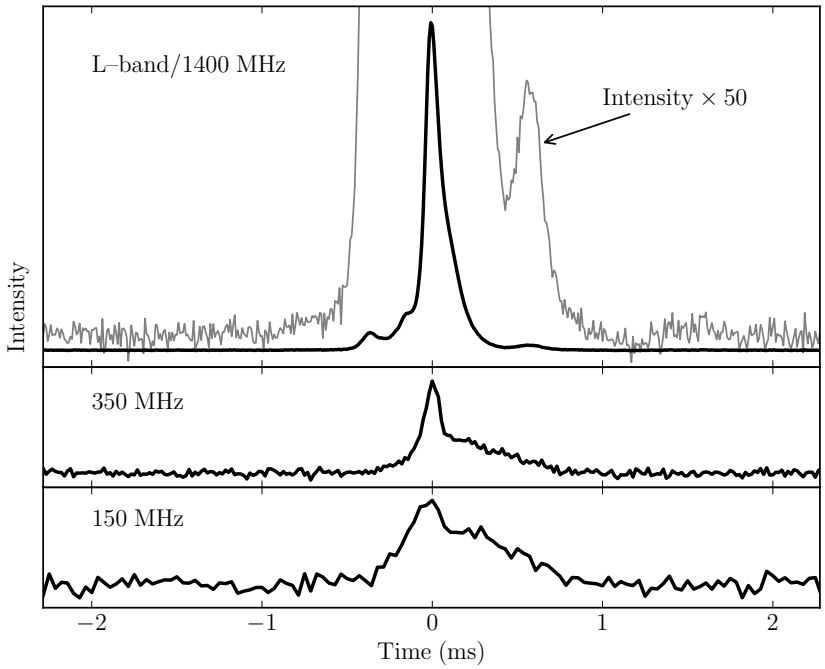

Figure 2.7: The grand average profile for all telescopes. The top panel was created across all bandwidths from those telescopes which observed at L-band/1.4 GHz. While it has been shown in §2 that there is some profile smearing occurring due to the pulse profile evolution with frequency, we sum in weighted fashion from individual subbands' residual values. The resulting profile has a S/N of ~ 4000, where the signal value is taken as the amplitude at the maximum value of the summed pulse and the noise is taken in the first 100 phase bins of the off-pulse part of the combined profile. The bottom two panels show the grand average profiles for low frequencies, manifesting the significant profile evolution with frequency. The DM for all telescopes is set by the fitted L-band/1.4 GHz DM.

as burst, continuous wave, and memory bursts (see Arzoumanian et al. 2014 for current limits on continuous wave sources). The first results presented in this work provide a starting point on the subtleties that may emerge with an increasing dependence on PSR J1713+0747 and similar pulsars such as PSR J0437−4715 and PSR J1909−3744.

We plan to release papers on the following subjects, among others, based on this dataset:

The Noise Budget of the 24-Hour Global Observation of PSR J1713+0747: the question to be explored here is the degree to which one can dissect the noise present on the different timescales relevant in this observation. From single pulses at the μs resolution all the way to the full 24 hr, the statistical structure of noise in timing residuals can be probed using various diagnostics. Structure on different timescales can be probed by looking at the pulsar with the Allan variance function. Single pulses can also be exploited in order to search for smaller timescale structure such as giant pulses, mode changes, and drifting sub-pulses (see Shannon & Cordes 2010). Shape changes can be probed and possibly mitigated using various methods (Cordes 1993, Demorest 2007, Osłowski et al. 2011).

Interstellar Electron Density Variations and Pulse Profile Frequency Evolution: the all-telescope dynamic spectrum can yield interesting information in a further analysis. Given the data obtained at low-frequencies with LOFAR and WSRT, it will be informative to search for correlations between events occurring in the L-band/1.4 GHz dynamic spectrum and the highly scattered structure at 150 MHz and 350 MHz respectively. Analysis can be done using the LOFAR and WSRT data to obtain more accurate DM measurements, while taking into account the significant profile evolution between the two low-frequency observations and the L-band/1.4 GHz observations.

GiantLEAP: one of the signature objectives of this observation is to use the European telescopes, Arecibo, the GMRT, and the GBT as a single phased array, or at least to expand LEAP with some subset thereof. In particular, RFI excision using simultaneous data from a subset of telescopes might significantly improve the quality of the phased array over one more locally situated. Once the proper correlations are performed, in principle the timing rms of PSR J1713+0747 from

the largest simultaneous collecting area ever used will be obtained. However, what practical limitations will come into play at realizing this ideal would be the subject of future studies. Undoubtedly, whatever timing results will be obtained will be highly affected by the presence of pulse phase jitter.

Polarization Studies. Most telescopes in this study took polarimetric data (see Appendix) and studying the timescales of PSR J1713+0747's polarization over the 24 hours could provide new insights, particularly at the single pulse level.

2.6 Conclusions

We have presented an overview of the goals and data products of the 24-hour global campaign on PSR J1713+0747. This ~ 60 TB dataset is useful for many goals which will be explored in further papers, including but not limited to: better determination of the overall noise budget for PTAs, a wide-bandwidth, long-timespan examination of the effects of the ISM on pulsar timing, combining baseband data from simultaneous observations for the GiantLEAP experiment, an examination of single pulses and their phenomenology over the 24 hours, and many others.

In the first results presented here, some interesting conclusions can already be drawn. PSR J1713+0747's intrinsic pulse phase jitter ($\sim 27.0\,\mu$s for single pulses) can be measured by fitting a noise model across all telescopes, even when TOA integration times are as long as 120 s. The improvement of timing residual rms is not found to depart significantly from a factor of $1/\sqrt{N}$, where N is the number of integrated pulses. Finally, the diffraction scale at 1.4 GHz was seen to be $\ell_d \approx 2 \times 10^4$ km, much larger than the Earth, from the overlapping scintillation pattern seen in the dynamic spectrum in Figure 3.

2.7 Acknowledgments

We thank the IPTA for its ongoing international collaboration that motivated this project, which would have been challenging for any PTA consortium to execute alone. We would especially like to thank NSF-PIRE, the EPTA, and the PPTA for enabling the IPTA 2012 Meeting in Kiama, New South Wales, Australia, and the IPTA 2013 Meeting in Krabi, Thailand. During both these meetings, the unique synergy of many IPTA personnel interacting in the same place brought about both the idea for, and later, the execution of, this observation. We are grateful to the University of Sydney and the National Astronomical Research Institute of Thailand (NARIT) for hosting these meetings.

The work of SJC, JMC, PBD, TD, FJ, GJ, MTL, TJWL, JL, DRM, MAM, NP, SMR and KS was partially supported through the National Science Foundation (NSF) PIRE program award number 0968296. PL acknowledges the support of IMPRS Bonn/Cologne and FQRNT B2. We thank the telescope schedulers Hector Hernandez, Alex Kraus, Tony Minter, and many others for working hard to ensure that this observation was given adequate time, given the difficulty of scheduling nine telescopes for simultaneous observations. We thank the staff of the GMRT who have made these observations possible. The GMRT is run by the National Centre for Radio Astrophysics of the Tata Institute of Fundamental Research. NANOGrav research at University of British Columbia is supported by an NSERC Discovery Grant and Discovery Accelerator Supplement and by the Canadian Institute for Advanced Research. The National Radio Astronomy Observatory is a facility of the NSF operated under cooperative agreement by Associated Universities, Inc. The Arecibo Observatory is operated by SRI International under a cooperative agreement with the NSF (AST-1100968), and in alliance with Ana

G. Méndez-Universidad Metropolitana, and the Universities Space Research Association. The 100-m Effelsberg telescope is operated by the Max-Planck-Institut für Radioastronomie (MPIfR). LOFAR, the Low Frequency Array designed and constructed by ASTRON, has facilities in several countries, that are owned by various parties (each with their own funding sources), and that are collectively operated by the International LOFAR Telescope (ILT) foundation under a joint scientific policy. Access to the Lovell Telescope is supported through an STFC rolling grant. The Nançay radio telescope is part of the Paris Observatory, associated with the Centre National de la Recherche Scientifique (CNRS), and partially supported by the Région Centre in France. The Parkes Radio telescope is part of the Australia Telescope National Facility which is funded by the Commonwealth of Australia for operation as a National Facility managed by CSIRO. The Westerbork Synthesis Radio Telescope is operated by the Netherlands Foundation for Research in Astronomy (ASTRON) with support from the NWO (Netherlands Organisation for Scientific Research). Some of this work was supported by the ERC Advanced Grant "LEAP", Grant Agreement Number 227947 (PI M. Kramer). Part of this research was carried out at the Jet Propulsion Laboratory, California Institute of Technology, under a contract with the National Aeronautics and Space Administration. Analysis of LOFAR data was supported by ERC Starting Grant "DRAGNET" (337062; PI J. Hessels).

Finally, we thank the anonymous referee for the helpful suggestions.

Table 2.3. Timing Model Parameters

Parameter	Value	Held Fixed in Fit?[a]	Parameter Uncertainty
Right Ascension, α (J2000)	17:13:49.5331497	Y	5×10^{-7}
Declination, δ (J2000)	07:47:37.492844	Y	1.4×10^{-5}
Proper motion in α, ν_α (mas yr^{-1})	4.922	Y	0.002
Proper motion in δ, ν_δ (mas yr^{-1})	-3.909	Y	0.004
Parallax, π (mas)	0.88	Y	0.03
Spin Frequency (Hz)	218.81184381090227	Y	7×10^{-14}
Spin down rate (Hz^2)	$-4.083907 \times 10^{-16}$	Y	8×10^{-22}
Reference epoch (MJD)	54971	Y	
Dispersion Measure (pc cm^{-3})	15.99113	N	1×10^{-5}
Profile frequency dependency parameters			
FD1	1.328×10^{-5}	Y	4×10^{-8}
FD2	-3.73×10^{-5}	Y	2×10^{-7}
FD3	3.24×10^{-5}	Y	7×10^{-7}
FD4	-1.07×10^{-5}	Y	5×10^{-7}
Solar System ephemeris	DE421	Y	
Reference clock	TT(BIPM)	Y	
Binary Type	T2[b]	Y	
Projected semi-major axis, x (lt-s)	32.34242245	Y	1.2×10^{-7}
Eccentricity, e	7.49414×10^{-5}	Y	6×10^{-10}
Time of periastron passage, T_0 (MJD)	54914.0602	Y	0.0003
Orbital Period, P_b (day)	67.825147	Y	5×10^{-6}
Angle of periastron, ω (deg)	176.1978	Y	0.0015
Derivative of periastron angle, $\dot{\omega}$ (deg)	0.00049	Y	0.00014
Companion Mass, M_c ($M_\odot$)	0.29	Y	0.01

[a]We also fit for arbitrary jumps between telescopes, which are not astrophysical and not shown here.
[b]Damour & Deruelle (1986)

2.8 Appendix

2.8.1 Additional Observing Details

Most information about the observation can be found in Table 1. TEMPO2 parameters are in this Appendix in Table 3, most of which derive from the parameters calculated in (Zhu et al. 2015; provided as preliminary values prior to publication).

2.8.2 Effelsberg 100-m Radio Telescope

Effelsberg's data taking began with 9.3 hr of contiguous observing at 1380 MHz. The PSRIX instrument (Karuppusamy et al. 2014, in preparation) was used for both baseband and folding modes (after real-time coherent de-dispersion). There were two baseband sessions, one 30 min and the other 1 hr. In folding mode, PSRIX was configured to coherently de-disperse and fold 8×25 MHz bands. Each resulting file has 200 MHz of bandwidth (though some channels are removed due to RFI), 128 channels, 1024 phase bins of 4.47 μs each, 10 s subintegrations, and full polarization information. In total there were ~ 6 hr (2.1 GB) of folding mode data. In baseband mode, data was recorded as 8×16 MHz (128 MHz) subbands in order to be compatible with other LEAP telescopes. The data were flux calibrated using the noise diode, which in turn was calibrated using a North-On-South triplet of observations of 3C 218 following the 24-hr campaign. The data were recorded in "Timer Archive" format. They were converted to PSRFITS format as part of Effelsberg's standard data reduction pipeline.

2.8.3 Giant Meterwave Radio Telescope

The GMRT used 22 antennas, employing two observing modes – a total offline coherent filterbank mode with 65.1 kHz spectral and 61.44 μs time resolution, and a coherent array voltage mode with a single subband for the baseband portion of the observation. Both these modes are described in Roy et al. (2010). The frequency range was from 1371 MHz to 1404 MHz. There were 7×1 hr recording scans interleaving with phasing scans for the array, as well as a 50 min coherent array baseband voltage recording scan. This resulted in 436 GB of raw filterbank data and 460 GB of voltage data. The GMRT filterbank data (61.44 μs time resolution) are 16-bit and in a format compatible with the PRESTO[2] searching suite. The GMRT coherent array voltage data (15 ns time resolution) are 8-bit and in a DSPSR friendly format. The GMRT coherent array provides some built-in immunity to RFI as the processing pipeline adjusts the antenna phases to correct for the effect of rotation of the sky signals, which in turn de-correlates the terrestrial signals. Interleaved calibrator observations (QSO J1822–096 in this case) every 2 hr were required to optimize the coherent array sensitivity at the observing frequencies. The antenna-based gain offsets are also corrected using this calibrator before making the coherent beam.

2.8.4 Lovell Telescope at Jodrell Bank Observatory

L-band/1.4 GHz observations of PSR J1713+0747 were obtained with the Lovell telescope at Jodrell Bank over an 11.5 hr timespan. The data are continuous except for a few brief gaps due to the telescope being parked for wind constraints. Two

[2] `http://www.cv.nrao.edu/~sransom/presto/`

instruments were used; i) the DFB performed real-time folding with incoherent de-dispersion, producing folded 10 s subintegrations of 1024 pulse phase bins of 4.47 μs in size, 0.5 MHz channels over a 384 MHz wide band centered at 1532 MHz, ii) the ROACH, using a Reconfigurable Open Architecture Computing Hardware FPGA board performing real-time folding with coherent de-dispersion using the PSRDADA[3] and DSPSR software packages. This provided 10 s subintegrations with 2048 pulse phase bins of 2.23 μs in size and covered 400 MHz wide band centered at 1532 MHz, split into 25 subbands of 16 MHz, each channelized to provide 0.25 MHz channels. The ROACH was also used to record baseband data during the times when Nançay and Arecibo observed the pulsar. Dual polarization, Nyquist sampled baseband data, 8-bits digitized, was recorded for the lower 8 subbands of 16 MHz (1332 to 1460 MHz), while the remaining seventeen 16 MHz subbands performed real-time folding with coherent de-dispersion as before. At the end of the observations the baseband data was folded and coherently de-dispersed with the same parameters as for the real-time folding to give one continuous observing run. The spectral kurtosis method by Nita et al. (2007) for identifying and flagging RFI, as implemented in DSPSR, was used to excise RFI in real time. After the observations a combination of manual and automatic RFI excision was performed to clean the data further. The folded profiles were polarization calibrated using the Single Axis model (van Straten 2004) using observations of the noise diode and observations of pulsars with known polarization properties.

[3] `http://psrdada.sourceforge.net`

2.8.5 Low Frequency Array

LOFAR observed from 110 – 190 MHz using the BG/P beam-former and correlator (see van Haarlem et al. 2013). The sampling time was 5.12 μs and 400 subbands of 0.195 MHz each were recorded. Full polarization information was taken in complex voltage mode; see Stappers et al. (2011) for more information on pulsar observing modes with LOFAR. The raw data volume (32-bit) was 4.5 TB/hr, yielding 40 TB of complex-voltage raw data (of which only 1 hr, 4.5 TB, of raw data has been archived long-term; the rest is only available as folded archives, as summarized in Table 1) The 40 TB value not included in total the 60 TB value for the all-telescope data. These data were coherently de-dispersed and folded offline using DSPSR. The following 23 LOFAR Core stations were combined for the 9-hr observation: CS001, CS002, CS003, CS004, CS005, CS006, CS007, CS011, CS017, CS021, CS024, CS026, CS028, CS030, CS031, CS032, CS101, CS103, CS201, CS301, CS302, CS401, and CS501. See van Haarlem et al. (2013) for more specific location information; by default the phase center of the tied-array beam is placed at the position of CS002.

2.8.6 Nançay Decimetric Telescope

Nançay observed using the NUPPI (Nançay Ultimate Pulsar Processing Instrument) backend at L-band/1.4 GHz with a total bandwidth of 512 MHz, split into 32×16 MHz channels and 8-bits digitized. The profiles were folded and integrated over 1 min and finally stored in a 29 MB PSRFITS file. All data were coherently de-dispersed and the total Nançay observation lasted for $\sim$ 1 hr. The PSRCHIVE program PAC was used to do the polarization calibration with the Single Axis

model and automatic zapping was then applied with the PAZ program. The TOAs were produced with PAT using a high S/N template.

2.8.7 Parkes 64 m Telescope

The Parkes 64 m radio telescope observed PSR J1713+0747 at 1362 MHz using both fold-mode and baseband mode in parallel for ~ 6 hr. This time included four 3 min noise diode calibration scans, between 64 min blocks of folding. The backends DFB3/4 (incoherent filterbank, 60 s foldings, 1024 frequency channels over 256 MHz bandwidth, 1024 phase bins of 4.47 μs each), APSR (real-time coherent filterbank, 30 s foldings, 512 frequency channels over 256 MHz bandwidth, 1024 phase bins of 4.47 μs each), and CASPSR (30 s foldings, 400 MHz bandwidth with ~ 10 MHz band edges, 1024 phase bins of 4.47 μs each) observed in parallel, allowing for simultaneous baseband and folding mode observations. RFI was removed, and consistent results were obtained with all backends using a median filter in the frequency domain. Polarization and flux calibration for the DFB data used the standard monthly flux calibrations on the Hydra A radio galaxy (Manchester et al. 2013). CASPSR was calibrated for differential gain and phase but nothing else. RFI was mitigated using the radio-frequency domain filter implemented in the PSRCHIVE command PAZ (Hotan et al. 2004). Additionally, the CASPSR instrument mitigates RFI in real time by rejecting portions of the data that show distribution inconsistent with receiver noise by using a spectral kurtosis filter. Digital filterbank data were calibrated for cross coupling using a model for the feed derived from long-track observations of the bright source PSR J0437−4715. Observations over these wide parallactic angles enable the measurement of the feed cross coupling and ellipticity to be measured (van Straten 2004). The model used

was the average of many long-track observations because the feed parameters were not found to change significantly with time. CASPSR observations were not calibrated for this cross coupling. PSR J1713+0747 is only a modestly polsarized pulsar and the effects of correction for these effects were found to be negligible improvement on its long term timing precision (Manchester et al. 2013). Details of this calibration are further described in Manchester et al. (2013). All the data are digitised with 8-bit digitisers. The baseband dataset is 30 TB, with 7.5 GB for the fold-mode dataset. The fold mode used the PSRFITS data format, and the baseband mode used the PSRDADA format.

2.8.8 Westerbork Synthesis Radio Telescope

WSRT is a 14×25 m dish East-West array, which for pulsar observations is used in tied-array mode and is phased up before the observations for all observing bands used. There were no absolute flux calibrations done for these observations. Full polarization information was stored. Due to the array-nature of the telescope there is usually very little RFI and therefore any remaining leftover narrow-channel RFI zapping is done offline using PSRCHIVE tools. For these observations we had 11 out of the total 14 dishes available. The WSRT observations made use of PuMa-II instrument (Karuppusamy et al. 2008), observing at both L-band/1.4 GHz and 350 MHz each with 8 separate bands, which are each either 10 MHz wide (for the 350 MHz observations) or 20 MHz wide (for the 1380 MHz observations). The individual bands overlapped by 2.5 MHz of the 10 MHz bandwidth for the 350 MHz observations. At L-band/1.4 GHz the bands overlapped by 4 MHz out of the 20 MHz bandwidth to ensure full overlap with the 16 MHz bands at the Effelsberg, Lovell and Nançay telescopes and allow for coherent addition of the data. For each there

are 10 s subintegrations stored with 256 bins of 17.9 μs each across the profile and 64 channels across each band (which is 10 or 20 MHz depending on the frequency). The low frequency TOAs were made using PSRCHIVE templates, created using the PAAS (analytic template) routine based on a high-S/N summation of many other observations.

2.8.9 Arecibo Observatory and the NRAO Green Bank Telescope

Both Arecibo and the GBT, as mentioned earlier, used non-folded intensity recording for their non-baseband portions of the observation so that single-pulse data would be available over the entire span of the observation, without the cost in bandwidth. Unlike baseband data, no voltage, and thus no electromagnetic phase information, is present. This observation mode is essentially a pulsar search mode with coherent de-dispersion, according to the source's DM. Calibrations at the start of the observations at both GBT and Arecibo were performed with a noise diode switched at 25 Hz, including the polarization calibration. Absolute flux measurements, also including the polarization calibration, were performed on QSO B1442+101 at the GBT and QSO J1413+1509 at Arecibo. We apply these calibrations via the Single Axis model using the the PSRCHIVE program PAC.

Green Bank Telescope

GBT began its observation starting with baseband mode, switching to an hour of intensity integration observing mode, switching back to baseband mode for 30 min, and then returning to intensity integration mode for the remaining seven

hours. The two baseband sessions would be simultaneous with other telescopes. The intensity integration mode had 256×3.125 MHz frequency channels and had a time resolution of $5.12\,\mu$s. The same was planned for the PUPPI backend at Arecibo. Full polarization information was recorded. Intensity integrations are effectively search mode but coherently de-dispersed with the known DM. During the switch from the first baseband time block to the first intensity integration time block, some time was lost due to a problem with the observing mode on GUPPI, and so to ensure a safer data rate, the observing mode was switched to 128×6.25 MHz channels with a time resolution of $2.56\,\mu$s. For this reason, the settings on GUPPI were different from PUPPI. The tradeoff is that with slightly wider channels in PUPPI, although yielding a better set of phase bins, cannot in principle excise RFI as efficiently. This interruption and restart caused a small gap in the data, visible in Figure 3. GBT's backend employing real-time cyclic spectroscopy (Jones et al. 2014, in preparation) was also used in parallel during the folding mode observations, with 65 MHz of bandwidth centered at 1398 MHz.

Arecibo Observatory

Finally, Arecibo joined the observation. Beginning with 30 min of baseband observing in order to contribute to GiantLEAP, it them switched over to PUPPI intensity integration mode, a different mode used than that at GBT as just described.

BIBLIOGRAPHY

Archibald, A. M., Kondratiev, V. I., Hessels, J. W. T., & Stinebring, D. R. 2014, ApJL, 790, L22

Arzoumanian, Z., et al. 2014, ApJ, 794, 141

Arzoumanian, Z., et al. 2015, ApJ, 813, 65

Bassa, C., et al. 2016, MNRAS, 456, 2196

Bogdanov, S., Pruszyńska, M., Lewandowski, W., & Wolszczan, A. 2002, ApJ, 581, 495

Caprini, C., Durrer, R., & Siemens, X. 2010, Phys. Rev. D, 82, 063511

Chatterjee, S., et al. 2009, ApJ, 698, 250

Cognard, I., & Backer, D. C. 2004, ApJL, 612, L125

Cordes, J. M. 1993, in Astronomical Society of the Pacific Conference Series, Vol. 36, Planets Around Pulsars, ed. J. A. Phillips, S. E. Thorsett, & S. R. Kulkarni, 43

Cordes, J. M. 2013, Classical and Quantum Gravity, 30, 224002

Cordes, J. M., & Downs, G. S. 1985, ApJS, 59, 343

Cordes, J. M., & Jenet, F. A. 2012, ApJ, 752, 54

Cordes, J. M., Kramer, M., Lazio, T. J. W., Stappers, B. W., Backer, D. C., & Johnston, S. 2004, NewAR, 48, 1413

Cordes, J. M., & Rickett, B. J. 1998, ApJ, 507, 846

Cordes, J. M., & Shannon, R. M. 2010, arXiv:1010.3785

Cordes, J. M., Wolszczan, A., Dewey, R. J., Blaskiewicz, M., & Stinebring, D. R. 1990, ApJ, 349, 245

Craft, H. D., Jr. 1970, Ph.D. thesis, CORNELL UNIVERSITY.

Damour, T., & Deruelle, N. 1986, Ann. Inst. Henri Poincaré Phys. Théor., Vol. 44, No. 3, p. 263 - 292, 44, 263

Demorest, P. B. 2007, Ph.D. thesis, University of California, Berkeley

Demorest, P. B. 2011, MNRAS, 416, 2821

Demorest, P. B., et al. 2013, ApJ, 762, 94

Detweiler, S. 1979, ApJ, 234, 1100

DuPlain, R., Ransom, S., Demorest, P., Brandt, P., Ford, J., & Shelton, A. L. 2008, in Society of Photo-Optical Instrumentation Engineers (SPIE) Conference Series, Vol. 7019, Society of Photo-Optical Instrumentation Engineers (SPIE) Conference Series

Espinoza, C. M., Antonopoulou, D., Stappers, B. W., Watts, A., & Lyne, A. G. 2014, MNRAS, 440, 2755

Espinoza, C. M., Lyne, A. G., Stappers, B. W., & Kramer, M. 2011, MNRAS, 414, 1679

Finn, L. S., & Lommen, A. N. 2010, ApJ, 718, 1400

Foster, R. S., & Backer, D. C. 1990, ApJ, 361, 300

Foster, R. S., Wolszczan, A., & Camilo, F. 1993, ApJL, 410, L91

Grishchuk, L. P. 2005, Physics Uspekhi, 48, 1235

Hankins, T. H., & Rickett, B. J. 1975, in Methods in Computational Physics. Volume 14 - Radio astronomy, ed. B. Alder, S. Fernbach, & M. Rotenberg, Vol. 14, 55

Hankins, T. H., & Rickett, B. J. 1986, ApJ, 311, 684

Hassall, T. E., et al. 2013, A&A, 552, A61

Hassall, T. E., et al. 2014, *in preparation*

Hellings, R. W., & Downs, G. S. 1983, ApJL, 265, L39

Hobbs, G. 2013, Classical and Quantum Gravity, 30, 224007

Hobbs, G., Archibald, A., Arzoumanian, Z., et al. 2010, Classical and Quantum Gravity, 27, 084013

Hobbs, G. B., Edwards, R. T., & Manchester, R. N. 2006, MNRAS, 369, 655

Hotan, A. W., van Straten, W., & Manchester, R. N. 2004, PASA, 21, 302

Jenet, F. A., Lommen, A., Larson, S. L., & Wen, L. 2004, ApJ, 606, 799

Jones, G., et al. 2014, *in preparation*

Karuppusamy, R., Stappers, B., & van Straten, W. 2008, PASP, 120, 191

Karuppusamy, R., et al. 2014, *in preparation*

Kaspi, V. M., Taylor, J. H., & Ryba, M. F. 1994, ApJ, 428, 713

Keith, M. J., Coles, W., Shannon, R. M., et al. 2013, MNRAS, 429, 2161

Kramer, M., & Champion, D. J. 2013, Classical and Quantum Gravity, 30, 224009

Kramer, M., Lange, C., Lorimer, D. R., Backer, D. C., Xilouris, K. M., Jessner, A., & Wielebinski, R. 1999, ApJ, 526, 957

Kuzmin, A. D., & Losovsky, B. Y. 2001, A&A, 368, 230

Lazio, T. J. W. 2013, Classical and Quantum Gravity, 30, 224011

Liu, K., Desvignes, G., Cognard, I., et al. 2014, MNRAS, 443, 3752

Lommen, A. N., & Backer, D. C. 2001, ApJ, 562, 297

Lommen, A. N., & Demorest, P. 2013, Classical and Quantum Gravity, 30, 224001

Lorimer, D. R., Kramer, M., Ellis, R., et al. 2004, Handbook of pulsar astronomy, by D.R. Lorimer and M. Kramer. Cambridge observing handbooks for research astronomers, Vol. 4. Cambridge, UK: Cambridge University Press, 2004

Madison, D. R., Cordes, J. M., & Chatterjee, S. 2014, ApJ, 788, 141

Manchester, R. N., & IPTA 2013, Classical and Quantum Gravity, 30, 224010

Manchester, R. N., et al. 2013, PASA, 30, 17

Matsakis, D. N., Taylor, J. H., & Eubanks, T. M. 1997, A&A, 326, 924

McLaughlin, M. A. 2013, Classical and Quantum Gravity, 30, 224008

Nita, G. M., Gary, D. E., Liu, Z., Hurford, G. J., & White, S. M. 2007, PASP, 119, 805

Osłowski, S., van Straten, W., Demorest, P., & Bailes, M. 2013, MNRAS, 430, 416

Osłowski, S., van Straten, W., Hobbs, G. B., Bailes, M., & Demorest, P. 2011, MNRAS, 418, 1258

Pennucci, T. T., Demorest, P. B., & Ransom, S. M. 2014, ApJ, 790, 93

Rickett, B. J. 1970, MNRAS, 150, 67

Roy, J., Gupta, Y., Pen, U.-L., Peterson, J. B., Kudale, S., & Kodilkar, J. 2010, Experimental Astronomy, 28, 25

Sanidas, S. A., Battye, R. A., & Stappers, B. W. 2013, ApJ, 764, 108

Sazhin, M. V. 1978, SvA, 22, 36

Sesana, A. 2013, MNRAS, 433, L1

Sesana, A., Vecchio, A., & Volonteri, M. 2009, MNRAS, 394, 2255

Shannon, R. M., & Cordes, J. M. 2010, ApJ, 725, 1607

Shannon, R. M., & Cordes, J. M. 2012, ApJ, 761, 64

Shannon, R. M., Osłowski, S., Dai, S., et al. 2014, MNRAS, 443, 1463

Shannon, R. M., et al. 2013, Science, 342, 334

Stairs, I. H., Thorsett, S. E., Taylor, J. H., & Wolszczan, A. 2002, ApJ, 581, 501

Stappers, B. W., Hessels, J. W. T., Alexov, A., et al. 2011, A&A, 530, A80

Starobinskiĭ, A. A. 1979, Soviet Journal of Experimental and Theoretical Physics Letters, 30, 682

Stinebring, D. 2013, Classical and Quantum Gravity, 30, 224006

Taylor, J. H. 1992, Royal Society of London Philosophical Transactions Series A, 341, 117

van Haarlem, M. P., et al. 2013, A&A, 556, A2

van Haasteren, R., & Levin, Y. 2010, MNRAS, 401, 2372

van Haasteren, R., et al. 2011, MNRAS, 414, 3117

van Straten, W. 2004, ApJS, 152, 129

van Straten, W., Demorest, P., & Osłowski, S. 2012, Astronomical Research and Technology, 9, 237

Verbiest, J. P. W., Bailes, M., Coles, W. A., et al. 2009, MNRAS, 400, 951

Walker, M. A., Demorest, P. B., & van Straten, W. 2013, ApJ, 779, 99

You, X. P., Hobbs, G. B., Coles, W. A., Manchester, R. N., & Han, J. L. 2007, ApJ, 671, 907

Zhu, W., et al. 2015, ApJ, 809, 41

CHAPTER 3

PULSAR TIMING ERRORS FROM ASYNCHRONOUS MULTI-FREQUENCY SAMPLING OF DISPERSION MEASURE VARIATIONS

Free electrons in the interstellar medium cause frequency-dependent delays in pulse arrival times due to both scattering and dispersion. Multi-frequency measurements are used to estimate and remove dispersion delays. In this paper, we focus on the effect of any non-simultaneity of multi-frequency observations on dispersive delay estimation and removal. Interstellar density variations combined with changes in the line-of-sight from pulsar and observer motions cause dispersion measure variations with an approximately power-law power spectrum, augmented in some cases by linear trends. We simulate time series, estimate the magnitude and statistical properties of timing errors that result from non-simultaneous observations, and derive prescriptions for data acquisition that are needed in order to achieve a specified timing precision. For nearby, highly stable pulsars, measurements need to be simultaneous to within about one day in order that the timing error from asynchronous DM correction is less than about 10 ns. We discuss how timing precision improves when increasing the number of dual-frequency observations used in dispersion measure estimation for a given epoch. For a Kolmogorov wavenumber spectrum, we find about a factor of two improvement in precision timing when increasing from two to three observations but diminishing returns thereafter.

Published: Lam, M. T., Cordes, J. M., Chatterjee, S., & Dolch, T. 2015, ApJ, 801, 130

3.1 Introduction

One of the goals of precision pulsar timing is the detection of low-frequency ($\sim$ nanohertz) gravitational waves (GWs) from sources at cosmological distances and possibly from Galactic sources (Detweiler 1979; Hellings & Downs 1983; Chernoff 2009; Sesana 2013). Such a detection requires sub-microsecond timing precision, which is challenging due to a variety of astrophysical and instrumentation effects that must either be mitigated or fitted for in timing models (e.g. Jenet et al. 2005). The measurement model for pulse times-of-arrival (TOAs) includes: (i) deterministic contributions from spin kinematics, orbital motions, and interstellar propagation delays; (ii) stochastic timing noise from pulsars themselves and from the interstellar medium; and (iii) measurement noise (Ryba & Taylor 1991; Stairs et al. 1998; Lorimer & Kramer 2012).

The ionized interstellar medium (ISM) induces various frequency-dependent effects on TOAs from dispersion, refraction, and scattering (Cordes 2013; Stinebring 2013). Any such effects that are larger than the TOA precision required for GW detection need to be removed by using multiple-frequency observations. In this paper, we consider some of the requirements for removing the dispersive delay, which is the largest frequency-dependent interstellar effect. For a cold, unmagnetized plasma, a pulse observed at radio frequency ν is delayed compared to one at infinite frequency by an amount $t_{\rm DM} \propto {\rm DM}/\nu^2$, where the dispersion measure (DM) is the line-of-sight (LOS) integral of the electron density. DM is epoch-dependent because the LOS changes from motions of the pulsar and the Earth and because of turbulent and bulk motions within the ISM itself (Phillips & Wolszczan 1991; Cordes & Rickett 1998). Therefore, the dispersion delay must be removed on an epoch-by-epoch basis. Measurements at two or more frequencies are used to

estimate DM and then subtract the dispersion delay to obtain infinite-frequency TOAs that are intended to be devoid of interstellar plasma delays.

Pulsar timing arrays (PTAs) are ensembles of recycled, millisecond pulsars (MSPs) that can potentially provide high precision TOAs usable for GW detection. Currently, TOAs are typically obtained in observing campaigns with a roughly monthly cadence between epochs (Demorest et al. 2013; Hobbs 2013; Kramer & Champion 2013). However, TOAs may be measured at individual frequencies over a period of several days around each of these epochs. Variations in DM over this time range can contaminate the estimated DM and consequently also the infinite-frequency TOAs. Though variations in DM are small over periods of days ($\Delta\mathrm{DM}/\mathrm{DM} \sim 10^{-4} - 10^{-5}$), they are large enough to add significantly to the timing error budget.

The North American Nanohertz Observatory for Gravitational Waves (NANOGrav; McLaughlin 2013) observes MSPs using two facilities, the Arecibo Observatory and the Green Bank Telescope (GBT). Most pulsars in the PTA are observed roughly once a month for 20-30 minutes in each of two frequency bands, chosen on a per-pulsar basis to optimize the precision of the DM correction. The mechanical agility of the receiver turret at Arecibo allows two frequency bands to be observed sequentially on the same day. The system at the GBT requires physical switching between receivers at different foci of the telescope used for each frequency. This switching must be done on a pulsar-by-pulsar basis and is time-inefficient. Instead, pulsars are observed at both frequencies on separate days, resulting in gaps between observations ranging from roughly one day to a week. These gaps have been mitigated in the NANOGrav processing pipeline by combining observations in 15-day wide bins and evaluating DM with a piecewise constant

model (Demorest et al. 2013) that is fitted to the multifrequency data within each bin under the assumption that DM is constant over 15 days.

There are additional frequency-dependent effects that we do not address in this work, including refraction and scattering in the ISM (Cordes et al. 1986; Romani et al. 1986; Rickett 1990; Foster & Cordes 1990) and frequency-dependent variations of pulse shapes that are intrinsic to each pulsar (Craft 1970; Hankins & Rickett 1986; Kramer et al. 1999; Hassall et al. 2012; Pennucci et al. 2014). Other interstellar effects on pulsar timing are also being investigated. Cordes et al. (2016) analyze the dependence of DM on frequency that results from spatial averaging due to multipath scattering. In another (Lam et al. 2016b), we diagnose contributions to DM variations that result from both the change in pulsar distance and from the change in direction of the LOS. Here we focus on the timing uncertainties that result specifically from the non-simultaneity of the multi-frequency observations. Our work gives an exact treatment over the analysis presented in Cordes & Shannon (2010).

In §2, we present the mathematical framework of the effect of non-simultaneous observations on DM estimation and the associated timing errors. In §3, we describe our simulations of DM time series and in §4 we present the results of these simulations. We conclude in §5 by describing the overall impact on the timing noise budget and GW sensitivity.

3.2 Timing Errors from DM Mis-estimation

Consider TOA measurements made at two epochs $t_1 = t$ and $t_2 = t + \tau$ at frequencies ν_1 and ν_2, respectively. For specificity, we assume $\nu_1 > \nu_2$. A perfect timing

model would allow the pulse arrival time to be predicted with zero error. However, timing perturbations are expected from both achromatic effects (e.g. due to GWs and from errors in the pulsar spin or orbital parameters) and chromatic, interstellar effects. Chromatic cold plasma effects always decrease with increasing frequency, so TOAs are referenced to infinite frequency. Defining Δt_∞ as the achromatic, infinite frequency perturbation, we write the total timing perturbation from both achromatic effects and dispersion as

$$\Delta t_i = \Delta t_\infty(t_i) + K\nu_i^{-2}\mathrm{DM}(t_i), \tag{3.1}$$

where the subscript $i = 1, 2$ denotes the epoch and $K \equiv cr_e/2\pi \approx 4.149$ ms GHz^2 pc^{-1} cm^3 is the dispersion constant in observationally convenient units, with c the speed of light and r_e the classical electron radius (Lorimer & Kramer 2012). For simultaneous observations ($\tau = 0$), DM($t_{1,2}$) is constant and $\Delta t_\infty(t)$ can be solved for exactly assuming there is no measurement error.

For non-simultaneous observations ($\tau \neq 0$), estimation of DM and correction to infinite frequency will be in error according to the change in actual DM between the two epochs. If the difference in TOA offsets is attributed *solely* to dispersion delays with a fixed value of DM and if the achromatic offset Δt_∞ is the same at the two epochs, the estimated DM fluctuation[1] at epoch t is

$$\widehat{\mathrm{DM}}(t,\tau) = \frac{\Delta t_1 - \Delta t_2}{K\left(\nu_1^{-2} - \nu_2^{-2}\right)} = \frac{\mathrm{DM}(t) - r^2\mathrm{DM}(t+\tau)}{1 - r^2}. \tag{3.2}$$

for a frequency ratio $r = \nu_1/\nu_2$. We use the DM increment over the interval between observations,

$$\Delta\mathrm{DM}(t,\tau) \equiv \mathrm{DM}(t) - \mathrm{DM}(t+\tau), \tag{3.3}$$

[1]To simplify notation, we will assume that the average DM has been removed from all DM time series.

to express the difference between true and estimated DM as

$$\delta\widehat{\mathrm{DM}}(t,\tau) \equiv \mathrm{DM}(t) - \widehat{\mathrm{DM}}(t,\tau) = \frac{r^2 \Delta\mathrm{DM}(t,\tau)}{r^2-1}. \quad (3.4)$$

When the (mis)estimated DM in Equation (3.2) is used to correct the measured TOA at epoch t to infinite frequency, the systematic error is

$$\delta\hat{t}_\infty(t,\tau) = K\nu_1^{-2}\,\delta\widehat{\mathrm{DM}}(t,\tau) \quad (3.5)$$

The TOA error vanishes for $\tau = 0$. However, it has the curious property of a decline with increasing r but is asymptotic to a constant value as r goes to infinity. Note that flipping ν_1 and ν_2 will cause a change in $\delta\widehat{\mathrm{DM}}$ but not $\delta\hat{t}_\infty$.

3.3 DM Variations from ISM Structure

Epoch-dependent DM variations are well known, e.g. for the Crab Pulsar (Isaacman & Rankin 1977), for B1937+21 (Rawley et al. 1988; Cordes et al. 1990; Kaspi et al. 1994; Ramachandran et al. 2006), for B1821–24 (Cognard & Lestrade 1997), and numerous other cases (Phillips & Wolszczan 1991; Backer et al. 1993; You et al. 2007; Keith et al. 2013). In some cases, $\mathrm{DM}(t)$ is consistent with sampling of stochastic electron-density variations while in others, linear trends in time are prominent.

A linear trend in DM, modeled as $\mathrm{DM}(t) = \mathrm{DM}_0 + (d\mathrm{DM}/dt)t$, would give a timing error at frequency ν_1 (in GHz)

$$\begin{aligned}\delta\hat{t}_\infty(t,\tau) &= K\nu_1^{-2}\,(d\mathrm{DM}/dt)\tau \\ &\approx 1.14\ \mathrm{ns}\,\nu_1^{-2}\tau_d\left(\frac{d\mathrm{DM}/dt}{10^{-4}\ \mathrm{pc\ cm^{-3}\ yr^{-1}}}\right), \end{aligned} \quad (3.6)$$

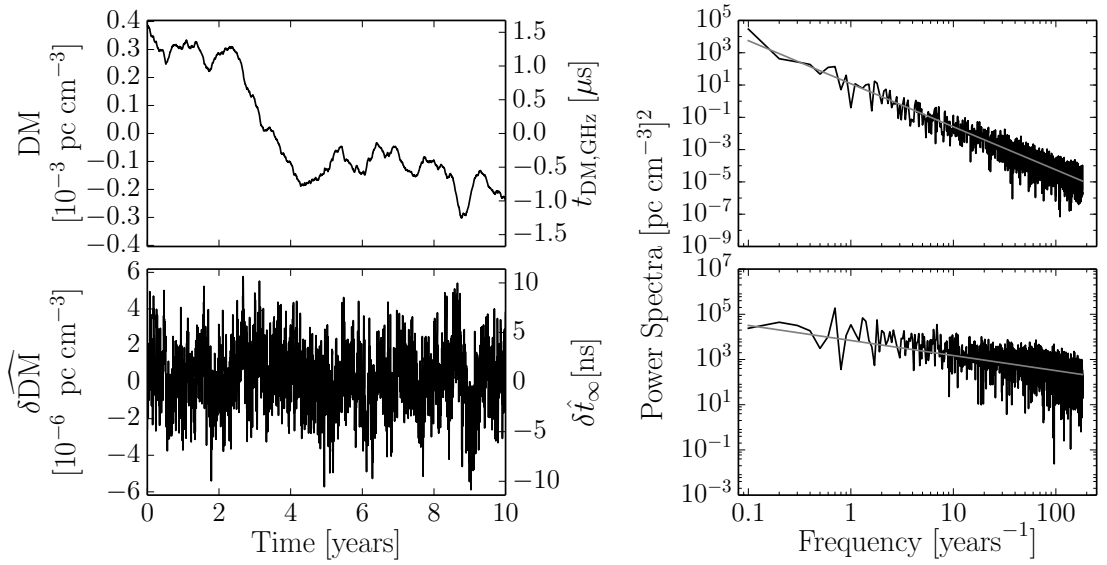

Figure 3.1: A single realization of a simulated DM time series that results from density variations along the LOS in a medium with a Kolmogorov wavenumber spectrum and from changes in the LOS due to relative motions. The power spectrum for DM(t) scales as $f^{-\gamma}$ with $\gamma = 8/3$. Top left: DM(t) as a perturbation added to a mean DM with the left-hand scale in DM units and the right-hand scale giving the time delay $t_{\rm DM}$ in microseconds for $\nu = 1$ GHz. Top right: Power spectrum of δDM(t) overplotted with a fitted straight line of slope $\gamma = 8/3$. Bottom left: The difference between estimated and true DM, $\delta\widetilde{\rm DM}(t, \tau)$, for a lag $\tau = 1$ day between dual-frequency measurements at $\nu_1 = 1.5$ and $\nu_2 = 0.8$ GHz with the right-hand scale set for the infinite-frequency TOA perturbation given by Equation (3.5). Bottom right: Power spectrum of the DM difference overplotted with a fitted straight line of slope $\gamma = 2/3$.

where the approximate value is scaled to a nominal value of $d{\rm DM}/dt$ and with τ in days. Measured DM derivatives range from $d{\rm DM}/dt \approx 10^{-5}$ to 10^{-2} pc cm^{-3} yr^{-1}, so timing errors as large as 114 ns will occur for lags of one day for LOSs with the largest DM derivatives. However, a large linear trend is easy to recognize in timing data and a wide range of epochs can be used to estimate and remove it. In the remainder of our analysis, we will therefore ignore the contribution from linear trends in DM and focus on stochastic variations.

Fluctuations in DM(t) arise from density variations in the ISM that combine

with the change in LOS from transverse motions of the observer, pulsar, and medium[2]. To describe electron-density variations, we use a power law wavenumber spectrum with cutoffs q_1 and q_2 and spectral coefficient C_n^2,

$$P_{\delta n_e}(\boldsymbol{q}) = \mathrm{C}_\mathrm{n}^2 q^{-\beta}, \quad q_1 \leq q \leq q_2, \tag{3.7}$$

that depends only on the magnitude of the wavenumber q, which applies to isotropic density irregularities consistent with many LOSs (see Brisken et al. 2010 for evidence of anisotropic scattering towards B0834+06) . For $\beta > 3$ and $\mathrm{q_1} \ll \mathrm{q_2}$, the rms electron density is dominated by the largest scales, $2\pi/q_1$. Kolmogorov turbulence is a benchmark model commonly used to describe fluctuations in the ISM consistent over many length scales (see Rickett 1990 for an overview). The Kolmogorov case corresponds to $\beta = 11/3$. Example time series are shown in Fig 3.1.

Density fluctuations impose phase perturbations on electromagnetic waves that are manifested as variations in DM and as intensity variations (interstellar scintillations, ISS). The phase structure function (SF), $D_\phi(b) = \langle[\phi(\mathbf{x}) - \phi(\mathbf{x}+\mathbf{b})]^2\rangle$, is closely related to measurable ISS quantities (e.g. Rickett 1990). It scales as $D_\phi(b) \propto b^{\beta-2}$ for spatial separations b intermediate between the smallest and largest scales in the ISM, $2\pi/q_2 \ll b \ll 2\pi/q_1$ along with $2 < \beta < 4$, which appears to be the range of β that best characterizes ISS observations (Bhat et al. 2004; Löhmer et al. 2004). For brevity, we refer to this set of constraints as the 'scintillation regime.'

Measurements of the ISS timescale Δt_ISS in the strong scintillation regime correspond to $D_\phi(v_{\mathrm{eff}_\perp}\Delta t_\mathrm{ISS}) = 1$ rad^2, where $v_{\mathrm{eff}_\perp}$ is a weighted combination of transverse velocities of the pulsar, observer, and ISM. The phase structure function can

[2]Linear trends result, in part, from radial motions along the LOS, so transverse motions are relevant to our discussion.

be extrapolated to much longer time scales, subject to consistency with the above criteria on $b = v_{\mathrm{eff}_\perp}\tau$, using (e.g. Foster & Cordes 1990),

$$D_\phi(\tau) = (1 \text{ rad}^2)\left[\frac{\tau}{\Delta t_{\mathrm{ISS}}(\nu)}\right]^{\beta-2}. \tag{3.8}$$

DM variations are related to phase variations by $\delta\mathrm{DM} = -\nu\phi/cr_e$. The time series $\delta\mathrm{DM}(t)$ is a red noise process with a power-law spectrum that scales as $S_{\mathrm{DM}}(f) \propto f^{-\gamma}$ where $\gamma = \beta - 1$ in the scintillation regime. The corresponding structure function for DM, $D_{\mathrm{DM}}(\tau) = \left\langle[\Delta\mathrm{DM}(t,\tau)]^2\right\rangle$, with $\Delta\mathrm{DM}(t,\tau)$ defined in Equation (3.3), is

$$D_{\mathrm{DM}}(\tau) = \frac{D_\phi(v_{\mathrm{eff}_\perp}\tau)}{(\lambda r_e)^2} = \frac{\nu^2}{(cr_e)^2}\left[\frac{\tau}{\Delta t_{\mathrm{ISS}}(\nu)}\right]^{\beta-2}. \tag{3.9}$$

The scintillation time varies with frequency as $\Delta t_{\mathrm{ISS}} \propto \nu^{2/(\beta-2)}$, so the quantity $\nu^2[\Delta t_{\mathrm{ISS}}(\nu)]^{-(\beta-2)}$, and therefore $D_{\mathrm{DM}}(\tau)$, is independent of frequency.

3.3.1 DM and Timing Errors

The rms estimation error in DM, $\sigma_{\widehat{\delta\mathrm{DM}}}(\tau)$, follows from Equation (3.4)

$$\sigma_{\widehat{\delta\mathrm{DM}}}(\tau) = \left|\frac{r^2}{r^2-1}\right| D_{\mathrm{DM}}^{1/2}(\tau) \propto \tau^{(\beta-2)/2} \tag{3.10}$$

and the rms error in the infinite-frequency TOA is

$$\sigma_{\delta\hat{t}_\infty}(\tau) \;=\; K\nu_1^{-2}\left|\frac{r^2}{r^2-1}\right| D_{\mathrm{DM}}^{1/2}(\tau) \propto \tau^{(\beta-2)/2}. \tag{3.11}$$

While we consider the case where $r > 1$, the formalism presented thus far also holds for $r < 1$. Again we note that $\sigma_{\widehat{\delta\mathrm{DM}}}$ can be reduced by switching ν_1 and ν_2, as the lower frequency TOA is more sensitive to changes in DM. However, the quantity of interest, $\sigma_{\delta\hat{t}_\infty}$, will remain the same.

For τ measured in days and the scintillation time $\Delta t_{\rm ISS}$ evaluated at 1 GHz referenced to 1000 s, the DM structure function for a Kolmogorov medium is

$$D_{\rm DM}(\tau) = \left(1.57 \times 10^{-6} \text{ pc cm}^{-3}\right)^2 \left(\frac{\tau_d}{\Delta t_{\rm ISS}(1 \text{ GHz})/10^3 \text{ s}} \right)^{5/3} \tag{3.12}$$

and so the rms error in the DM estimate is

$$\sigma_{\delta\widehat{\rm DM}}(\tau) = 1.57 \times 10^{-6} \text{ pc cm}^{-3} \left| \frac{r^2}{r^2 - 1} \right| \left(\frac{\tau_d}{\Delta t_{\rm ISS}(1 \text{ GHz})/10^3 \text{ s}} \right)^{5/6} . \tag{3.13}$$

The rms error in the infinite-frequency TOA is

$$\sigma_{\delta\hat{t}_\infty}(\tau) \approx \frac{6.5 \text{ ns}}{\nu_1^2} \left| \frac{r^2}{r^2 - 1} \right| \left(\frac{\tau_d}{\Delta t_{\rm ISS}(1 \text{ GHz})/10^3 \text{ s}} \right)^{5/6} . \tag{3.14}$$

In practice, the statistical quantities are estimated through averages over a data set of length T, which is typically several to many years. Time averaging does not appear in the analytical results because the statistical quantities have stationary statistics and we have assumed implicitly that the scintillation time $\Delta t_{\rm ISS}$ is epoch-dependent. However, scintillation parameters are known to vary on some LOSs (Johnston et al. 1998; Levin et al. 2016), so a more detailed treatment would average the structure function over time.

3.3.2 Spectral Properties

As presented, our results do not depend on the length of the overall data span T of a timing data set. If, hypothetically, the electron density were sampled directly to form a time series, a steep Kolmogorov-like spectrum would yield a variance that depends strongly on T. Also, a Fourier-transform based power-spectral estimate would be heavily biased by spectral leakage.

The lack of dependence of our results on T follows because the observable quantity, DM, is a one-dimensional integral of the electron density and has a temporal

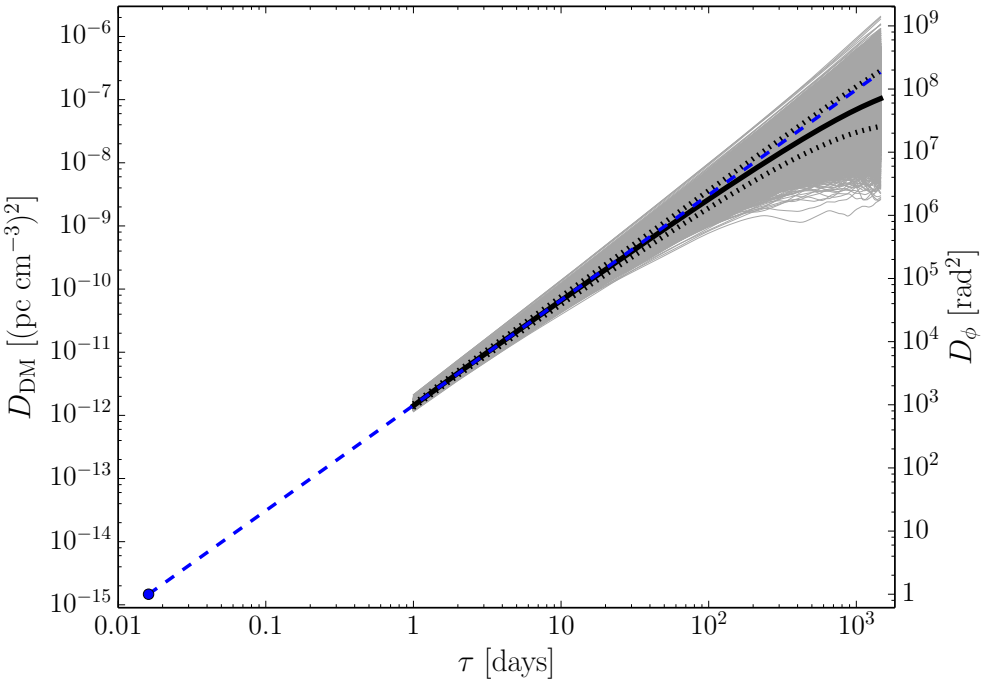

Figure 3.2: Structure functions for $\beta = 11/3$. The solid, thick black line denotes the structure function (SF) geometrically averaged over 10^4 realizations and the dotted lines represent $\pm 1\sigma$ deviations from the mean. The SFs for each realization are shown as thin gray lines. The filled circle at the bottom left and the dashed line show the SF extrapolated from the scintillation timescale at 1 GHz, $\Delta t_{\rm ISS,GHz} = 1388$ s (Keith et al. 2013), to larger lags using Equation (3.12). Note the small bias between the average SF and the extrapolation at large τ.

power spectrum that is shallower than that of the electron density variations (from Equation (3.7)), i.e. $S_{\rm DM}(f) \propto f^{-\gamma}$ with spectral index $\gamma = \beta - 1$ in the scintillation regime, as noted above. The DM difference $\Delta{\rm DM}(t, \tau)$ that we analyze (e.g. Equation (3.3)) is similar to a first derivative for small τ. Since the Fourier transform of a first derivative in the time domain multiplies the transformed function in the frequency domain by one power of f, the power spectrum $S_{\rm DM}$ is multiplied by f^2 and therefore has a spectral index $\beta - 3$ that is less than unity for the regime of interest. For such shallow spectra, the variance should be independent of T and spectral leakage is negligible. We demonstrate these effects for the anticipated

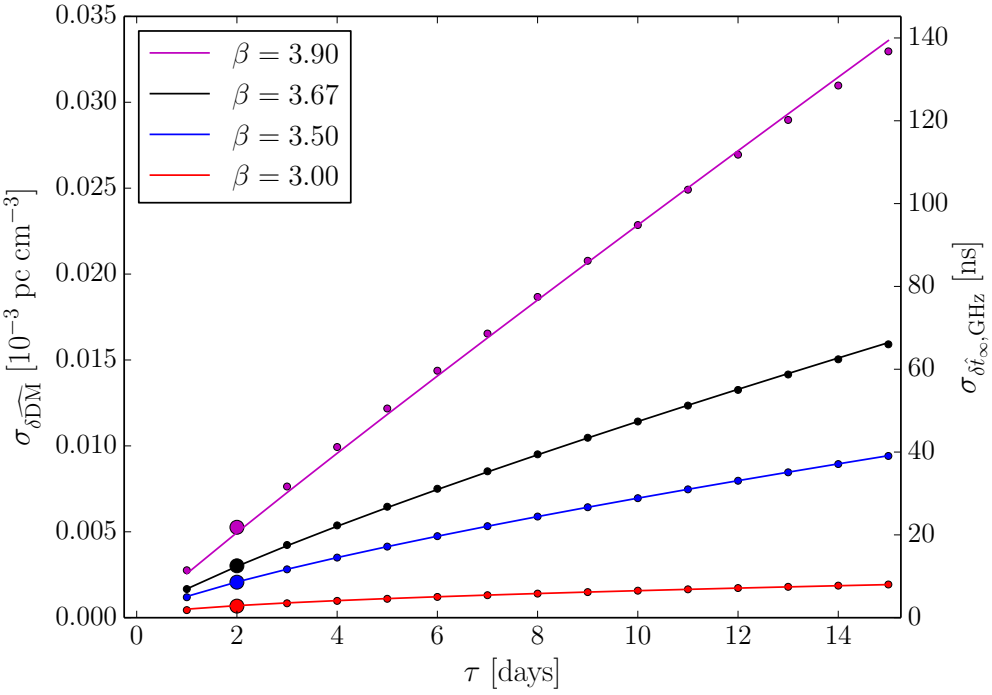

Figure 3.3: $\sigma_{\delta\widehat{\mathrm{DM}}}$ versus multi-frequency observation offset τ for four values of β (in the same order as the legend from top to bottom). Error bars are smaller than the plotted symbols. On the right axis we show $\sigma_{\delta\hat{t}_\infty}$ scaled to 1 GHz. The larger dots emphasize the value of $\sigma_{\delta\widehat{\mathrm{DM}}}$ for the median τ from the distribution shown in Figure 3.4. Solid lines indicate the analytic function of $\sigma_{\delta\widehat{\mathrm{DM}}}$ as per Equation (3.13). The deviations of the simulation from the analytic form come from biases in the structure function that scale with increasing β.

spectral cutoffs using simulations in the next section.

The ensemble-average structure function can be written in terms of the power spectrum for DM,

$$D_{\mathrm{DM}}(\tau) = 4 \int df\, S_{\mathrm{DM}}(f) \sin^2(\pi f \tau). \tag{3.15}$$

If the integrand is dominated by frequencies where $f\tau \ll 1$ for $\tau \sim$ days, then $\sin^2(\pi f\tau) \propto (f\tau)^2$ and the structure function has a square-law form in τ.

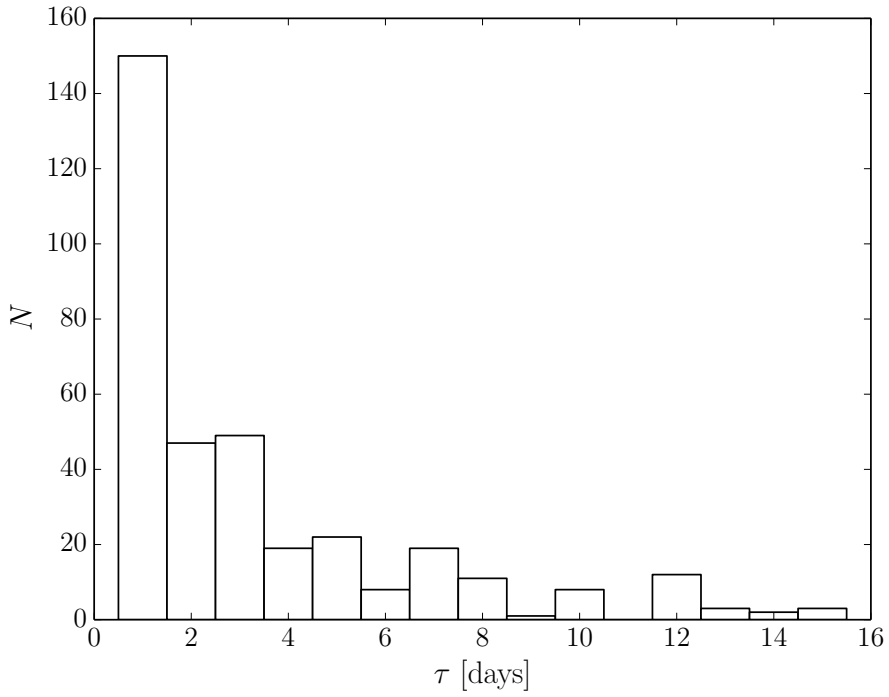

Figure 3.4: Histogram of τ for the 10 pulsars observed with GBT in Demorest et al. (2013). Here we have taken τ to be the absolute value of the time difference between observations at the two different frequency bands. The median $\tau = 2$ days.

3.4 Simulations

We simulated DM variations consistent with the wavenumber spectrum of Equation (3.7) by scaling complex white noise in the frequency domain and transforming to the time domain. Wavenumber cutoffs are outside the range of corresponding timescales we probe and therefore are not implemented. We used 10^4 realizations of DM(t) as a red-noise process over a range of power-law indices γ in the scintillation regime, including the Kolmogorov value $\gamma = 8/3$, each 10 years long with one-day time resolution. For specificity, we use the scintillation time scale of the MSP J1909–3744, one of the best timed objects, to set the coefficient of the phase and DM structure functions. J1909–3744 has a scintillation timescale typical of the

low-DM MSPs used for GW detection (Demorest et al. 2013; Keith et al. 2013). Scaled to 1 GHz, it has $\Delta t_{\rm ISS} = 1388$ s. We emphasize that no white noise has been added to model measurement errors, so we effectively assume that DM can be recovered with no error when $\tau = 0$. We compute time series $\delta\widehat{\rm DM}(t, \tau)$ using Equation (3.4) and a frequency ratio $r = 1.5$ GHz / 0.8 GHz $= 1.875$ to match the center frequencies of observing bands at the GBT.

Figure 3.1 shows representative results for a single realization of DM(t) due to density variations in a medium with a Kolmogorov spectrum along the LOS coupled with changes in the LOS from relative motion. The left column shows time series DM(t) at top after the mean value has been removed and $\delta\widehat{\rm DM}(t, \tau = 1$ day) at bottom while the right column shows the respective power spectra. Note the relative flatness of the δDM spectrum with low spectral index $\gamma = 2/3$.

Table 3.1. Predicted Timing Errors for Selected Millisecond Pulsars
$\sigma_{\delta\hat{t}_\infty}$ at 1.5 GHz for $\beta = 11/3, r = 2$

Pulsar	$\Delta t^{a}_{\rm ISS,GHz}$ [s]	$\sigma_{\delta\hat{t}_\infty}(\tau$ days) [ns]			$\sigma_{\rm TOA}$ [ns]	Observatory
		$\tau = 1$	$\tau = 3$	$\tau = 5$		
J0437–4715	1528	3	7	9	38[b]	Parkes
J1713+0747	1755	2	6	8	50[c]	Arecibo/GBT
B1855+09	900	4	11	13	250[c]	Arecibo
J1909–3744	1388	3	7	9	150[c]	GBT
B1937+21	201	15	37	47	35[b]	Parkes

[a]All values from Keith et al. (2013).
[b]Median TOA uncertainty at 1.5 GHz for 256 MHz bandwidth from Hobbs (2013).
[c]Median TOA uncertainty at 1.5 GHz for 4 MHz bandwidth from Demorest et al. (2013).

3.5 Results

Structure functions of the closely related quantities, DM and ϕ, derived from simulations are shown in Figure 3.2 for multiple realizations with $\beta = 11/3$. The left-hand axis gives DM units and the right-hand axis phase units for $\Delta t_{\rm ISS}$ measured at 1 GHz. The extrapolation of the structure functions from the scintillation time matches simulated results but there is a small bias between the average structure function and the extrapolation at large lags that are comparable to the length of the time series; this is a common feature of structure function estimates and underscores that structure functions need to be interpreted with caution.

We estimate the rms error in DM for an observation gap τ, $\sigma_{\delta\widehat{\rm DM}}(\tau)$, by averaging over the 10^4 realizations. Figure 3.3 shows $\sigma_{\delta\widehat{\rm DM}}$ vs τ for several nominal values of β near the Kolmogorov case. Even though the analytic value in Equation

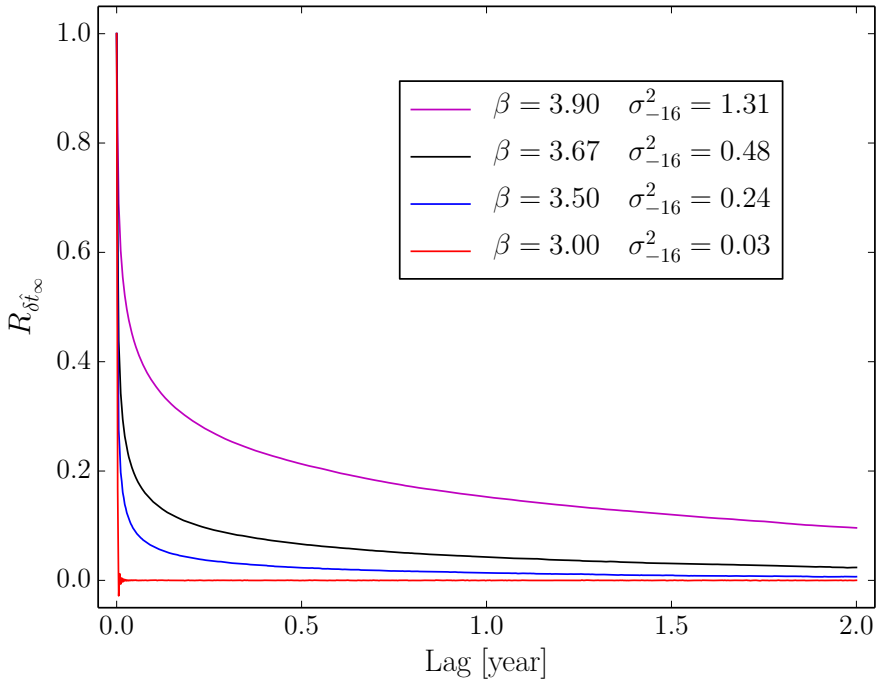

Figure 3.5: Normalized, average autocorrelation functions of $\delta\hat{t}_\infty$ at 1 GHz for four values of β (in the same order as the legend from top to bottom) and $\tau = 1$ day based on 10^4 realizations. The normalization factor is the zero lag value $\sigma^2_{\delta\hat{t}_\infty} = 10^{-16}\ \sigma^2_{-16}\ \mathrm{s}^2$, which is the average total variance in each time series, determined by the scintillation timescale of J1909–3744 and using Equation (3.9). The particular case of $\beta = 3$ shows small Gibbs ringing near the zero lag.

(3.13) matches our simulations well, slight biases will cause mismatches that scale with increasing β (Rutman 1978; Cordes & Downs 1985). We expect the simple $\tau^{\beta-2}$ scaling only in the scintillation regime for $2 < \beta < 4$ but we also need τ to be at an intermediate value such that $f_2^{-1} \ll \tau \ll f_1^{-1}$ where f_1 is the lower frequency cutoff and f_2 is the upper frequency cutoff. The simple $\tau^{\beta-2}$ scaling is perturbed once lags become comparable to the data span length. The perturbation is why we see a slight deviation of the structure function from the simple scaling law for larger lags. Once $\beta > 4$, the structure function will have a square-law form $\propto \tau^2$ for most lag values. Note that for $\beta < 2$ the simple scaling no longer holds.

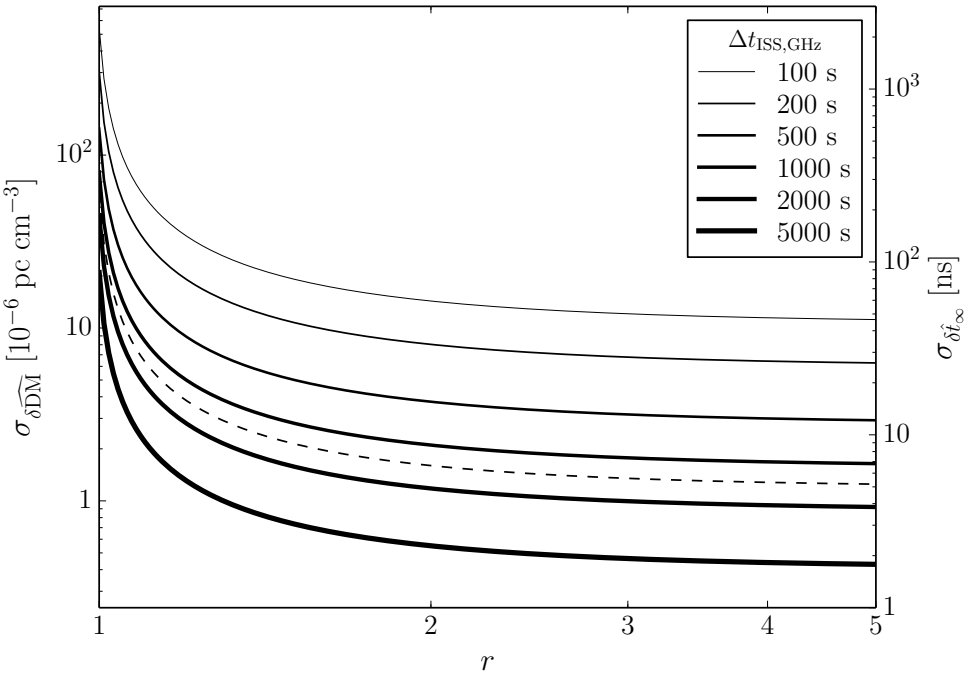

Figure 3.6: Analytic evaluation of $\sigma_{\widehat{\delta \mathrm{DM}}}$ in Equation (3.10) as a function of observational frequency ratio $r = \nu_1/\nu_2$ for different pulsar scintillation timescales Δt_{ISS}, assuming a Kolmogorov medium with $\beta = 11/3$ and $\tau = 1$ day. The dashed line shows the value expected for J1909–3744 (Keith et al. 2013).

Figure 3.4 shows a histogram of offsets between 1.5 GHz and 0.8 GHz observations from GBT observations of 10 pulsars in the NANOGrav five-year data set (Demorest et al. 2013). The median $\tau = 2$ days implies ~ 13 ns of timing error for a pulsar such as J1909–3744 at 1 GHz, a non-negligible fraction of the five-year weighted timing rms of 38 ns (Demorest et al. 2013).

It is instructive to diagnose the amount of temporal correlation expected in the time series for $\delta \hat{t}_\infty$. Autocorrelation functions (ACFs) of $\sigma_{\delta \hat{t}_\infty}$ averaged over realizations are shown in Figure 3.5 for four values of β. The amplitudes of the ACFs are set by the extrapolation of the DM structure function from the scintillation timescale. The correlation timescale, estimated by the width of the ACF, increases with β, indicating that red noise is introduced into timing residuals but

with a spectral index (i.e. from the power spectrum) that is no more than unity.

Figure 3.6 shows $\sigma_{\delta\widehat{\mathrm{DM}}}$ (see Equation (3.13)) as a function of the frequency ratio r for various scintillation timescales Δt_{ISS} of a given pulsar. An increase in the frequency ratio r will reduce the amount of error expected from non-simultaneous observations. The DM and TOA errors asymptote to constant values for large r though most of the reduction in these errors is obtained for $r = 2$. These errors can also be reduced by decreasing the number of days of separation between observations τ. We re-emphasize that our analysis excludes measurement errors.

In reality, errors in DM estimation from additive noise can be improved by an increase in r, up to a point dependent on the pulsar's intrinsic frequency spectrum, regardless of the systematic error from non-simultaneous observations. Therefore, timing campaigns need to optimize the two kinds of error with respect to a choice of r on a pulsar-by-pulsar basis.

We show the analytic values of $\sigma_{\delta\hat{t}_\infty}$ scaled to 1.5 GHz for several of the best-timed MSPs in Table 1. Errors on the order of 10 ns can be expected at the level of our target timing precision for GW detection and a significant fraction of the TOA uncertainty due to radiometer noise even as telescope backends improve. As a comparison, we list the smallest published median template fitting errors, σ_{TOA}, across bands centered close to 1.5 GHz. Values between observatories scale approximately as $B^{-1/2}$ for a bandwidth B, though scintillation can change these numbers somewhat. We see that for the selected best-timed MSPs, errors from non-simultaneous observations become non-negligible, even for small values of τ, and we should attempt to reduce these errors accordingly. When τ cannot be zero (e.g. due to telescope constraints), one alternate method of error reduction is to add additional DM measurements by increasing the number of observing epochs.

3.6 Extension to N-Point Sampling

We can extend our analysis from two-point sampling of DM to N-point sampling. For simplicity, we start with the three-point case and assume the three TOA measurements are spaced by τ days of separation, i.e. $t_1 = t - \tau, t_2 = t, t_3 = t + \tau$, at frequencies ν_1, ν_2, and ν_3, respectively. We can define the estimated DM fluctuation between epochs t_i and t_j to be analogous as previously defined,

$$\widehat{\mathrm{DM}}_{ij}(t,\tau) = \frac{\Delta t_i - \Delta t_j}{K(\nu_i^{-2} - \nu_j^{-2})}. \tag{3.16}$$

If we reference the DM measurements to time t, we find the overall DM estimate to be

$$\widehat{\mathrm{DM}}(t,\tau) = \frac{1}{2}\left[\widehat{\mathrm{DM}}_{21}(t,\tau) + \widehat{\mathrm{DM}}_{32}(t,\tau)\right], \tag{3.17}$$

the average of both pairs of measurements.

While the frequency ratio used for $\widehat{\mathrm{DM}}_{21}$ and $\widehat{\mathrm{DM}}_{32}$ need not be the same, we will assume $\nu_1 = \nu_3$, so that for $r_{ij} = \nu_i/\nu_j$ we have $r_{21} = r_{23} = r$. We can then write the difference between the true and estimated DM as

$$\delta\widehat{\mathrm{DM}}(t,\tau) = \frac{1}{2}\left(\frac{r^2}{r^2-1}\right)\Delta^{(2)}\mathrm{DM}(t,\tau), \tag{3.18}$$

where the superscript (2) denotes the second increment of DM, defined to be

$$\Delta^{(2)}\mathrm{DM}(t,\tau) \equiv \mathrm{DM}(t-\tau) - 2\mathrm{DM}(t) + \mathrm{DM}(t+\tau). \tag{3.19}$$

The second-order structure function, $D^{(2)}_{\mathrm{DM}}(\tau) = \left\langle \left[\Delta^{(2)}\mathrm{DM}(t,\tau)\right]^2 \right\rangle$, allows us to write the rms estimation error,

$$\sigma^{(2)}_{\widehat{\delta\mathrm{DM}}}(\tau) = \frac{1}{2}\left|\frac{r^2}{r^2-1}\right|\left[D^{(2)}_{\mathrm{DM}}(\tau)\right]^{1/2} \tag{3.20}$$

Similarly to the two-point case, the ensemble-average, second-order structure function can also be written in terms of the power spectrum for DM,

$$D^{(2)}_{\rm DM}(\tau) = 16 \int df\, S_{\rm DM}(f) \sin^4(\pi f \tau). \tag{3.21}$$

Combining Eqs. (3.10) and (3.20) with (3.15) and (3.21), and converting to time units, we can solve for the ratio of rms estimation errors between the three-point and two-point sampling cases,

$$R(\tau) = \frac{\sigma^{(2)}_{\delta\hat{t}_\infty}(\tau)}{\sigma^{(1)}_{\delta\hat{t}_\infty}(\tau)} = \frac{1}{2}\left[\frac{D^{(2)}_{\rm DM}(\tau)}{D^{(1)}_{\rm DM}(\tau)}\right]^{1/2} = \left[\frac{\int df\, S_{\rm DM}(f)\sin^4(\pi f\tau)}{\int df\, S_{\rm DM}(f)\sin^2(\pi f\tau)}\right]^{1/2}. \tag{3.22}$$

For $S_{\rm DM}(f) \propto f^{-\gamma}$ in the scintillation regime $1 < \gamma < 3$, we can solve for this ratio (now labeled with subscript γ) exactly as $R_\gamma(\tau) = \sqrt{1 - 2^{\gamma-3}}$, for values of τ that satisfy the inequalities in §5 and as the lower frequency cutoff $f_1 = 1/T$ tends to zero. The Kolmogorov case implies $R_{8/3} \approx 0.45$ and three-point sampling allows for a greater than factor of two improvement over two-point sampling on the rms estimation error. Since the second-order structure function removes linear trends from the time series, whereas the first-order structure function only removes constant terms, R will decrease even further if DM(t) is slope-dominated as is the case for even steeper wavenumber spectra.

For an arbitrary number of epochs N used in DM estimation, N-point sampling will involve an (N-1)-order structure function. The increased cost of observing time will yield diminishing improvements in the rms error. Following Equation (3.22) for the reduction in rms error, the integrand in the numerator will contain increased powers of $\sin^{2(N-1)}(\pi f\tau)$. Since the (N-1)-order increment will have a power spectrum with associated power-law index $\gamma - 2(N-1)$ for small values of $f\tau \ll 1$, increasing the number of sampling epochs N will cause the spectral index to become more positive, i.e. the spectral slope will become more positive, and the

ratio of rms estimation errors between the N-point and the two-point cases will grow. For a Kolmogorov spectrum, we find that the three-point case results in the greatest reduction in error. For steeper wavenumber spectra, increased sampling may become important.

At a telescope like the GBT, the cost of implementing a three-point sampling scheme involves $\sim 50\%$ added time to observing at one frequency band over each set of observations, but could yield an important reduction in the timing noise budget for MSPs like J1713+0747 and J1909–3744. A high-low-high frequency observing scheme at the GBT will mean both a doubling of higher signal-to-noise TOAs measured at 1.5 GHz as well as an improvement in DM estimation as $r < 1$. As in the two-point case, $\sigma_{\delta\widehat{\mathrm{DM}}}$ can be reduced for $r < 1$ but $\sigma_{\hat{t}_\infty}$ cannot. While we only consider an extension to three-point sampling here, arbitrarily increasing the number of sampling days should improve the DM estimate, though with a further increased cost of observing time. The best-case scenario involves the construction of new high-sensitivity, ultra-wideband receiver systems spanning enough bandwidth to allow for accurate enough DM estimation that would eliminate the need for multi-epoch observations altogether.

3.7 Discussion and Conclusions

Our simulations of non-simultaneous, multi-frequency observations indicate a lower bound to timing errors on the order of $\sim$ 10s of nanoseconds for LOSs with scintillation timescales comparable to those of current MSPs sampled in PTAs. The timing error results from mis-estimation of the DM and any additional measurement errors will increase the DM errors and therefore the TOA uncertainty further.

For the Kolmogorov case, we find a "pink" noise spectrum for the time series of DM errors proportional to $f^{-2/3}$. Any red noise present in timing residuals can affect the sensitivity of a PTA to GWs. For identical observational parameters in a timing program, these campaigns will be limited by the induced DM measurement error largely related to the scintillation timescale for a given pulsar. TOA errors scale as $\sigma_{\delta\widehat{\mathrm{DM}}} \propto \Delta t_{\mathrm{ISS}}^{-5/6}$, so timing measurements of pulsars with larger Δt_{ISS} will have smaller errors.

While we analyze DM variations with power-law wavenumber spectra and wavenumber cutoffs outside of the corresponding timescales we probe, observed interstellar DM variations have a minimum characteristic timescale that is determined by spatial smoothing from scattering and is equal to the refraction timescale (Cordes & Shannon 2010), $t_r \sim 2.4$ days $(D/D_s)(\nu_{\mathrm{GHz}}/\Delta\nu_{\mathrm{ISS,0.01}})(\Delta t_{\mathrm{ISS}}/1000$ s), where D is the distance to the pulsar, D_s is the distance between the pulsar and the scattering screen, $\Delta\nu_{\mathrm{ISS,0.01}}$ is the scintillation bandwidth is in units of 10 MHz. For J1909-3744, the scintillation bandwidth is 37 MHz at 1.5 GHz (Keith et al. 2013), which means that the refraction timescale is on the order of a day unless $D_s \ll D$, changing the effective higher wavenumber spectrum cutoff. Because $t_r \propto \nu/\Delta\nu_{\mathrm{ISS}} \propto \nu^{-17/5}$, the relevant smoothing time is from the *higher* of a pair of frequencies. The difference in smoothing at the two frequencies gives rise to other effects that are discussed in a separate paper (Cordes et al. 2016).

As we discover MSPs farther out in the Galactic plane, we expect an increase in DM along these LOSs. While MSPs with higher DMs have the potential to be suitable for inclusion into a PTA, mitigation of increased scattering effects may prove challenging. We expect that $\Delta t_{\mathrm{ISS}} \propto \mathrm{DM}^{-3/5}$ for a homogenous, Kolmogorov medium (e.g. Equation (46) of Cordes & Lazio 1991). With decreasing Δt_{ISS}, more

stringent constraints on τ will become important for the population of newer, more distant pulsars.

Equation (3.5) describes the timing error associated with any DM differences between observations. While we have only considered electron-density variations from fluctuations in the ISM so far, local variations, such as in the ionosphere, can also add to the TOA error. Ionospheric changes in electron density correlate with incident flux from the Sun. Daily changes due to Earth's rotation, yearly changes due to Earth's orbit, and eleven-year cycles due to solar magnetic activity, are all observed, leading to electron-density variations that can vary by up to $\sim 10^{-5}$ pc cm^{-3}, or a TOA uncertainty of $\sim$ 40 ns at 1 GHz, on any of these timescales (Huang & Roussel-Dupré 2006). Extreme solar events can produce a bigger effect. The observed electron density will also increase for LOSs that pass through large zenith angles. The uncertainty in DM can increase even for small values of τ if the pulsar is observed at widely different hour angles. Since the ionosphere varies spatially across the globe as well as temporally, DM differences, and therefore associated TOA errors, can potentially exist in simultaneous, multi-frequency observations for separate telescopes at a level larger than the rms error in Equation (3.13). We suggest that the best practice is for observations to be spatially coincident as well as simultaneous.

Equation (3.13) can be used to quantify the tolerance level in non-simultaneous observations for minimal acceptable levels of noise. Observations requiring DM correction should ensure a frequency ratio $r \gtrsim 2$, which is well within the goal of future wideband timing systems. Timing campaigns should strive for same day observations, though alternatively, measurements with multiple (> 2) observations per epoch may partially improve DM estimation and the overall TOA uncertainty.

Errors from non-simultaneous multi-frequency measurements may become a large contribution to the total timing noise budget for pulsars with the highest-timing precision, for pulsars observed with next-generation telescopes with improved sensitivity, and for PTAs as a whole since sensitivity is often dominated by the best-timed pulsars in the array.

Work on pulsar timing at Cornell University is supported in part by NSF PIRE program award number 0968296.

BIBLIOGRAPHY

Backer, D. C., Hama, S., van Hook, S., & Foster, R. S. 1993, ApJ, 404, 636

Bhat, N. D. R., Cordes, J. M., Camilo, F., Nice, D. J., & Lorimer, D. R. 2004, ApJ, 605, 759

Brisken, W. F., Macquart, J.-P., Gao, J. J., et al. 2010, ApJ, 708, 232

Chernoff, D. F. 2009, arXiv:0908.4077

Cognard, I., & Lestrade, J.-F. 1997, A&A, 323, 211

Cordes, J. M. 2013, Classical and Quantum Gravity, 30, 224002

Cordes, J. M., & Downs, G. S. 1985, ApJS, 59, 343

Cordes, J. M., & Lazio, T. J. 1991, ApJ, 376, 123

Cordes, J. M., Pidwerbetsky, A., & Lovelace, R. V. E. 1986, ApJ, 310, 737

Cordes, J. M., & Rickett, B. J. 1998, ApJ, 507, 846

Cordes, J. M., & Shannon, R. M. 2010, arXiv:1010.3785

Cordes, J. M., Shannon, R. M., & Stinebring, D. R. 2016, ApJ, 817, 16

Cordes, J. M., Wolszczan, A., Dewey, R. J., Blaskiewicz, M., & Stinebring, D. R. 1990, ApJ, 349, 245

Craft, H. D., Jr. 1970, PhD thesis, Cornell Univ.

Demorest, P. B., Ferdman, R. D., Gonzalez, M. E., et al. 2013, ApJ, 762, 94

Detweiler, S. 1979, ApJ, 234, 1100

Foster, R. S., & Cordes, J. M. 1990, ApJ, 364, 123

Hankins, T. H., & Rickett, B. J. 1986, ApJ, 311, 684

Hassall, T. E., Stappers, B. W., Hessels, J. W. T., et al. 2012, A&A, 543, A66

Hellings, R. W., & Downs, G. S. 1983, ApJL, 265, L39

Hobbs, G. 2013, Classical and Quantum Gravity, 30, 224007

Huang, Z., & Roussel-Dupré, R. 2006, Radio Science, 41, RS6004

Isaacman, R., & Rankin, J. M. 1977, ApJ, 214, 214

Jenet, F. A., Hobbs, G. B., Lee, K. J., & Manchester, R. N. 2005, ApJL, 625, L123

Johnston, S., Nicastro, L., & Koribalski, B. 1998, MNRAS, 297, 108

Kaspi, V. M., Taylor, J. H., & Ryba, M. F. 1994, ApJ, 428, 713

Keith, M. J., Coles, W., Shannon, R. M., et al. 2013, MNRAS, 429, 2161

Kramer, M., & Champion, D. J. 2013, Classical and Quantum Gravity, 30, 224009

Kramer, M., Lange, C., Lorimer, D. R., et al. 1999, ApJ, 526, 957

Lam, M. T., Cordes, J. M., Chatterjee, S., et al. 2016, ApJ, 821, 66

Levin, L., McLaughlin, M. A., Jones, G., et al. 2016, ApJ, 818, 166

Löhmer, O., Mitra, D., Gupta, Y., Kramer, M., & Ahuja, A. 2004, A&A, 425, 569

Lorimer, D. R., & Kramer, M. 2012, Handbook of Pulsar Astronomy, by D. R. Lorimer , M. Kramer. Cambridge Observing Handbooks for Research Astronomers, Vol. 4. Cambridge, UK: Cambridge University Press, 2012

McLaughlin, M. A. 2013, Classical and Quantum Gravity, 30, 224008

Pennucci, T. T., Demorest, P. B., & Ransom, S. M. 2014, ApJ, 790, 93

Phillips, J. A., & Wolszczan, A. 1991, ApJL, 382, L27

Ramachandran, R., Demorest, P., Backer, D. C., Cognard, I., & Lommen, A. 2006, ApJ, 645, 303

Rawley, L. A., Taylor, J. H., & Davis, M. M. 1988, ApJ, 326, 947

Rickett, B. J. 1990, ARA&A, 28, 561

Romani, R. W., Narayan, R., & Blandford, R. 1986, MNRAS, 220, 19

Rutman, J. 1978, IEEE Proceedings, 66, 1048

Ryba, M. F., & Taylor, J. H. 1991, ApJ, 371, 739

Sesana, A. 2013, Classical and Quantum Gravity, 30, 224014

Stairs, I. H., Arzoumanian, Z., Camilo, F., et al. 1998, ApJ, 505, 352

Stinebring, D. 2013, Classical and Quantum Gravity, 30, 224006

You, X. P., et al. 2007, MNRAS, 378, 493

CHAPTER 4

SYSTEMATIC AND STOCHASTIC VARIATIONS IN PULSAR DISPERSION MEASURES

We analyze deterministic and random temporal variations in dispersion measure (DM) from the full three-dimensional velocities of pulsars with respect to the solar system, combined with electron-density variations on a wide range of length scales. Previous treatments have largely ignored the pulsar's changing distance while favoring interpretations involving the change in sky position from transverse motion. Linear trends in pulsar DMs seen over 5-10 year timescales may signify sizable DM gradients in the interstellar medium (ISM) sampled by the changing direction of the line of sight to the pulsar. We show that motions parallel to the line of sight can also account for linear trends, for the apparent excess of DM variance over that extrapolated from scintillation measurements, and for the apparent non-Kolmogorov scalings of DM structure functions inferred in some cases. Pulsar motions through atomic gas may produce bow-shock ionized gas that also contributes to DM variations. We discuss possible causes of periodic or quasi-periodic changes in DM, including seasonal changes in the ionosphere, annual variation of the solar elongation angle, structure in the heliosphere-ISM boundary, and substructure in the ISM. We assess the solar cycle's role on the amplitude of ionospheric and solar-wind variations. Interstellar refraction can produce cyclic timing variations from the error in transforming arrival times to the solar system barycenter. We apply our methods to DM time series and DM gradient measurements in the literature and assess consistency with a Kolmogorov medium. Finally, we discuss the

Published: Lam, M. T., Cordes, J. M., Chatterjee, S., et al. 2016, ApJ, 821, 66

implications of DM modeling in precision pulsar timing experiments.

4.1 Introduction

Free electrons in the interstellar medium (ISM) affect pulsar signals by introducing a frequency-dependent dispersion delay. Dispersion delays need to be removed as part of search algorithms in pulsar surveys and for precision time-of-arrival (TOA) measurements that are used for determinations of orbital elements, tests of General Relativity and other theories of gravity, and detection of long-wavelength gravitational waves. Besides being used for correction, dispersion measures (DMs) are the the primary means for determining electron column densities on Galactic and, in some cases, extragalactic lines of sight (LOSs). They serve as important input data for Galactic models of the electron density and in studies of stochastic variations in electron density on length scales $\sim$ 1–100 AU. Dispersion and scattering, a related frequency-dependent phenomenon due to multi-path propagation, are assumed to result from cold plasma in the high-frequency limit with negligible contributions from magnetic fields (see Cordes 2002 or Lorimer & Kramer 2012 for a review).

In this paper, we discuss the inferences that can be made about the ISM using epoch-dependent DM measurements. We analyze DMs in terms of the full three-dimensional motions of pulsars, the changes in electron density along the entire LOS, and the solar system motion through the ISM. The dispersion measure is the LOS integral

$$\mathrm{DM}(t) = \int_0^{D(t)} ds\, n_e(s\hat{\mathbf{n}}(t), t), \tag{4.1}$$

where $D(t)$ is the pulsar's distance, n_e is the electron density, and $\hat{\mathbf{n}}(t)$ is a unit vector from the observer to the pulsar, with all three quantities generally epoch-

dependent. Many pulsars have much higher velocities than bulk ISM motion, so variations in DM are usually dominated by the changing LOS, including both the distance and direction. Therefore, we generally drop the explicit time dependence of the electron density, though we will show that this assumption does not hold within the solar system. While epoch-dependent distances are an obvious consequence of high velocities, most quantitative analyses of DMs have focused on how the LOS changes from transverse motions.

We report on measured DM variations in the literature in §4.2. In §4.3 we develop the formalism for DM variations from changing LOS integrals through electron-filled media and we discuss resulting linear trends in DM time series in §4.4. We consider the DM struture function (SF) and contributions to it from stochastic DM variations in §4.5. In §4.6 we discuss the impact of refraction on timing delays and subsequently the measured DM. We interpret the causes of linear and non-monotonic trends seen in several pulsars in the literature in §4.7 and periodic DM variations in §4.8. In §5.6, we report the impact of DM variations on ISM study and on timing precision. We summarize our findings and conclusions in §6.7. A list of symbols and acronyms used throughout the paper can be found in Table 4.1.

4.2 Measured DM Variations

Time variability in DM is a well-known phenomenon in pulsar timing. Epoch-dependent variations were first detected in the Crab Pulsar (Rankin & Roberts 1971). Isaacman & Rankin (1977) measured DM variations in the Crab Pulsar over a five-year span and suggest that the changes in DM come from within the

Crab Nebula. Hamilton et al. (1985) found a large gradient in the DM of the Vela Pulsar over 15 years and attributed it to the LOS changing with the transverse velocity of the pulsar relative to the supernova remnant. Spatial variations in DM on sub-parsec scales have also been seen (see Manchester et al. 1991 and Freire et al. 2001, who discuss changes in DM over different LOSs to pulsars in the center of the globular cluster 47 Tucanae).

Published time series of DM in the literature show several types of behavior. Some show deterministic linear trends superposed with correlated, stochastic variations. A few show piecewise linear variations that signify change points in the time derivative $d\mathrm{DM}/dt$ associated with structure in the ISM on scales of 1–100 AU. Many also show periodic variations, either smoothly sinusoidal or sharp with distinct features, often with a period of roughly one year. The amplitudes of these variations have also been seen to change with time. In some cases, both linear and periodic variations are seen. Others show only correlated, stochastic variations without an obvious trend.

Phillips & Wolszczan (1991) reported results on five pulsars, four of which show long-term trends with slopes $|d\mathrm{DM}/dt| \sim 10^{-3}$ pc cm^{-3} yr^{-1} (increasing: PSRs B0823+26, B0834+06, and B1237+25; decreasing: PSR B0919+06). They assert that the rms of the DM variations is correlated with the average DM but with significant scatter about a best fit relation $\sigma_{\mathrm{DM}} \propto \mathrm{DM}^{1.3\pm0.3}$. A trend of this type would generally signify that the DM variations are associated with accumulated effects along the LOS, but the correlation is affected by the long-term trends that may be due to parallel motion through ionized gas near the pulsars.

Keith et al. (2013, see also You et al. 2007; Petroff et al. 2013) give $\mathrm{DM}(t)$ time series over roughly ~ 6 yr for 20 millisecond pulsars (MSPs) that are monitored

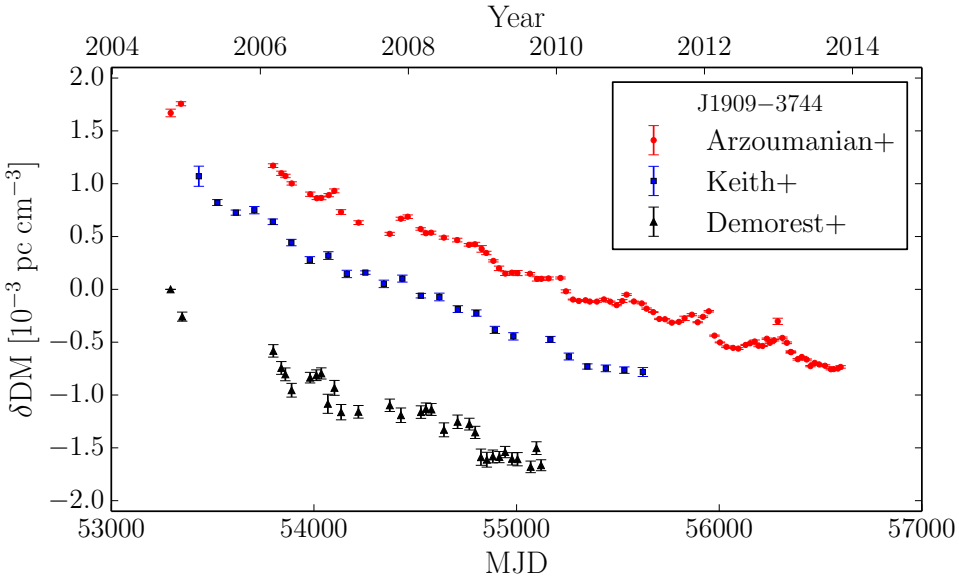

Figure 4.1: DM offsets $\delta\mathrm{DM}(t) = \mathrm{DM}(t) - \mathrm{DM}_{\mathrm{nominal}}$ for PSR J1909-3744, reported in Arzoumanian et al. (2015b, red circles), Keith et al. (2013, blue squares), Demorest et al. (2013, black triangles). $\mathrm{DM}_{\mathrm{nominal}} = 10.394680, 10.392717, 10.392031$ pc cm^{-3}, respectively. The nominal DM differs due to different methods to account for frequency-dependent pulse shape changes in the timing models.

in the Parkes Pulsar Timing Array (PPTA) program. Of these, 11 show prevailing trends of increasing DM (PSRs J1024−0719, J1730−2304, J1732−5049, and J1857+0943) or decreasing DM (PSRs J1045−4509, J1600−3053, J1643−1224, J1744−1134, J1909−3744, J1939+2134 and J2129−5721). Two others show overall trends but with a localized DM 'event' that breaks the trend (PSRs J1603−7202 and J1824−2452). The remaining seven objects show non-monotonic variations with various degrees and timescales of temporal correlation. Reardon et al. (2016) find evidence for significant linear trends in 13 pulsars and sinusoidal, annual variations in four pulsars in the extended PPTA data release 1. The approximate derivative for PSR J1939+2134 (B1937+21) is about half the value of the 20-year trend reported by Ramachandran et al. (2006) and is consistent with changes in slope seen in the 20-year time series.

Demorest et al. (2013) present DM(t) time series for 14 out of 17 pulsars that were part of the first data release of the North American Nanohertz Observatory for Gravitational Waves (NANOGrav), based on five years of data. Of these, the seven objects that overlap with the Keith et al. (2013) sample show consistent trends. Of the others, several objects show very weak DM variation while two pulsars, PSRs B1855+09 and J2317+1439, show strong trends superposed with correlated, stochastic variations.

Table 4.1. Symbols and Acronyms Used

Symbols	Definition	Characteristic Units
a	Characteristic scale of ISM structure	Length
A	Spectral coefficient	
c	Speed of light	cm s^{-1}
C	Arbitrary amplitude	
C_1	Constant in uncertainty relation, $2\pi\Delta\nu_{\rm ISS}\tau_{\rm ISS} = C_1$	
$C_{\rm n}^2$	Coefficient in electron-density wavenumber spectrum	Length$^{-(\beta+3)}$
D	Earth-Pulsar distance	kpc
DM	Dispersion Measure	pc cm^{-3}
$D_{\rm DM}$	DM structure function	[pc cm^{-3}]^2
D_t	Time structure function	s^2
D_ϕ	Phase structure function	radians^2
$\dot{E}$	Pulsar energy loss rate	erg s^{-1}
f	Spectral frequency	Time^{-1}
f_1,f_2	Lower and upper spectral cutoffs of $S_{\rm DM}$	Time^{-1}
f_β	Numerical factor in DM structure function	
h	Planck constant	erg s
h_s	Height above Earth's surface	km
H	Characteristic thickness of ionospheric layer	km
k	Boltzmann constant	erg K^{-1}
K	Dispersion constant ($\equiv cr_e/2\pi$)	ms GHz^2 pc^{-1} cm^{-3}
l	Characteristic scale of ISM structure	Length
l_g,b_g	Galactic coordinates (longitude, latitude)	deg
$l_{\rm HI}$	Mean free path for neutral-hydrogen-ionizing radiation	cm
m_p	Proton mass	g
n_e	Electron density	cm^{-3}
$n_{\rm HI}$	Effective hydrogen density	cm^{-3}
n_p	Proton density	cm^{-3}
N_e	Electron column density	cm^{-2}
$N_{\rm HI}$	Hydrogen column density	cm^{-2}
$P_{\delta n_e}$	Wavenumber spectrum for the electron density	Length^{-3}
q	Wavenumber	Length^{-1}
q_1,q_2	Lower and upper wavenumber cutoffs of $P_{\delta n_e}$	Length^{-1}

Table 4.1 (cont'd)

Symbols	Definition	Characteristic Units
r	Position	Length
r_e	Classical electron radius	cm
r_s	Bow-shock standoff radius	cm
$r_\oplus$	Earth-Sun distance	AU
$R_{d\mathrm{DM}/dt}$	ratio of linear trend to rms linear trend from a Kolmogorov medium	
R_{rms}	ratio of rms DM after and before a linear trend is removed	
s	Represents a generic position along the LOS	Length
S	Power spectrum	
SM	Scattering Measure	kpc $\mathrm{m}^{-(\beta+3)}$
t	Time	Time
T	Total observing span	Time
v	Velocity	km/s
x	Position	Length
z	Represents a position along the LOS	Length
α	Arbitrary spectral index	
α_e,δ_e	Equatorial coordinates (RA, declination)	deg
β	Exponent in wavenumber spectrum for n_e	
Γ	Gamma function	
γ	Exponent in power-law of red noise process	
Δ	Difference/Increment	
$\Delta\nu_{\mathrm{ISS}}$	Scintillation bandwidth	MHz
Δt	Time delay	Time
Δt_{ISS}	Scintillation timescale	s
η_s	Shock compression factor	
θ_i	Incidence angle	rad
θ_r	Refraction angle	rad
θ_z	Zenith angle	deg
λ, ν	Electromagnetic wavelength and frequency	cm, GHz
λ_e,β_e	Ecliptic coordinates (longitude, latitude)	deg
λ_h,β_h	Heliographic coordinates (longitude, latitude)	deg
ρ	Mass density	g cm^{-3}

Table 4.1 (cont'd)

Symbols	Definition	Characteristic Units
σ	rms	
$\sigma_{\rm HI}$	Photoionoization cross section for neutral hydrogen	$\rm cm^{-2}$
τ	Time lag	Time
$\tau_{\rm ISS}$	Scattering timescale	μs
ϕ	Phase perturbation from refractive index perturbations	rad
ϕ_g,λ_g	Geographic coordinates (latitude, longitude)	deg
φ	Sinusoidal phase	rad
ω	Sinusoidal angular frequency	Angle/Time

PSR J1909−3744 exemplifies several types of variations in DM that motivate our study. Demorest et al. (2013) see a monotonic decrease in DM over 5 years. Keith et al. (2013) also note the linearity of DM(t), with a change in 1.85×10^{-3} pc cm^{-3} over 6 years, and find that the SF of their time series exceeds, for every lag, the SF prediction from dynamic spectrum estimates by a factor of ~ 5. They suggest the SF excess implies an electron-density wavenumber spectrum steeper than that of a turbulent, Kolmogorov medium. Recently, the NANOGrav Nine-Year Data Release (Arzoumanian et al. 2015b; hereafter NG9) showed that the decreasing trend continued, spanning all nine years of data, along with a superposed annual variation. Figure 4.1 shows the DM offsets $\delta{\rm DM}(t) = {\rm DM}(t) - {\rm DM}_{\rm nominal}$ as presented by the three data sets, where ${\rm DM}_{\rm nominal} = 10.394680$ pc cm^{-3} for Demorest et al. (2013), 10.392717 pc cm^{-3} for Keith et al. (2013), and 10.392031 pc cm^{-3} for NG9. Differences in the absolute DM are caused by different methods of frequency-dependent pulse shape variation removal from the TOAs. An in-depth analysis of the DM variations of all of the MSPs in NG9 will be presented in the future (M. L. Jones et al. in preparation).

Fonseca et al. (2014) present DM(t) for the relativistic binary PSR B1534+12

and fit for derivatives $d\mathrm{DM}/dt$ in five separate time blocks. The overall trend is a decrease with time that is interrupted by episodic flattenings or increases in DM. The variation of $\mathrm{DM}(t)$ from 1990 to 2012 is dominated by five piecewise linear segments lasting three to five years with slopes $d\mathrm{DM}/dt = \{-3.16, -0.43, -2.94, 10.1, -0.1\} \times 10^{-4}$ pc cm^{-3} yr^{-1}. The DM SF scales as $\tau^{3.70\pm0.04}$ for lags between 70 and 90 days, consistent with a Kolmogorov scaling. The best-fit SF implies a diffractive scintillation timescale of $\Delta t_{\mathrm{ISS}} = 3.0 \pm 0.8$ min at 0.43 GHz, considerably smaller than the range 11 ± 3 min directly measured by Bogdanov et al. (2002) from 2D autocorrelation functions of dynamic spectra. While epoch-dependent scintillation may play a role in this difference, the shorter time scale inferred from the SF fit is consistent with the presence of contamination from non-Kolmogorov fluctuations on length scales relevant to the DM variations.

4.3 Line of Sight Integrals

In the following, we will develop the mathematical framework for variations in DM that we will use in following sections. Consider changes in DM that result from the relative motion of the pulsar and observer, which changes both the distance to the pulsar and the direction of the LOS, as shown in Figure 4.2. For an initial pulsar position $\mathbf{x}_{p0}$ and Earth position $\mathbf{x}_{e0}$, the initial distance $D_0 = |\mathbf{x}_{p0} - \mathbf{x}_{e0}|$ increases (to first order in time) as

$$D(t) \approx D_0 + (\mathbf{v}_p - \mathbf{v}_e) \cdot \hat{\mathbf{n}}_0 \; t \equiv D_0 + \Delta v_{\parallel} t, \tag{4.2}$$

where $\mathbf{v}_p$ and $\mathbf{v}_e$ are the pulsar and Earth velocity vectors, respectively, $\hat{\mathbf{n}}_0 = \Delta\mathbf{x}_0/D_0 = (\mathbf{x}_{p0} - \mathbf{x}_{e0})/D_0$ is the unit vector to the pulsar at $t = 0$, and $\Delta v_{\parallel}$ is the apparent velocity of the pulsar parallel to the LOS. The next, quadratic term,

$(\Delta v_\perp t)^2/2D_0$, where $\Delta v_\perp$ is the apparent velocity of the pulsar perpendicular to the LOS, is a factor $\Delta v_\perp t/D_0 \sim 10^{-6}$ times smaller than the linear term for typical parameters of $\Delta v \sim 100$ km s^{-1} (Faucher-Giguère & Kaspi 2006), time span $T \sim 10$ years, and $D \sim 1$ kpc (Cordes & Lazio 2002), and therefore can be ignored in calculating the distance. Conversely, the change in direction is determined by the transverse velocity

$$\hat{\mathbf{n}}(t) = \hat{\mathbf{n}}_0 + D_0^{-1}\Delta\mathbf{v}_\perp t. \tag{4.3}$$

Let the initial LOS at $t = 0$ be the z-axis and integrate over locations $\mathbf{x}_0(z) = z\hat{\mathbf{z}}$ to get the initial DM,

$$\mathrm{DM}_0 = \int_{z_{e_0}}^{z_{p_0}} dz\, n_e(\mathbf{x}_0(z)). \tag{4.4}$$

For $t > 0$ we integrate over a new interval $[z_e, z_p]$ where

$$z_e = z_{e0} + v_{e_\parallel}\, t, \quad z_p = z_{p0} + v_{p_\parallel}\, t. \tag{4.5}$$

The sampled locations are now $\mathbf{x}(z,t) = \mathbf{r}(z,t) + z\hat{\mathbf{z}}$ where $\mathbf{r}(z,t)$ is transverse to $\hat{\mathbf{z}}$,

$$\mathbf{r}(z,t) = \mathbf{v}_{\mathrm{eff}_\perp}(z)t \tag{4.6}$$

$$\mathbf{v}_{\mathrm{eff}_\perp}(z) = \mathbf{v}_{e_\perp} + (\mathbf{v}_{p_\perp} - \mathbf{v}_{e_\perp})\left(\frac{z - z_e}{z_p - z_e}\right). \tag{4.7}$$

The locations z_e and z_p are evaluated at time t and it is assumed that there is no significant acceleration correction over times of interest (weeks to decades). The effective transverse velocity, $\mathbf{v}_{\mathrm{eff}_\perp}$, is a weighted sum of the pulsar's and Earth's velocities. It is consistent with that given in Eq. 3 of Cordes & Rickett (1998), which also includes a term $-V_m$ for the velocity of the medium, and also with Eq. C15 of Gupta et al. (1994).

The simplest approach is to evaluate the electron density for the $t > 0$ LOS in terms of its values for the initial LOS,

$$\begin{aligned} n_e(\mathbf{x}(z,t)) &= n_e(\mathbf{x}_0(z)) + [n_e(\mathbf{x}(z,t)) - n_e(\mathbf{x}_0(z))] \\ &\equiv n_e(\mathbf{x}_0(z)) + \Delta n_e(\mathbf{x}(z,t)). \end{aligned} \tag{4.8}$$

The DM integral over $[z_e, z_p]$ can be expanded into integrals over the three intervals $[z_{e_0}, z_p]$, $[z_{e_0}, z_e]$, and $[z_{p_0}, z_p]$ to get

$$\begin{aligned} \mathrm{DM}(t) &= \int_{z_e}^{z_p} dz\, n_e(\mathbf{x}(z,t)) \\ &= \int_{z_{e_0}}^{z_{p_0}} dz\, n_e(\mathbf{x}(z,t)) + \int_{z_{p_0}}^{z_p} dz\, n_e(\mathbf{x}(z,t)) \\ &\quad - \int_{z_{e_0}}^{z_e} dz\, n_e(\mathbf{x}(z,t)). \end{aligned} \tag{4.9}$$

For the first integral we expand the integrand using Eq. 4.8 to get

$$\int_{z_{e_0}}^{z_{p_0}} dz\, n_e(\mathbf{x}(z,t)) = \mathrm{DM}_0 + \int_{z_{e_0}}^{z_{p_0}} dz\, \Delta n_e(\mathbf{x}(z,t)). \tag{4.10}$$

This gives

$$\begin{aligned} \mathrm{DM}(t) &= \mathrm{DM}_0 + \int_{z_{e_0}}^{z_{p_0}} dz\, \Delta n_e(\mathbf{x}(z,t)) \\ &\quad + \int_{z_{p_0}}^{z_p} dz\, n_e(\mathbf{x}(z,t)) - \int_{z_{e_0}}^{z_e} dz\, n_e(\mathbf{x}(z,t)). \end{aligned} \tag{4.11}$$

DM_0 is the DM measured at time $t = 0$, the first integral is the change in DM over the initial LOS (density fluctuation term), the second integral is the change in DM due to the pulsar's motion through its local environment (pulsar term), and the third integral is the change in DM due to the Earth/Solar System's motion through its local environment (Earth term).

The integrand $\Delta n_e(\mathbf{x}(z,t))$ of the density fluctuation term needs to be considered only if electron density variations are significant on length scales of order

the offset between the LOS at t and the initial LOS at $t = 0$, i.e., $|\Delta\mathbf{x}(z,t)| = |\mathbf{x}(z,t) - \mathbf{x}_0(z)| \ll D_0$. For example, this offset $\ell \sim 20$ AU $v_{\mathrm{eff}_{\perp}100} t_{\mathrm{yr}}$ for a fiducial velocity of 100 km s^{-1} and a year-long time span. All evidence from the last few decades of interstellar scintillation studies are consistent with there being variations on these (multiples of AU) and smaller scales (Coles et al. 1987; Armstrong et al. 1995; Rickett et al. 2000). However, the detailed spectrum of variations on AU scales is not well known and appears to differ between the LOSs to different pulsars (Stinebring et al. 2000).

The pulsar and Earth terms in Eq. 4.11 are over small intervals $z_p - z_{p_0} = v_{p_\parallel} t$ and $z_e - z_{e_0} = v_{e_\parallel} t$ so, to first order in these intervals, the two terms give $\overline{n}_e(\overline{\mathbf{x}}_p) v_{p_\parallel} t$ and $\overline{n}_e(\overline{\mathbf{x}}_e) v_{e_\parallel} t$, where $\overline{n}_e(\overline{\mathbf{x}}_p)$ and $\overline{n}_e(\overline{\mathbf{x}}_e)$ are averages over the respective intervals centered on $\overline{\mathbf{x}}_p = \mathbf{x}_{p_0} + (v_{p_\parallel} t/2)\hat{\mathbf{n}}(t)$ and $\overline{\mathbf{x}}_e = \mathbf{x}_{e_0} + (v_{e_\parallel} t/2)\hat{\mathbf{n}}(t)$, respectively. Unless there are large variations over the intervals, these average locations can be taken as the initial ones at $t = 0$. The DM variations from these two terms are a simple consequence of the change in pulsar distance due to parallel motion because, as noted earlier, the transverse velocities enter only to second order and so are negligible in these terms.

We assume that true *temporal* changes in electron density are negligible. This is often a good assumption because turbulent ISM velocities (of order a few km/s) are typically much smaller than pulsar velocities (Faucher-Giguère & Kaspi 2006; Frisch et al. 2011). For slow pulsars and fast plasma screens (e.g., shock fronts), the ISM velocity needs to be included and adds a term $-\mathbf{v}_m(z)$ (with m for medium) to the effective velocity defined in Eq. 4.7. For a purely turbulent medium, the velocity is stochastic and would depend on wavenumber. However, a moving screen is easily described with a translational velocity.

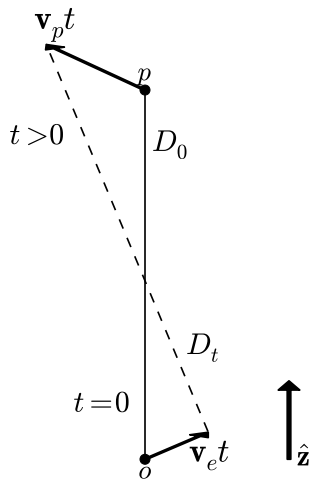

Figure 4.2: Geometry showing change in LOS due to motion of pulsar p and observer o. DM is calculated by integrating along the z-axis taking into account the change in LOS.

4.4 Linear Trends in DM

For a perfectly uniform medium with density n_e the difference $\Delta n_e(\mathbf{x}(z,t))$ vanishes and the total DM (found by combining Eqs. 4.5 and 4.11) is

$$\mathrm{DM}(t) = \mathrm{DM}_0 + n_e(v_{p_\parallel} - v_{e_\parallel})t, \tag{4.12}$$

giving a time derivative

$$\begin{aligned} \frac{d\mathrm{DM}}{dt} &= n_e(v_{p_\parallel} - v_{e_\parallel}) \\ &\approx 10^{-5}\ v_{100} n_{e_{0.1}}\ \mathrm{pc\ cm^{-3}\ yr^{-1}}, \end{aligned} \tag{4.13}$$

where the approximate estimate uses a fiducial relative velocity of 100 km s^{-1} and an electron density of 0.1 cm^{-3} (Frisch et al. 2011). Observed DM derivatives range from approximately the nominal value in Eq. 4.13 up to values as large as 0.01 pc cm^{-3} yr^{-1}, indicating that if the changing distance is the primary contribution to the observed trend, that the product $v_{100} n_{e_{0.1}}$ is as large as 1000.

A slightly different form results for a medium with changes in density only on large length scales $\gg |v_{p_\parallel} - v_{e_\parallel}|t$,

$$\frac{d\mathrm{DM}}{dt} = n_e(\mathbf{x}_{p_0})v_{p_\parallel} - n_e(\mathbf{x}_{e_0})v_{e_\parallel}, \tag{4.14}$$

which indicates that changes in DM are affected by the local electron density on both ends of the LOS. For similar electron densities at the two locations, we expect the pulsar term to dominate because pulsar velocities are typically much larger than the Earth's orbital motion and the Sun's peculiar motion through the Local Interstellar Cloud (LIC), the latter about 28 km s^{-1} (Faucher-Giguère & Kaspi 2006; Frisch et al. 2011). There will be exceptions, of course, for pulsars with low velocities or with small parallel velocity components.

The LIC is about 2.5 pc across and has an internal gas density of $\approx 0.1 - 0.2$ cm^{-3} at a temperature of 7000 K (Frisch et al. 2011). Assuming a completely ionized, uniform medium, the total DM through the cloud is at most $\mathrm{DM_{LIC}} \approx 0.5$ pc cm^{-3} and the maximum derivative is

$$\frac{d\mathrm{DM_{LIC}}}{dt} \approx 5.7 \times 10^{-6} \text{ pc cm}^{-3} \text{ yr}^{-1}. \tag{4.15}$$

The Earth's orbital motion is not relevant for the calculation of DM variations due to parallel motions because the Earth resides inside the heliosphere. A simplified form of Eq. 4.11 is therefore

$$\mathrm{DM}(t) = \mathrm{DM}_0 + \left[n_e(\mathbf{x}_{p_0})v_{p_\parallel} - n_e(\mathbf{x}_{e_0})v_{e_\parallel}\right] t + \int_{z_{e_0}}^{z_{p_0}} dz\, \Delta n_e(\mathbf{x}(z,t)). \tag{4.16}$$

However, the Earth's motion will matter when we later consider the interplanetary medium. In addition, the Earth term raises the interesting possibility that DM variations are partially correlated between different LOSs with an angular dependence that depends on the local ISM and on the direction of the Sun's peculiar velocity.

While linear trends in DM(t) have been recognized for many years, it is not *a priori* obvious whether they should be associated with the explictly linear term or with the density fluctuation term, which may quantify gradients transverse to the LOS. Some pulsars will show DM(t) variations where parallel motion is more important than transverse motion, and vice versa. The two kinds of variations may be distinguishable. If gradients and transverse motion are dominant, there should also be epoch-dependent refraction and flux-density variations on the same timescales. However, parallel-motion effects need not be accompanied by strong modulations of scintillation parameters and flux densities because the structure of the ISM along the LOS will remain the same. We note that DM(t) will vary with time from parallel motion alone regardless of whether the ISM is uniform or not; no gradients in electron density n_e are needed. The variations will be monotonically increasing or decreasing with time if there is no transverse motion (of the pulsar, solar system, or medium). However, DM variations from transverse motion alone require gradients in n_e that have components transverse to the LOS, i.e., $\nabla n_e \cdot \boldsymbol{r}(z,t) \neq 0$. Any gradients in n_e will generally be manifested from both parallel and transverse motion. DM variations from parallel motion do not depend on the pulsar distance but the transverse change in LOS depends on location along the LOS, therefore influencing the observable effect from a transverse gradient. When the Earth's orbital velocity is important, such as for an MSP with low translational velocity, the contribution to DM(t) depends on $\nabla n_e \cdot \mathbf{v}_{\mathrm{eff}_\perp}(z,t)$ and therefore will show a sinusoidal variation.

4.5 Stochastic Variations in DM

Electron-density variations in the ISM can cause fluctuations in DM(t) that combine with the DM variations previously discussed. Many DM(t) time series have been shown to be consistent with purely stochastic variations in electron density; a list of references for epoch-dependent DM variations can be found in Lam et al. (2015). Following their treatment, we can describe the stochastic variations by a power-law wavenumber spectrum

$$P_{\delta n_e}(\mathbf{q}) = \mathrm{C}_\mathrm{n}^2 q^{-\beta}, \qquad q_1 \leq q \leq q_2, \tag{4.17}$$

where the wavenumber cutoffs, related to the inner and outer physical scales ℓ_2 and ℓ_1, respectively, are $q_1 = 2\pi/\ell_1$ and $q_2 = 2\pi/\ell_2$ and C_n^2 is the spectral coefficient. Eq. 4.17 assumes that the scattering irregularities are isotropic and the spectrum depends only on the magnitude of the wavenumber. Evidence for anisotropic scattering exists along certain LOSs (e.g., Brisken et al. 2010) but the analysis is accordingly more tedious. The rms electron density is dominated by the largest scales ($\sim 1 - 100$ pc except in dense, compact regions) for $\beta > 3$ and $q_1 \ll q_2$. For a Kolmogorov medium, $\beta = 11/3$ (Rickett 1990).

One useful statistic for quantifying DM variations is the DM structure function (SF),

$$D_\mathrm{DM}(\tau) \equiv \left\langle [\mathrm{DM}(t+\tau) - \mathrm{DM}(t)]^2 \right\rangle = \left\langle \left| \Delta^{(1)}\mathrm{DM}(t,\tau) \right|^2 \right\rangle, \tag{4.18}$$

where $\Delta^{(1)}\mathrm{DM}(t,\tau)$ is the first-order DM increment, because it removes any constant term and is closely related to the spectral index of the wavenumber spectrum when β is in the scintillation regime (for wavenumbers $q_1 \ll q \ll q_2$ and $2 < \beta < 4$; Lam et al. 2015). We can relate it to similar SFs found in the literature for the electromagnetic phase perturbation imposed by the interstellar plasma ϕ and for the

resulting dispersive time delay, t. These are respectively $\phi = -cr_e\nu^{-1}\mathrm{DM}$, where r_e is the classical electron radius, and $t = d\phi/2\pi d\nu = K\nu^{-2}\mathrm{DM}$ with $K \equiv cr_e/2\pi$. We thus have

$$D_t(\tau) = K^2\nu^{-4} D_{\mathrm{DM}}(\tau) = (2\pi\nu)^{-2}\, D_\phi(\tau). \tag{4.19}$$

The DM SF includes the effects of the systematic DM term due to the change in distance as well as the term involving the integrated difference $\Delta n_e(\mathbf{x}(t))$. Small scale, discrete structures on AU scales can contribute to $\Delta n_e(\mathbf{x}(t))$ along with stochastic variations.

Together, discrete structures and the changing distance will produce contributions to the SF that are *quadratic* in τ and will contaminate the SF of the stochastic variations. A general feature of SFs is that they are quadratic when the lag τ is smaller than any characteristic timescale in the time series. So for structures in the ISM with scale sizes ℓ of tens of AU that have characteristic crossing times $\ell/v_{\mathrm{eff}} \sim$ many years, quadratic SFs will be seen for lags of a few years or less. For the case where only the distance-change term is relevant, $\mathrm{DM}(t+\tau) - \mathrm{DM}(t) \propto \tau$, it is easy to show that the SF is

$$D_{\mathrm{DM}}(\tau) = \left[n_e(\mathbf{x}_{p0}) v_{p_\parallel} - n_e(\mathbf{x}_{e0}) v_{e_\parallel} \right]^2 \tau^2. \tag{4.20}$$

More generally, if DM variations are dominated by a linear gradient $d\mathrm{DM}/dt$, the SF is

$$D_{\mathrm{DM}}^{(\mathrm{lin})}(\tau) = \left[\frac{d\mathrm{DM}}{dt} \right]^2 \tau^2. \tag{4.21}$$

The SF of purely periodic variations in DM of the form $\mathrm{DM}(t) = C\cos(\omega t + \varphi)$ can easily be calculated as

$$D_{\mathrm{DM}}^{(\mathrm{per})}(\tau) = C^2 \left[1 - \cos(\omega\tau) \right]. \tag{4.22}$$

While the DM SF is typically calculated with time lags of days to years, it can be related to the implied phase SF on the diffractive interstellar scintillation (DISS) timescale of minutes to hours. To do so, we use Eq. 4.19 along with the fact that the scintillation timescale $\Delta t_{\rm ISS}$ corresponds to $D_\phi(\Delta t_{\rm ISS}) \equiv 1$ rad^2. The corresponding DM SF value (using $\lambda = c/\nu$) is

$$\begin{aligned} D_{\rm DM}(\Delta t_{\rm ISS}) &= (\nu/2\pi K)^2 \, D_\phi(\Delta t_{\rm ISS}) = (\lambda r_e)^{-2} \\ &= 1.47 \times 10^{-15} \nu^2_{\rm GHz} \ ({\rm pc\ cm^{-3}})^2 \end{aligned} \tag{4.23}$$

Similarly

$$D_t(\Delta t_{\rm ISS}) = (2\pi\nu)^{-2} = 0.0253 \nu^{-2}_{\rm GHz} \ {\rm ns}^2. \tag{4.24}$$

The SF can be extrapolated to larger time lags, and for the stochastic, Kolmogorov medium where $\beta = 11/3$,

$$D^{\rm (sto)}_{\rm DM}(\tau) = (\lambda r_e)^{-2} \, (\tau/\Delta t_{\rm ISS})^{5/3} \tag{4.25}$$

$$D^{\rm (sto)}_{t}(\tau) = (2\pi\nu)^{-2} \, (\tau/\Delta t_{\rm ISS})^{5/3} \, . \tag{4.26}$$

In general, the total DM SF can be written as the sum of the contribution from the systematic term and from the extrapolated stochastic term,

$$D^{\rm (tot)}_{\rm DM}(\tau) = D^{\rm (sys)}_{\rm DM}(\tau) + D^{\rm (sto)}_{\rm DM}(\tau). \tag{4.27}$$

However, the systematic term cannot be separated as it will contain cross-terms if two or more components (e.g., linear plus periodic) are added together. For cases where the systematic term is significant, the time series for DM could be de-trended before calculating the SF, though de-trending can remove variance due to the electron density wavenumber spectrum. Equivalent to other discussions in the literature, when a power-law wavenumber spectrum dominates electron-density

variations the SF is essentially the SF of the density fluctuation term given in Eq. 4.11.

We can relate the the DM SF from the random component to the rms of the DM variations. For a power-law wavenumber spectrum, the DM SF is

$$D_{\rm DM}(\tau) = f_\beta \int_{z_{e_0}}^{z_{p_0}} dz\, {\rm C_n^2}(z) \left[v_{\rm eff_\perp}(z)\tau\right]^{\beta-2}, \tag{4.28}$$

where (Cordes & Rickett 1998, Eq. B6)

$$f_\beta = \frac{8\pi^2}{(\beta-2)2^{\beta-2}} \frac{\Gamma(2-\beta/2)}{\Gamma(\beta/2)}. \tag{4.29}$$

The numerical factor is $f_{11/3} = 88.3$ for a Kolmogorov wavenumber spectrum. Using the effective velocity of Eq. 4.7 evaluated for the case where it is dominated by the pulsar velocity and assuming $\rm C_n^2$ is constant along the LOS, the DM SF yields an rms DM on a timescale τ for a Kolmogorov medium

$$\begin{aligned}
\sigma_{\rm DM}(\tau) &= \left[\frac{1}{2} D_{\rm DM}(\tau)\right]^{1/2} \\
&= \left(\frac{\sqrt{3} f_{11/3}}{4}\right) {\rm SM}^{1/2} \left(\mathbf{v}_{\rm p_\perp}\tau\right)^{5/6} \\
&= 1.9\times10^{-4}\ {\rm pc\ cm^{-3}} \left(\frac{\rm SM}{10^{-4}\,{\rm kpc\ m^{-20/3}}}\right)^{1/2} \left(\mathbf{v}_{p_\perp 100}\tau_{\rm yr}\right)^{5/6},
\end{aligned} \tag{4.30}$$

where the scattering measure (SM) is the LOS integral (Cordes & Lazio 1991)

$$\rm SM = \int_0^D ds\ C_n^2(s). \tag{4.31}$$

When the effective velocity is instead dominated by the Earth's velocity, as can be the case for some slow moving MSPs, the same expression applies but with $\mathbf{v}_{p_\perp}$ replaced by $\mathbf{v}_{e_\perp}$. If both velocities are important, the integral in Eq. 4.28 needs to be evaluated explicitly.

Following Eq. 4.30, an estimate of the rms DM gradient is

$$\sigma_{\rm dDM/dt} \approx \frac{\sigma_{\rm DM}(\tau)}{\tau} = 1.9\times10^{-4}\ {\rm pc\ cm^{-3}\ yr^{-1}} \left(\frac{\rm SM}{10^{-4}\ {\rm kpc\ m^{-20/3}}}\right)^{1/2} {\rm v}_{p_\perp 100}^{5/6} \tau_{\rm yr}^{-1/6}. \quad (4.32)$$

The rms can be evaluated by using scintillation measurements to evaluate the scattering measure SM (Cordes & Lazio 1991) and by using proper motion measurements with distance estimates (from parallaxes or from DM and a Galactic electron-density model) to estimate the pulsar velocity.

One approach for comparing measured DM gradients with those expected from a Kolmogorov medium with no change in distance is to calculate the signal-to-noise-like ratio

$$R_{d{\rm DM}/dt} = \frac{|d{\rm DM}/dt|}{\sigma_{\rm dDM/dt}}. \quad (4.33)$$

When the gradient exceeds the prediction for a Kolmogorov model by a large factor, one of two interpretations may apply. First, the medium may not have a Kolmogorov spectrum that encompasses both the small length scales that cause scintillation and the large 1–100 AU scales associated with DM variations. Alternately, the excess derivative amplitudes can be caused by the changing pulsar distance as described above. Identifying which of these interpretations apply requires consideration of other factors. Transverse motions of the pulsar that cause the LOS to sample different irregularities will yield DM derivatives that are correlated with the absolute DM value whereas parallel motions that change the distance will not.

Another approach compares the rms of the DM time series before and after the removal of a linear trend. Letting $\sigma_{\rm tot}^2 = \sigma_{\rm sto}^2 + \sigma_{\rm lin}^2$ be the total variance of the time series, we can define the ratio of rms after the removal of a linear trend to

the rms before the removal as

$$R_{\rm rms} = \frac{\left(\sigma_{\rm tot}^2 - \hat{\sigma}_{\rm lin}^2\right)^{1/2}}{\sigma_{\rm tot}} \tag{4.34}$$

where $\hat{\sigma}_{\rm lin}^2$ is the estimated variance of the linear trend. This definition restricts $0 \leq R_{\rm rms} \leq 1$. Realizations of DM time series will appear more linear when the wavenumber spectral index β is large and the removal of the best-fit line for the time series will absorb low-frequency power from the frequency spectrum of DM. Conversely, when β is low, the time series will appear closer to a white noise process, and the removal of a best-fit line will not change the resultant time series greatly.

We can solve for how $\sigma_{\rm sto}$ and $\sigma_{\rm lin}$ scale with observing time span T. Let the stochastic DM variation be a power spectrum $S_{\rm DM}(f) = Af^{-\gamma}$, where A is a spectral coefficient related to $\Delta t_{\rm ISS}$ and $\gamma = \beta - 1$ (see Appendix 4.12.1 for more details). The variance is then

$$\sigma_{\rm sto}^2 = \int_{f_1}^{f_2} S_{\rm DM}(f) df = \int_{f_1}^{f_2} Af^{-\gamma} df, \tag{4.35}$$

where f_1 and f_2 are the low- and high-frequency cutoffs, respectively, related to the wavenumber cutoffs q_1 and q_2. In the scintillation regime with $1 < \gamma < 3$, assuming $f_1 \ll 1/T \ll f_2$, the integral can be approximated as

$$\sigma_{\rm sto}^2 \approx \frac{A}{\gamma - 1} T^{\gamma - 1}, \tag{4.36}$$

which for the Kolmogorov case implies $\sigma_{\rm sto} \propto T^{5/6}$. The variance from a deterministic, linear trend is

$$\begin{aligned} \sigma_{\rm lin}^2 &= \frac{1}{T} \int_{-T/2}^{T/2} \left(\frac{d{\rm DM}}{dt} t \right)^2 dt \\ &= \frac{1}{12} \left(\frac{d{\rm DM}}{dt} \right)^2 T^2. \end{aligned} \tag{4.37}$$

Therefore $\sigma_{\rm lin} \propto T$ and if a deterministic, linear trend is present, $\sigma_{\rm lin}$ will increase over $\sigma_{\rm sto}$ and $R_{\rm rms}$ will increase for longer observing timespans.

In addition to single, linear trends in DM, we can test for discrete changes in underlying linear trends in DM, such as from an ionizing bow shock (see § 4.7.2), versus stochastic changes from the turbulent medium by calculating the second-order increments of DM(t), $\Delta^{(2)}{\rm DM}(t,\tau) = {\rm DM}(t-\tau) - 2{\rm DM}(t) + {\rm DM}(t+\tau)$, which remove linear components and relate to the curvature of the time series. The increments at a given τ will have a Gaussian distribution and deviations from this distribution will be indicative of structure other than from a turbulent medium. We can determine the variance in the distribution of increments at a given τ, $\sigma^2_{\Delta^{(2)}{\rm DM}}(\tau)$, from the second-order DM SF, which can be written as

$$D^{(2)}_{\rm DM}(\tau) \;=\; \left\langle \left|\Delta^{(2)}{\rm DM}(t,\tau)\right|^2 \right\rangle \tag{4.38}$$

For a Kolmogorov wavenumber spectrum, the second-order SF is related to the first-order SF, as well as the variance in the second-order increments, by

$$D^{(2)}_{\rm DM}(\tau) = \sigma^2_{\Delta^{(2)}{\rm DM}}(\tau) \approx 0.8252 D^{(1)}_{\rm DM}(\tau). \tag{4.39}$$

The derivation is provided in Appendix 4.12.1. We can use Eqs. 4.25 and 4.39 to analytically estimate the rms of the second-order DM increments given $\Delta t_{\rm ISS}$, which we use to analyze the slope changes in DM(t) for PSR B1534+12 in §4.7.

4.6 Refraction Effects and Timing

Refraction of a radio point source by a high-density region in the ISM has been known to cause irregularities in electron-density time series. See Clegg et al. (1998) and references therein for the case of a Gaussian plasma lens, to be considered

shortly, and Coles et al. (2015) for recent evidence of scattering events in pulsar timing data. One of the timing delays associated with refraction scale as ν^{-2} and is therefore degenerate with the dispersion delay, causing changes in the estimated DM. Consider a single ionized cloud that has characteristic scales $a_{\parallel}$ parallel and $a_{\perp}$ transverse to the LOS and with a column density $\mathrm{DM}_c = N_{e_c} \sim n_{e_c} a_{\parallel}$ through the cloud along the LOS. The maximum phase change due to the clump is $|\phi_c| \sim \lambda r_e N_{e_c}$ and the dispersion delay is

$$\Delta t_{\mathrm{DM}c} = \frac{\phi_c}{2\pi\nu} = \frac{\lambda^2 r_e N_{e_c}}{2\pi c}. \tag{4.40}$$

The phase gradient across the LOS is then $|\nabla_{\perp}\phi| \sim \lambda r_e N_{e_c}/a_{\perp}$ and the refraction angle is

$$\theta_{r_c} = \frac{\lambda|\nabla_{\perp}\phi|}{2\pi} \sim \frac{\lambda^2 r_e N_{e_c}}{2\pi a_{\perp}} \sim \frac{c\Delta t_{\mathrm{DM}c}}{a_{\perp}}. \tag{4.41}$$

There are two time delays introduced by refraction into barycentric arrival times. The first is associated with the translation of topocentric TOAs by the propagation delay from the geocenter to the solar system barycenter. The direction to the pulsar is a key part of the translation, and refraction will induce an error in the barycentered arrival times. Chromatic refraction causes the angle of arrival to differ from an assumed direction, implying a delay (Foster & Cordes 1990) that varies sinusoidally with an annual period and an amplitude

$$\Delta t_{\mathrm{bary}_c} \sim \frac{r_{\oplus}\theta_{r_c}}{c} \sim \left(\frac{r_{\oplus}}{a_{\perp}}\right)\Delta t_{\mathrm{DM}c} \sim \frac{\Delta t_{\mathrm{DM}c}}{a_{\perp\mathrm{AU}}}, \tag{4.42}$$

where $r_{\oplus} = 1$ AU. The second delay is the geometric increase in propagation path that is roughly

$$\Delta t_{\mathrm{geo}_c} \sim \frac{D\theta_{r_c}^2}{2c} \sim \frac{cD(\Delta t_{\mathrm{DM}c})^2}{2{a_{\perp}}^2} \sim \frac{cD}{2r_{\oplus}^2}\left(\frac{\Delta t_{\mathrm{DM}c}}{a_{\perp\mathrm{AU}}}\right)^2. \tag{4.43}$$

For a single clump, Eqs. 4.42 and 4.43 indicate that barycentric delay $\Delta t_{\mathrm{bary}_c}$ and geometric delay $\Delta t_{\mathrm{geo}_c}$ are linear and quadratic, respectively, in the dispersion

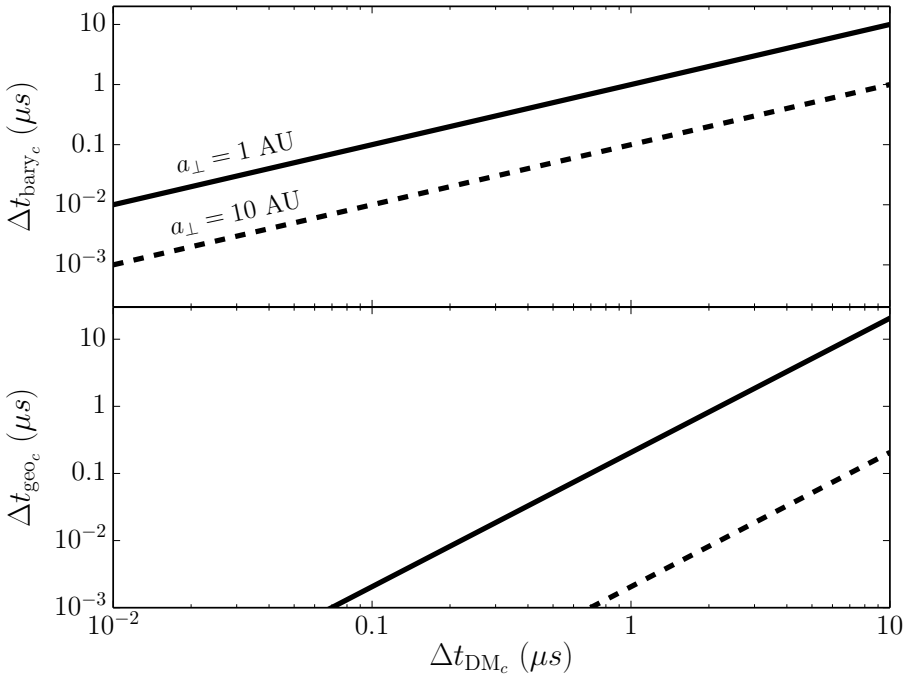

Figure 4.3: Refraction delays plotted against DM delay from a single cloud at a distance $D = 1$ kpc. (Top) The barycentric delay for two clump scale sizes, as labeled. (Bottom) The geometric delay for the same two clump sizes.

delay, $\Delta t_{\mathrm{DM}c}$ ($\propto \nu^{-2}$ and ν^{-4}, respectively). The barycentric and geometric delays are comparable for pulsars within about 1 kpc because $\theta_r \sim 1$ mas and $D\theta_r \sim 1$ AU, though there are wide variations of these values.

Numerically, the refraction and dispersion delays are comparable for nominal parameter values but any one of the three delays can dominate the the other two for reasonable distances and transverse scale lengths,

$$\Delta t_{\mathrm{bary}_c} \sim 1\ \mu s \left(\frac{\Delta t_{\mathrm{DM}c,\mu s}}{a_{\perp \mathrm{AU}}} \right), \tag{4.44}$$

and

$$\Delta t_{\mathrm{geo}_c} \sim 0.2\ \mu s\, D_{\mathrm{kpc}} \left(\frac{\Delta t_{\mathrm{DM}c,\mu s}}{a_{\perp \mathrm{AU}}} \right)^2. \tag{4.45}$$

Figure 4.3 shows $\Delta t_{\mathrm{bary}_c}$ and $\Delta t_{\mathrm{geo}_c}$ plotted against $\Delta t_{\mathrm{DM}c}$ for $D = 1$ kpc and

for two transverse scale lengths ($a_\perp = 1$ and 10 AU).

A final consideration is multiple imaging. Clegg et al. (1998) analyze flux variations and caustics for an interstellar Gaussian plasma lens, i.e., a cloud with a Gaussian electron density profile. The focal distance $D_{\rm f}$ of a clump is the minimum distance from the clump at which rays can cross,

$$D_{\rm f} \sim \frac{a_\perp}{\theta_{r_c}} \sim \frac{{a_\perp}^2}{c\Delta t_{{\rm DM}c}} \sim 2.4 \text{ kpc } {a_\perp}^2_{\rm AU} \Delta t_{{\rm DM}c,\mu s}. \tag{4.46}$$

We therefore do not expect ray crossing and multiple images from nearby pulsars unless a clump is small and dense.

We can solve for the three time delays associated with refraction (dispersion, barycentric, geometric) by considering rays traveling through a Gaussian lens in the ISM. Following the treatment in Clegg et al. (1998), for a thin-screen approximation of the lens, the column density in two-dimensions can be written as

$$N_{e_c}(\mathbf{x}) = N_0 \exp\left(-[|\mathbf{x} - \mathbf{x}_c|/a]^2\right), \tag{4.47}$$

where N_0 is the maximum central column density and a is the characteristic size of the lens. The screen phase ϕ is related to the electron density by

$$\phi(\mathbf{x}) = -\lambda r_e \int_{\rm screen} dz\ n_e(\mathbf{x}, z) \equiv -\lambda r_e N_e(\mathbf{x}). \tag{4.48}$$

For the Gaussian cloud, we therefore have

$$\phi_c(\mathbf{x}) = -\lambda r_e N_0 \exp\left(-[|\mathbf{x} - \mathbf{x}_c|/a]^2\right). \tag{4.49}$$

Using Eq. 4.41, the refraction angle is

$$\boldsymbol{\theta}_{r_c}(\mathbf{x}) = \frac{\lambda^2 r_e N_0}{\pi a^2} \mathbf{x} \exp\left(-[|\mathbf{x} - \mathbf{x}_c|/a]^2\right), \tag{4.50}$$

In general, the location of the incident ray paths on the Earth at location $\mathbf{x}_e$ intersecting the cloud at $\mathbf{x}_c$ from a pulsar at $\mathbf{x}_p$ must satisfy the equation

$$\mathbf{x}_e = \mathbf{x}_c - \left[\boldsymbol{\theta}_{r_c}(\mathbf{x}_c) + \boldsymbol{\theta}_i(\mathbf{x}_p)\right] D \tag{4.51}$$

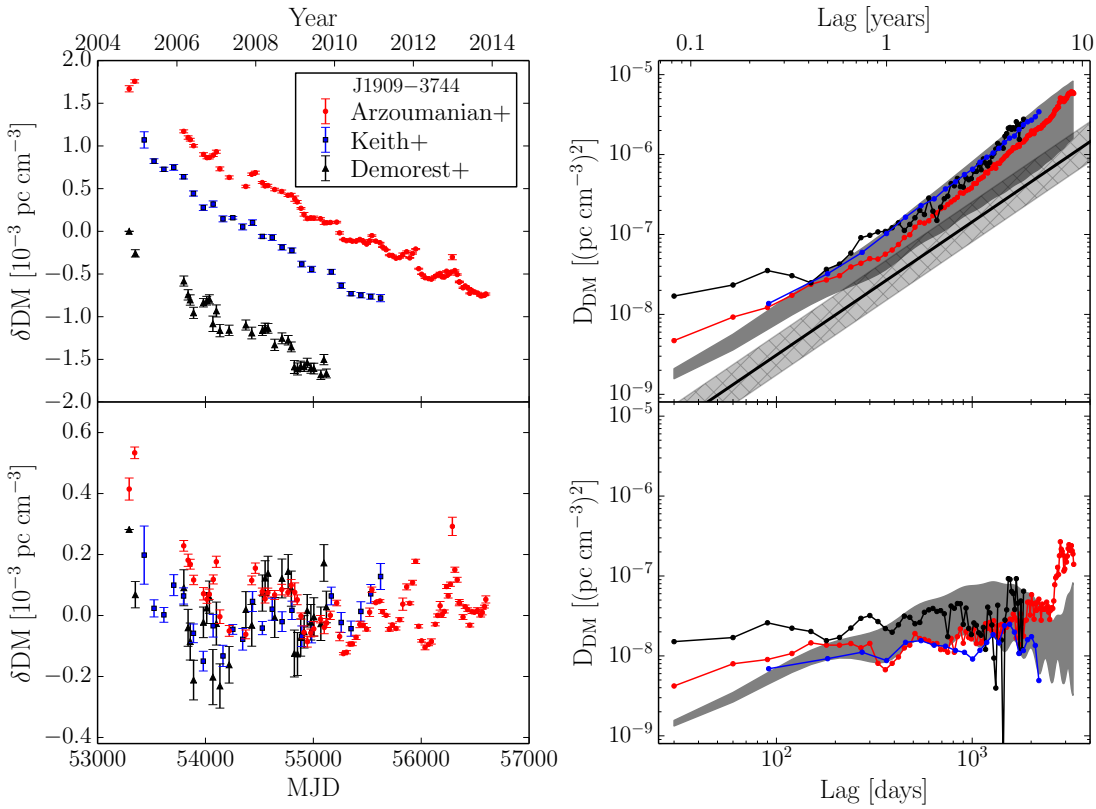

Figure 4.4: Analysis of DM time series and SFs for PSR J1909−3744. Top left: DM offsets $\delta\mathrm{DM}(t)$ reported in Arzoumanian et al. (2015b, red circles), Keith et al. (2013, blue squares), Demorest et al. (2013, black triangles), see Figure 4.1 for more details. Top right: DM SFs for the three time series in the top left (with matching colors). The solid black line indicates the value of the SF inferred from the scintillation timescale and assuming DM variations only from a Kolmogorov wavenumber spectrum for the ISM. The light gray, hatched region shows nominal errors on the inferred SF from a multiplicative factor of $\sqrt{2}$ error on the scintillation timescale. The dark gray region indicates the $\pm 1\sigma$ deviations from the mean SF for simulations of DM variations over nine years that include a Kolmogorov medium, a linear component from motion parallel to the LOS, a sinusoidal component, and measurement errors (see text for more information). Bottom left: DM offsets of the time series in the top left after a linear trend has been removed. Bottom right: DM SFs for the three time series in the bottom left. The gray region indicates the same as in the top right except that the best-fit linear trend has been removed from the simulated time series before calculating the SF.

where $\boldsymbol{\theta}_i$ is the incidence angle of the pulsar rays on the screen.

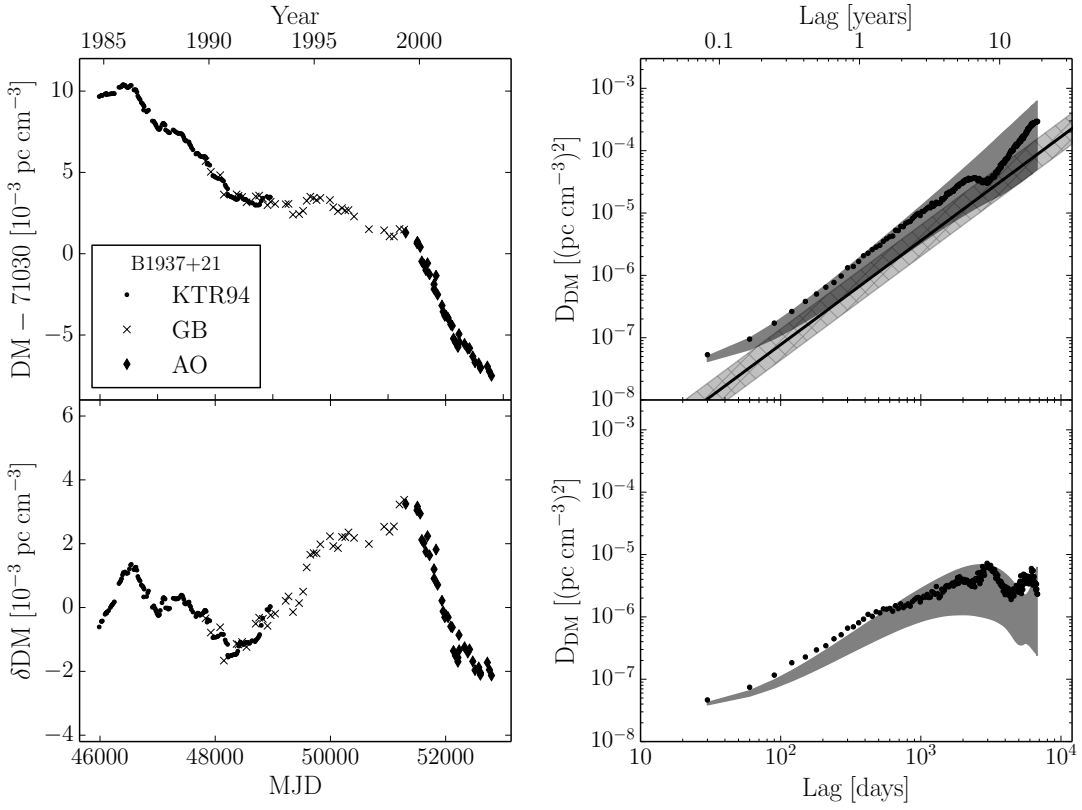

Figure 4.5: Analysis of DM time series and SFs for PSR B1937+21. The format is the same as in Figure 4.4. The dots are from Kaspi et al. (1994) while the crosses and diamonds are from Ramachandran et al. (2006) for the Green Bank (GB) 140-foot telescope and Arecibo Observatory (AO), respectively.

4.7 Interpretation of Observed Pulsar Phenomena

4.7.1 Linear Trends Versus Stochastic Variations

We look at several examples of deterministic, linear DM trends seen in the literature below. To test our interpretations, we compare the time series against simulated DM variations with a Kolmogorov wavenumber spectral index following the same procedure as described in Lam et al. (2015) by transforming scaled, complex white noise in the frequency domain to the time domain. The power spectrum of the

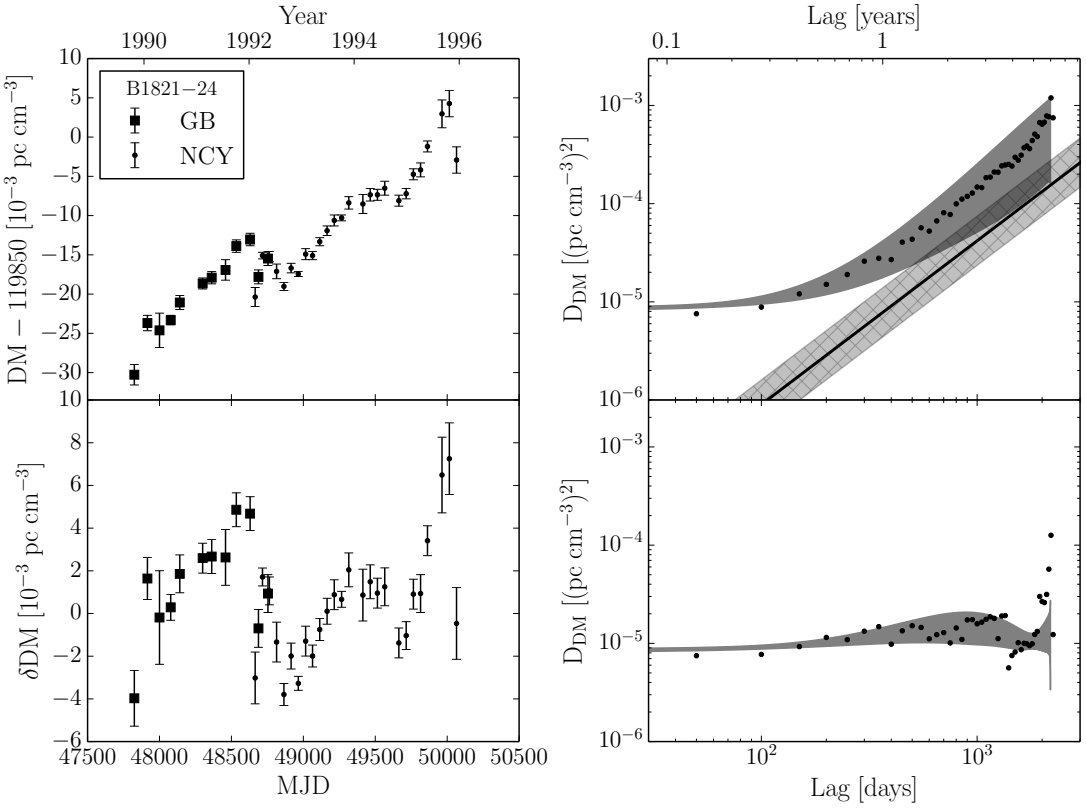

Figure 4.6: Analysis of DM time series and SFs for PSR B1821−24. The format is the same as in Figure 4.4. The squares show measurements from the Green Bank (GB) 140-foot telescope (Backer et al. 1993) while dots show measurements from the Nançay radio telescope (NCY) (Cognard & Lestrade 1997).

electron density variations, $S_{\rm DM}(f) \propto f^{-\gamma}$, has a spectral index $\gamma = \beta - 1 = 8/3$ for the Kolmogorov case. The scalings of the coefficient of the power spectrum are consistent with the extrapolation of the SF $D_{\rm DM}$ by the scintillation timescale (see Eq. 4.25).

PSR J1909−3744

As described in §2, the DM time series shows a decreasing, linear trend (Demorest et al. 2013; Keith et al. 2013; Arzoumanian et al. 2015b) over a $\sim$ 9-year timespan.

Keith et al. (2013) compare SFs of dispersion delay D_t on long timescales with the extrapolations from the DISS timescale assuming a Kolmogorov spectrum. In several cases they find that the actual measurements exceed the extrapolation by large factors and that the slope of D_t is larger than the Kolmogorov slope of 5/3. They conclude that the wavenumber spectrum is steeper than Kolmogorov. In the case of PSR J1909−3744, they find that the value of the DM SF for measured lags is about a factor of five higher than the extrapolation from the DISS timescale using a Kolmogorov scaling.

We present an alternative interpretation that recognizes that the contribution to DM(t) from Kolmogorov fluctuations combined with transverse motion of the LOS can be contaminated by the changing distance between pulsar and Earth from parallel motion as discussed previously (see Eq. 4.27). This contamination contributes a term to the SFs that scales as τ^2, i.e., steeper than Kolmogorov, and that can dominate the overall amplitude of the SFs.

The top left panel of Figure 4.4 is identical to Figure 4.1 and shows the time series of the DM offsets, δDM(t), as reported in Demorest et al. (2013), Keith et al. (2013), and Arzoumanian et al. (2015b, NG9). Again, the total measured DM is found by adding a constant $\mathrm{DM_{nominal}}$ to the DM offsets, though the values will still differ due to other frequency-dependent parameters included in the timing models in each paper. Since the SF removes the mean, the differences are not important here. The bottom left panel shows δDM(t) after a linear trend has been removed. A periodic trend remains in the time series with a roughly one-year period. The panels on the right show the corresponding DM SFs of the time series on the left. In the top right, we show the extrapolation of D_{DM} assuming a purely Kolmogorov medium and using a scintillation timescale of 2258 s at 1.5 GHz (solid black line,

Keith et al. 2013) and note that all three SFs do lie well above this extrapolation. We calculate the SF for the Keith et al. (2013) DM(t) with lag bins that are multiples of 0.25 yr (91.3 days), equal to the minimum sampling time for Keith et al. (2013). For the other two SFs, we use bins that are multiples of 30 days. The light gray, hatched region denotes nominal errors in the extrapolation from a multiplicative error of $\sqrt{2}$ on the scintillation timescale, known for PSR B1937+21 Cordes et al. (1986, 1990); Keith et al. (2013). The dark gray region shows the $\pm 1\sigma$ deviations from the mean DM SF on simulations of nine years of DM variations that include: a Kolmogorov wavenumber spectrum; the best-fit linear trend of the data ($d\mathrm{DM}/dt = -2.27 \pm 0.04 \times 10^{-4}$ pc cm^{-3} yr^{-1}); a sinusoid with a one-year period and an amplitude of 5×10^{-5} pc cm^{-3}; and white, Gaussian noise with an rms of $\sigma_n = 2.4 \times 10^{-5}$ pc cm^{-3} in the first five years and 1.2×10^{-5} pc cm^{-3} in the last four years, equal to the median error corresponding to each of the backends used in the NG9 data set. The DM SF from NG9 is consistent with these simulations. In the bottom right, we show the results of simulations when all of the above are included but a linear trend is fit and subsequently removed from the time series before computing the SF, which can remove power from both the linear component and some low-frequency structure in a given time series. The shape of the gray region matches some of the shape present in the SF, though the position indicates that the sinusoidal term should possibly have a smaller amplitude with a more peaked shape. Few numbers of DM increments in bins at large time lags lead to deviations from the mean SF. A more detailed analysis of the DM time series for PSR J1909−3744 will be presented by M. L. Jones et al. (in preparation).

Using Eq. 4.14 and its assumption of density changes occurring at large length scales only, we can use our measured, best-fit $d\mathrm{DM}/dt$ to infer the electron density at the pulsar, $n_e(\mathbf{x}_{p_0})$. The transverse components of velocity are $v_\alpha = -50.61 \pm$

0.01 km s^{-1} and $v_\delta = -192.32 \pm 0.01$ km s^{-1} with a distance of $1.14^{+0.04}_{-0.03}$ kpc (Jacoby et al. 2005; Antoniadis 2013). The barycentric, systemic radial velocity is -37 ± 11 km s^{-1} (J. Antoniadis, priv. comm.). We find the pulsar parallel velocity component $v_{p_\parallel}$ by removing the local solar motion and correcting for differential Galactic rotation. We take the local solar motion to be 18.0 ± 0.9 km s^{-1} in the direction $(l_g, b_g) = (47.9^\circ \pm 3.0^\circ, 23.8^\circ \pm 2.0^\circ)$ and assume a locally flat, galactic rotation curve (Frisch et al. 2011). PSR J1909−3744 lies nearly in the direction of the Galactic center with $(l_g, b_g) = (359.7^\circ, -19.6^\circ)$ and therefore the change in the velocity vector due to differential galactic rotation is negligible and we can ignore transverse components in our calculation. Taking the electron density of the LIC to be $n_e(\mathbf{x}_{e_0}) \approx 0.15 \pm 0.05$ cm^{-3} (Frisch et al. 2011), we find $n_e(\mathbf{x}_{p_0}) = 7.6 \pm 2.9$ cm^{-3}, about two orders of magnitude greater than the average local electron density of the galaxy in that region (Cordes & Lazio 2002; Frisch et al. 2011).

PSR B1937+21

Ilyasov et al. (2005) show a long-term trend in a 20-year DM time series extending to $\sim$ 2003.5 (MJD 52800) that has a strong, decreasing trend with an average derivative $d\mathrm{DM}/dt \approx -1.14 \pm 0.03 \times 10^{-3}$ pc cm^{-3} yr^{-1}. Ramachandran et al. (2006) show similar results. Long-term correlated variations are superposed with the linear trend. The best-fit line of the SF is $\beta = 3.66 \pm 0.04$, though the analysis from Kaspi et al. (1994) on DM variations up to 1993 alone suggests $\beta = 3.874 \pm 0.011$. Both Kaspi et al. (1994) and Ramachandran et al. (2006) fit the $D_\phi(\tau)$ to determine Δt_{ISS}, which will be a biased estimator if a deterministic, linear trend is present.

We repeat our SF analysis as before, shown now in Figure 4.5, using the Ra-

machandran et al. (2006) data. They include the time series from Kaspi et al. (1994, circles), measured at 1400 and 2200 MHz. The crosses are measurements from the Green Bank (GB) 140-foot telescope between 800 and 1400 MHz, the diamonds are measurements from the Arecibo Observatory (AO) between 1400 and 2200 MHz. Differences in DM estimation and frequency-dependent delays used mean that we currently cannot align the Ramachandran et al. (2006) time series with the Keith et al. (2013) time series measured at later epochs. Therefore, we ignore the latter time series here and in subsequent analyses.

We measure $d\mathrm{DM}/dt = -8.39 \pm 0.14 \times 10^{-4}$ pc cm^{-3} yr^{-1} for the Ramachandran et al. (2006) data, suggesting a long-term linear trend remains present in the time series. We again simulate a Kolmogorov medium with $\Delta t_{\mathrm{ISS}} = 327$ s at 1.5 GHz (Keith et al. 2013) and include a linear trend with slope measured above and additive, Gaussian white noise. The varying scintillation timescale over years is not included in the realizations and biases our overall results but not the conclusions. We find the rms of the noise by modeling the SF as $D_{\mathrm{DM}}(\tau) = C\tau^{\alpha} + 2\sigma_n^2$ (see Appendix 4.12.2 for more details) and find $\sigma_n = 1.3 \times 10^{-4}$ pc cm^{-3}. Again, the measured SF shows good agreement with our realizations.

Table 4.2. Measurements of DM derivatives and $R_{d\mathrm{DM}/dt}$

Pulsar Parameters				Scintillation Parameters[a]			DM Derivatives[b]		Derived Results	
Pulsar	DM[c] pc cm^{-3}	PM[c] mas yr^{-1}	D[d] kpc	ν GHz	$\Delta\nu_{\mathrm{ISS}}$ MHz	Δt_{ISS} s	T yr	$d\mathrm{DM}/dt$[e] 10^{-3} pc cm^{-3}	$\sigma_{d\mathrm{DM}/dt}$ yr^{-1}	$R_{d\mathrm{DM}/dt}$
J0358+5413	57.14	12.3 ± 0.3	1.1 ± 0.2	1.0	0.789	-	16.4	-2.6 ± 0.8[f]	0.24	11.1
J0543+2329	77.71	22 ± 8	2.06	1.0	0.069	-	20.7	-4.9 ± 0.6[f]	1.3	3.7
J0835−4510	67.99	57.98 ± 0.08	0.29 ± 0.02	0.61	1.5×10^{-4}	3	5.7	5 ± 1[g]	9.4	0.53
J1024−0719	6.49	59.7 ± 0.3	0.53 ± 0.22	1.5	268	4180	15.1	0.22 ± 0.06	0.047	4.7
J1045−4509	58.17	8.0 ± 0.2	0.30 ± 0.17	1.5	0.094	119	17.0	-3.66 ± 0.13	0.90	4.1
B1534+12[h]	11.62	25.328 ± 0.012	1.051 ± 0.005	0.43	1.1	660	3.3	-0.316 ± 0.010	0.081	3.9
							5.0	-0.043 ± 0.008	0.076	0.57
							4.7	-0.294 ± 0.007	0.077	3.8
							2.3	1.01 ± 0.03	0.086	11.7
							2.3	-0.01 ± 0.05	0.086	0.12
J1543+0929	35.24	8.13 ± 0.07	7.7 ± 1.2	1.0	0.299	-	21.4	26 ± 5[f]	0.54	48.5
J1600−3053	52.33	7.2 ± 0.3	5.0 ± 3.8	1.5	0.09	271	9.1	-0.63 ± 0.3	0.50	1.3
J1643−1224	62.41	7.3 ± 0.3	0.45 ± 0.08	1.5	0.022	582	17.0	-1.23 ± 0.05	0.24	5.2
J1730−2304	9.62	20.27 ± 0.06	0.53	1.5	12.4	1615	16.9	0.56 ± 0.05	0.10	5.5
J1732−5049	56.82	9.9 ± 0.3	1.41	1.5	5.4	1200	8.0	-0.88 ± 0.12	0.15	6.0
J1744−1134	3.14	21.02 ± 0.03	0.42 ± 0.02	1.5	60	2070	16.1	-0.132 ± 0.018	0.084	1.9
J1833−0827	411	34 ± 6	4.5	1.0	1.6×10^{-4}	-	5.7	-130 ± 20[g]	40.6	3.2

Table 4.2 (cont'd)

Pulsar Parameters				Scintillation Parameters[a]			DM Derivatives[b]		Derived Results	
Pulsar	DM[c] pc cm^{-3}	PM[c] mas yr^{-1}	D[d] kpc	ν GHz	$\Delta\nu_{\rm ISS}$ MHz	$\Delta t_{\rm ISS}$ s	T yr	$d{\rm DM}/dt$[e] 10^{-3} pc cm^{-3}	$\sigma_{d{\rm DM}/dt}$ yr^{-1}	$R_{d{\rm DM}/dt}$
J1909+1102	149.98	9 ± 8	4.8	1.0	0.012	-	15.1	-15.8 ± 1.2[f]	1.9	8.3
J1909−3744	10.39	37.10 ± 0.02	1.27 ± 0.03	1.5	37	2258	8.2	-0.297 ± 0.006	0.087	3.4
J1935+1616	158.52	16.13 ± 0.15	4.55	0.61	0.002	18	34.1	2.3 ± 0.3[f]	1.6	1.5
B1937+21	71.02	0.421 ± 0.003	7.7 ± 3.8	1.5	1.2	327	15.5	-0.59 ± 0.03	0.39	1.5
J2129−5721	31.85	13.3 ± 0.1	0.53 ± 0.25	1.5	17.1	3060	15.4	-0.16 ± 0.04	0.061	2.6

[a]Parameters for $\nu = 0.43$ GHz measurements from Bogdanov et al. (2002), for $\nu = 0.61$ GHz measurements from Stinebring et al. (2000), for $\nu = 1.0$ GHz measurements from PSRCAT (Manchester et al. 2005, using $2\pi\Delta\nu_{\rm ISS}\tau_{\rm ISS} = C_1 = 1.16$), and for $\nu = 1.5$ GHz measurements from Keith et al. (2013). The number of significant digits are provided by the individual references.

[b]Timespan and $d{\rm DM}/dt$ references match.

[c]Column data from PSRCAT (Manchester et al. 2005) unless otherwise marked.

[d]Distances with errors from parallax measurements (`http://www.astro.cornell.edu/research/parallax/` and references therein), distances without errors from NE2001 (errors are $\sim 20\%$), and distance for PSR B1534+12 from binary orbital period derivative (Fonseca et al. 2014).

[e]Values from Reardon et al. (2016) unless otherwise marked.

[f]Hobbs et al. (2004).

[g]Petroff et al. (2013).

[h]All values from Fonseca et al. (2014) except the scintillation parameters (Bogdanov et al. 2002).

PSR B1821−24

Cognard & Lestrade (1997, see also Backer et al. 1993) show a DM time series with a long-term increasing trend with $d\mathrm{DM}/dt \approx 0.005$ pc cm^{-3} yr^{-1} over a six-year period. Again we ignore DM variations from Keith et al. (2013) because of the absolute DM difference. Using measurements from GB and the Nançay radio telescope, Cognard & Lestrade (1997) find that the spectral index of the wavenumber spectrum is $\beta = 3.727 \pm 0.211$. Figure 4.6 shows our SF analysis, with red noise realizations with $\Delta t_{\mathrm{ISS}} = 75$ s at 1.5 GHz (Keith et al. 2013) and an estimated $\sigma_n = 2.1 \times 10^{-3}$ pc cm^{-3}. The LOS to PSR B1821−24 is also consistent with a Kolmogorov medium.

Deterministic Linear Trends from DM Derivatives

We calculate $R_{d\mathrm{DM}/dt}$ for pulsars in the literature with measured $d\mathrm{DM}/dt$. To calculate $\sigma_{d\mathrm{DM}/dt}$, we use pulsars with a measured scintillation bandwidth $\Delta\nu_{\mathrm{ISS}}$ or those that can be estimated from the scattering timescale τ_{ISS} using $2\pi\Delta\nu_{\mathrm{ISS}}\tau_{\mathrm{ISS}} = C_1$, where $C_1 = 1.16$ for a uniform medium with a Kolmogorov wavenumber spectrum. Assuming such a medium, we estimate the SM using Eq. 10 of Cordes & Lazio (2002) as

$$\mathrm{SM} \;=\; 7.15 \times 10^{-4}\ \mathrm{kpc\ m^{-20/3}} \left(\Delta\nu_{\mathrm{ISS,MHz}}\nu_{\mathrm{GHz}}^{-22/5} D_{\mathrm{kpc}}\right)^{-5/6}. \qquad (4.52)$$

We either use parallax distances or binary orbital period derivative ($\dot{P}_b$) distances to estimate SM when available, and otherwise use DM distances from NE2001 (Cordes & Lazio 2002). We convert proper motion measurements into pulsar perpendicular velocities assuming $\mathbf{v}_{p_\perp}$ dominates $\mathbf{v}_{\mathrm{eff}_\perp}$ (which may not be true for slow moving MSPs) and differential galactic rotation is negligible, both of which may contribute

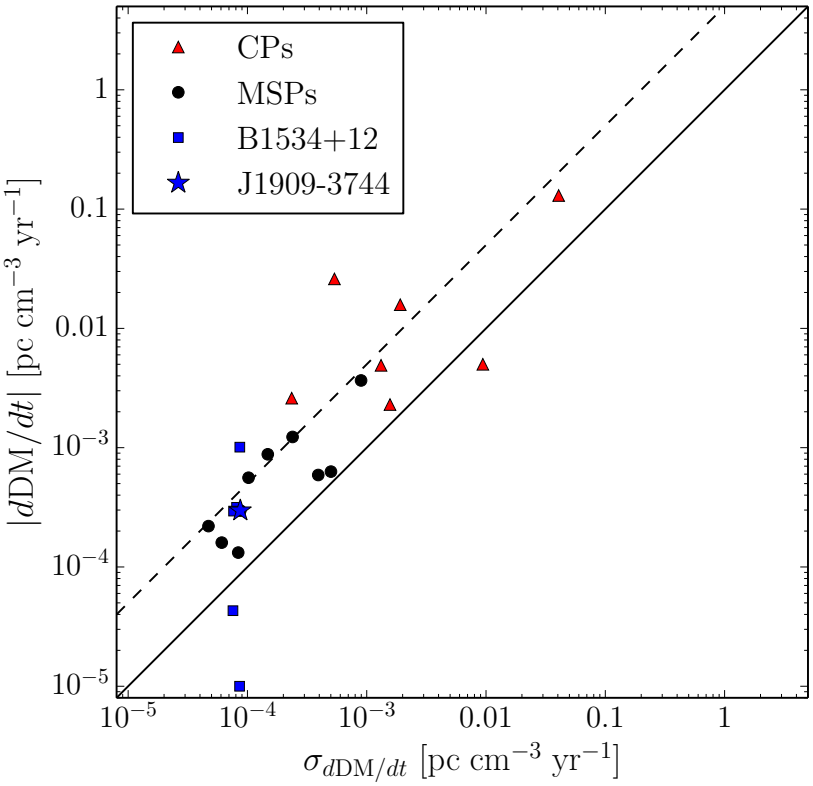

Figure 4.7: DM time derivative $d\mathrm{DM}/dt$ versus the rms DM gradient $\sigma_{d\mathrm{DM}/dt}$. Canonical pulsars (CPs) are shown in red triangles and MSPs in black circles. We highlight the linear DM segments of the MSP B1534+12 in blue squares and the blue star for MSP J1909−3744. Two of the blue squares for B1534+12 closely overlap with J1909−3744. The solid line represents $R_{d\mathrm{DM}/dt} = 1$ whereas the dashed line represents $R_{d\mathrm{DM}/dt} = 5$, exponentially increasing to the top left.

systematic uncertainties in our analysis. However, under these assumptions, we combine SM, $\mathbf{v}_{p\perp}$, and the total observing span T to calculate $\sigma_{d\mathrm{DM}/dt}$ and thus $R_{d\mathrm{DM}/dt}$.

Table 4.2 lists pulsar values we use in the literature in our analysis and the results. Figure 4.7 shows $|d\mathrm{DM}/dt|$ versus $\sigma_{d\mathrm{DM}/dt}$ for slow-period canonical pulsars (CPs, red triangles) and MSPs (black circles). We also highlight the five linear trends of the MSP B1534+12 (blue squares; discussed in the following section) and J1909−3744 (blue star). The lines represent $R_{d\mathrm{DM}/dt} = 1$ (solid) and 5

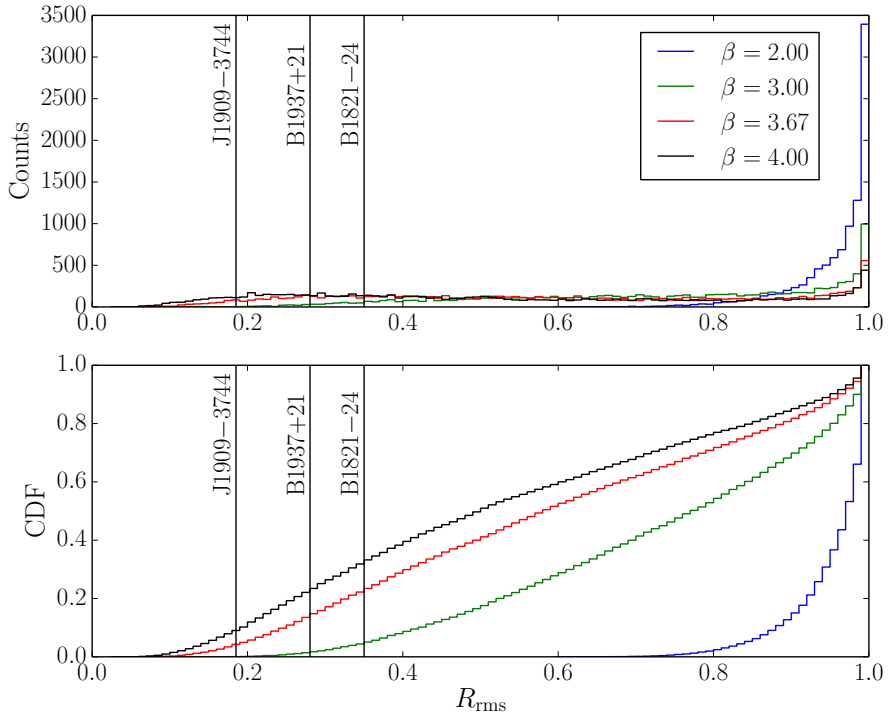

Figure 4.8: Top: Histograms of the ratio $R_{\rm rms}$ for 10000 red noise process realizations with spectral index $\gamma = \beta - 1$. Bottom: Cumulative distribution functions of the histograms. The value of the $R_{\rm rms}$ is shown for the three pulsars in our analysis with single, linear trends. Lines towards the left indicate potential deviations from a wavenumber spectrum with spectral index β.

(dashed), where higher $R_{d{\rm DM}/dt}$ (increasing exponentially to the top left) is greater inconsistency with a Kolmogorov medium. J1909−3744 shows some evidence for deviations from a Kolmogorov medium. Several other pulsars show marginal or large deviations, including some MSPs with known chromatic timing noise such as PSR J1643−1224 in NG9 (see also Arzoumanian et al. 2015a). Figure 4.8 shows the ratio $R_{\rm rms}$ (Eq. 4.34) for the DM time series of the pulsars examined so far, with J1909−3744 showing the most deviation (more toward the left) from a Kolmogorov spectral index, consistent with the conclusion from the $R_{d{\rm DM}/dt}$ metric.

4.7.2 Non-Monotonic Trends from Electron-Density Structures in the ISM

DM(t) time series from pulsars show a combination of linear trends, stochastic variations, and, in a few cases, fast changes in slope that are both positive and negative. Apparent slope changes can appear in particular realizations of a stochastic process with a red power spectrum. But they can also result from slab-like structures if they are suitably oriented relative to the LOS and the pulsar velocity. Such slabs may represent static increases and deficits over the local mean electron density that contribute as the LOS changes with time. Alternatively, they could be time-dependent owing to motions of the shock front through neutral gas. Bow shocks produced by the pulsars themselves may ionize atomic (and, less likely, molecular) structures as they move through the ISM.

Backer et al. (1993) proposed that plasma wedges are responsible for linear trends in DM(t). A plasma wedge has linearly increasing column density $N_e(\mathbf{x})$ transverse to the LOS. As the LOS moves across it, DM(t) will change linearly until the wedge boundary is reached, if there is one. The wedge will also refract by a constant refraction angle. Unlike other structures, however, a wedge of this type will have zero transverse second derivative (except at the boundaries) and therefore will not cause changes in measured flux density.

The effects of different geometries include:

Transverse motion ($v_{p_\parallel} = 0$): For a density enhancement that is aligned with the LOS, $\mathrm{DM}_{\mathrm{slab}}(t)$ will consist of a positive-going 'pulse' with duration equal to the pulsar travel time across the slab thickness. For a density deficit (e.g., from encountering a slab of atomic gas), the

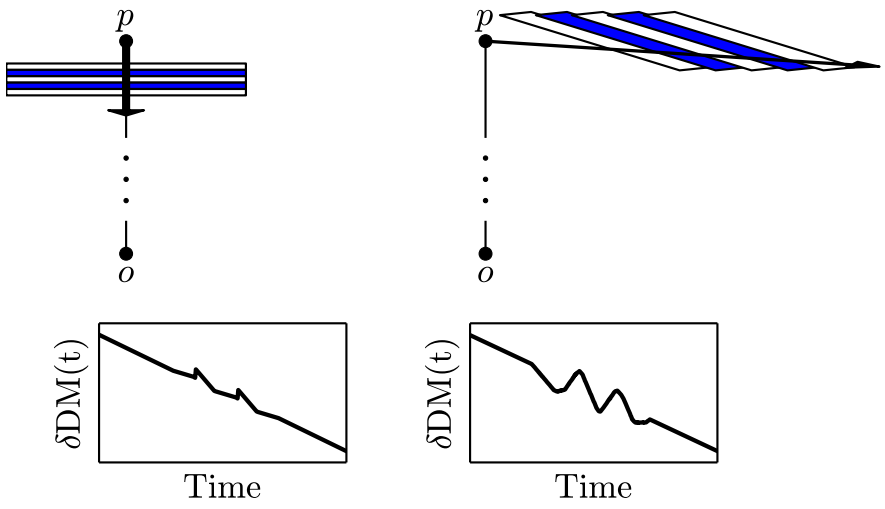

Figure 4.9: Two cartoon geometries for a pulsar p moving in different directions with respect to the line of sight between the pulsar at p and the observer at o. Blue reprents high-density structures and white represents low-density structures. The bottom graphics show DM variations, $\delta\mathrm{DM}(t)$, that are monotonic on long timescales.

pulse will be negative going. To first order, the pulsar distance does not change so the unperturbed DM is constant in time.

Pulsar velocity component along the LOS ($v_{p_\parallel} \neq 0$) and aligned slabs: When the density slabs are aligned with the LOS, DM(t) again show square-wave type pulses. The prevailing trend is for DM(t) to decrease as the pulsar distance gets smaller, but this is interrupted by the density deficits and enhancements.

Pulsar velocity component along the LOS ($v_{p_\parallel} \neq 0$) and slanted slabs: When the density slabs are slanted from the LOS, DM(t) can show a saw-tooth pattern where it has a larger slope than the prevailing trend or a slope with opposite sign. As in the previous case, the prevailing trend is for DM(t) to decrease as the pulsar distance gets smaller, but this is interrupted by the density deficits and enhancements.

Pulsar velocity toward the observer ($v_{p_\perp} = 0$): In this case, the pulsar can ionize atomic hydrogen as it passes into the slab. The DM can increase even if the pulsar moves toward the observer and the prevailing trend is for a declining DM.

Some examples of the geometries can be seen in Figure 4.9.

Ionized Bow Shocks

So far, we have assumed that ISM structures are static. However, the pulsar can actively modify its local environment. An extreme case is where the pulsar's motion toward the observer takes it through *atomic* hydrogen (HI) structures on scales of tens of AU and larger, including filaments, with a typical column density of order $N_{\rm HI} \sim 10^{-20}$ cm^{-2} (e.g. Stanimirović et al. 2007; Gibson 2007; McClure-Griffiths et al. 2007). As the pulsar nears a filament, it will ionize the atomic gas through a combination of radiation from the neutron star/magnetosphere and shock heating. The standoff radius of the bow shock is given by the balance of ram pressure and the pulsar's relativistic wind,

$$r_s = \left(\frac{\dot{E}}{4\pi \rho v_p^2 c} \right)^{1/2} \approx 266 \text{ AU } \dot{E}_{33}^{1/2} n_{\rm HI}^{-1/2} v_{p100}^{-1} \tag{4.53}$$

for $\dot{E} = 10^{33} \dot{E}_{33}$ erg s^{-1}, a pulsar velocity in units of 100 km s^{-1}, and an effective hydrogen density $n_{\rm HI}$ cm^{-3}. For the measured ranges of pulsar velocities, energy-loss rates ($\dot{E}$), and ISM densities, the standoff radius of the bow shock is tens of AU to ~ 0.1 pc. Therefore, DM(t) can show temporary increases even though the prevailing trend would be a decrease because of the decreasing distance.

Bow shocks will cause changes in DM only if the pulsar moves through a changing gas density (see, for example, PSRs J2124−3358 and B2224+65; Gaensler et

al. 2002; Chatterjee & Cordes 2004). For completely ionized gas there may be a weak effect from the shock-enhanced gas density. A much larger effect will occur from neutral gas that is shock ionized or pre-ionized by radiation from shocked gas. The mean free path for ionizing radiation with $h\nu = 13.6$ eV for a cross section $\sigma_{\rm HI} = 6.3 \times 10^{-18}$ cm^2 is

$$l_{\rm HI} = (\sigma_{\rm HI} n_{\rm HI})^{-1} \approx \frac{1.1 \times 10^4 \ {\rm AU}}{n_{\rm HI,cm^{-3}}}, \tag{4.54}$$

much larger than both the nominal standoff radius and the distance traveled by a pulsar in one year. However, for anticipated gas densities and temperatures (e.g., a shock temperature $T_s \approx 3 m_p v_p^2/k \approx 3.6 \times 10^6$ K; m_p = proton mass, v_p = pulsar velocity, k = Boltzmann constant), there are insufficient photons to ionize a region of this size. This is why Hα bow shocks are seen around some pulsars (e.g., PSRs B1957+20, B2224+65, and J0437−4715; Brownsberger & Romani 2014) in thin shells of pre-shocked atomic hydrogen that define the bow-shocks contours. For velocities ~ 100 km s^{-1} and densities $n_{\rm HI} \approx 1$ to 10 cm^{-3}, the distance traveled by the pulsar over years is less than or comparable to the standoff radius. The DM increment associated with shock ionized atomic gas is roughly

$$\delta{\rm DM}_{\rm bow} \approx \eta_s r_s n_{\rm HI} \approx 1.3 \times 10^{-3} \ {\rm pc \ cm^{-3}} \eta_s v_{p_{100}}^{-1} (n_{\rm HI} \dot{E}_{33})^{1/2}, \tag{4.55}$$

where $\eta_s \sim 4$ is a factor that takes into account the compression of interstellar gas and its distribution inside the termination shock (Clegg et al. 1988). The nominal value of $\delta{\rm DM}_{\rm bow}$ is sufficiently large to be interesting. Given the phase structure of the ISM, we expect that most pulsars will not reside in atomic gas but perhaps 40% will (Draine 2011).

Small-Scale Electron Density Variations

Because the ionized ISM contains a wide range of length scales (Armstrong et al. 1995), the density fluctuation term in Eq. 4.11 involving $\Delta n_e(\mathbf{x}(t))$ also needs to be considered. Its contribution to DM is

$$\delta\mathrm{DM}(t) = \int_{z_{e_0}}^{z_{p_0}} dz\, \Delta n_e(\mathbf{x}(z,t)). \tag{4.56}$$

Typical scales transverse to the LOS are $|\mathbf{r}| \sim v_\perp t \sim 20$ AU $v_{\perp 100} t_{\rm yr}$. The relevant velocity $\mathbf{v}_{\mathrm{eff}_\perp}(z)$ is largest at the pulsar position (c.f. Eq. 4.7) for cases where the proper-motion velocity is larger than the Earth's velocity. Elsewhere along the LOS and for slowly moving MSPs, the transverse scale can be substantially smaller.

There is evidence for individual structures in the ISM on AU scales based on refraction effects in pulsar dynamic spectra, extreme scattering events, and intraday variable sources. These are likely confined to a small fraction of the LOS and will produce maximum contributions to DM of order $10^{-5} n_e \ell_{10\mathrm{AU}}$ pc cm^{-3} where $\ell_{10\mathrm{AU}}$ is the path length through the structure. The timescale for changes depends on the density, size, and velocity of the structure so the derivative $d\mathrm{DM}/dt$ can be comparable to or much smaller or larger than the contribution from the changing distance analyzed in the previous subsection.

Implications for PSR B1534+12

We make use the second-order SF approach developed in §4.5 to analyze the DM time series presented in Fonseca et al. (2014). While they note five significant linear trends in DM, they have no temporal information in the first block and so we remove it from our analysis.

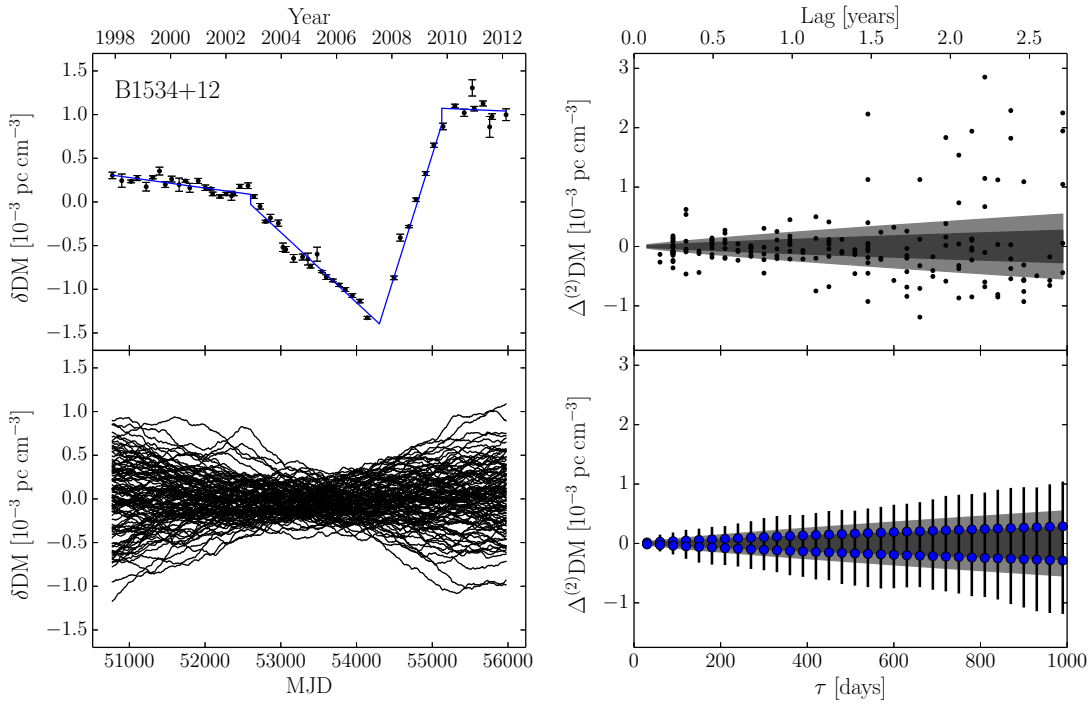

Figure 4.10: Analysis of DM time series and SFs for PSR B1534+12. Top left: The DM offsets $\delta\mathrm{DM}(t)$ from Fonseca et al. (2014, the first, isolated epoch has been removed) with their best fit linear trends overplotted. Top right: Second-order increments of DM, $\Delta^{(2)}\mathrm{DM}(t,\tau)$. The gray regions indicate the 1 and 2σ expected regions in Eq 4.39 assuming a Kolmogorov wavenumber spectrum and the appropriate scintillation timescale, $\Delta t_{\mathrm{ISS}} = 660$ s. Bottom left: 100 realizations of $\delta\mathrm{DM}(t)$ from a Kolmogorov medium scaled to the appropriate scintillation timescale. Bottom right: The second-order increments of the DM realizations in the bottom left. The shaded regions are the same as in the top right. The black bars indicate the range of increments as calculated from all of the realizations, with the blue circles indicating the 1σ bounds, matching the expectation.

Figure 4.10 shows the DM time series along with the second-order increments of DM, which we use to indicate the presence of discrete changes in linear trends over the expectation from a purely Kolmogorov medium. To account for the unequal sampling in $\delta\mathrm{DM}(t)$, we calculate increments as a function of τ by finding two points separated from the central time t, one within the range $\tau \pm \tau/2$ and the other within $-\tau \pm \tau/2$. Increasing τ by 30 days at a time, we plot the second-order increments in the top right panel. Combining Eqs 4.25 and 4.39, the probability dis-

tribution of the increments will be a Gaussian function. Using $\Delta t_{\rm ISS} = 660 \pm 180$ s measured at 430 MHz (Bogdanov et al. 2002), the 1 and 2σ expected regions are shown in the gray bands. The points in the top right of the plot outside of the bands and at $\tau > 500$ days all result from the concave up turnover between the second and third linear components and represent a $\sim 7 - 14\sigma$ deviation from the expectation of a purely Kolmogorov medium. Points well below the bands come from either of the other two changepoints. The points deviating from zero at low lags are purely from the noise in the measurements, not accounted for in the gray bands. The bottom left shows 100 realizations of DM purely from Kolmogorov power-law wavenumber spectra and the full range (minimum to maximum value) of second-order increments for each τ on the bottom right from all 10,000 realizations. We show the results of our simulations to demonstrate that there is good agreement between the rms of the second-order increments from simulations and the analytic solution. Again, the fact that several measured increments for PSR B1534+12, notably the ones associated with the second changepoints, fall outside of the expectations from simulations imply that the upturn in DM cannot be due to a purely Kolmogorov medium. The time series is similar to those shown in Figure 4.9 after a linear trend has been removed, suggesting that there are interleaved density structures along the LOS. Contemporaneous scintillation parameters and pulsar flux density measurements would be valuable for testing whether the DM time series is at all contaminated by diffraction and refraction effects.

4.8 Periodic Variations in DM

In this section, we determine how periodic trends can appear in DM time series. DM(t) will vary as the LOS passes across spatial gradients in electron density.

Local electron-density variations in time will also cause DM variations. We assess the periodicites and phases associated with each periodic contribution to DM.

4.8.1 Ionosphere

Changes in the electron-density within the ionosphere can cause differences in DM between observatories. The changes correlate with the incident solar flux at a particular location. Variations are known to occur daily from Earth's rotation, yearly due to Earth's orbital motion, and on 11-year cycles due to changes in solar magnetic activity (see Huang & Roussel-Dupré 2006, for an ionospheric electron-density model over a specific LOS). Measurements of the electron density can be peformed by satellite, rocket, incoherent scatter radar, and ionosonde.

The ionosphere can be represented as a series of semi-Epstein layers (Rawer 1982) with electron density as a function of the normalized distance parameter z,

$$n_e(z) = \frac{4n_0}{\left[1 + \exp\left(z\right)\right]^2} \exp\left(z\right) \tag{4.57}$$

with the peak electron density of the layer, n_0, and $z = (h_s - h_0)/H$, where h_s is the height above the Earth's surface, h_0 is the height of the peak electron density, and H is the characteristic thickness of the layer. Note that as $h_s \gg h_0$, $n_e(z)$ tends towards zero.

Nava et al. (2008, NeQuick 2[1]) model the E, F1, and F2 ionospheric layers using one semi-Epstein layer to describe the bottomside and topside of each layer. They introduce a "fadeout" function that multiplies z in the E and F1 layer functions to prevent secondary maxima around the F2 peak height. The peak heights, peak

[1] `http://t-ict4d.ictp.it/nequick2`

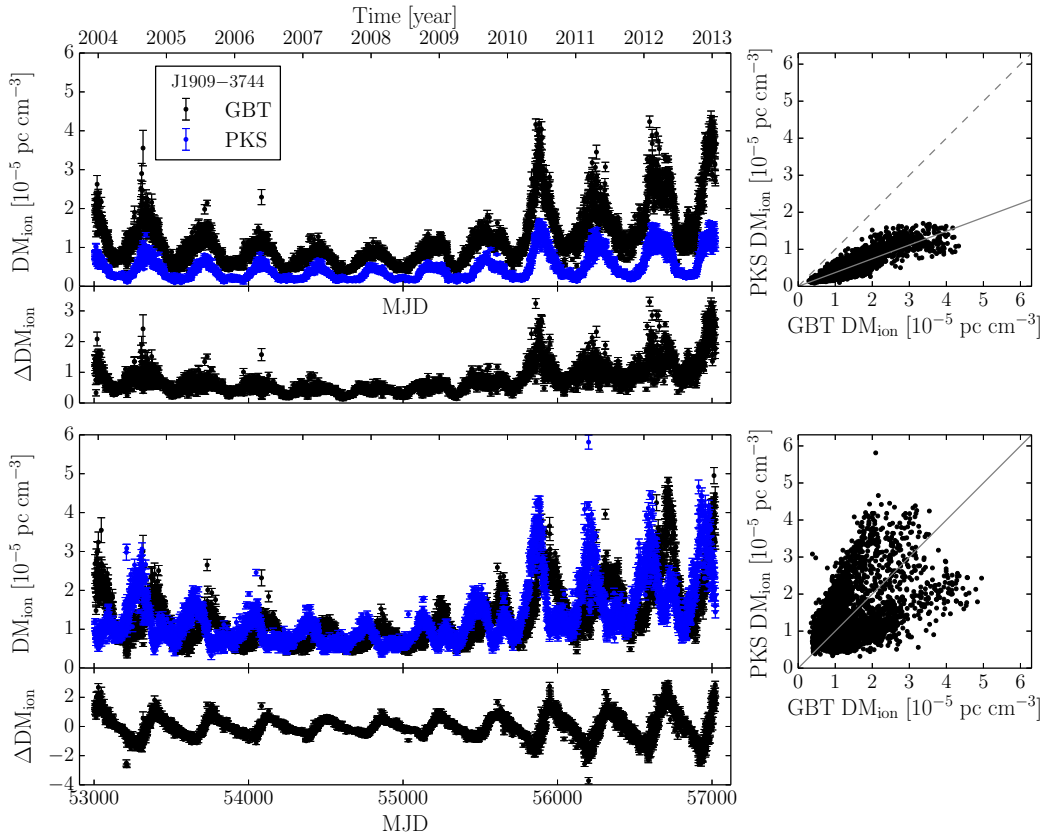

Figure 4.11: Estimates of the ionospheric contribution to DM from interpolated global navigation system satellite measurements along the LOS to PSR J1909−3744 from Green Bank Telescope (GBT, black) and the Parkes Telescope (PKS, blue) daily over nine years. Top left: Measurements of DM computed daily when J1909−3744 transits each telescope. The difference between the GBT and PKS DM estimates are shown in the panel beneath. Top right: DM estimated from Parkes at transit versus from GBT at transit. The dashed, diagonal line represent the same value at both sites while the solid line is the difference in the geometric factor $G(\theta_z)$ between both sites. Bottom: Similar to the top except that DM estimates were determined simultaneously, approximately two hours after transit at GBT so that $G(\theta_Z)$ was the same at both sites.

electron densities, and thicknesses of each layer change as a function of latitude and longitude, (ϕ_g, λ_g), over the Earth's surface due to the structure of its time-varying magnetic field. There are additional time-dependent factors regarding the incident solar flux at a given (ϕ_g, λ_g), including the change in the Sun's zenith angle over a day, the change in the seasons for a given latitude ϕ_g, and the variable

solar flux that changes both daily and over a solar cycle. Therefore, the three layer parameters, n_0, h_0, and H, are all complex functions of longitude, latitude, and time.

In general, the DM is the integral of electron density over some path s through the atmosphere that depends on the geographic coodinates of the observatory and the apparent coordinates (i.e., altitude and azimuth) of the pulsar, which in turn depend on the equatorial coordinates of the source (α_e, δ_e) and time t. The path to integrate over is then $s(\phi_g, \lambda_g, \alpha_e, \delta_e, t)$ and the total ionospheric contribution to DM is simply the line integral

$$\mathrm{DM}_{\mathrm{ion,NeQuick}}(t, \phi_g, \lambda_g, \alpha_e, \delta_e) = \int_0^{s_{\max}} \sum_{i=\mathrm{E,F1,F2}} n_{e,i}(s(t, \phi_g, \lambda_g, \alpha_e, \delta_e), \phi_g, \lambda_g, t) ds \quad (4.58)$$

up to some maximum distance $s_{\max}$, where we sum the total electron over each layer.

We study the variations of electron density in the ionosphere using two methods. The first estimates the ionospheric contribution to DM using global navigation satellite system (GNSS) measurements from the International GNSS Service (IGS; Dow et al. 2009). The total electron content (TEC) is measured via frequency-dependent signal propagation delays similarly to pulsar timing delays but between a ground receiver and a transmitting satellite along a given LOS. Using multiple LOSs at a given time, the IGS constructs a 2D surface map of the ionospheric electron density. These maps typically have time resolution of two hours and spatial resolution of 2.5 $\times$ 5.0 degrees in latitude and longitude, respectively. We linearly interpolate intermediate TEC values in both space and time. While the original measurements between receiver and satellite are along some altitude and azimuth, the reported TEC values are in the zenith direction. Therefore, we must adjust the measurements for a particular LOS. To simplify, we approximate the

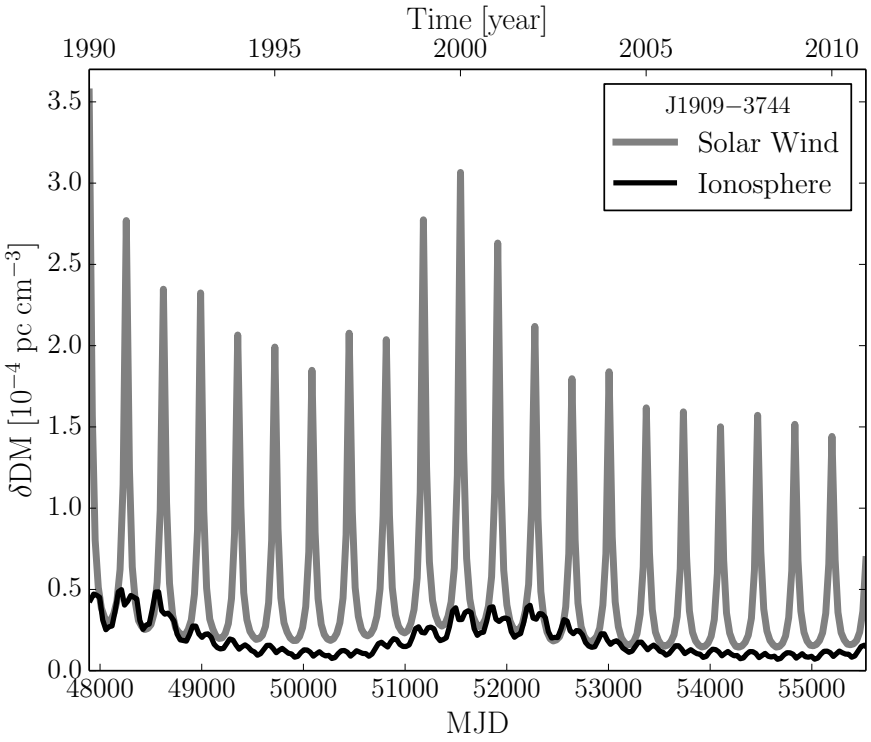

Figure 4.12: Comparison between solar wind and ionospheric DM variations, the latter as computed by the NeQuick 2 model.

ionosphere as a uniform slab of electrons with an inner ($s_{\min}$) and outer ($s_{\max}$) height of 60 and 600 km above the Earth's surface, respectively. Therefore, we can estimate the TEC along a LOS by multiplying the zenith TEC by a geometric factor $G(\theta_z)$ that accounts for the increase in path length through the ionosphere and depends only on the zenith angle θ_z to the pulsar,

$$\mathrm{DM}_{\mathrm{ion,IGS}}(t, \phi_g, \lambda_g, \alpha_e, \delta_e) = n_e(\phi_g, \lambda_g, t)(s_{\max} - s_{\min})G(\theta_z(\phi_g, \lambda_g, \alpha_e, \delta_e, t)). \quad (4.59)$$

Figure 4.11 shows our daily estimates of $\mathrm{DM}_{\mathrm{ion}}(t)$ along the LOS to PSR J1909−3744 from both the Green Bank Telescope (GBT, black) in the Northern Hemisphere and the Parkes Telescope (PKS, blue) in the Southern Hemisphere using the method in Eq. 4.59. The top panel shows DM measurements at transit on each day. Error bars come from the GNSS measurement errors alone, multi-

plied by the same geometric factor dependent on the zenith angle. The overall amplitude shift is a result of the constant difference in the zenith angle of the pulsar at transit between the two sites. Differences in DM between GBT and PKS are shown in the sub-panel beneath. The right panel shows the estimated DM observed with PKS versus GBT, with the solid gray line representing the ratio of the geometric factors. For reference, the median DM measurement error at the GBT for this pulsar is $\sim 1 \times 10^{-5}$ pc cm^{-3} for the latest backends (see NG9 for information on the GUPPI backend) whereas the value at PKS is $\sim 3 \times 10^{-5}$ pc cm^{-3}. Variations in the DM annually and over the solar cycle are visible. The bottom panels of Figure 4.11 shows the result of simultaneous observations of the pulsar at low elevation angles at both telescopes, such that the ratio of geometric factors is 1:1, i.e., variability is due solely to differences in the ionosphere at different local times. Such an observation occurs 110 minutes after the pulsar transits the GBT when the zenith angle is $\approx 80.3°$, yielding a geometric factor of ≈ 3 increase over the zenith TEC measurement. The sites are separated by $\sim 112°$ of longitude and observe the pulsar at nearly opposite local times. As the Earth's orbital position shifts, the local observing times shift, producing a phase difference between the two time series. Smaller peaks separated from the yearly peaks by approximately six months are visible as the solar cycle maximum is approached just past the end of the time series (again see Huang & Roussel-Dupré 2006, for this intra-annual variability). Again, the right panel shows the PKS-estimated ionospheric DM versus the GBT-estimated DM, where the estimates in DM can differ by measurable amounts even when observed at the same time. The bimodality results from ionospheric differences between day and night between the sites.

The second method to study the ionospheric DM variations uses the mathematical description above, implemented in the NeQuick 2 model (Nava et al. 2008).

NeQuick 2 uses ionosonde measurements to determine the parameters of the semi-Epstein layers (Eq. 4.57), along with solar radio flux measurements and a model for the magnetic inclination that describes the shape of the Earth's magnetic field lines as a function of latitude, longitude, and time. For more details on the implementation, refer to Report ITU-R P.2297-0 (2013). By default, NeQuick 2 contains parameters with a monthly time resolution, and a time series for PSR J1909−3744 is shown in comparison to the DM contribution from the solar wind, discussed in the following sub-section, in Figure 4.12.

4.8.2 Solar Wind

Particles from the solar corona have enough kinetic energy to escape the Sun's gravity, becoming part of the interplanetary medium. The speeds and compositions of these particles are not uniform, and measurements of the electron density are carried out both from ground-based observing and in situ. Splaver et al. (2005) model the electron density along the LOS to PSR J1713+0747 due to the solar wind as a power-law $n_e(r) = n_0\ (1\ \mathrm{AU}/r)^2\ \mathrm{cm}^{-3}$, where n_0 is the electron density in cm^{-3} at the Earth, based on measurements from the *Ulysses* spacecraft (Issautier et al. 2001). They note that while the scaling holds over a large range of heliocentric latitudes, it does not consider spatial variations with ecliptic latitude β_e, namely the higher-density slow wind at lower latitudes and the lower-density fast wind at higher latitudes, nor does it consider temporal variations. They find that $n_0 = 5 \pm 4\ \mathrm{cm}^{-3}$. You et al. (2007) present a generic two-piece model that accounts for the positional variations using daily solar magnetic field maps from Wilcox Solar Observatory but do not consider temporal variations; the coefficients for their power-law components come mostly from observations taken at minima in

the solar cycle. See references cited by You et al. (2007) therein for more details.

Sokół et al. (2013) (see also Provornikova et al. 2014) find that the total number density of solar wind protons is $\sim 2-10$ cm^{-3} at 1 AU over a range of heliolatitudes β_h and over the course of a solar cycle. The highest densities comes from $|\beta_h| \lesssim 20°$. At solar cycle maxima, the total density at 1 AU is a weak function of heliolatitiude with a value of ~ 6 cm^{-3}. Heading towards solar cycle minima, the proton density becomes more peaked at central heliolatitudes though the overall quantity drops. We follow the methods in Sokół et al. (2013) to create an empirical model of Carrington rotation-averaged (one period is 27.2753 days) proton density as a function of heliolatitude and time spanning from 1990 to 2011. We linearly interpolate in both heliolatitude and time for smoother sampling of the proton density. Inspection of time series from the *Solar Wind Observations Over the Poles of the Sun* (SWOOPS[2]) experiment on the *Ulysses* spacecraft show that $n_e \sim n_p$, which we will assume to obtain the electron density at 1 AU, $n_0(\beta_h, t)$ (Bame et al. 1992). The model assumes an $n_e \propto r^{-2}$ dependence, which is supported elsewhere in the literature (e.g. Issautier et al. 1998). Therefore, we can write the solar wind DM in the direction of the pulsar as

$$\mathrm{DM_{sw}}(t, \beta_h) = 4.848 \times 10^{-6} \text{ pc cm}^{-3} \int \left(\frac{n_0(\beta_h, t)}{\text{cm}^{-3}} \right) \left(\frac{1 \text{ AU}}{r} \right)^2 ds, \qquad (4.60)$$

where the integration path $s = s(\beta_h, r)$. We limit the integration to within 100 AU of the Sun. The typical solar wind speed is of the order several hundred kilometers per second and so the propagation time to the integration boundary is of order one year (Sokół et al. 2013). However, because of the r^{-2} factor, only the electron density within the inner $\lesssim 10$ AU contribute to any currently measurable DM variation, which has a propagation time of approximately one Carrington rotation. Since the intrinsic time-averaging with the model is of this order, exclusion of the

[2] `http://spdf.sci.gsfc.nasa.gov/pub/data/ulysses/plasma/swoops/ion/hires/`

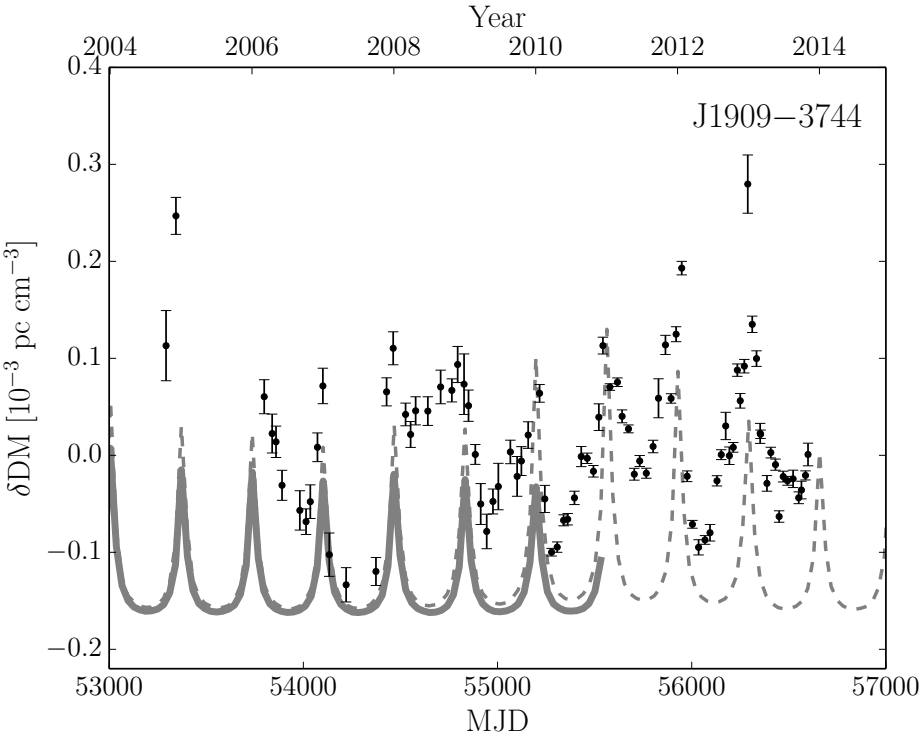

Figure 4.13: Time series of DM for PSR J1909−3744 from NG9 after a weighted, quadratic trend has been removed as in Figure 4.1. The solid gray line shows the model $DM_{sw}(t)$ from Figure 4.12 with an arbitrary vertical offset added. The dashed gray line shows the model shifted forward in time by 11 years (one average solar cycle) to provide a comparison of the periodicity and shape of the model time series with the data at later times.

time-varying mean speeds of the electrons should not greatly affect our results. We note that Eq. 4.60 only accounts for the average behavior of the solar wind over Carrington rotations and does not include components from transient events such as solar flares or coronal mass ejections.

Figure 4.12 shows the model solar wind DM and the ionospheric DM from the NeQuick 2 model along the LOS to J1909−3744. For the ionospheric component, we set the observation during pulsar transit once per month. Again, the median error on DM for J1909−3744 measured with GBT is $\sim 1 \times 10^{-5}$ pc cm^{-3}, which implies that the ionospheric contribution is marginally detectable in the time series,

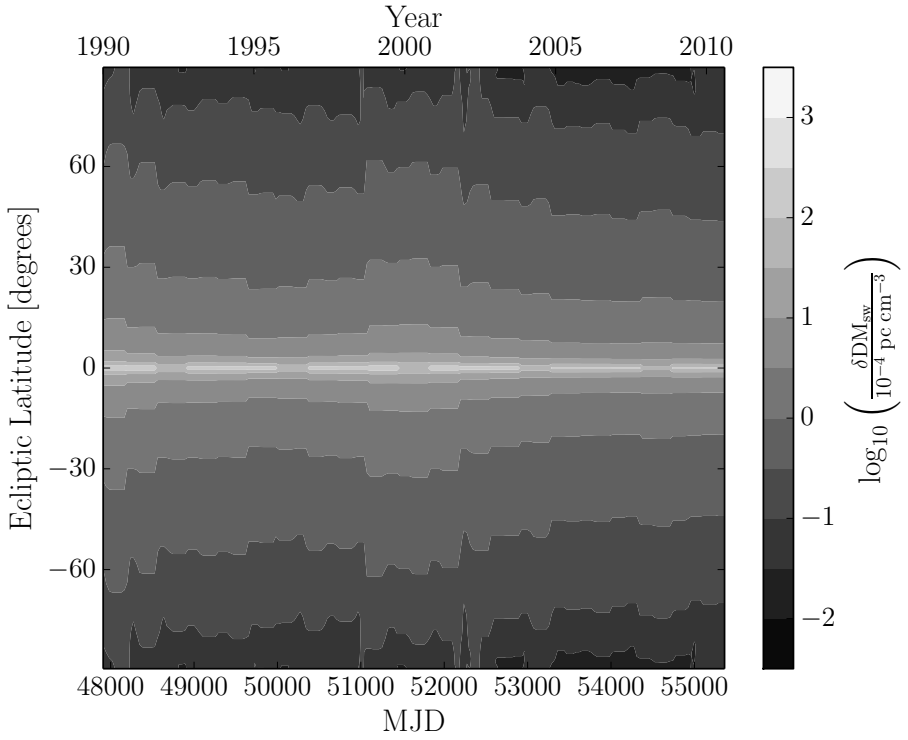

Figure 4.14: Maximum change in model solar wind DM centered around a one-year smoothing window at each given epoch for a pulsar at a given ecliptic latitude.

whereas the solar wind contribution is significantly measurable. Figure 4.13 shows the predicted solar wind contribution plotted against the J1909−3744 time series with the best-fit quadratic trend removed for clarity. The vertical offset of the predicted time series was set arbitrarily to roughly match the DM offsets (as the nominal DM has already been removed). Even without including transient solar events, our model agrees with the overall periodic trend in the time series, both in phase and peakedness of the yearly maxima.

Figure 4.14 shows the peak-to-peak change in the DM contribution from the solar wind model in a given one-year smoothing window as a function of ecliptic latitude. Pulsars lying closer to the ecliptic plane will have a much greater peak DM since the LOS will cross near the Sun and the electron density scales as r^{-2}. Pulsars observed far out of the plane will show minimal amounts of solar wind

DM variations. For reference, PSR J1909−3744 has $\beta_e \approx -15.2°$ with the mean peak-to-peak change around 1.45×10^{-4} pc cm^{-3}, which can also be seen as the predicted amplitude of variations in Figure 4.13.

4.8.3 Heliosphere

Particles comprising the solar wind interact with the surrounding ISM at the heliospheric boundary. As the Sun moves through the ISM, it creates a bow shock towards the nose (upwind) direction with a long tail opposite the direction of the Solar System's motion. Turbulence generated at the interface creates spatial and temporal variations in electron density. In general, the DM for a specific LOS can be written as

$$\mathrm{DM}_{\mathrm{hel}}(t, \beta_e, \lambda_e) = \int n_{e,\mathrm{hel}}(s(t, \beta_e, \lambda_e), t) ds \tag{4.61}$$

where (λ_e, β_e) are ecliptic longitude and latitude. The path s depends on the position of the Earth in its orbit. For reference, the nose direction of the heliosphere is roughly $(\lambda_e, \beta_e) \approx (254°, 5°)$ (Kurth & Gurnett 2003), equivalent to $(\alpha_e, \delta_e) \approx (253.3°, -17.5°)$ or $(l_g, b_g) \approx (2.6°, 16.4°)$.

Opher et al. (2015) simulate the heliosphere region extending from 30 to 1500 AU. They assume a spherically symmetric solar wind flow at the inner boundary with a given speed, number density, and temperature, along with a radial and azimuthal solar magnetic field. The outer boundary interacts with the ISM and also has a relative velocity, number density, and temperature. The interstellar magnetic field is slanted with respect to the downwind direction. They find that the solar magnetic field forces the solar wind plasma into jets which are then blown into the tail direction by the interstellar wind. Turbulent instabilities form into

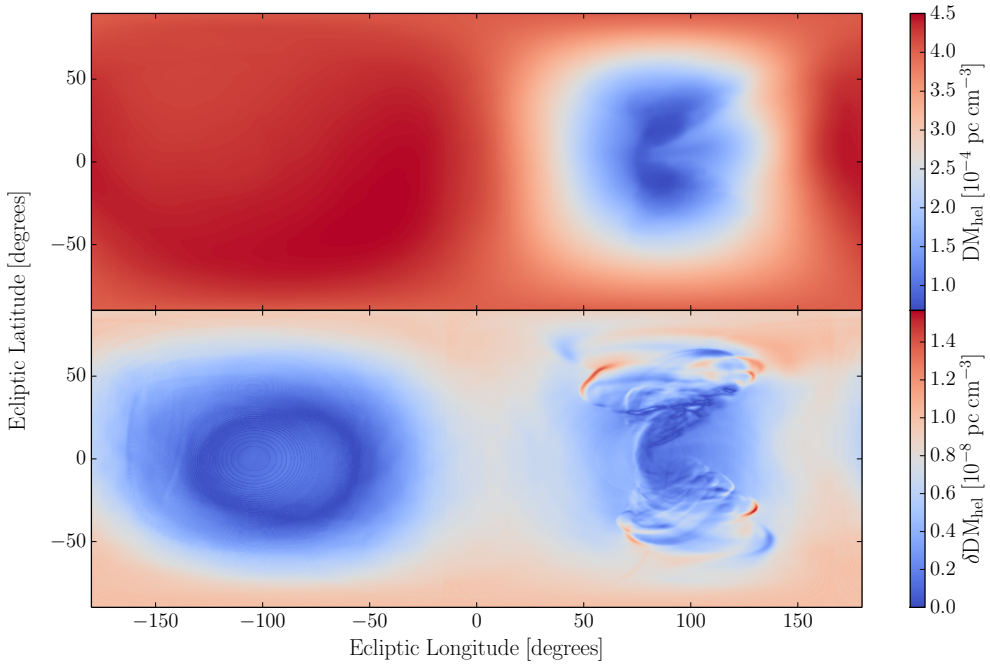

Figure 4.15: Top: Map of $\mathrm{DM_{hel}}(\lambda_e, \beta_e)$. The nose direction is in the center of the left half of the image whereas the tail direction is in the center of the right half. Bottom: Maximum change in DM due to the Earth's orbital motion around the Sun. Note the different scales between the two panels. The thin, ringed structures visible in the nose direction (not the broad ringed structure) are a result of sampling errors in the 3D grid.

two tails and the heliosphere retains a two-lobed structure as the tails remain separated.

Figure 4.15 shows the electron density from simulations in Opher et al. (2015) integrated out to a distance of 1500 AU from the Sun. The heliosphere is several times denser through the bow shock region in the nose direction than through the tail direction. The bottom panel shows the peak-to-peak variations in DM due to the changing LOS from the Earth orbiting the Sun to the stationary pulsar. The maximum change is $\sim 10^{-8}$ pc cm^{-3} when looking at turbulence through the tail. The effect of the heliosphere, therefore, is approximately three orders of magnitude

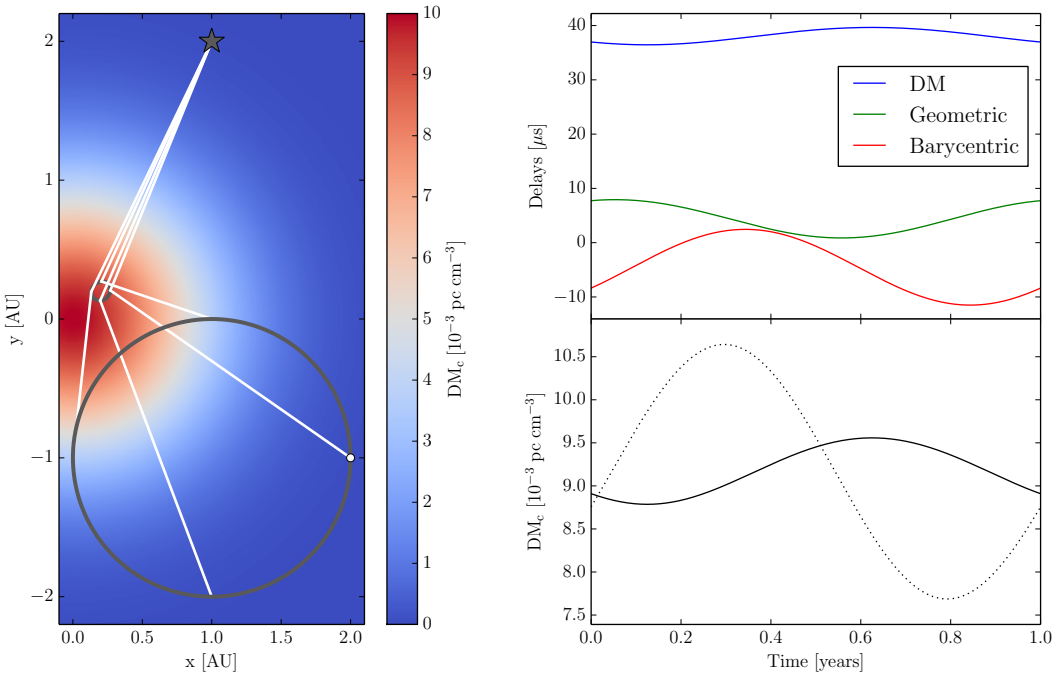

Figure 4.16: Effects of a Gaussian cloud on timing measurements. Left: Example ray-tracing geometry of emission (where the z-direction has been collapsed in the image) from a pulsar (gray star) located at (1 AU, 2 AU, 1 kpc) traveling through a cloud with $N_0 = 0.01$ pc cm^{-3} and $a = 1$ AU located at (0 AU, 0 AU, 0.5 kpc) hitting the Earth in an orbit centered around the Sun located at (1 AU, –1 AU, 0 kpc). The orbit of the Earth (large gray circle, $t = 0$ yr is given by the white dot) is in the plane of the image (i.e., $z = 0$ AU at all times). The background colors represent the column density profile of the cloud. The smaller gray circle drawn over the cloud represents the sampling of the cloud screen due to the Earth's orbital motion and the position of the pulsar. We integrate at points over the entire orbit; four rays (white lines) have been shown to demonstrate the integration paths from the pulsar to the Earth. Top right: The three delays $\Delta t_{\rm DM}$ (blue), $\Delta t_{\rm geo}$ (green), $\Delta t_{\rm bary}$ (red) in order from top to bottom. Bottom right: DM due solely to the integral of electron density over the ray paths (solid) as compared with the measured DM when all three delays are summed together (dotted).

smaller than current sensitivity (for PSR J1909−3744 in NG9) and requires ~ 0.05 ns timing precision to measure. While the heliosphere does change over time, the overall structure remains similar. Since the crossing time for solar wind particles through the heliosphere is of the order years, changes in the electron density along

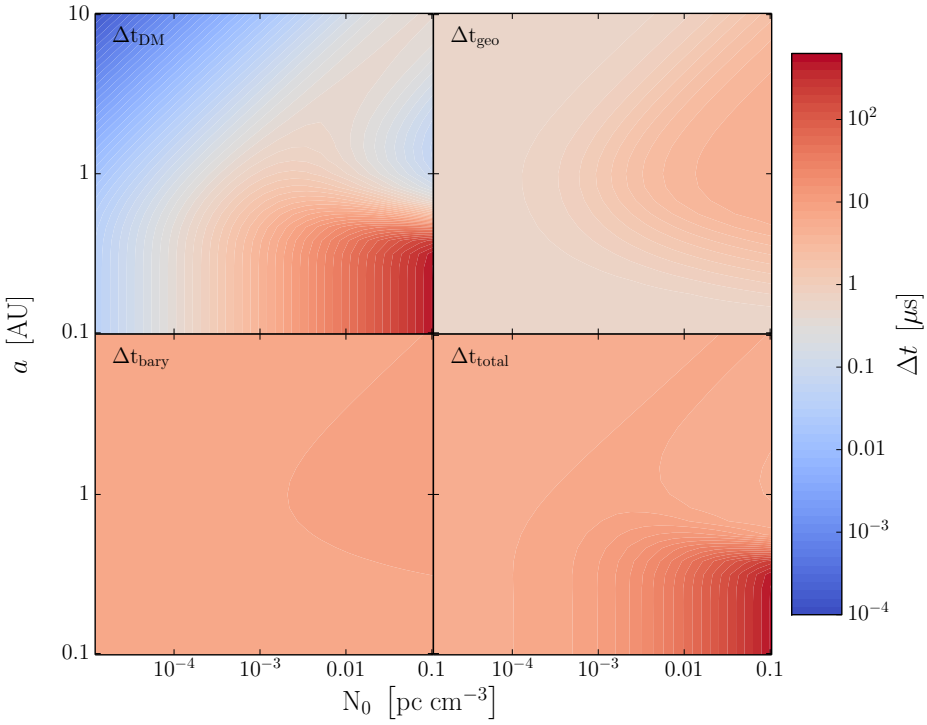

Figure 4.17: Timing delays associated with refraction due to a Gaussian plasma lens as a function of N_0 and a. Top left: Dispersion delay $\Delta t_{\rm DM}$. Top right: Geometric delay $\Delta t_{\rm geo}$. Bottom left: Barycentric delay $\Delta t_{\rm bary}$. Bottom right: Sum of all three delays. The amplitude of the timing delays typically increases towards the bottom right.

a given LOS will be small from epoch to epoch. Given that the overall amplitude of the heliospheric DM is below current sensitivity to DM, we do not consider temporal variations in the heliosphere.

4.8.4 Gaussian Plasma Lens in the ISM

Using the formalism in §4.6, we simulate a Gaussian, electron density cloud and solve Eq. 4.51 to trace incident rays back from the Earth to the pulsar. We show an example calculation of the ray paths through a cloud with central column density

$N_0 = 0.01$ pc cm^{-3} and size $a = 1$ AU in Figure 4.16. The pulsar is at a distance of 1 kpc and the cloud is halfway in between.

We numerically integrate through our example cloud and show the delays in the top right panel of Figure 4.16. The bottom right panel shows the DM delay purely as the integral of the electron density along the ray path (i.e., proportional to $\Delta t_{\rm DM}$ alone; solid line) along with the estimated DM when all three delays are summed together (dotted line). In our example, both the amplitude and phase change significantly.

To explore the possible parameter space of N_0 and a, we place a pulsar at (1 AU, 2 AU, 1 kpc), directly in line with the Gaussian cloud at (0 AU, 0 AU, 0.5 kpc). The Sun is located at (1 AU, –1 AU, 0 kpc) with the Earth orbiting in the $z = 0$ plane. Figure 4.17 shows the peak-to-peak variations in the time delays separately and then when all three are added together.

While we consider the case of the LOS crossing through a Gaussian cloud periodically, the same formalism can be applied to single crossing events (Clegg et al. 1998). Clouds with a small perpendicular velocity will cause periodic DM variations modulated by an envelope with width equal to the timescale of the cloud crossing. In general, the phase of DM$_c(t)$ can be arbitrary with respect to previously mentioned periodic contributions.

4.9 Implications for ISM Study and Precision Timing

Analysis of DM variations can enable the study of the electron density along the entire LOS to a pulsar. While we see that the ISM is consistent with a Kol-

mogorov medium, interpretations of DM SFs could be used to search for a different wavenumber spectral index or anisotropies along certain LOSs. Measurements of DMs coming from an array of pulsars distributed across the sky has the potential to probe the structure of the ISM and solar wind. Changing DMs due to pulsar motion through the ISM can also be valuable inputs to large-scale electron density models of the Galaxy.

Assuming that the only chromatic effect on pulses is the dispersive delay, DM can be estimated on a per-epoch basis using a wide range in frequency coverage. In that case, variations in DM will not affect pulsar TOAs used for precision timing experiments. Numerous chromatic effects are however known to exist.

- Frequency-dependent variations of the pulse profile will change the measured TOAs by a constant offset per frequency and lead to a large error in DM if not globally fit for over a many-epoch data set (Liu et al. 2012; Pennucci et al. 2014). Profile evolution is assumed to be time-independent in many pulsars (see Lyne et al. 2010 for counterexamples). A simultaneous fit over parameters that describe the profile evolution and the DM will reduce their covariance. Profile evolution coupled with amplitude modulation from interstellar scintillation will cause an effective shift in the reference frequency that changes the estimated DM on the order of a diffractive timescale.
- Estimates of DM will be contaminated by other chromatic timing effects that result from refraction and multipath propagation. As shown by Foster & Cordes (1990), if refraction is allowed to contaminate DM estimates, the SF will show excess amplitude on long times compared to extrapolation from the diffraction timescale and will also lead to an overestimated wavenumber spectral index. Multipath propagation causes temporal broadening of pulse

shapes that increase with lower frequency. Pulse broadening will couple with intrinsic profile shape changes, adding additional time-dependent TOA errors, and thus producing apparent DM changes (Levin et al. 2016).

- Scattering causes spatial averaging over the ISM in any single-epoch measurement of DM (Cordes et al. 2016). DM is therefore a function of frequency.
- DM measured with asynchronous multi-frequency measurements will be misestimated as the LOS integral will change, due to stochastic changes in the ISM and to systematic effects such as the increasing Earth-pulsar distance (Lam et al. 2015).
- Even simultaneous measurements from different locations on the Earth can result in different observed values of DM due to separate LOSs through the ionosphere.

High-precision timing experiments require minimization of all possible TOA errors, especially those correlated in time. Therefore, the combination of data from multiple telescopes will require care to avoid contamination from the various achromatic effects listed.

Inclusion of DM terms that describe linear or periodic variations can reduce the number of model parameters in a timing fit but will also be highly covariant with other parameters included in the fit (Splaver et al. 2005). Linear terms for DM evolution in a timing model are covariant with pulsar spin and spin-down parameters. In a pulsar timing array experiment to detect and study gravitational waves (GWs), such terms also remove sensitivity to the lowest-frequency GWs. Annual and semi-annual variations will be covariant with astrometric parameters and GWs with the same frequencies.

Removal of frequency-dependent terms other than DM, such as profile evolution parameters or scattering delays, in a timing model will change the absolute DM measured. The absolute differences must be taken into account when combining DM measurements obtained by different methods; TOAs incur additional errors otherwise. In addition, even with the same frequency-dependent terms included, different methods exist for DM estimation and removal from TOAs. Keith et al. (2013) utilize information regarding the correlations between epochs in their DM determination; Demorest et al. (2013) do not. Since DM is not independent from epoch to epoch, timing models should account for the correlations between measurements. However, due to the stochastic component of the DM variations, it may be impossible to completely remove per-epoch DM determination from a timing model. Optimal DM estimation and removal strategies are therefore necessary to minimize TOA uncertainties.

4.10 Summary and Conclusions

DM time series show a wide range of correlated variations. We model the possible contributions to DM variations as the sum of systematic and stochastic effects along the LOS through the media between the observatory and the pulsar. Linear trends arise from the average motion of the LOS through the ISM and the full 3D motion of the pulsar should be taken into consideration when studying linear trends in DM time series. Disentangling the effects of changing distance and changing LOS from parallel and transverse motion, respectively, is possible if scintillation parameters (including flux density) are also measured. The change in distance over a few years will have no effect on these parameters whereas transverse gradients in the ISM density will.

Changes in the LOS due to Earth's annual motion, coupled with a variety of effects that will be weighted differently for different pulsars, result in periodic variations in DM. Any DM contribution from the ionosphere, solar wind, or heliosphere will be correlated across pulsars depending on their sky positions and the relative position of the Sun. The relative phases of the three contributions may be misaligned, again depending on the specific positions of the pulsars, and so it is possible to disentangle the effects for a subset of pulsars. In the case of the ionosphere, the periodicity may be semi-annual. In general, both types of variations, linear and periodic, will contrbute to DM time series, along with a stochastic component resulting from the turbulent ISM. The relative importance of each component can only be determined on a pulsar-by-pulsar basis.

SFs are useful statistics for analyzing DM variations. DM time series will generally include systematic trends along with stochastic variations from density variations on a wide range of scales (e.g., Kolmogorov-like variations). The stochastic term can be contaminated by any systematic trend in the time series, so time series should be de-trended before using DM(t) to infer the properties of the ISM along the LOS. Estimates of the wavenumber spectral index or the scintillation timescale from the SF should also include realization errors. We show that once the linear trends and realization errors are taken into account, PSRs J1909−3744, B1937+21, and B1821−24 show time series consistent with a Kolmogorov electron-density wavenumber spectra. PSR B1534+12, with its non-monotonic trends in DM, is inconsistent with a simple Kolmogorov ISM.

Decomposition of DM time series into known, deterministic causes will allow for the study of the local and interstellar electron density. Future studies of DM time series should model known components to further probe the relative contributions

of DM fluctuations along the LOS. Pulsars in a pulsar timing array with many LOSs will see correlated DM variations from the ionosphere and solar wind. As we have shown with PSR J1909−3744, we can probe the local electron density around a pulsar after careful determination of its radial velocity.

Differences in DM correction methods will become increasingly important in the near future. Optimal correction methods must be implemented for the proper combination of multi-telescope data. By appropriately removing the effects of DM variations from TOAs, we will be able to maximize pulsar timing array sensitivity.

4.11 Acknowledgments

Work on pulsar timing at Cornell University and West Virginia University is supported in part by NSF PIRE program award number 0968296 and NSF Physics Frontier Center award number 1430284. For JWA the research described here was carried out at the Jet Propulsion Laboratory, California Institute of Technology, under a contract with the National Aeronautics and Space Administration. MTL was partially supported by NASA New York Space Grant award number NNX15AK07H. We would like to thank Merav Opher and Bertalan Zieger of Boston University for access to their simulated heliosphere data. We thank Paul Demorest and Ryan Shannon for data and assistance relating to PSR B1937+21, Emmanuel Fonseca for data relating to PSR B1534+12, and Michael Keith for data relating to PSRs J1909−3744, B1937+21, and B1821−24. We would also like to thank Bruno Nava for the source code to the NeQuick 2 model, David Nice for assistance regarding solar wind modeling, John Antoniadis for discussions on the 3D velocity of PSR J1909−3744, the NANOGrav Interstellar Medium

Mitigation working group for useful conversations throughout the duration of this project, and the anonymous referee for a very careful readthrough of this work. We acknowledge NASA/GSFC's Space Physics Data Facility's ftp service for *Ulysses*/SWOOPS (`ftp://nssdcftp.gsfc.nasa.gov/spacecraft_data/ulysses/plasma/swoops/ion/hires/`) data collection.

4.12 Appendix

4.12.1 Functional forms for Structure Functions of a Power-Law Wavenumber Spectrum

We will consider the relationships between different SFs of a time-varying $\mathrm{DM}(t)$. By taking the Fourier transform of the first-order increment $\Delta^{(1)}\mathrm{DM}(t,\tau) = \mathrm{DM}(t) - \mathrm{DM}(t+\tau)$, we can write the ensemble-average SF in terms of the power spectrum $S_{\mathrm{DM}}(f)$ (see Eq. 15 of Lam et al. 2015),

$$D^{(1)}_{\mathrm{DM}}(\tau) \;=\; \left\langle \left[\Delta^{(1)}\mathrm{DM}(t,\tau)\right]^2 \right\rangle = 4\int df\, S_{\mathrm{DM}}(f)\sin^2(\pi f\tau). \tag{4.62}$$

A wavenumber spectrum (Eq. 4.17) with spectral index β will be a red noise process $\mathrm{DM}(t)$ with an associated power-law spectrum that scales as $S_{\mathrm{DM}}(f) = Af^{-\gamma}$ where $\gamma = \beta - 1$ and A is a spectral coefficient. For a wavenumber spectrum in the scintillation regime ($2 < \beta < 4$, $1 < \gamma < 3$), the integral can be solved as

$$4A\int_0^\infty df f^{-\gamma}\sin^2(\pi f\tau) = -2A\Gamma\left(-[\gamma-1]\right)\cos\left(\frac{\pi[\gamma-1]}{2}\right)(2\pi\tau)^{\gamma-1}, \tag{4.63}$$

where Γ is the Gamma function (Gradshteyn et al. 2007, Eq. 3.823). We can relate the spectral coefficient A to the scintillation timescale Δt_{ISS} by equating this to

Eq. 4.23,

$$A = -\frac{\nu^2}{2(cr_e)^2\Gamma(-[\gamma-1])\cos\left(\pi[\gamma-1]/2\right)\left(2\pi\Delta t_{\rm ISS}\right)^{\gamma-1}}. \tag{4.64}$$

Therefore, a Kolmogorov wavenumber spectrum with $\beta = 11/3$ and a time-series power-law spectral index of $\gamma = 8/3$ will have a SF equal to

$$D^{(1)}_{\rm DM}(\tau) = A\Gamma\left(-5/3\right)\sqrt{3}(2\pi\tau)^{5/3} \tag{4.65}$$

with

$$A = -\frac{\nu^2}{(cr_e)^2\Gamma(-5/3)\sqrt{3}\left(2\pi\Delta t_{\rm ISS}\right)^{5/3}}, \tag{4.66}$$

which reduces to Eq. 4.25 when combined. In general, the scintillation timescale will vary with frequency as $\Delta t_{\rm ISS} \propto \nu^{2/(\beta-2)}$, so the SF, proportional to $\nu^2[\Delta t_{\rm ISS}(\nu)]^{-(\beta-2)}$, will always be independent of frequency in the scintillation regime ($2 < \beta < 4$) (Lam et al. 2015).

Following a similar procedure using the second-order increment $\Delta^{(2)}{\rm DM}(t,\tau) = {\rm DM}(t-\tau) - 2{\rm DM}(t) + {\rm DM}(t+\tau)$, the second-order SF can be written as (Eq. 21 of Lam et al. 2015)

$$D^{(2)}_{\rm DM}(\tau) \;=\; \left\langle \left[\Delta^{(2)}{\rm DM}(t,\tau)\right]^2 \right\rangle = 16\int df\, S_{\rm DM}(f)\sin^4(\pi f\tau) \tag{4.67}$$

Using trigonometic identities, we can write $\sin^4(\theta) = \sin^2(\theta) - (1/4)\sin^2(2\theta)$ and then solve using similar integrals to before. The second-order SF can then be related to the first-order SF for a power-law spectrum

$$\begin{aligned} D^{(2)}_{\rm DM}(\tau) &= -\left(8 - 2^{-\gamma}\right) A\Gamma\left(-(\gamma-1)\right)\cos\left(\frac{\pi(\gamma-1)}{2}\right)(2\pi\tau)^{\gamma-1} \\ &= \left(4 - 2^{\gamma-1}\right) D^{(1)}_{\rm DM}(\tau), \end{aligned} \tag{4.68}$$

which is roughly $0.8252 D^{(1)}_{\rm DM}(\tau)$ for the Kolmogorov case. This is equal to the variance of the second-order increments, $\sigma^2_{\Delta^{(2)}{\rm DM}}(\tau)$. Thus, for a pulsar with scintillation timescale $\Delta t_{\rm ISS}(\nu)$ measured at frequency ν, the second-order increments

at a given τ will be drawn from a Gaussian distribution with standard deviation

$$\begin{aligned}\sigma_{\Delta^{(2)}\mathrm{DM}}(\tau) &= \left[D^{(2)}_{\mathrm{DM}}(\tau)\right]^{1/2} \\ &= \sqrt{4-2^{\gamma-1}}\left[D^{(1)}_{\mathrm{DM}}(\tau)\right]^{1/2} \\ &= \sqrt{4-2^{\beta-2}}\left(\frac{\nu}{cr_e}\right)\left[\frac{\tau}{\Delta t_{\mathrm{ISS}}(\nu)}\right]^{(\beta-2)/2}. \end{aligned} \tag{4.69}$$

While Eq. 4.30 has the variance of DM(t) equal to half the DM SF, we note that the variance of DM increments will be equal to the SF only, which is defined as the expectation value of the square of the increments.

4.12.2 Structure Function Slope Mis-Estimation from Additive Noise

The presence of additive noise will also bias the slope α of a power-law SF, $D_x(\tau) = C\tau^{\alpha}$, for a time series $x(t)$. Assuming for now that a linear trend has been removed, since the SFs listed above all have the same slope for a Kolmogorov medium, we let $y(t) = x(t) + n(t)$ be the measured values of a generic, random process, where $x(t)$ is the random process of interest (e.g., DM variations) and $n(t)$ is the measurement error with rms σ_n. The SF of $y(t)$ is then

$$D_y(\tau) = (1-\delta_{\tau 0})\,2\sigma_n^2 + D_x(\tau) \tag{4.70}$$

where $\delta_{\tau 0}$ is the Kronecker delta. The slope of the SF of y might be used as an estimate for α. For $\tau > 0$, it can be shown that the estimated slope is

$$\hat{\alpha} = \frac{d\ln D_y(\tau)}{d\ln\tau} \equiv \frac{\tau}{D_y(\tau)}\frac{dD_y(\tau)}{d\tau} = \alpha\left[\frac{\tau C\tau^{\alpha-1}}{D_y(\tau)}\right] = \frac{\alpha}{1+2\sigma_n^2/D_x(\tau)}. \tag{4.71}$$

Therefore, we see that α is always underestimated if the additive noise contribution to the SF is significant. One method of mitigatng the bias is to use a model for the

SF that includes a constant term, $\hat{D}_y(\tau) = c\tau^a + b$, where estimates of the three parameters of the least-squares fit would correspond to α, $2\sigma_n^2$, and C. It is better to do the fit in log-log space because the dynamic ranges of τ and $D_y(\tau)$ can be large. The estimated slope $\hat{\alpha}$ will take a more complicated form if the linear trend has not been removed.

BIBLIOGRAPHY

Antoniadis, J. I. 2013, Ph.D. thesis, Univ. of Bonn

Armstrong, J. W., Rickett, B. J., & Spangler, S. R. 1995, ApJ, 443, 209

Arzoumanian, Z., Brazier, A., Burke-Spolaor, S., et al. 2015, ApJ, 810, 150

Arzoumanian, Z., Brazier, A., Burke-Spolaor, S., et al. 2015, ApJ, 813, 65

Bame, S. J., McComas, D. J., Barraclough, B. L., et al. 1992, A&AS, 92, 237

Backer, D. C., Hama, S., van Hook, S., & Foster, R. S. 1993, ApJ, 404, 636

Bogdanov, S., Pruszyńska, M., Lewandowski, W., & Wolszczan, A. 2002, ApJ, 581, 495

Brisken, W. F., Macquart, J.-P., Gao, J. J., et al. 2010, ApJ, 708, 232

Brownsberger, S., & Romani, R. W. 2014, ApJ, 784, 154

Chatterjee, S., & Cordes, J. M. 2004, ApJL, 600, L51

Clegg, A. W., Chernoff, D. F., & Cordes, J. M. 1988, in AIP Conf. Proc. 174, Radio Wave Scattering in the Interstellar Medium, ed. J. M. Cordes, B. J. Rickett, & D. C. Baker (Melville, NY: AIP), 174

Clegg, A. W., Fey, A. L., & Lazio, T. J. W. 1998, ApJ, 496, 253

Cognard, I., & Lestrade, J.-F. 1997, A&A, 323, 211

Coles, W. A., Rickett, B. J., Codona, J. L., & Frehlich, R. G. 1987, ApJ, 315, 666

Coles, W. A., Kerr, M., Shannon, R. M., et al. 2015, ApJ, 808, 113

Cordes, J. M. 2002, in ASP Conf. Ser. 278, Single-Dish Radio Astronomy: Techniques and Applications, ed. S. Stanimirovic et al. (San Francisco, CA: ASP), 227

Cordes, J. M., Pidwerbetsky, A., & Lovelace, R. V. E. 1986, ApJ, 310, 737

Cordes, J. M., Wolszczan, A., Dewey, R. J., Blaskiewicz, M., & Stinebring, D. R. 1990, ApJ, 349, 245

Cordes, J. M., & Lazio, T. J. 1991, ApJ, 376, 123

Cordes, J. M. & Rickett, B. J. 1998, ApJ, 507, 846

Cordes, J. M., & Lazio, T. J. W. 2002, arXiv:astro-ph/0207156

Cordes, J. M., Shannon, R. M., & Stinebring, D. R. 2016, ApJ, 817, 16

Demorest, P. B., Ferdman, R. D., Gonzalez, M. E., et al. 2013, ApJ, 762, 94

Dow, J.M., Neilan, R. E., & Rizos, C. 2009, The International GNSS Service in a changing landscape of Global Navigation Satellite Systems, Journal of Geodesy 83:191198

Draine, B. T. 2011, Physics of the Interstellar and Intergalactic Medium by Bruce T. Draine. Princeton University Press, 2011. ISBN: 978-0-691-12214-4,

Faucher-Giguère, C.-A., & Kaspi, V. M. 2006, ApJ, 643, 332

Fonseca, E., Stairs, I. H., & Thorsett, S. E. 2014, ApJ, 787, 82

Foster, R. S., & Cordes, J. M. 1990, ApJ, 364, 123

Freire, P. C., Camilo, F., Lorimer, D. R., et al. 2001, MNRAS, 326, 901

Frisch, P. C. 2007, in ASP Conf. Ser. 365, SINS - Small Ionized and Neutral Structures in the Diffuse Interstellar Medium, ed. M. Haverkorn & W. M. Goss (San Francisco, CA: ASP), 227

Frisch, P. C., Redfield, S., & Slavin, J. D. 2011, ARA&A, 49, 237

Gaensler, B. M., Jones, D. H., & Stappers, B. W. 2002, ApJL, 580, L137

Gibson, S. J. 2007, SINS - Small Ionized and Neutral Structures in the Diffuse Interstellar Medium, 365, 59

Gradshteyn, I. S., Ryzhik, I. M., Jeffrey, A., & Zwillinger, D. 2007, Table of Integrals, Series, and Products, Seventh Edition by I. S. Gradshteyn, I. M. Ryzhik, Alan Jeffrey, and Daniel Zwillinger. Elsevier Academic Press, 2007. ISBN 012-373637-4

Gupta, Y., Rickett, B. J., & Lyne, A. G. 1994, MNRAS, 269, 1035

Hamilton, P. A., Hall, P. J., & Costa, M. E. 1985, MNRAS, 214, 5P

Hobbs, G., Lyne, A. G., Kramer, M., Martin, C. E., & Jordan, C. 2004, MNRAS, 353, 1311

Huang, Z., & Roussel-Dupré, R. 2006, Radio Science, 41, RS6004

Ilyasov, Y. P., Imae, M., Hanado, Y., et al. 2005, Astronomy Letters, 31, 30

Isaacman, R., & Rankin, J. M. 1977, ApJ, 214, 214

Issautier, K., Meyer-Vernet, N., Moncuquet, M., & Hoang, S. 1998, J. Geophys. Res., 103, 1969

Issautier, K., Hoang, S., Moncuquet, M., & Meyer-Vernet, N. 2001, Space Sci. Rev., 97, 105

International Telecommunications Union 2013, Electron Density Models and Data for Transionospheric Radio Propagation, Report ITU-R P.2297-0 (Geneva, Switzerland)

Jacoby, B. A., Hotan, A., Bailes, M., Ord, S., & Kulkarni, S. R. 2005, ApJL, 629, L113

Kaspi, V. M., Taylor, J. H., & Ryba, M. F. 1994, ApJ, 428, 713

Keith, M. J., Coles, W., Shannon, R. M., et al. 2013, MNRAS, 429, 2161

Kurth, W. S., & Gurnett, D. A. 2003, Journal of Geophysical Research (Space Physics), 108, 8027

Lam, M. T., Cordes, J. M., Chatterjee, S., & Dolch, T. 2015, ApJ, 801, 130

Levin, L., McLaughlin, M. A., Jones, G., et al. 2016, ApJ, 818, 166

Liu, K., Keane, E. F., Lee, K. J., et al. 2012, MNRAS, 420, 361

Löhmer, O., Kramer, M., Mitra, D., Lorimer, D. R., & Lyne, A. G. 2001, ApJL, 562, L157

Löhmer, O., Mitra, D., Gupta, Y., Kramer, M., & Ahuja, A. 2004, A&A, 425, 569

Lorimer, D. R., & Kramer, M. 2012, Handbook of Pulsar Astronomy, by D. R. Lorimer , M. Kramer, Cambridge, UK: Cambridge University Press, 2012

Lyne, A., Hobbs, G., Kramer, M., Stairs, I., & Stappers, B. 2010, Science, 329, 408

Maitia, V., Lestrade, J.-F., & Cognard, I. 2003, ApJ, 582, 972

Manchester, R. N., Lyne, A. G., Robinson, C., Bailes, M., & D'Amico, N. 1991, Nature, 352, 219

Manchester, R. N., Hobbs, G. B., Teoh, A., & Hobbs, M. 2005, AJ, 129, 1993

McClure-Griffiths, N. M., Dickey, J. M., Gaensler, B. M., Green, A. J., & Haverkorn, M. 2007, in ASP Conf. Ser. 365, SINS - Small Ionized and Neutral Structures in the Diffuse Interstellar Medium, ed. M. Haverkorn & W. M. Goss (San Francisco, CA: ASP), 65

Nava, B., Coïsson, P., and Radicella, S. M. (2008), Journal of Atmosphere and Solar-Terrestrial Physics, 70(15):1856-1862.

Opher, M., Drake, J. F., Zieger, B., & Gombosi, T. I. 2015, ApJL, 800, L28

Pennucci, T. T., Demorest, P. B., & Ransom, S. M. 2014, ApJ, 790, 93

Petroff, E., Keith, M. J., Johnston, S., van Straten, W., & Shannon, R. M. 2013, MNRAS, 435, 1610

Phillips, J. A., & Wolszczan, A. 1991, ApJL, 382, L27

Provornikova, E., Opher, M., Izmodenov, V. V., Richardson, J. D., & Toth, G. 2014, ApJ, 794, 29

Ramachandran, R., Demorest, P., Backer, D. C., Cognard, I., & Lommen, A. 2006, ApJ, 645, 303

Rankin, J. M., & Roberts, J. A. 1971, in IAU Symp. 46, The Crab Nebula, ed. R. D. Davies & F. Graham-Smith (Dordrecht: Reidel), 114

Rawer, K. Advances in Space Research, 1982, 2, 10, 183

Reardon, D. J., Hobbs, G., Coles, W., et al. 2016, MNRAS, 455, 1751

Rickett, B. J. 1990, ARA&A, 28, 56

Rickett, B. J., Coles, W. A., & Markkanen, J. 2000, ApJ, 533, 304

Sokół, J. M., Bzowski, M., Tokumaru, M., Fujiki, K., & McComas, D. J. 2013, Sol. Phys., 285, 167

Splaver, E. M., Nice, D. J., Stairs, I. H., Lommen, A. N., & Backer, D. C. 2005, ApJ, 620, 405

Stanimirović, S., Heiles, C., & Kanekar, N. 2007, in ASP Conf. Ser. 365, SINS - Small Ionized and Neutral Structures in the Diffuse Interstellar Medium, ed. M. Haverkorn & W. M. Goss (San Francisco, CA: ASP), 22

Stinebring, D. R., Smirnova, T. V., Hankins, T. H., et al. 2000, ApJ, 539, 300

Stinebring, D. 2007, in ASP Conf. Ser. 365, SINS - Small Ionized and Neutral Structures in the Diffuse Interstellar Medium, ed. M. Haverkorn & W. M. Goss (San Francisco, CA: ASP), 254

You, X. P., Hobbs, G., Coles, W. A., et al. 2007, MNRAS, 378, 493

You, X. P., Hobbs, G. B., Coles, W. A., Manchester, R. N., & Han, J. L. 2007, ApJ, 671, 907

CHAPTER 5

THE NANOGRAV NINE-YEAR DATA SET: NOISE BUDGET FOR PULSAR ARRIVAL TIMES ON INTRADAY TIMESCALES

The use of pulsars as astrophysical clocks for gravitational wave experiments demands the highest possible timing precision. Pulse times of arrival (TOAs) are limited by stochastic processes that occur in the pulsar itself, along the line of sight through the interstellar medium, and in the measurement process. On timescales of seconds to hours, the TOA variance exceeds that from template-fitting errors due to additive noise. We assess contributions to the total variance from two additional effects: amplitude and phase jitter intrinsic to single pulses and changes in the interstellar impulse response from scattering. The three effects have different dependencies on time, frequency, and pulse signal-to-noise ratio. We use data on 37 pulsars from the North American Nanohertz Observatory for Gravitational Waves to assess the individual contributions to the overall intraday noise budget for each pulsar. We detect jitter in 22 pulsars and estimate the average value of rms jitter in our pulsars to be $\sim 1\%$ of pulse phase. We examine how jitter evolves as a function of frequency and find evidence for evolution. Finally, we compare our measurements with previous noise parameter estimates and discuss methods to improve gravitational wave detection pipelines.

Published: Lam, M. T., Cordes, J. M., Chatterjee, S., et al. 2016, ApJ, 819, 155

5.1 Introduction

Pulsar timing is used for a variety of unique applications in astrophysics and fundamental physics. These include mass determinations of neutron stars (NSs) and their binary companions to contrain compact object formation mechanisms and equations-of-state (Demorest et al. 2010; Antoniadis 2013); precision tests of general relativity and other theories of gravity (Will 2014); limits on changes in fundamental constants (Lazaridis et al. 2009; Shao & Wex 2013; Zhu et al. 2015); and, especially recently, using arrays of pulsars as detectors of low-frequency (nanohertz) gravitational waves (GWs; e.g., Arzoumanian et al. 2015a, 2016). Improvements in the accuracy of measured arrival times continue to yield benefits in these applications. In this paper, we present a detailed assessment of the time-of-arrival (TOA) noise budget that is applicable to measurements made on relatively short timescales, ranging from single pulse periods to integration times of $10 - 10^4$ s. The work discussed here complements other studies that address noise contributions from variations in the spin rates of neutron stars (e.g., Hobbs et al. 2010; Shannon & Cordes 2010), the frequency dependence of pulse shapes (Pennucci et al. 2014), and from propagation through the interstellar medium (ISM; Armstrong 1984; Blandford et al. 1984; Rickett 1990; Foster & Cordes 1990; Cordes & Shannon 2010).

Pulsar timing relies on a foundation of pulsar phenomena that have been demonstrated over the nearly half century since pulsars were discovered (see Cordes 2013 for a review). Rotational stability, especially for recycled millisecond pulsars (MSPs), allows pulse arrival times to be predicted over long time scales so that small deviations from solar system and astrophysical effects can be determined (Verbiest et al. 2009). Radio emission beams appear to be locked to the crust of

the neutron star and single pulses have phases that vary with respect to a fiducial phase that is also locked to the crust (Kramer 1998; Cordes & Shannon 2010). Averages of N_p single pulses at a specific frequency converge to a stable pulse shape with fractional deviations $\sim 1/\sqrt{N_p}$, as expected for pulse fluctuations that are largely statistically independent (e.g., Dolch et al. 2014). While average pulse shapes do vary with frequency (Kramer et al. 1998), the pulse shapes of radio pulsars, including those objects having two or more stable shapes associated with metastable state of the magnetosphere (i.e., the shapes do not show evolution in time), are stable and show no secular evolution except for a few pulsars in NS-NS binaries where geodetic precession alters the orientation of the beam (Perera et al. 2010) and in the Crab pulsar in which larges changes in pulse shape are seen over a few decades (Lyne et al. 2013). Magnetars also show secular changes in pulse shapes (e.g., Yan et al. 2015).

Intrinsic variations in pulses appear to have stationary statistics (Liu et al. 2011, 2012) in the same way that the average profile formed by averaging a large number of single pulses converges to a shape that appears to be epoch independent (see Craft 1970; Backer et al. 1975; Phillips & Wolszczan 1992; Hassall et al. 2012; Pilia et al. 2015). Consequently, pulse-to-pulse variations can be characterized for each pulsar and can be incorporated into timing studies that require a noise model, such as GW detection. Within a Bayesian framework, the average pulse profile and the pulse variations comprise some of the prior information that underlie modeling of pulsar orbits and GW detection (van Haasteren et al. 2009; Lentati et al. 2014).

In this paper, we focus on timescales smaller than one day and as short as a single spin period. Longer time spans require consideration of other phenomena, including pulsar spin variations and changes in the free-electron content along

the line of sight. Intrinsic pulse variations comprise only one contribution to the arrival time variance on short timescales. A second contribution is the template-fitting error due to additive noise in the measured pulse shape which therefore, unlike single pulse variations, depends on the signal-to-noise ratio of the average pulse (Cordes & Shannon 2010). A third contribution is due to changes in the interstellar impulse response from multipath scattering, which depends strongly on radio frequency (Cordes et al. 1990). The measured impulse response (or pulse broadening function, PBF) at a given time is caused by diffractive interstellar scattering/scintillation (DISS) and it varies as the finite number of constructive intensity maxima ('scintles') appearing in the measurement bandwidth changes. These white-noise contributions to arrival-time errors are referred to as pulse jitter, template-fitting errors, and scintillation noise, respectively. They have distinct correlations with time and frequency that can used to separate them empirically.

In §5.2, we describe the white-noise model. In §6.3, we briefly describe observations from the North American Nanohertz Observatory for Gravitational Waves (NANOGrav) and the data sets used in our analysis. We discuss the analysis of individual objects in §5.4, discuss the collective results in §5.5, and analyze pulse jitter statistics in MSPs in §5.5.1. In §5.6 we compare our results with the parameterized Bayesian noise analysis reported in Arzoumanian et al. (2015b) and discuss the implications for pulsar timing array (PTA) optimization. We summarize our conclusions in §6.7.

5.2 Model for Short-term Timing Variance

We characterize the three white-noise contributions through appropriate analysis of short ($\sim$ 30 min) timing observations. Typical observing epochs are separated by several days or weeks, over which time each of the three contributions is uncorrelated, thus appearing as a white-noise perturbation of arrival times, $\Delta t(\nu, t)$. The total combined variance of the residuals[1] on short timescales is

$$\sigma_{\mathcal{R}}^2 = \sigma_{\rm S/N}^2 + \sigma_{\rm J}^2 + \sigma_{\rm DISS}^2, \tag{5.1}$$

where $\sigma_{\rm S/N}$ is the template-fitting error from a finite pulse signal-to-noise ratio (S/N) primarily due to radiometer noise, $\sigma_{\rm J}$ is the error due to pulse phase and amplitude jitter, and $\sigma_{\rm DISS}$ is due to scintillation noise. Spin noise, measurable over roughly yearly timescales, is negligible over a single epoch, as are changes in dispersion measure (DM $= \int dl\, n_e$, the integral of the electron density over the line of sight) and in the mean shape of the PBF (see Appendix 5.9.1 for more details). For most objects we find $\sigma_{\rm S/N} > \sigma_{\rm J} \gg \sigma_{\rm DISS}$, while a few have $\sigma_{\rm J} \gtrsim \sigma_{\rm S/N}$ at some epochs of high S/N from periods of strong scintillation. Several objects show $\sigma_{\rm DISS}$ as the dominant timing error at particular radio frequencies (see §5.5).

In the following, we will consider the pulse shape model and individually discuss the TOA errors resulting from template fitting of finite S/N pulses, jitter, and scattering.

[1]Residuals $\equiv$ (data$-$model), as discussed in §6.3. For the white-noise errors we consider, there is little difference between the pre-and-post-fit variance. The differences are discussed in §5.4 and Appendix 5.9.1.

5.2.1 Pulse Shapes

Radio pulses are subject to a variety of perturbations as they travel between the pulsar and the Earth. To model the changes in pulse shape and intensity, we will assume that all chromatic delays have been perfectly removed or are negligible over each narrowband channel. These include the dispersive delay from DM, scattering, and frequency-dependent pulse profile evolution. We also assume that the signal polarization has been calibrated perfectly.

Under these assumptions, we model pulse shapes $I(\phi, \nu, t)$ as a function of phase ϕ obtained in short integrations longer than the pulse period, centered on time t and in a sub-band centered on frequency ν. The dominant remaining effect from scattering is the DISS intensity modulation associated with a small number of scintles in a time-frequency resolution cell. Refractive interstellar scintillation (RISS) will also modulate the signal strength but typically varies more slowly than DISS and is broadband (though still chromatic; Stinebring et al. 2000). It is assumed in the following discussion that we can resolve relevant pulse structure and scintillation fluctuations though in reality observing practices may not always allow for scintles to be fully resolved for a given pulsar. We also include a telescope bandpass function $H_{\rm tel}(\nu)$ that lumps together all frequency-dependent gains from the feed antenna to the output of the digital filterbank channel. The pulse shape model is then

$$\begin{aligned} I(\phi,\nu,t) &= H_{\rm tel}(\nu)\,\{g_{\rm RISS}(\nu,t) g_{\rm DISS}(\nu,t)\times \\ &\quad [S_i(\nu) p_i(\phi,\nu,t) * h_{\rm PBF}(\phi,\nu,t)] + n(\phi,\nu,t)\} \end{aligned} \tag{5.2}$$

where $g_{\rm RISS}$ is the RISS modulation, $g_{\rm DISS}$ is the DISS modulation, S_i is the intrinsic spectrum of the pulsar, p_i is the intrinsic pulse shape normalized to unit area, $h_{\rm PBF}$ is the pulse broadening impulse response function, and n is additive radiometer

noise. The intrinsic pulse shape is stochastic and includes contributions from phase and amplitude jitter. We assume that the time-averaged intrinsic pulse shape, $\langle p_i(\phi, \nu, t)\rangle_t$, converges to a pulse template, $U(\phi, \nu)$, that is stable over long timescales. The template shape evolves as a slow function of frequency and the shape of each individual pulse is as well.

5.2.2 Template-Fitting Errors

Template matching yields an rms error in the TOAs that depends on the S/N of the pulse. We assume for now that the data profile is a scaled and shifted version of the template with additive noise, the condition for matched filtering to yield the minimum possible TOA error (Turin 1960; Taylor 1992). This assumption breaks down when considering pulse phase jitter and the finite scintle effect, which change the profile dynamically and are discussed in the following subsections. Let $U(\phi)$ be the pulse template as a function of pulse phase ϕ normalized to unit amplitude, where we have dropped the explicit frequency dependence. The measured pulse intensity $I(\phi)$ at any epoch is then modeled as

$$I(\phi) = S\sigma_{\rm n} U(\phi - \phi_0) + n(\phi), \tag{5.3}$$

where S is the signal-to-noise ratio of the pulse profile (peak to off-pulse rms, written this way for clarity as a variable in equations), $n(\phi)$ is additive noise with rms amplitude $\sigma_{\rm n}$, and ϕ_0 is the TOA. The TOA can be determined either through a cross-correlation analysis with proper interpolation of the cross correlation function to find the maximum or by least-squares fitting of the model template to the data. Mathematically, the two approaches are identical. The peak of the cross-correlation function (CCF) of the template and pulse profile has a S/N related to

S as (J. M. Cordes et al. in preparation)

$$S_{\rm CCF} = S \left[\sum_{i=0}^{N_\phi - 1} U^2(\phi_i) \right]^{1/2} \tag{5.4}$$

and is larger by a factor equal to the square root of the effective number of samples across the pulse if $n(\phi)$ is uncorrelated between phase bins. Template matching will fail when $S_{\rm CCF} \lesssim 1$.

For a pulse template with N_ϕ phase bins, the template-fitting error is (Cordes & Shannon 2010)

$$\sigma_{\rm S/N} = \frac{W_{\rm eff}}{S\sqrt{N_\phi}}, \tag{5.5}$$

where $W_{\rm eff}$ is an effective width[2] given by

$$W_{\rm eff} = \frac{P}{N_\phi^{1/2} \left[\sum_{i=1}^{N_\phi - 1} [U(\phi_i) - U(\phi_{i-1})]^2 \right]^{1/2}} \tag{5.6}$$

for a pulsar with period P. We note that for Eq. 5.5, if profiles are smoothed by n_s samples to increase $S \propto n_S^{1/2}$, the effective number of phase bins $N_\phi \propto n_s^{-1}$, leaving the product $N_\phi^{1/2} S$ invariant. The effective width is useful because it is unique to each pulsar-frequency combination and does not depend on any observational parameters. Therefore, it can be calculated using data obtained from one receiver-backend system and then the TOA error can be calculated for any value of S/N and number of phase bins. Any instrumental change, such as a change in $H_{\rm tel}(\nu)$ over time, that alters the pulse shape will have to be taken into account, however. The expression for $\sigma_{\rm S/N}$ yields the same value as the frequency-domain expression given by Taylor (1992).

[2]This is a different definition than given in Cordes & Shannon (2010) although the rms error expressions are the same.

The Role of DISS

The finite S/N causes the TOA to have a Gaussian error PDF under the assumption of the central limit theorem, $f_{\Delta t}(\Delta t|S) = \mathcal{N}(0, \sigma^2_{\mathrm{S/N}})$. DISS causes the S/N of the pulse to be modulated by a scintillation "gain", g. The gains have an exponential PDF $f_g(g) = \exp(-g)\Theta(g)$ where $\Theta(g)$ is the Heaviside step function (see Appendix B of Cordes & Chernoff 1997). Multiple scintillation maxima in the time-frequency plane will alter the PDF, which, given n_{ISS} scintles, is

$$f_g(g|n_{\mathrm{ISS}}) = \frac{(gn_{\mathrm{ISS}})^{n_{\mathrm{ISS}}}}{g\Gamma(n_{\mathrm{ISS}})} e^{-gn_{\mathrm{ISS}}} \Theta(g), \tag{5.7}$$

where Γ is the gamma function. When pulse shapes and TOAs are calculated, typically $n_{\mathrm{ISS}} \gtrsim 1$ scintles are averaged over the bandwidth and integration time, decreasing the variations in the scintillation gains.

We can transform the PDF of gains to the PDF of the observable pulse S/Ns with a change of variable to $g = S/S_0$, where S_0 is the mean S/N. The PDF is written as

$$f_S(S|n_{\mathrm{ISS}}) = \frac{(Sn_{\mathrm{ISS}}/S_0)^{n_{\mathrm{ISS}}}}{S\Gamma(n_{\mathrm{ISS}})} e^{-Sn_{\mathrm{ISS}}/S_0} \Theta(S). \tag{5.8}$$

As $n_{\mathrm{ISS}} \to \infty$, $f_S(S|n_{\mathrm{ISS}}) \to \delta(S - S_0)$, and the pulse S/N will be constant.

The PDF of the TOA errors is

$$f_{\Delta t}(\Delta t|n_{\mathrm{ISS}}) = \frac{1}{\sigma_{S_0}\sqrt{2\pi}} \left(\sqrt{2}n_{\mathrm{ISS}} \frac{\sigma_{S_0}}{|\Delta t|}\right)^{n_{\mathrm{ISS}}+1} H_{-(n_{\mathrm{ISS}}+1)} \left(\frac{n_{\mathrm{ISS}}\sigma_{S_0}}{\sqrt{2}\,|\Delta t|}\right) \tag{5.9}$$

where σ_{S_0} is the rms from template-fitting errors when no scintillation occurs (S is constant) and $H_n(x)$ is a Hermite polynomial of order n. See Appendix 5.9.2 for more details. In general, the distribution of measured S/N, $f_S(S)$, will be a convolution of several distributions, including the distribution of S/N intrinsic to the pulsar $f_{S_{\mathrm{int}}}(S)$, the DISS modulation $f_{S_{\mathrm{DISS}}}(S)$, and the RISS modulation $f_{S_{\mathrm{RISS}}}(S)$, which will also affect the distribution of TOA errors.

Example of a Single-Component Gaussian Pulse

For a Gaussian pulse having width W (FWHM), the effective width (using Eq. 5.6) is

$$W_{\rm eff} = \frac{(WP)^{1/2}}{(2\pi \ln 2)^{1/4}} \tag{5.10}$$

For this case, the effective width is proportional to the geometric mean of the period and actual pulse width. The TOA error is

$$\sigma_{\rm S/N} = \frac{(WP)^{1/2}}{(2\pi \ln 2)^{1/4} N_\phi^{1/2} S} = \frac{W}{2 (\ln 2)^{1/2} S_{\rm CCF}}, \tag{5.11}$$

where we have used Eq. 5.4 to calculate

$$\begin{aligned} S_{\rm CCF} &= \frac{S}{2} \left(\frac{2\pi}{\ln 2}\right)^{1/4} \left(\frac{W N_\phi}{P}\right)^{1/2} \\ &\approx 5.55 \left[\left(\frac{W/P}{0.02}\right)\left(\frac{N_\phi}{2048}\right)\right]^{1/2} S. \end{aligned} \tag{5.12}$$

The quantity W/P represents the fiducial duty cycle for an MSP. $S_{\rm CCF}$ must be of order unity or larger for template matching to fit appropriately.

5.2.3 Single Pulse Amplitude and Phase Variations ("Jitter")

Single pulses of both canonical pulsars and MSPs have been shown to have stochastic amplitude and phase variations (Cordes & Downs 1985; Cordes et al. 1990; Liu et al. 2012; Shannon & Cordes 2012; Shannon et al. 2014; Dolch et al. 2014). When averaged over $N_{\rm p}$ pulses to form a pulse profile, pulse jitter causes the underlying pulse shape to differ from that of the template, causing an error that is qualitatively different from additive noise. The jitter TOA error is independent of S/N. We

define a dimensionless parameter $k_{\rm J} \equiv \sigma_{\rm J,1}/P$ as the ratio of rms phase variation of individual pulses $\sigma_{\rm J,1} = \sigma_{\rm J}\sqrt{N_{\rm p}}$ (in time units) to the period P of the pulsar. Cordes & Downs (1985) and Cordes & Shannon (2010) define a jitter parameter $f_{\rm J} = \sigma_{\rm J,1}/\sigma_U$, where σ_U is the equivalent rms width of the template. Since pulse profiles often display multiple components with potentially different jitter statistics, using $k_{\rm J}$ to compare the intrinsic jitter between pulsars is less dependent on the properties of the different components.

We note that single-component pulses that show phase variations only will have an rms jitter but those that show amplitude variations only will not display jitter. However, for pulses with multiple components, amplitude variations without phase variations will yield an rms jitter but only if the components overlap in pulse phase. An in-depth analysis on the role of multiple components in jitter will be presented in J. M. Cordes et al. (in preparation). As an example, we consider a single component, Gaussian-shaped pulse with both a Gaussian phase jitter PDF with dimensionless phase variations $k_{\rm J,c}$ and amplitude variations with a modulation index $m_{\rm I,c}$ (defined as rms intensity divided by mean pulse amplitude). We use the subscript 'c' to explicitly denote that the parameters describe the single component, whereas the parameter $k_{\rm J}$ is defined as the overall timing variation of the pulse. The TOA error is then (modified from the form in Cordes & Shannon 2010)

$$\sigma_{\rm J} = \frac{k_{\rm J} P}{\sqrt{N_{\rm p}}} = k_{\rm J,c} P \left(\frac{1 + m_{\rm I,c}^2}{N_{\rm p}} \right)^{1/2} . \tag{5.13}$$

Comparing the TOA errors from additive noise and jitter in Eqs. 5.5 and 5.13, we can define a transition S/N at which the two contributions are equal, $\sigma_{\rm S/N} = \sigma_{\rm J}$. The single-pulse S/N implied by a profile calculated from $N_{\rm p}$ pulses, assuming statistical independence of jitter between pulses, is $S_1 = N_{\rm p}^{-1/2} S$. For a Gaussian-shaped pulse, we find the single-pulse transition S/N, by setting Eqs. 5.11 and 5.13

equal when $N_{\rm p} = 1$, to be

$$\begin{aligned} S_{1,\rm trans} &= k_{\rm J,c}^{-1} \left(\frac{W}{P}\right)^{1/2} (2\pi \ln 2)^{-1/4} \left[N_\phi \left(1 + m_{\rm I,c}^2\right)\right]^{-1/2} \\ &\approx 0.216 \left(\frac{k_{\rm J,c}}{0.007}\right)^{-1} \left(\frac{W/P}{0.02}\right)^{1/2} \left(\frac{N_\phi}{2048}\right)^{-1/2} \left(\frac{1 + m_{\rm I,c}^2}{2}\right)^{-1/2} \end{aligned} \quad (5.14)$$

and the corresponding S/N of the CCF is

$$S_{\rm CCF1,trans} \approx 1.20 \left(\frac{k_{\rm J,c}}{0.007}\right)^{-1} \left(\frac{W/P}{0.02}\right) \left(\frac{1 + m_{\rm I,c}^2}{2}\right)^{-1/2}, \quad (5.15)$$

where we set the fiducial $k_{\rm J} = k_{\rm J,c}(1 + m_{\rm I,c}^2)^{1/2} = 0.01$ based on our analysis in §5.5.1. When the single-pulse cross-correlation S/N is greater than about unity, the jitter error becomes larger than the template-fitting error.

The same pulsar-intrinsic effects that cause frequency-dependent template evolution will cause jitter to be a slow function of frequency as well. Over an observing band, we might approximate jitter as being frequency-independent (see Shannon et al. 2014 for evidence of decorrelation over widely-separated frequencies) but frequency-dependence of the pulse template can be measurable (Pennucci et al. 2014; Dolch et al. 2014). We therefore note that jitter will be strongly correlated in frequency but not in time. DISS has a correlation bandwidth and timescale that can vary widely from pulsar to pulsar and between epochs for the same pulsar. Template-fitting errors are uncorrelated between time samples and frequency sub-bands.

5.2.4 Scintillation Timing Noise: Finite Scintle Effect

The time-frequency plane is made up of independent intensity fluctuations called scintles that are 100% modulated and have characteristic time and frequency scales

$\Delta t_{\rm d}$ and $\Delta\nu_{\rm d}$, respectively. The scintillation structure is related to the temporal broadening of pulses, resulting in a time delay (Cordes et al. 1990; Cordes & Shannon 2010). Since a finite number of scintles will occupy the time-frequency plane, the instantaneous PBF will be different from the ensemble average shape. This produces an error that is statistically independent between two epochs and is therefore white noise in time.

The number of scintles for an observation of duration T and bandwidth B is approximately

$$n_{\rm ISS} \approx \left(1 + \eta_t \frac{T}{\Delta t_{\rm d}}\right)\left(1 + \eta_\nu \frac{B}{\Delta\nu_{\rm d}}\right). \tag{5.16}$$

The filling factors η_t,η_ν are less than unity and are in the range of 0.1 to 0.3 (Cordes & Shannon 2010; Levin et al. 2016), depending on the definitions of the characteristic timescale and bandwidth.

When $n_{\rm ISS}$ is large, the TOA error is

$$\sigma_{\rm DISS} \approx \frac{\tau_{\rm d}}{\sqrt{n_{\rm ISS}}} \tag{5.17}$$

where $\tau_{\rm d} = C_1/(2\pi\Delta\nu_{\rm d})$ is the scattering timescale with C_1 a coefficient of order unity. For a thin scattering screen with uniscale irregularities, $C_1 = 1$ but for a Kolmogorov screen, $C_1 = 0.96$. For uniform, thick media, $C_1 = 1.53$ and 1.16, respectively, for uniscale and Kolmogorov media (Cordes & Rickett 1998). When there is only one scintle or a partial scintle across the band, the TOA error is approximately $\tau_{\rm d}$, or some fraction of it.

Table 5.1. Errors in Initial Timing Model

Effect	Typical Δt	Appendix Section	Comments
Pulse profile smearing			
spin period error	$\lesssim$10 ps	A.1.1	systematic
binary parameter errors	$\lesssim$10 ns	A.1.2	systematic
DM variations	$\lesssim$400 ns	A.1.3	stochastic
polarization calibration gain errors	$\lesssim$1 μs	A.1.4	stochastic
Deviations from the polynomial fit			
binary orbit parameter errors	$\lesssim$10 ps	A.2.1	systematic
ionospheric DM variations	$\lesssim$1 ns	A.2.2	stochastic
cross-coupling errors	?	A.2.3	systematic, highly pulsar-dependent
rotation measure (RM) variations	$\lesssim$1 ps	A.2.4	stochastic
spin noise	$\lesssim$0.1 fs	A.2.5	stochastic
stochastic GW background	$\lesssim$1 fs	A.2.6	stochastic

5.3 Observational Data

5.3.1 NANOGrav Timing Observations

We used pulse profile data from the NANOGrav nine-year data set described in Arzoumanian et al. (2015b, hereafter NG9) for our analysis. NG9 contains multi-frequency pulse profiles of thirty-seven MSPs observed at the Green Bank Telescope (GBT) and Arecibo Observatory (AO). Two generations of backends were used, the GASP/ASP backend earlier, processing up to 64 MHz (Demorest 2007; Demorest et al. 2013), and the GUPPI/PUPPI backends later, processing 100, 200, or 800 MHz of bandwidth (DuPlain et al. 2008; Ford et al. 2010). The larger bandwidth of GUPPI and PUPPI yields an increase in S/N from increased averaging of radiometer noise combined with a higher probability for large scintillation maxima

(Pennucci et al. 2014). Because we wish to maintain homogeneity of the inferred parameters of our pulsars (e.g., consistent scintillation statistics), we analyze pulses observed with GUPPI/PUPPI only.

Each pulsar was observed at each epoch with at least two receivers. At GBT, the 820 and 1400 MHz bands were used, and at AO, the 430 and 1400 MHz or 1400 and 2300 MHz bands were used. PSRs B1937+21 and J1713+0747 were observed at both AO and GBT and we analyze both observatories' data sets independently to check for consistency across varying S/Ns. In addition, PSR J2317+1439 contained data from the 327 MHz band in addition to the 430 and 1400 MHz bands. We also used processed 430 MHz data available for PSRs B1937+21 and J2017+0603 though they were not included in NG9.

Pulse profiles were computed in real time by averaging together single pulses according to an initial timing model that includes the pulsar's spin kinematics and the orbital motions of the Earth and, if needed, the pulsar binary orbit. Model parameters were obtained by fitting to earlier observations. Raw data profiles from GUPPI/PUPPI were folded and de-dispersed in ~ 10 s and ~ 15 s subintegrations at AO and GBT, respectively, and every eight subintegrations were averaged together to reduce data volume through the NG9 pipeline. Some Arecibo 1400 MHz observations were initially recorded in ~ 1 s subintegrations to aid in radio frequency interference (RFI) excision and then combined to form the ~ 10 s "raw" subintegrations. Observations for a given epoch typically spanned about 0.5 hr. All profiles were divided into 2048 phase bins.

Arzoumanian et al. (2015b) describe the polarization calibration algorithm, as well as the RFI excision methods, for creating calibrated data profiles using

the PSRCHIVE[3] software package (Hotan et al. 2004; van Straten et al. 2012). A broadband noise source was locally injected into the two polarization signal paths at each observatory prior to every pulsar observation and is recorded by the backend systems. Both differential gain and phase between the two hands of polarization were calibrated using the correlated noise source observation. The noise source power in each hand of polarization was not assumed to be equal and was measured separately roughly once per month per telescope per frequency by observing the noise source after pointing on and off a bright, unpolarized quasar. After balancing the gains of the two orthogonal polarizations, the intensity profiles were produced by summing the two polarization profiles. Future papers will discuss the complete polarization and flux calibration solutions at AO and GBT. Frequency channels known to consistently contain RFI signals were removed first. If the off-pulse variation in a 20-channel wide frequency window was four times the median variation value, those channels were also removed.

We took the calibrated profiles with ~ 80 s (AO) and ~ 120 s (GBT) subintegration lengths and average the profiles together into sub-bands of 50 MHz resolution. Frequency-averaging builds S/N for each pulse to avoid mis-estimation of the TOA in the low-S/N limit (see Appendix B of Arzoumanian et al. 2015b). We note that frequency-dependent profile shape changes across the entire observing band can be significant for some sources over the full band (e.g., see Pennucci et al. 2014) but are small over a 50 MHz channel.

We implemented a Fourier-domain TOA estimation algorithm (Taylor 1992) that determines the amplitude $S\sigma_n$, the TOA, and template-fitting uncertainty of an intensity profile $I(\phi, \nu, t)$. Template shapes $U(\phi)$ are determined from de-

[3] `http://psrchive.sourceforge.net`, accessed via scripts available at `https://github.com/demorest/nanopipe`

noised average profiles, smoothed by thresholding the coefficients of a wavelet decomposition of the pulse shape. One template is generated from all data for each pulsar, backend, and frequency band combination[4]. Timing offsets from profile frequency evolution are not accounted for here but will be accounted for in the analysis in the following section. We determined the off-pulse window for each pulse template used to measure σ_n by finding the rolling eighth (256 out of 2048 phase bins) of phase that has the smallest integrated intensity. The pulse baseline is defined as the mean of the off-pulse region and the noise σ_n is the rms amplitude of the region. Once we knew the best-fit amplitude and rms noise, we then calculated the associated S/N for each pulse. Our code is freely available in the PyPulse software package[5].

5.3.2 Scintillation Parameters

Scintillation bandwidths and timescales were taken or estimated (using the scaling relations as a function of observing frequency in Cordes & Lazio 2002) from Keith et al. (2013) and Levin et al. (2016) and references therein. We used these measurements to derive values of $\sigma_{\rm DISS}$ given by Eq. 5.17 assuming $\eta_\nu = \eta_t = 0.2$, $C_1 = 1$ (Lambert & Rickett 1999; Cordes & Shannon 2010; Levin et al. 2016), and integration time/bandwidth values equal to that of the profiles from each telescope. When scintillation parameters were not available, we estimated all other values using the NE2001 electron density model (Cordes & Lazio 2002).

[4]Templates are available in the NG9 data release at `https://data.nanograv.org`
[5]https://github.com/mtlam/PyPulse

5.4 Single Pulsar Analysis

We are interested in quantifying noise on intraday timescales. We therefore independently analyze individual NANOGrav observations, typically of duration 30 min or less. During an observation, the incoming data were folded using a precomputed model pulsar ephemeris. We assumed that this ephemeris is sufficiently accurate that there is very little drift in pulse arrival times over an observation. We calculated pulse phases within an observation, "initial timing residuals" $\delta t(\nu, t)$, using the Fourier-domain estimation algorithm of Taylor (1992). We assumed that the initial timing model used for folding will yield polynomial expansions of phase and spin period that represent the state of the Earth-pulsar line of sight at a given epoch to high accuracy. We also assumed that the initial timing model is accurate such that pulse smearing will be negligible for our subintegration lengths. We then calculated "short-term" residuals $\mathcal{R}(\nu, t)$ over a single observation by fitting a polynomial model over all $\delta t(\nu, t)$ observed that includes a constant offset for TOAs from each frequency channel and a parabolic fit in time common to all TOAs. The initial and short-term models can be written as

$$\delta t(\nu, t) = K(\nu) + at + bt^2 + n(\nu, t) \tag{5.18}$$

$$\mathcal{R}(\nu, t) \equiv \hat{n}(\nu, t) = \delta t(\nu, t) - \left[\hat{K}(\nu) + \hat{a}t + \hat{b}t^2\right]. \tag{5.19}$$

Here, a and b are frequency-independent coefficients, $n(\nu, t)$ is additive noise in both time and frequency that includes the three white-noise components in Eq. 5.1, and $K(\nu)$ represents a constant offset that varies with frequency, resulting from pulse profile evolution or epoch-dependent dispersion and scattering. Variables with carets denote estimated quantities. Thus, $\mathcal{R}(\nu, t)$ is the estimated additive noise, calculated by subtracting the estimated model parameters from the TOAs. We assumed that subtraction of the offsets removes any frequency-dependence

between sub-bands. The variance removed by the fit for a, b, and $K(\nu)$ to obtain $\mathcal{R}(\nu, t)$ will be small for white-noise components that are uncorrelated in time.

Differences between the initial timing model and the short-term timing model for a given epoch can result from a number of possible effects that we account for with the quadratic fit in Eq. 5.19. Table 5.1 lists the effects and their approximate amplitudes. We provide details of the estimates in Appendix 5.9.1.

5.4.1 An In-Depth Analysis of Jitter and Frequency-dependent Jitter Evolution in PSR J1713+0747

PSR J1713+0747 is not only one of the best-timed pulsars but it is the pulsar with the highest S/N pulses in our entire data set and is thus most sensitive to jitter error. The S/N peaked at $S \approx 2000$ at 1400 MHz for one of two observations on MJD 56380. Figure 5.1 shows the residuals of sub-bands for that observation in panel (a); strong correlation between sub-bands is evident and indicative of pulse jitter (Cordes & Shannon 2010; Shannon et al. 2014). Along with the $\sim$ 80 s data, we processed the $\sim$ 10 s subintegration raw data from this observation to demonstrate the lack of temporal correlation in the residuals, shown in panel (b), as expected when jitter noise becomes dominant. The results in Figure 5.1 are presented with the 80 s subintegrations displayed in the left panels and the 10 s subintegrations on the right.

Within each subintegration, we typically saw a monotonic increase or decrease in the residual with frequency, which is most evident in the second-to-last subintegration of the low-time-resolution residuals, highlighted with a black arrow in panel (a). Each line in panels (c) and (d) shows the residuals as a function of

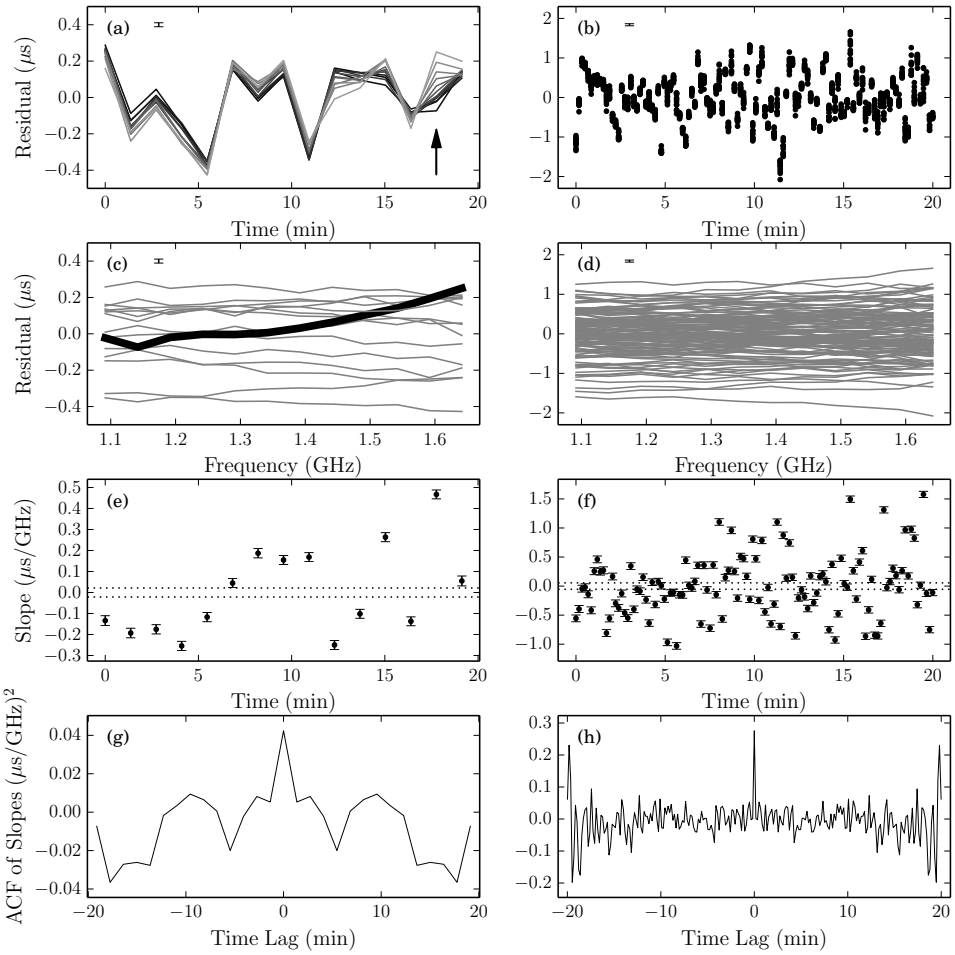

Figure 5.1: Analysis of jitter in residuals for the highest S/N epoch for PSR J1713+0747. The panels on the left side show the analysis for the ~ 80 s subintegration data while the panels on the right side are for the ~ 10 s subintegration data. Panel (a): Low-time-resolution residuals as a function of time. Each frequency channel is shaded differently, with darker lines indicating lower frequencies. The arrow indicates the subintegration with the greatest change in residual versus frequency. Typical TOA errors are shown in the top left of panels (a)-(d). Panel (b): High-time-resolution residuals as a function of time, where we have plotted residuals as points for clarity. Panels (c),(d): Residuals as a function of frequency, where each line represents one subintegration. The thick, black line in panel (c) corresponds to the subintegration highlighted with the arrow in panel (a). Panels (e),(f): Slopes of fitted lines to the residuals versus frequencies for each subintegration. The horizontal, dotted lines indicate the median fitting error. Panels (g),(h): Autocorrelation functions (ACFs) of the time series in panels (e) and (f), respectively.

frequency for each subintegration. The subintegration highlighted with the arrow in panel (a) is marked with a thick, black line in panel (c) and demonstrates the trend increasing with frequency. We fit the slope of each line and plot the results in panels (e) and (f). The slope values show a deviation much larger than the median of the fitting errors, denoted by the dotted, horizontal lines. While the points in the time series in panel (e) appear correlated, they do not in panel (f), suggesting the slope changes are uncorrelated. The autocorrelation functions (ACFs) of the time series in panels (e) and (f) are shown in panels (g) and (h), respectively, and the flatness at non-zero lags demonstrates that the slope changes are consistent with uncorrelated, white noise in time.

The roughly monotonic slope of the residuals with frequency in each subintegration indicates that there is a systematic variation of the pulse shape for each subintegration (and thus TOAs) versus frequency, indicative of frequency-dependent jitter evolution, which is distinctly different from frequency-dependent pulse profile evolution, though related. These slopes are uncorrelated between subintegrations, indicating that longer averages of larger numbers of pulses will show less variation with frequency. Nonetheless, it is known that the average pulse shape of PSR J1714+0747 varies systematically with frequency (Arzoumanian et al. 2015b; Dolch et al. 2014) and those must reflect the variations occurring on the single-pulse level. For the high-time-resolution data, the rms slope is ≈ 0.53 μs/GHz.

5.4.2 Distributions of Residuals from Jitter and Scintillation

We modeled the variance in the residuals separately for each pulsar/backend/frequency band combination using Eq. 5.1. While all three terms scale as $N_{\rm p}^{-1}$, only the template-fitting term depends on the S/N of the pulse profile whereas the jitter and the DISS terms do not. Therefore, we used a one-parameter model for the variance as a function of S/N,

$$\sigma^2_{\mathcal{R}}(S) = \sigma^2_{\rm S/N}(S) + \sigma^2_{\rm C} = \left(\frac{W_{\rm eff}}{S\sqrt{N_\phi}}\right)^2 + \sigma^2_{\rm C}. \tag{5.20}$$

where $\sigma^2_{\rm C} = \sigma^2_{\rm J} + \sigma^2_{\rm DISS}$, as implied by Eq. 5.1, is the variance that is constant in S/N. At high S/N, $\sigma_{\rm S/N} \to 0$ and $\sigma^2_{\rm C}$ becomes the dominant term. We took the scintillation parameters to be constant for all epochs so that $\sigma_{\rm DISS}$ is fixed, though measurements of these parameters indicate small variations (factor of $\lesssim 2$) over many years, with some pulsar showing larger fluctuations (e.g., Coles et al. 2015).

The observed S/N PDF depends on the intrinsic pulse amplitude distribution, on modulations from DISS and RISS, and on variations of the system equivalent flux density (SEFD) of the receiver. We assumed that the average *intrinsic* flux density of the pulsar and SEFD were constant over all times. Therefore, the mean S/N, S_0, is constant for our many-period pulse averages (large $N_{\rm p}$), i.e., $f_{S_0}(S) = \delta(S - S_0)$, assuming that changes in the S/N are due solely to modulation from DISS. RISS has been shown to change the observed flux density by a factor of $\lesssim 2$ on the timescale of 10s of days (Stinebring et al. 2000). Since we observed S/N variations spanning over an order of magnitude from the mean in some cases, we ignored the contribution to the S/N PDF from RISS.

We assumed that residuals at a given S/N follow a Gaussian distribution

$$f_{\mathcal{R}|S}(\mathcal{R}|S,\sigma_{\rm C}) = \frac{1}{\sqrt{2\pi\sigma_{\mathcal{R}}^2}} e^{-\mathcal{R}^2/(2\sigma_{\mathcal{R}}^2)}, \tag{5.21}$$

where again $\sigma_{\mathcal{R}}$ is a function of both S and $\sigma_{\rm C}$ (Eq. 5.20). The normality assumption is a good approximation due to the fact that while residuals must lie within one cycle of pulse phase, $|\mathcal{R}| \lesssim 0.001P$ and deviation from a Gaussian distribution is negligible. We removed all residuals with $S < 10^{0.5}$ (≈ 3) to avoid contamination by low-significance noise being fit by the template matched filtering (see Appendix B of Arzoumanian et al. 2015b), which excluded five pulsar/backend/frequency band residual sets and two pulsars from our analysis entirely. We excised evident RFI beyond the methods described in §6.3 by inspection of the residuals and the corresponding pulse profiles.

We performed a maximum likelihood (ML) analysis over the residuals $\{S_i, R_i\}$ given the three parameters S_0, $n_{\rm ISS}$, and $\sigma_{\rm C}$. To include our cut in S/N, we included a parameter $S_{\rm min}$ and determined the factor that properly normalizes the distribution in S. The normalized distribution is

$$f_S(S|S_0, n_{\rm ISS}, S_{\rm min}) = f_s(S|S_0, n_{\rm ISS})\Theta(S - S_{\rm min})\frac{\Gamma(n_{\rm ISS})}{\Gamma(n_{\rm ISS}, n_{\rm ISS}S_{\rm min}/S_0)}, \tag{5.22}$$

where $\Gamma(\alpha, x)$ is the incomplete Gamma function and $\Gamma(\alpha, 0) = \Gamma(\alpha)$ (see Eqs. 3.381.3-4 of Gradshteyn et al. 2007, for the relevant integrals).

The likelihood function can be calculated by combining Eqs. 5.7, 5.21, and 5.22,

$$\begin{aligned}\mathcal{L}(S_0, n_{\rm ISS}, \sigma_{\rm C}|\{S_i, R_i\}, S_{\rm min}) &= \prod_i f_{\mathcal{R},S}(\mathcal{R}_i, S_i|S_0, n_{\rm ISS}, \sigma_{\rm C}, S_{\rm min}) \\ &= \prod_i f_{\mathcal{R}|S}(\mathcal{R}_i|S_i, \sigma_{\rm C}) f_S(S_i|S_0, n_{\rm ISS}, S_{\rm min}),\end{aligned} \tag{5.23}$$

where i labels the individual residuals. We performed a grid search in the three-dimensional parameter space to estimate the values and uncertainties on the three

model parameters. The likelihood function can be expressed as the product of individual likelihoods

$$\mathcal{L}(S_0, n_{\rm ISS}, \sigma_{\rm C}|\mathcal{R}, S, S_{\rm min}) = \mathcal{L}(\sigma_{\rm C}|\mathcal{R}, S, S_{\rm min})\mathcal{L}(S_0, n_{\rm ISS}|S, S_{\rm min}), \tag{5.24}$$

so that we could perform the grid search in $\sigma_{\rm C}$ independently from the search in $S_0, n_{\rm ISS}$ space. We limited our search in $n_{\rm ISS}$ with a lower bound of 1 so that the minimum number of degrees of freedom across both the time and frequency dimensions is 2 (Cordes & Chernoff 1997), or that each pulse must come from at least one ray path through the ISM. An F-test was used to determine the significance of $\sigma_{\rm C}$ with a significance value of 0.05 (i.e., 2σ significant). If not, we computed the 95% upper limit on $\sigma_{\rm C}$.

Figure 5.2 shows the results for one of NANOGrav's best-timed pulsars, PSR J1713+0747 observed at 1400 MHz at AO. The top panel shows the residuals $\mathcal{R}_i(S_i)$ with the $\pm 3\sigma_{\mathcal{R}}$ ranges plotted in the blue lines. At higher S/N, the rms of the residuals asymptotes to a constant value, $\sigma_{\rm C}$, represented by the constant width scatter of points, and is indicative of jitter and scintillation noise and the S/N regime over which they dominate the template-fitting error. A histogram of the residuals R_i are shown at right with bins $\Delta\mathcal{R} = 0.1$ μs and a histogram of S_i with logarithmic bins of $\Delta \log_{10} S = 0.0625$ is shown below with Poisson uncertainties shown by the error bars. We plot $S f_S(S|S_0, n_{\rm ISS}, S_{\rm min})$ in the middle panel to properly compare the scaled PDF to the logarithmically binned histogram, with S_0 and $n_{\rm ISS}$ determined in the ML analysis.

The bottom panel shows the rms residual for the same logarithmic binning of the data. The dashed line shows the predicted rms from template-fitting error only given by Eq. 5.5. We emphasize that the dashed line is not a fit to the data points in this plot. We see agreement between the dashed line and the points at low S/N

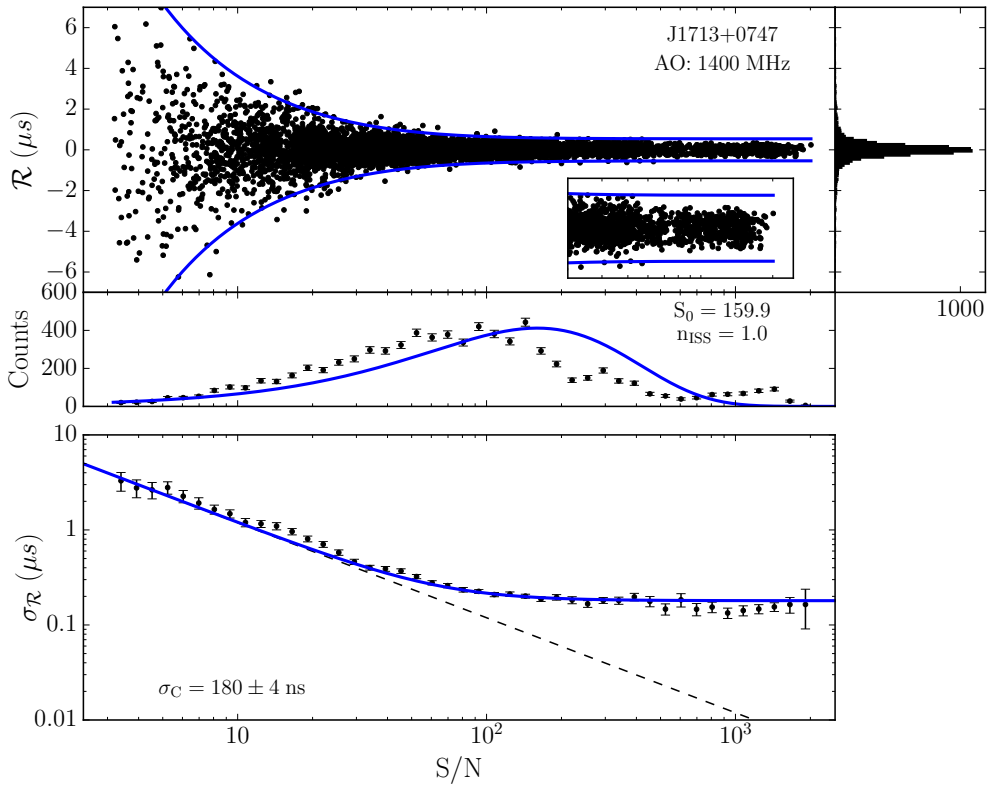

Figure 5.2: Analysis of residuals for PSR J1713+0747 observed at 1400 MHz with AO, containing the highest S/N residuals in our sample. Top: Residuals $\mathcal{R}$ vs S/N. The solid lines (blue) show the $\pm 3\sigma_{\mathcal{R}}(S)$ ranges from the maximum likelihood analysis. The inset shows the residuals for S/N greater than 70% of the maximum. Histograms of $\mathcal{R}$ (right panel) and S/N (middle panel) are shown, with the solid (blue) lines showing the predicted histogram given the most-likely estimates for S_0 and $n_{\rm ISS}$. The error bars show the standard Poisson uncertainties for each bin only. Bottom: rms residual $\sigma_{\mathcal{R}}$ in bins of S/N. The dashed line is the predicted TOA template-fitting error (not a fit to the points on the graph) based on the template shape while the solid line shows the estimated $\sigma_{\mathcal{R}}(S)$ from Eq. 5.20 that includes a S/N-independent term.

for most pulsars, which indicates that Eq. 5.5 represents the template-fitting noise well. Deviation from the line can be explained by other systematic effects that can increase the variance, such as remaining RFI in the data. The blue line shows the best estimate $\sigma_{\mathcal{R}}(S)$ from the ML analysis. We note that the ML analysis is less susceptible to parameter mis-estimation from the effects of RFI in the data over

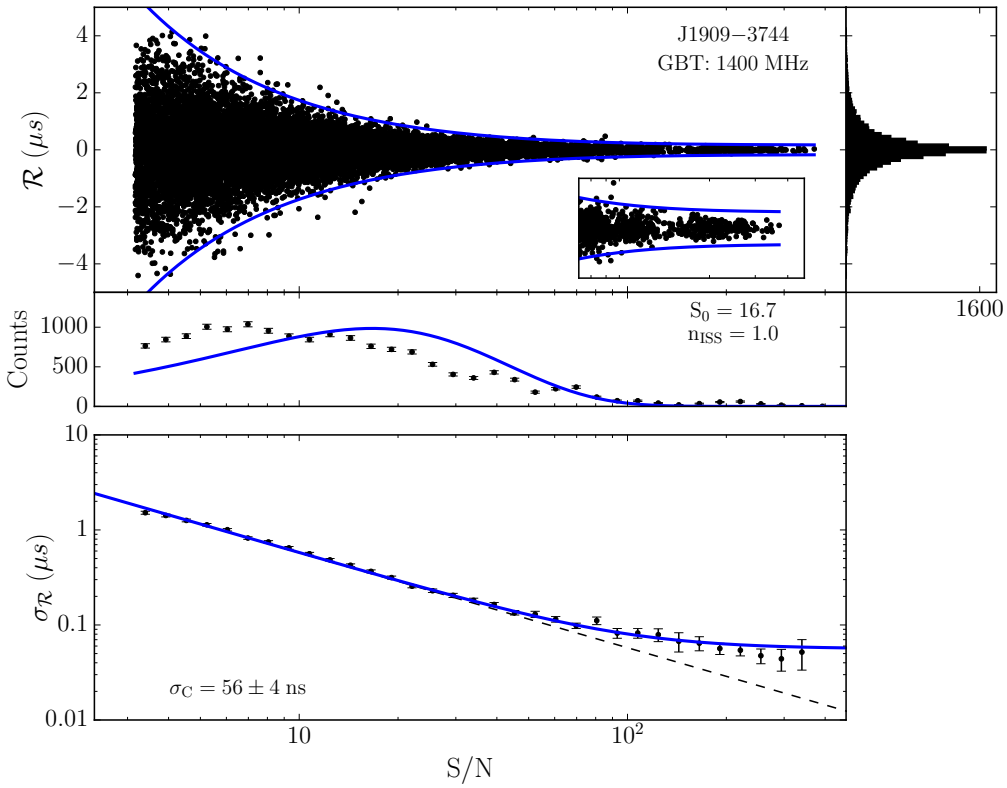

Figure 5.3: Analysis of residuals for PSR J1909−3744 observed at 1400 MHz with GBT. See the Figure 5.2 caption for more details.

a fit of Eq. 5.20 to the rms residual points because the ML analysis fits all of the data simultaneously.

Figures 5.3-5.6 show the same ML analysis for four other pulsars observed at 1400 MHz. While $\sigma_{\mathcal{R}}$ matches the data for PSR J1909−3744, the S/N histogram does not match well with the data and the PDF of $n_{\rm ISS}$ in the ML analysis peaks at the edge of the sampling space ($n_{\rm ISS} = 1$), expected since $\Delta\nu_{\rm d} = 39 \pm 14.7$ MHz and $\Delta t_{\rm d} = 2258$ s for the pulsar at a reference frequency of 1500 MHz (Keith et al. 2013; Levin et al. 2016), of order the pulse channel bandwidth and typical total observation length. We see a similar result with PSR J2317+1439 though

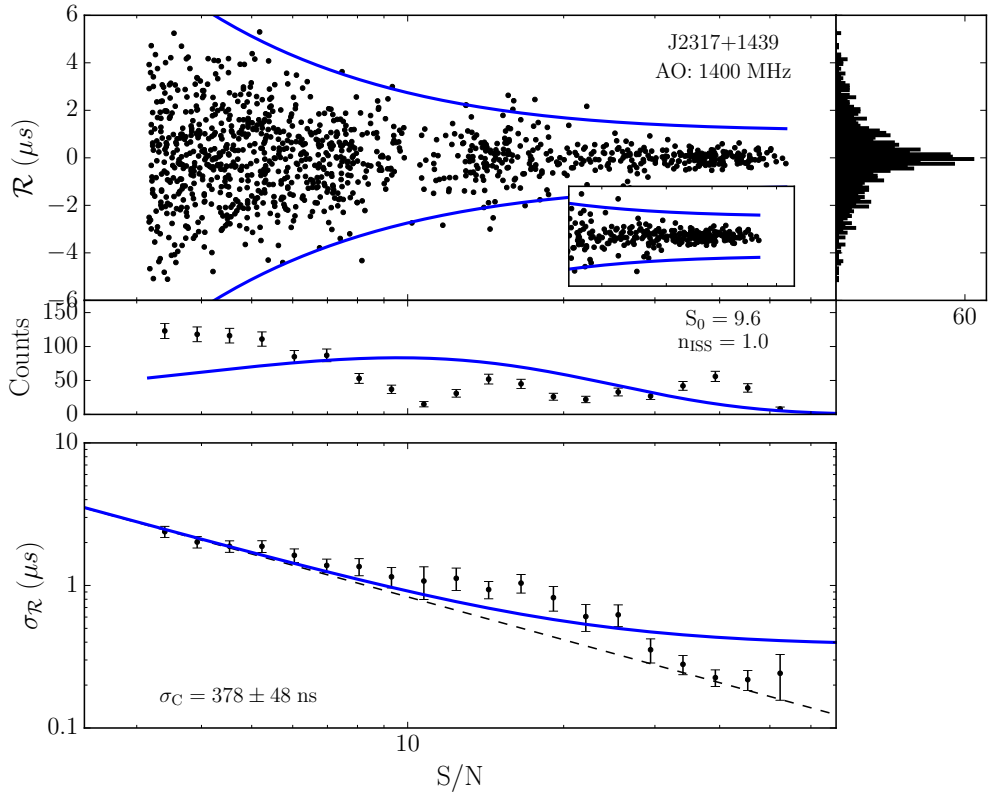

Figure 5.4: Analysis of residuals for PSR J2317+1439 observed at 1400 MHz with AO. See the Figure 5.2 caption for more details.

sparseness in the S/N histogram is a result of increased RFI excision for the pulsar. For PSR B1937+21, the S/N histogram is well described by the result of the ML analysis. The remaining low S/N residuals (S/N $\sim$ 10) are spurious noise spikes that pass our S/N cut criterion and lie close to the main pulse in phase. The narrowing of residuals at large S/N is not understood and may require further investigation of this pulsar. Lastly, we show the analysis for PSR J1918−0642 as a typical pulsar with an upper limit on σ_C.

To measure jitter values, we estimated σ_{DISS} as described in the previous section for 50 MHz sub-bands and subintegrations of length t_{sub} and then solved for

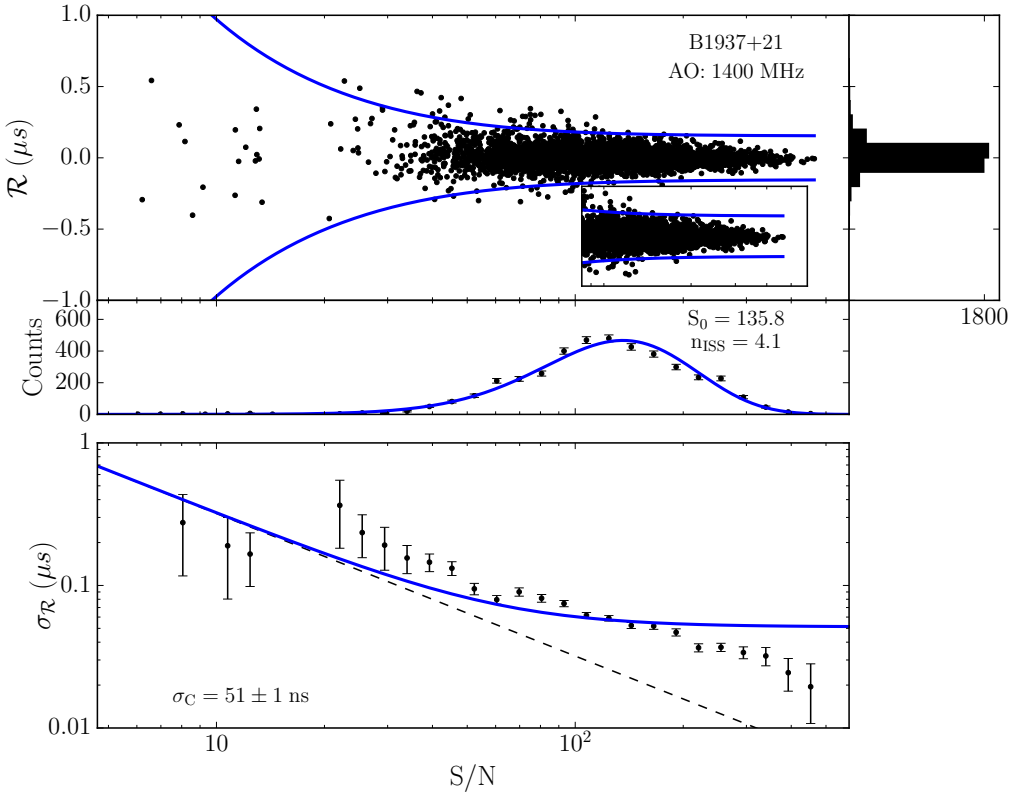

Figure 5.5: Analysis of residuals for PSR B1937+21 observed at 1400 MHz with AO. See the Figure 5.2 caption for more details.

σ_J given our measured σ_C (see Eq. 5.20). In several cases, the estimates of the scintillation noise from Eq. 5.17 were larger than the σ_C estimated from the ML analysis, which is supposed to encapsulate all possible variance at high S/N. We employed a correlation analysis described in the next sub-section to separate the jitter and scintillation noise values for PSR B1937+21 at 1400 MHz, the only pulsar where the estimated σ_{DISS} is larger than σ_C and the S/N of the residuals is high enough to perform such an analysis.

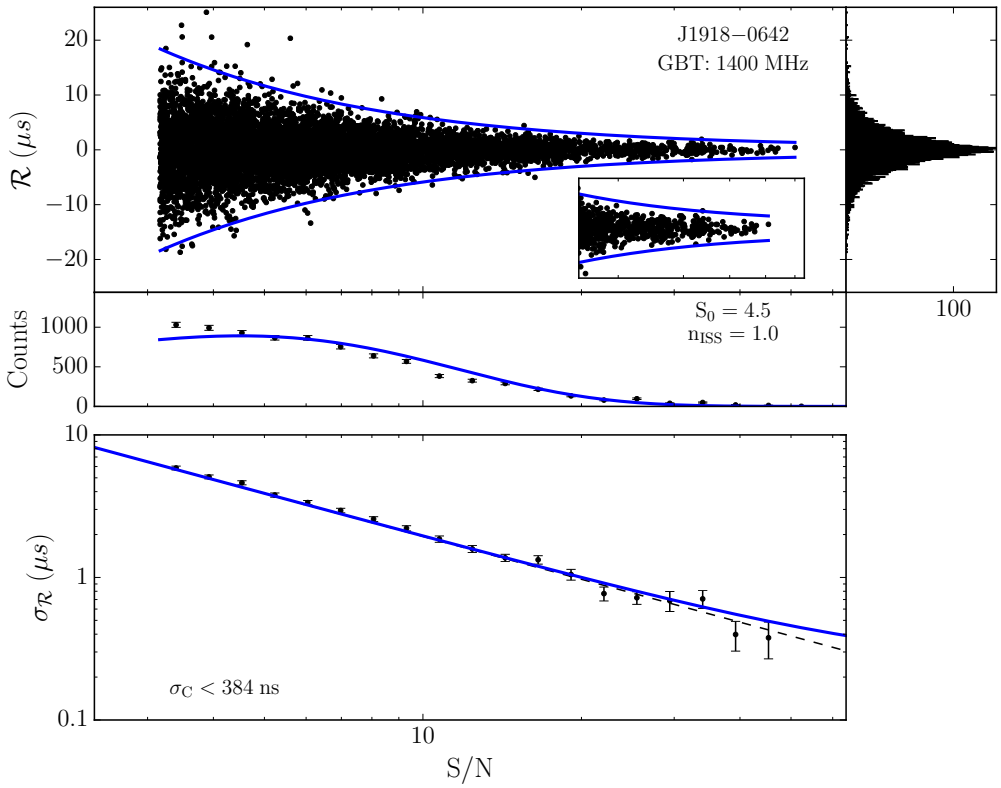

Figure 5.6: Analysis of residuals for PSR J1918−0642 observed at 1400 MHz with GBT. See the Figure 5.2 caption for more details. The 95% upper limit on σ_C is shown in the bottom left of the bottom panel, with the corresponding $\sigma_{\mathcal{R}}$ in blue.

5.4.3 Cross-Correlation Analysis Between Frequencies

Jitter causes simultaneously measured residuals at different frequencies to be correlated, which allows us to distinguish jitter noise from template-fitting noise. If the sub-band bandwidth is $\gtrsim \Delta\nu_d$, the residuals will not be correlated in frequency by DISS and we can distinguish jitter noise from scintillation noise as well. PSR B1937+21 has $\Delta\nu_d = 2.8 \pm 1.3$ MHz and $\Delta t_d = 327$ s at a reference frequency of 1500 MHz (Keith et al. 2013; Levin et al. 2016) and therefore residuals with 50 MHz of bandwidth will be correlated in frequency due to jitter only. We find $n_{ISS} \approx 4$ for PSR B1937+21 observed at 1400 MHz at AO with 50 MHz sub-bands

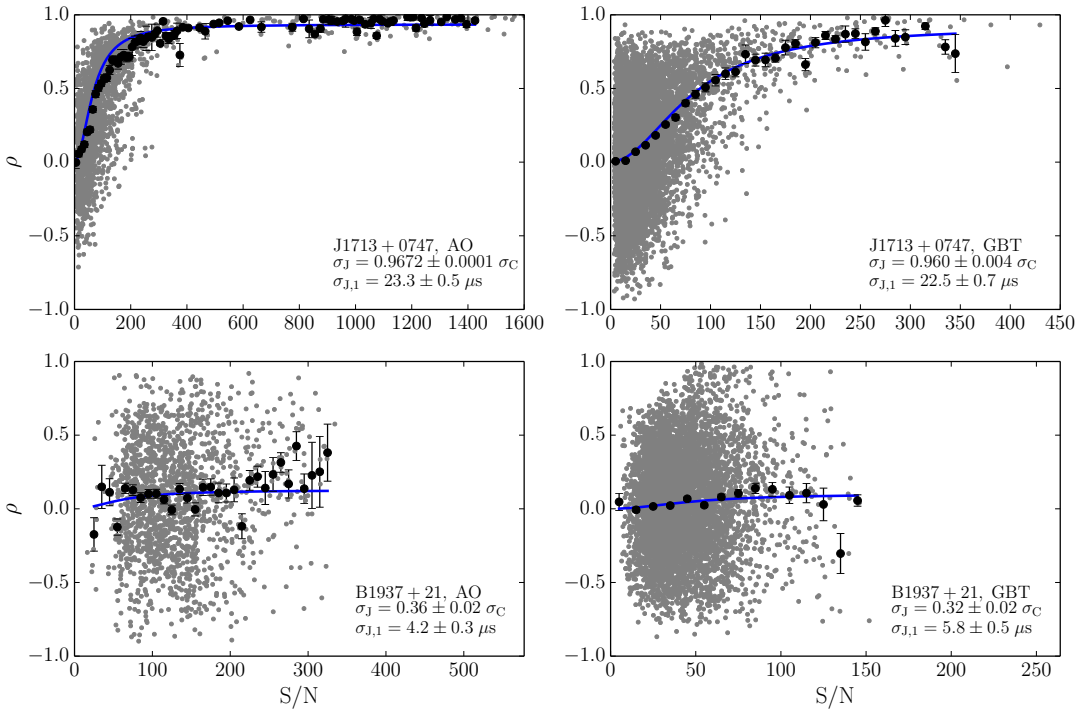

Figure 5.7: Correlation analysis for PSRs J1713+0747 (top) and B1937+21 (bottom) at AO (left) and GBT (right) for 1400 MHz band residuals. The gray points mark the correlation coefficient ρ of two different sub-bands of residuals on a given epoch as a function of the geometric average of the mean S/N of the pulse profiles for those sub-bands as $(\langle S_1 \rangle \langle S_2 \rangle)^{1/2}$. We show the median ρ in bins of S/N in black. The blue line marks the best-fit $\rho(S)$ to the black points.

and ~ 80 s subintegrations. Therefore, the finite scintle effect is prominent and we expect scintillation noise to be large for this pulsar.

We let the total residual be the sum of the fluctuations from the three contributions to white noise,

$$\mathcal{R}(\nu, t) = \mathcal{R}_{\rm S/N}(\nu, t) + \mathcal{R}_{\rm J}(\nu, t) + \mathcal{R}_{\rm DISS}(\nu, t), \tag{5.25}$$

where the subscripts denote the specific contribution. The cross-correlation coefficient between residuals from two sub-bands ν_i and ν_j is

$$\langle \mathcal{R}(\nu_i, t) \mathcal{R}(\nu_j, t) \rangle = \sigma_{\rm J}^2, \tag{5.26}$$

where we assumed that the scintles are statistically independent between sub-bands for PSR B1937+21 and therefore do not correlate. The autocorrelation coefficient $\langle \mathcal{R}(\nu_i, t)^2 \rangle$ reduces to the variance in Eq. 5.1 plus cross terms that tend towards zero in the ensemble average limit. The correlation coefficient ρ is the autocorrelation coefficient divided by the square root of the cross-correlation coefficients between sub-bands, which we assumed to be identical within a single band. Therefore,

$$\rho(S) = \frac{\sigma_{\rm J}^2}{\sigma_{\mathcal{R}}^2(S)} \tag{5.27}$$

and is a function of pulse S/N. Since we calculated ρ from residuals whose corresponding profiles differ in S/N, we took the average S/N for the profiles in a given sub-band and used the geometric mean $\left(\langle S_i \rangle \langle S_j \rangle\right)^{1/2}$ as a proxy for pulse S/N.

Figure 5.7 shows the correlation coefficients (gray) as a function of S, computed over all epochs observed at 1400 MHz for PSRs J1713+0747 (top) and B1937+21 (bottom) at AO (left) and GBT (right). Since PSR J1713+0747 has $\sigma_{\rm J} \approx \sigma_{\rm C}$ and high-S/N, we show the results of our correlation analysis to demonstrate how the method performs before applying it to PSR B1937+21. The black points show the median ρ with linear bins in S/N each increasing by 10. The blue lines show the best fit of Eq. 5.27 to the black points via a grid search in $\sigma_{\rm J}$, holding $\sigma_{\mathcal{R}}$ fixed from the ML analysis. Each panel shows $\sigma_{\rm J}$ as a fraction of $\sigma_{\rm C}$ as well as the single-pulse rms $\sigma_{\rm J,1}$, which accounts for the differences in $t_{\rm sub}$ between telescopes. The errors include both errors on $\sigma_{\rm C}$ and errors from the fit.

For PSR J1713+0747, we find consistency of $\sigma_{\rm J,1}$ between AO and GBT, with $\sigma_{\rm J,1} = 23.3 \pm 0.5$ μs, 22.5 ± 0.7 μs, respectively, which demonstrate a good check of the methods used in this paper. These values are generally consistent with, though somewhat lower than, measurements reported elsewhere. Dolch et al. (2014) report a measurement of jitter though their method includes the contribution from $\sigma_{\rm DISS}$.

They find $\sigma_{\mathrm{C},1} = 27.0 \pm 3.3$ μs, though we note that the σ_{DISS} contribution is not well-defined at the single-pulse level. Shannon & Cordes (2012) find $\sigma_{\mathrm{J},1} \approx 26$ μs from a cross-correlation analysis between frequency bands. Shannon et al. (2014) find $\sigma_{\mathrm{C},1} = 31.1 \pm 0.7$ μs (again including the contribution of σ_{DISS}) by adding Gaussian noise to the template, generating residuals, and subtracting the quadrature difference from the observed residuals. Even accounting for the small contribution from σ_{DISS}, their measurement formally disagrees with ours for reasons that are uncertain.

For PSR B1937+21, σ_{DISS} is comparable to the predicted values from the scaling relation (Eq. 5.17) for both AO and GBT at 1400 MHz. Differences between the estimated $\sigma_{\mathrm{J},1}$ between telescopes come from differences in the estimated σ_{C} whereas the ratio of rmss $\sigma_{\mathrm{J}}/\sigma_{\mathrm{C}}$ is consistent between the measurements at both observatories. Since the GUPPI observations span more years than the PUPPI observations (~ 3.6 yr versus ~ 1.6 yr, respectively), if the scintillation parameters differed in the first half of the GUPPI observations than the second half when PUPPI ran in coincidence, then the average σ_{DISS} would differ between the two sets of observations. The small scintle size at 1400 MHz means that we are unable to study the scintillation properties of this pulsar with the current NANOGrav data set.

5.5 Summary Results

Figures 5.8 and 5.9 show the results for the three white-noise contributions to the timing residuals per frequency band per pulsar. We performed the ML analysis independently for observations of PSRs J1713+0747 and B1937+21, which were

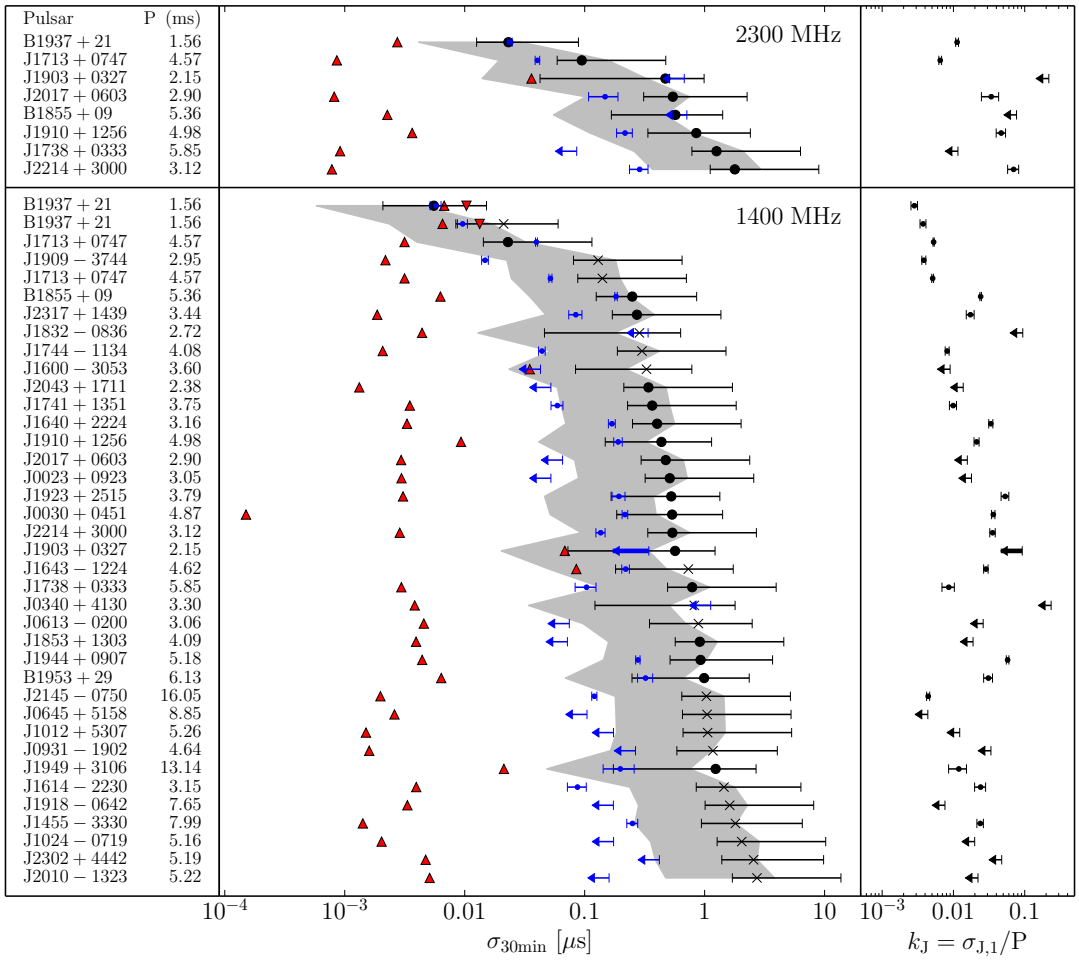

Figure 5.8: Summary of white-noise components for pulsars observed at the two highest frequency bands. The middle panel shows the three contributions, template-fitting noise as black circles (AO) or crosses (GBT), jitter noise as blue dots, and estimated DISS noise as red triangles. We observed PSRs J1713+0747 and B1937+21 with both telescopes and plot the separate analysis for each. The template-fitting and jitter contributions are for a 50 MHz bandwidth but scaled to a 30 min observating time. The gray bands represent the template-fitting noise scaled to the full receiver bandwidth to show the relative contribution with respect to jitter in a given NANOGrav observation. The DISS noise has been scaled to a 30 min observation and the appropriate total bandwidth for each band. Within each band, pulsars are ordered by increasing template-fitting noise (ordered by black points, not gray bands). The rightmost panel shows the single-pulse rms jitter divided by the period of the pulsar, k_{J}. For PSR B1937+21, the upside-down triangles indicate the measured DISS noise from the correlation analysis (see §5.4.3). The bold lines for PSR J1903+0327 at 1400 MHz indicates an upper limit on σ_{C} inconsistent with the estimate of σ_{DISS} (recall that σ_{DISS} has been scaled to the total bandwidth and a 30 min observing time and so appears smaller in the plot).

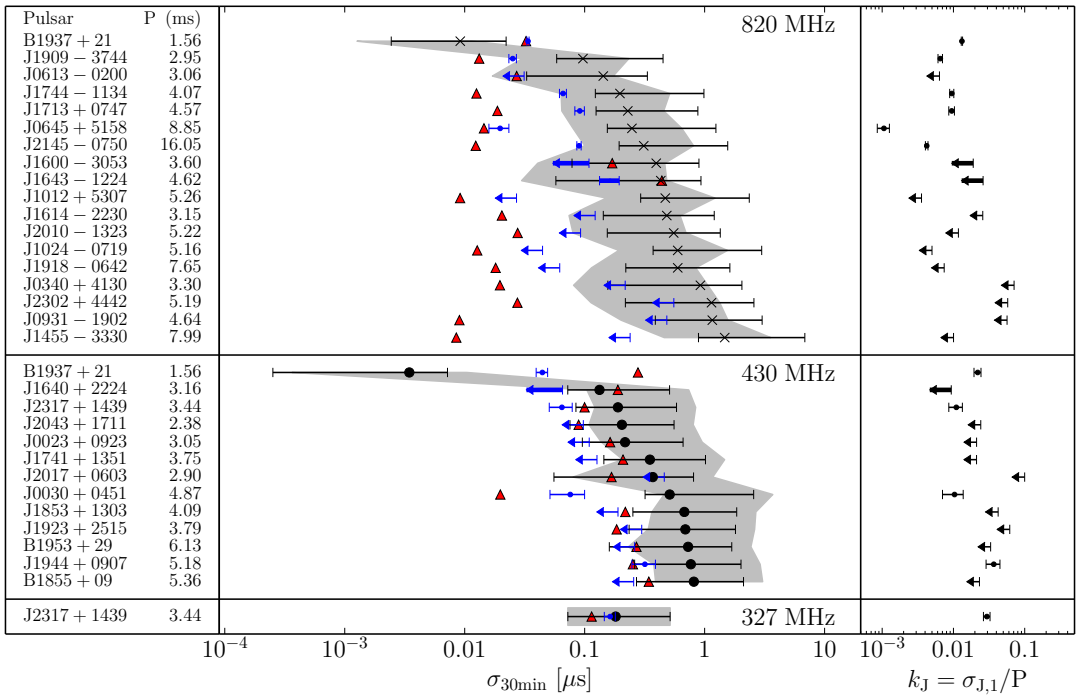

Figure 5.9: Summary of white-noise components for pulsars observed at the three lowest frequency bands. See the caption for Figure 5.8 for information. The bold upper limit lines for PSRs J1600−3053 and J1643−1224 at 820 MHz and J1640+2224 at 430 MHz, indicate an upper limit on $\sigma_{\rm C}$ inconsistent with the estimated $\sigma_{\rm DISS}$.

observed at both telescopes. For each frequency band, the pulsars are ordered in increasing amounts of template-fitting noise. Template-fitting noise values are calculated using Eq. 5.5 and using the median and 68.3% confidence limits from the PDFs of S/N for each pulsar. Jitter values are also 68.3% confidence intervals or upper limits at the 95% level. DISS noise is calculated through scattering measurements as discussed in §6.3 and according to Eq. 5.17. We scale the observation time T to 30 min and the bandwidth B equal to that of each receiver in NG9 (see Table 1 of Arzoumanian et al. 2015b).

To compare numbers expected over the length of a typical NANOGrav observation, we scaled all three contributions to 30 min. We multiplied the mean S/N, S_0 (see Eq. 5.7), by a factor of $\sqrt{30\ \mathrm{min}/t_{\rm sub}}$, where $t_{\rm sub}$ is the subintegration

time for either GBT ($\sim$ 120 s) or AO, ($\sim$ 80 s) to find the 30 min S/N for use in Eq. 5.5. Because the scintillation timescales are of the order of the typical observation length or longer for most of these MSPs (Levin et al. 2016), the simple scaling relation of Eq. 5.16 will hold on average though not exactly since the number of scintles in the time dimension is restricted. The scintillation noise term was scaled up in time and frequency using Eq. 5.17. The gray band shows the template-fitting error scaled to the full bandwidth B by a factor of $\sqrt{50 \text{ MHz}/B}$. The rightmost panel shows the jitter parameter $k_{\rm J} = \sigma_{\rm J,1}/P$.

The raw values from our analysis are reported in Table 5.2. In Table 5.3, we convert all three white-noise contribution measurements to 30 min TOA uncertainties and rank the pulsars according to each contribution and to the total white noise per frequency band (thus matching Figures 5.8 and 5.9).

5.5.1 Pulse Jitter Statistics

The preceding analysis provides detections of $\sigma_{\rm J}$ for over half of the NANOGrav pulsars for the 1400 MHz band. This large sample allows us to examine the statistics of the jitter distribution. We use the jitter parameter $k_{\rm J}$ to compare pulsars, since it is independent of the pulse period.

Table 5.2. Maximum Likelihood Analysis Output

Pulsar	Period (ms)	DM (pc cm^{-3})	Telescope	Frequency (MHz)	$W_{\rm eff}$ (μs)	W_{50} (μs)	$t_{\rm sub}$[a] (s)	S_0	$n_{\rm ISS}$	$\sigma_{\rm C}$ (ns)	$+\sigma_{\sigma_{\rm C}}$ (ns)	$-\sigma_{\sigma_{\rm C}}$ (ns)
J0023+0923	3.05	14.33	AO	430	335	72	84.6	8.4	2.7	<363	-	-
			AO	1400	430	201	84.6	5.8	1.0	<273	-	-
J0030+0451	4.87	4.33	AO	430	705	643	85.9	9.6	1.0	380	120	122
			AO	1400	540	505	85.9	5.2	5.1	1328	71	71
J0340+4130	3.30	49.58	GBT	800	545	189	126.0	3.5	27.6	<999	-	-
			GBT	1400	515	213	126.0	3.7	37.0	<3301	-	-
J0613−0200	3.06	38.78	GBT	800	250	66	126.5	10.5	13.7	<97	-	-
			GBT	1400	331	274	126.5	2.4	3.7	<328	-	-
J0645+5158	8.85	18.25	GBT	800	590	70	128.8	20.3	1.0	85	16	16
			GBT	1400	627	117	128.8	5.1	1.0	<268	-	-
J0931−1902	4.64	41.49	GBT	800	669	296	126.5	3.6	5.5	<1323	-	-
			GBT	1400	466	348	126.5	2.8	1.9	<786	-	-
J1012+5307	5.26	9.02	GBT	800	667	691	128.8	12.1	1.0	<102	-	-
			GBT	1400	634	584	128.8	5.1	1.0	<343	-	-
J1024−0719	5.16	6.49	GBT	800	553	338	128.8	7.9	1.0	<138	-	-
			GBT	1400	574	141	128.8	2.4	1.0	<541	-	-
J1455−3330	7.99	13.57	GBT	800	956	440	121.7	5.2	1.1	<541	-	-
			GBT	1400	996	207	121.7	3.9	1.7	1542	162	161
J1600−3053	3.60	52.33	GBT	800	485	102	122.5	7.2	19.2	<277	-	-
			GBT	1400	424	70	122.5	7.7	10.6	<236	-	-
J1614−2230	3.15	34.50	GBT	800	449	109	122.5	5.6	7.5	<348	-	-
			GBT	1400	391	84	122.5	2.1	1.2	385	71	68
J1640+2224	3.16	18.43	AO	430	383	96	84.6	17.5	1.5	<135	-	-
			AO	1400	465	220	84.6	8.0	1.0	648	43	43

Table 5.2 (cont'd)

Pulsar	Period (ms)	DM (pc cm^{-3})	Telescope	Frequency (MHz)	$W_{\rm eff}$ (μs)	W_{50} (μs)	$t_{\rm sub}$[a] (s)	S_0	$n_{\rm ISS}$	$\sigma_{\rm C}$ (ns)	$+\sigma_{\sigma_{\rm C}}$ (ns)	$-\sigma_{\sigma_{\rm C}}$ (ns)
J1643−1224	4.62	62.41	GBT	800	1040	390	122.5	14.0	46.7	555	106	101
			GBT	1400	973	315	122.5	7.9	11.5	899	65	64
J1713+0747	4.57	15.99	AO	1400	539	110	82.0	159.9	1.0	180	4	3
			AO	2300	512	104	82.0	36.8	1.0	223	10	10
			GBT	800	694	170	121.7	22.1	1.5	268	24	24
			GBT	1400	533	109	121.7	31.4	1.0	143	4	4
J1738+0333	5.85	33.77	AO	1400	643	120	83.4	5.6	1.0	421	84	83
			AO	2300	696	118	83.4	3.8	1.0	<472	-	-
J1741+1351	3.75	24.19	AO	430	458	109	85.0	7.0	3.2	<475	-	-
			AO	1400	390	86	85.0	7.4	1.0	247	28	28
J1744−1134	4.07	3.14	GBT	800	513	147	121.7	21.6	1.0	225	15	15
			GBT	1400	511	137	121.7	14.1	1.0	193	12	12
			GBT	1400	187	49	121.7	3.8	30.6	<1006	-	-
J1853+1303	4.09	30.57	AO	430	486	606	83.4	3.7	4.2	<1035	-	-
			AO	1400	346	125	83.4	2.6	1.0	<451	-	-
B1855+09	5.36	13.30	AO	430	796	653	85.2	5.0	5.6	<888	-	-
			AO	1400	750	518	85.2	17.4	1.9	1025	25	25
			AO	2300	716	485	85.2	6.3	7.7	<2722	-	-
J1903+0327	2.15	297.54	AO	1400	405	195	82.6	3.4	51.3	<760	-	-
			AO	2300	327	99	82.6	3.3	108.8	<2023	-	-
J1909−3744	2.95	10.39	GBT	800	279	53	121.7	23.1	1.1	99	7	7
			GBT	1400	261	41	121.7	16.7	1.0	56	4	4
J1910+1256	4.98	38.06	AO	1400	634	133	82.0	7.3	5.3	823	67	67
			AO	2300	574	108	82.0	3.5	3.6	1819	273	273

Table 5.2 (cont'd)

Pulsar	Period (ms)	DM (pc cm^{-3})	Telescope	Frequency (MHz)	$W_{\rm eff}$ (μs)	W_{50} (μs)	$t_{\rm sub}$[a] (s)	S_0	$n_{\rm ISS}$	$\sigma_{\rm C}$ (ns)	$+\sigma_{\sigma_{\rm C}}$ (ns)	$-\sigma_{\sigma_{\rm C}}$ (ns)
J1918−0642	7.65	26.59	GBT	800	979	184	121.7	10.2	4.3	<377	-	-
			GBT	1400	879	151	121.7	4.5	1.0	<384	-	-
J1923+2515	3.79	18.86	AO	430	448	175	83.9	3.3	5.3	<1319	-	-
			AO	1400	534	146	83.9	5.1	6.4	1355	168	168
B1937+21	1.56	71.02	AO	430	190	63	84.1	263.1	170.5	448	48	50
			AO	1400	145	37	84.1	135.8	4.1	51	1	1
			AO	2300	147	36	84.1	38.4	1.5	76	4	4
			GBT	800	153	54	120.9	98.6	9.7	128	3	3
			GBT	1400	146	37	120.9	43.6	3.5	66	2	1
J1944+0907	5.18	24.34	AO	430	1120	500	83.4	7.4	5.3	1524	341	336
			AO	1400	949	364	83.4	6.3	1.4	2354	99	99
J1949+3106	13.14	164.13	AO	1400	916	142	80.8	3.5	41.8	1996	608	561
B1953+29	6.13	104.58	AO	430	1293	481	84.6	8.7	15.1	<1505	-	-
			AO	1400	823	224	84.6	4.1	11.2	1615	235	230
J2010−1323	5.22	22.16	GBT	800	499	240	121.7	5.4	8.6	<342	-	-
			GBT	1400	527	247	121.7	1.6	1.0	<631	-	-
J2017+0603	2.90	23.92	AO	430	323	62	83.4	4.2	36.1	<1430	-	-
			AO	1400	242	64	83.4	3.5	1.0	<223	-	-
			AO	2300	234	61	83.4	2.7	1.3	578	162	157
J2043+1711	2.38	20.71	AO	430	222	35	83.5	5.6	4.3	<269	-	-
			AO	1400	178	21	83.5	3.6	1.0	<145	-	-
J2145−0750	16.05	9.01	GBT	800	1826	395	121.7	48.7	1.0	778	32	32
			GBT	1400	1823	339	121.7	14.6	1.0	815	40	40

Table 5.2 (cont'd)

Pulsar	Period (ms)	DM (pc cm^{-3})	Telescope	Frequency (MHz)	$W_{\rm eff}$ (μs)	W_{50} (μs)	$t_{\rm sub}$[a] (s)	S_0	$n_{\rm ISS}$	$\sigma_{\rm C}$ (ns)	$+\sigma_{\sigma_{\rm C}}$ (ns)	$-\sigma_{\sigma_{\rm C}}$ (ns)
J2214+3000	3.12	22.56	AO	1400	562	181	82.0	7.1	1.0	682	60	60
			AO	2300	551	180	82.0	2.1	1.0	1345	236	237
J2302+4442	5.19	13.76	GBT	800	608	345	128.8	3.2	20.9	<1588	-	-
			GBT	1400	682	347	128.8	2.0	1.5	<1307	-	-
J2317+1439	3.44	21.90	AO	327	395	152	85.7	11.6	3.5	677	71	72
			AO	430	392	169	85.7	11.4	2.6	266	58	57
			AO	1400	376	152	85.7	9.6	1.0	378	47	48

[a]Median subintegration length

Table 5.3. Summary of White Noise Contributions Scaled to 30 Minutes

Pulsar	Period (ms)	DM (pc cm^{-3})	Telescope	$\sigma_{S/N}$ (ns)	σ_J (ns)	σ_{DISS} (ns)	$\sigma_{\mathcal{R}}$ (ns)	Rank S/N	Rank J	Rank DISS	Rank Total
					327 MHz						
J2317+1439	3.44	21.90	AO	181	163	114	269	1	1	1	1
					430 MHz						
J0023+0923	3.05	14.33	AO	313	<90	163	<364	5	6	4	5
J0030+0451	4.87	4.33	AO	737	75	19	742	8	4	1	8
J1640+2224	3.16	18.43	AO	191	49[a]	189	198[a]	2	2	7	1
J1741+1351	3.75	24.19	AO	504	<105	208	<556	6	7	8	6
J1853+1303	4.09	30.57	AO	977	<158	218	<1014	9	8	9	9
B1855+09	5.36	13.30	AO	1173	<213	342	<1240	13	9	13	13
J1923+2515	3.79	18.86	AO	996	<249	184	<1043	10	11	6	10
B1937+21	1.56	71.02	AO	5.0	44	278	281	1	1	12	2
J1944+0907	5.18	24.34	AO	1108	317	252	1179	12	12	10	12
B1953+29	6.13	104.58	AO	1051	<217	270	<1106	11	10	11	11
J2017+0603	2.90	23.92	AO	533	<384	167	<678	7	13	5	7
J2043+1711	2.38	20.71	AO	295	<81	89	<318	4	5	2	4
J2317+1439	3.44	21.90	AO	273	64	99	298	3	3	3	3

Table 5.3 (cont'd)

Pulsar	Period (ms)	DM (pc cm^{-3})	Telescope	$\sigma_{S/N}$ (ns)	σ_J (ns)	σ_{DISS} (ns)	$\sigma_{\mathcal{R}}$ (ns)	Rank S/N	Rank J	Rank DISS	Rank Total
820 MHz											
J0340+4130	3.30	49.58	GBT	478	<181	19	<511	15	15	11	15
J0613−0200	3.06	38.78	GBT	74	<26	27	<83	3	4	13	3
J0645+5158	8.85	18.25	GBT	128	19	14	130	6	1	8	5
J0931−1902	4.64	41.49	GBT	600	<403	9.0	<723	17	17	2	16
J1012+5307	5.26	9.02	GBT	243	<22	9.2	<244	10	2	3	9
J1024−0719	5.16	6.49	GBT	309	<37	12	<311	13	6	6	13
J1455−3330	7.99	13.57	GBT	762	<199	8.5	<788	18	16	1	18
J1600−3053	3.60	52.33	GBT	204	<81[a]	169	<220[a]	8	10	17	8
J1614−2230	3.15	34.50	GBT	250	<101	20	<271	11	13	12	10
J1643−1224	4.62	62.41	GBT	223	162[a]	440	276[a]	9	14	18	11
J1713+0747	4.57	15.99	GBT	118	91	18	150	5	12	10	6
J1744−1134	4.07	3.14	GBT	102	66	12	122	4	8	5	4
J1909−3744	2.95	10.39	GBT	50	25	13	57	2	3	7	2
J1918−0642	7.65	26.59	GBT	309	<51	18	<314	14	7	9	14
B1937+21	1.56	71.02	GBT	4.8	33	32	47	1	5	16	1
J2010−1323	5.22	22.16	GBT	286	<77	27	<297	12	9	15	12
J2145−0750	16.05	9.01	GBT	161	89	12	184	7	11	4	7
J2302+4442	5.19	13.76	GBT	591	<461	27	<750	16	18	14	17

Table 5.3 (cont'd)

Pulsar	Period (ms)	DM (pc cm^{-3})	Telescope	$\sigma_{\rm S/N}$ (ns)	$\sigma_{\rm J}$ (ns)	$\sigma_{\rm DISS}$ (ns)	$\sigma_{\mathcal{R}}$ (ns)	Rank S/N	Rank J	Rank DISS	Rank Total
					1400 MHz						
J0023+0923	3.05	14.33	AO	142	<43	3.0	<149	16	6	15	12
J0030+0451	4.87	4.33	AO	149	216	0.2	263	18	29	1	21
J0340+4130	3.30	49.58	GBT	229	<935	3.8	<963	23	38	22	38
J0613−0200	3.06	38.78	GBT	247	<62	4.6	<255	24	13	27	19
J0645+5158	8.85	18.25	GBT	292	<87	2.6	<305	29	16	11	24
J0931−1902	4.64	41.49	GBT	327	<221	1.6	<394	31	31	5	29
J1012+5307	5.26	9.02	GBT	295	<145	1.5	<329	30	22	4	27
J1024−0719	5.16	6.49	GBT	568	<145	2.0	<587	36	23	8	35
J1455−3330	7.99	13.57	GBT	503	250	1.4	562	35	32	3	34
J1600−3053	3.60	52.33	GBT	91	<35	34	<104	10	4	36	7
J1614−2230	3.15	34.50	GBT	404	87	3.9	413	33	15	24	31
J1640+2224	3.16	18.43	AO	112	168	3.3	202	13	24	19	14
J1643−1224	4.62	62.41	GBT	204	219	85	311	21	30	38	25
J1713+0747	4.57	15.99	AO	6.4	39	3.2	40	3	5	17	4
			GBT	39	51	3.2	65	5	9	18	5
J1738+0333	5.85	33.77	AO	219	103	3.0	243	22	17	14	18
J1741+1351	3.75	24.19	AO	102	59	3.5	117	12	11	21	10
J1744−1134	4.08	3.14	GBT	83	44	2.1	94	9	8	9	6
J1832−0836	2.72	28.18	GBT	79	<281	4.4	<292	8	35	25	22
J1853+1303	4.09	30.57	AO	254	<59	3.9	<261	25	12	23	20
B1855+09	5.36	13.30	AO	69	182	6.3	195	6	25	30	13

Table 5.3 (cont'd)

Pulsar	Period (ms)	DM (pc cm^{-3})	Telescope	$\sigma_{\rm S/N}$ (ns)	$\sigma_{\rm J}$ (ns)	$\sigma_{\rm DISS}$ (ns)	$\sigma_{\mathcal{R}}$ (ns)	Rank S/N	Rank J	Rank DISS	Rank Total
J1903+0327	2.15	297.54	AO	158	257[a]	68	301[a]	20	33	37	23
J1909−3744	2.95	10.39	GBT	36	14	2.2	39	4	3	10	3
J1910+1256	4.98	38.06	AO	121	190	9.3	226	14	26	32	16
J1918−0642	7.65	26.59	GBT	451	<144	3.3	<474	34	21	20	33
J1923+2515	3.79	18.86	AO	147	193	3.1	242	17	27	16	17
B1937+21	1.56	71.02	AO	1.6	5.7	10	11	1	1	33	1
			GBT	5.9	9.6	13	17	2	2	34	2
J1944+0907	5.18	24.34	AO	258	277	4.4	379	26	34	26	28
J1949+3106	13.14	164.13	AO	344	198	21	398	32	28	35	30
B1953+29	6.13	104.58	AO	276	321	6.4	424	27	36	31	32
J2010−1323	5.22	22.16	GBT	762	<133	5.1	<773	38	19	29	36
J2017+0603	2.90	23.92	AO	132	<54	3.0	<143	15	10	13	11
J2043+1711	2.38	20.71	AO	94	<43	1.3	<104	11	7	2	8
J2145−0750	16.05	9.01	GBT	288	120	2.0	312	28	18	7	26
J2214+3000	3.12	22.56	AO	150	136	2.9	202	19	20	12	15
J2302+4442	5.19	13.76	GBT	713	<349	4.7	<794	37	37	28	37
J2317+1439	3.44	21.90	AO	76	84	1.9	113	7	14	6	9

Table 5.3 (cont'd)

Pulsar	Period (ms)	DM (pc cm^{-3})	Telescope	$\sigma_{S/N}$ (ns)	σ_J (ns)	σ_{DISS} (ns)	$\sigma_{\mathcal{R}}$ (ns)	Rank S/N	Rank J	Rank DISS	Rank Total
2300 MHz											
J1713+0747	4.57	15.99	AO	31	40	0.9	51	2	2	3	2
J1738+0333	5.85	33.77	AO	414	<71	0.9	<420	7	3	4	5
B1855+09	5.36	13.30	AO	188	<592	2.3	<621	5	8	5	7
J1903+0327	2.15	297.54	AO	155	<563	36	<585	3	7	8	6
J1910+1256	4.98	38.06	AO	280	217	3.6	354	6	5	7	4
B1937+21	1.56	71.02	AO	7.6	23	2.7	25	1	1	6	1
J2017+0603	2.90	23.92	AO	179	148	0.8	232	4	4	2	3
J2214+3000	3.12	22.56	AO	588	287	0.8	654	8	6	1	8

[a]When the estimated σ_{DISS} is larger than the measured σ_C, entries for σ_J are replaced by the values for σ_C. The total residual RMS $\sigma_{\mathcal{R}}$ is set equal to $\sqrt{\sigma_C^2 + \sigma_{S/N}^2}$

Since $\sigma_{\rm DISS} \ll \sigma_{\rm J}$ for most pulsars in our sample at 1400 MHz, we can use the likelihood functions $\mathcal{L}(\sigma_{\rm C})$ computed in the ML analysis (see Eq. 5.24) as a proxy for the likelihood functions $\mathcal{L}(\sigma_{\rm J})$. In the case of PSR B1937+21, we explicitly set $\mathcal{L}(\sigma_{\rm J}) = \mathcal{L}(\sqrt{\sigma_{\rm C}^2 - \sigma_{\rm DISS}^2})$. We ignore PSR J1903+0327 as the upper-limit $\mathcal{L}(\sigma_{\rm C})$ translates non-trivially to $\mathcal{L}(\sigma_{\rm J})$. We create a continuous histogram that is the sum of the individual likelihoods $\mathcal{L}(\sigma_{\rm J})$, shown in Figure 5.10. The black region shows the contributions from upper limit pulsar jitter values and the gray region shows the contributions from measured pulsar values. The median jitter parameter is $k_{\rm J} = \sigma_{\rm J}/P = 0.010^{+0.023}_{-0.006}$.

5.6 Noise Model and Implications for PTA Optimization

The noise covariance matrix for short timescales implied by our analysis is

$$\mathbf{C}_{\nu\nu',tt'} = \delta_{tt'} \left[\delta_{\nu\nu'} \sigma_{\rm S/N}^2(S) + \sigma_{\rm J}^2(T) \right] + \rho_{{\rm DISS},\nu\nu',tt'} \sigma_{\rm DISS}^2(T), \tag{5.28}$$

where δ is the Kronecker delta and $\rho_{{\rm DISS},\nu\nu',tt'}$ encapsulates the correlation scales for DISS and we assume that bandwidth is fixed for each receiver. Shannon et al. (2014) find that jitter decorrelates over a range of frequencies larger than the total bandwidth of any receiver used in NG9; a decorrelation term is therefore not included in our model. We re-emphasize that $\sigma_{\rm S/N}$ can be calculated directly from the template shape and $\sigma_{\rm J}$ is fixed for a given pulsar-frequency combination.

Pulsars dominated by template-fitting errors will see the greatest increase in timing precision from increased integration time and larger bandwidth instrumentation. Wideband timing systems allow for observations of an increased number of scintles and a reduction of $\sigma_{\rm DISS}$. Therefore, higher DM pulsars, dominated by scintillation noise, will improve in timing quality and will would then become

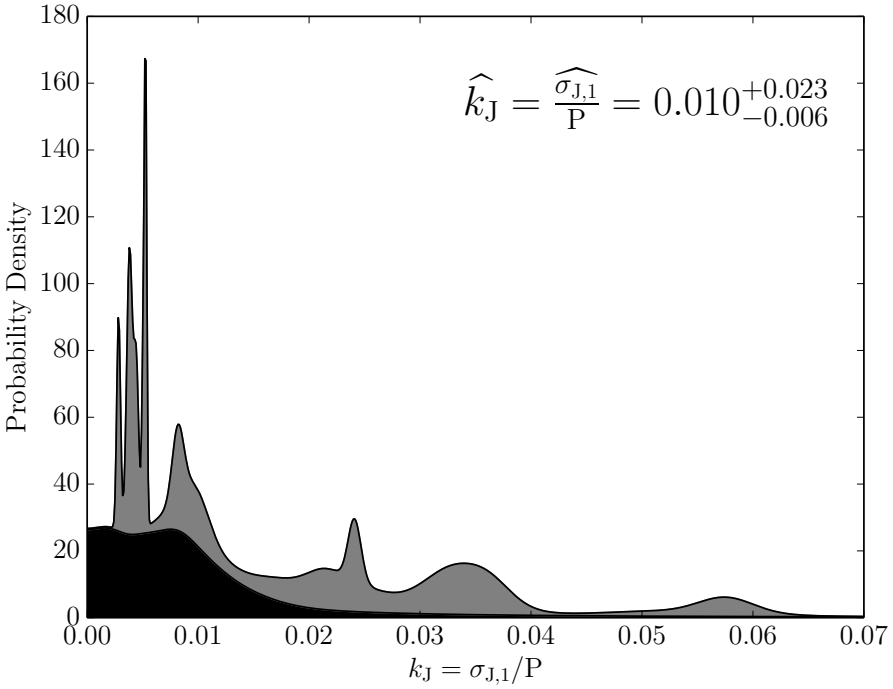

Figure 5.10: Continuous histogram of the jitter parameter $k_{\rm J} = \sigma_{\rm J,1}/P$. The shaded regions denote the probability density associated with measured values (gray) and upper limits (black) of $k_{\rm J}$.

attractive candidates for inclusion into PTAs. By contrast, pulsars dominated by jitter on many epochs do not benefit substantially from wideband timing, though their timing precision will always improve with the increased numbers of pulses observed.

Scintillation monitoring is required in order to characterize the time-varying scintillation parameters, which will not only change $\sigma_{\rm DISS}$ but change the PBF over timescales much greater than that of a single epoch. Changes in the PBF will alter pulse shapes and therefore introduce a timing delay into any TOA estimate and contribute to the total white-noise variance.

NG9 uses an empirical, parameterized noise model fit in the timing analysis (Arzoumanian et al. 2015a,b, 2016). For TOAs with an associated error $\sigma_{\rm S/N}$ from

template-fitting, the white-noise model is

$$\mathbf{C}_{\nu\nu',tt'} = \delta_{tt'}\left[\delta_{\nu\nu'}\left(\mathcal{F}^2\sigma^2_{\mathrm{S/N}}(S) + \mathcal{Q}^2\right) + \mathcal{J}^2\right], \tag{5.29}$$

where $\mathcal{F}$ (commonly referred to as EFAC) is a dimensionless, constant multiplier to the template-fitting error, $\mathcal{Q}$ (EQUAD) accounts for sources of Gaussian white noise added in quadrature to the template-fitting error, $\mathcal{J}$ (ECORR) accounts for sources of white noise correlated in frequency such as jitter. In NG9, $\mathcal{F} \approx 1$ for all pulsars, to within a factor of 2 for most pulsars. NG9 also fits a red noise model that is negligible on the timescales of a single epoch.

Figure 5.11 shows the comparison between measurements of $\mathcal{J}$ versus $\sigma_{\mathrm{J,30min}}$ in black, with the gray points showing values where at least one of the two estimates is an upper limit. We find that $\sigma_{\mathrm{J,30min}} \lesssim \mathcal{J}$, which suggests that ECORR is systematically measuring increases in the variance of the residuals, correlated in frequency, beyond pulse jitter. For example, broadband RFI can cause correlations in TOAs measured at different frequencies if unremoved. Replacement of the NG9 empirical white-noise model with our measurements will reduce the number of free parameters in the timing analysis and should improve overall sensitivity to GWs.

5.7 Conclusions

The short-term white-noise model for pulsar timing is well defined. We have estimated or placed limits on the contributions of the noise model's three white-noise components in the timing residuals of the NANOGrav PTA. The template-fitting errors are consistent with Eq. 5.5 and dominate TOA precision for many of the pulsars for many epochs, but scintillation makes jitter important for the higher

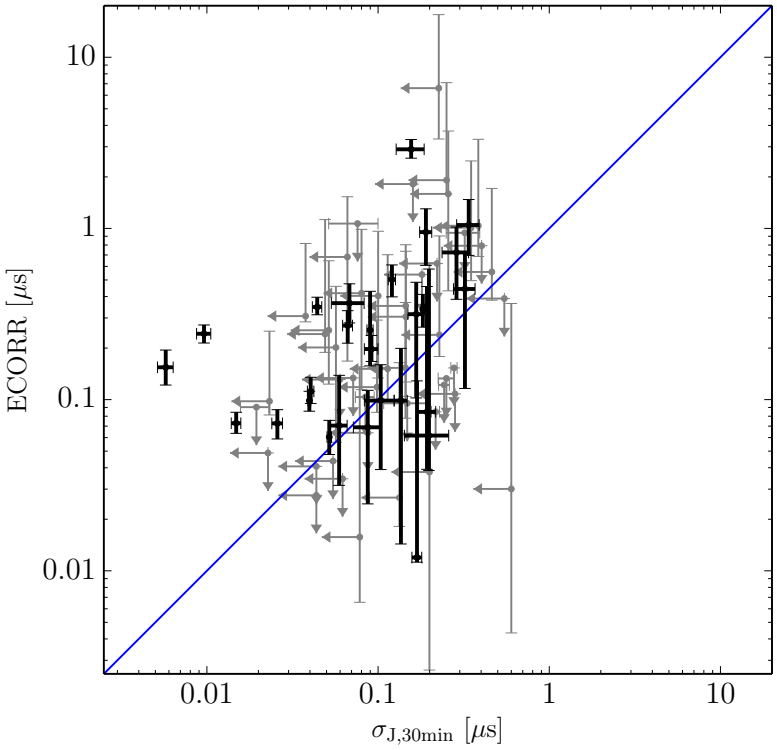

Figure 5.11: Comparison of ECORR from NG9 with jitter values from this work. Black points denote measurements in both while the gray points mark upper limits in at least one of the values for a given pulsar/receiver combination. The diagonal blue line shows where ECORR equals $\sigma_{\mathrm{J,30min}}$.

S/N epochs and TOAs. We find that the template-fitting and jitter errors can be estimated with only pulse S/N as a parameter. The total short-term variance needs contemporaneous measurements of scintillation parameters during observations to properly estimate the time-varying σ_{DISS} contribution. Errors in pulse polarization calibration, or those errors introduced from unremoved RFI, will produce extra variance on short timescales. Long-term observations spanning multiple epochs will have extra variance compared to the short-term model due to a variety of effects that are not included in our analysis.

A large subset of our observed pulsars are jitter-dominated on many epochs and

we have measured jitter values for 22 of 37 pulsars. Major improvements in TOA estimation can therefore only be made through increased integration time. For several pulsars, however, $\sigma_{\rm DISS}$ is an important if not dominant contribution to the residuals. Wideband timing systems can yield improvements in pulsars with higher DMs such as PSRs B1937+21, J1600−3053, J1903+0327, and even moderate-DM pulsars like J2317+1439. Such systems can also improve the average S/N over all epochs, and therefore gains in timing precision can still be made for nearly all of the NANOGrav pulsars.

Jitter appears to be correlated in frequency over each band but not in time. We find that the rms phase variations from jitter are of order 1% of the pulse period, though with an extended tail towards higher values of the jitter parameter $k_{\rm J}$. Current noise models, such as the one used in NG9, utilize an empirical parameterization that overestimates the rms jitter. Replacement of model fit parameters with those that can be fixed will ultimately increase sensitivity of the PTA to GWs.

Future telescopes with increased collecting area and sensitivity will become jitter- and DISS-noise dominated. Arrays can therefore be partitioned and pointed at multiple pulsars simultaneously rather than one after another, providing longer integration times for each pulsar and increasing the number of pulses being averaged to reduce the jitter error contribution. The sub-arrays can be partitioned to minimize TOA uncertainty per target pulsar using the formalism outlined here. Wideband timing systems that allow for fine frequency- and time-resolution are needed to fully characterize scintillation structures on a per-epoch basis.

5.8 Acknowledgments

Author contributions. MTL developed the mathematical framework, created the modified data set and residuals, undertook the analysis, and prepared the majority of the text, figures, and tables. JMC and SC helped with the development of the framework, the format of figures and tables, and generated some additional text. JAE, DRM, and XS contributed useful discussions regarding the development of the framework. PBD assisted in the initial creation of the modified data set. ZA, KC, PBD, TD, RDF, EF, MEG, GJ, MJ, MTL, LL, MAM, DJN, TTP, SMR, IHS, KS, JKS, and WWZ all ran observations and developed timing models for the NG9 data set. Additional specific contributions are described in Arzoumanian et al. (2015b). JAE developed the noise model in NG9 and assisted in the comparison analysis to this work. JMC, SC, GJ, and DJN helped with review of the manuscript.

Acknowledgments. We would like to thank Michael Jones for useful discussions on statistical methods. The NANOGrav Project receives support from NSF PIRE program award number 0968296 and NSF Physics Frontier Center award number 1430284. NANOGrav research at UBC is supported by an NSERC Discovery Grant and Discovery Accelerator Supplement and the Canadian Institute for Advanced Research. MTL acknowledges partial support by NASA New York Space Grant award number NNX15AK07H. JAE acknowledges support by NASA through Einstein Fellowship grant PF3-140116. Portions of this research were carried out at the Jet Propulsion Laboratory, California Institute of Technology, under a contract with the National Aeronautics and Space Administration. TTP was a student at the National Radio Astronomy Observatory (NRAO) while this project was undertaken. Data for the project were collected using the facilities of

the NRAO and the Arecibo Observatory. The NRAO is a facility of the NSF operated under cooperative agreement by Associated Universities, Inc. The Arecibo Observatory is operated by SRI International under a cooperative agreement with the NSF (AST-1100968), and in alliance with the Ana G. Méndez-Universidad Metropolitana, and the Universities Space Research Association.

5.9 Appendix

5.9.1 Deviations from the Initial Timing Model

Errors in the initial timing model parameters used for pulse folding and dedispersion cause effects that can be separated into two related categories: an increase in TOA uncertainties from pulse shape changes on the subintegration timescale $t_{\rm sub}$, and correlated TOA errors over the observation duration T. The quadratic fit of initial timing residuals in Eq. 5.19 will remove the latter, whereas the former cannot be mitigated after data collection. In part 5.9.1 we discuss the non-removable pulse shape changes, in part 5.9.1 we discuss the systematic deviations from the initial timing residuals that we remove with our quadratic fit, and in part 5.9.1 we discuss other miscellaneous effects that can cause departures from the initial timing model.

Irreversible Pulse Profile Smearing

1. Spin period errors: If the initial folding period is incorrect by an amount δP, pulse profiles will be smeared by an amount

$$\sigma_P \sim \frac{\delta P}{P} t_{\rm sub}. \tag{5.30}$$

For isolated pulsars, the dominant folding error is due to an error in spin period,

$$\sigma_P \sim 10 \text{ ps } \left(\frac{\delta P}{10^{-16} \text{ s}}\right) t_{100\rm s} P_{\rm ms}^{-1}, \tag{5.31}$$

where the typical error in the initial folding period is 10^{-16} s for pulsars in the NANOGrav data set. Note that periods fit over many years of data are known to much higher precision.

2. Binary orbit parameter errors: For binary pulsars, the observed pulse period for low-eccentricity MSPs is Doppler-shifted by an amount (Lorimer & Kramer 2012)

$$\begin{aligned}\sigma_{P_b} &\sim P\frac{\delta v_\parallel}{c} \sim \frac{2\pi P}{c}\delta\left(\frac{a\sin i}{P_b}\right) \sim \frac{2\pi P a \sin i}{c P_b}\sqrt{\left(\frac{\delta a}{a}\right)^2 + \left(\frac{\delta(\sin i)}{\sin i}\right)^2 + \left(\frac{\delta P_b}{P_b}\right)^2} \\ &\sim 72.7 \text{ ns } P_{\rm ms}\ a_{\rm lsec}\ \sin i\ P_{b,\rm day}^{-1}\sqrt{\left(\frac{\delta a}{a}\right)^2 + \left(\frac{\delta(\sin i)}{\sin i}\right)^2 + \left(\frac{\delta P_b}{P_b}\right)^2}\end{aligned} \tag{5.32}$$

where a is the semi-major axis, i is the inclination angle, and P_b is the binary orbital period, and we assume that the errors in the binary parameters are uncorrelated. The error on these three parameters is much larger than the spin period error, with $\delta(\sin i)/\sin i \sim 10^{-3}$ dominating the other two binary error terms in the NANOGrav initial timing models even when $\sin i$ is well-measured. Therefore, for typical pulsar parameters and when $\sin i$ is measurable, the profile smearing error will be comparable to the spin period error but still negligible. Otherwise, the timing error will be of the order of 10s of nanoseconds.

3. DM variations: Differences in the initial timing model DM from the actual DM will cause smearing of pulse profiles. The timing perturbation is roughly the error in the dispersive delay across a frequency channel (Cordes 2002):

$$\delta t_{\rm DM} \simeq 8.3\ \mu{\rm s}\ \delta{\rm DM}\ B_{\rm MHz}\nu_{\rm GHz}^{-3}, \tag{5.33}$$

with δDM measured in units of pc cm^{-3}. The typical range in total DM variation in the NANOGrav data set is $\sim 10^{-3}$ pc cm^{-3}, which given a 50 MHz channel bandwidth and an observing frequency of 1 GHz, yields a timing perturbation of ~ 400 ns. A constant DM over the observation is removed by the term $K(\nu)$ in the timing model fit. Intra-observation DM variations are discussed later in 5.9.1.2.

4. Polarization calibration errors: Incorrect gain calibration and summation of the polarization profiles into the intensity profiles will cause pulse shape changes that lead to TOA uncertainties when fitting with a template. The TOA error from gain variation for circularly polarized channels is (Cordes et al. 2004)

$$\delta t_{\rm pol} \sim 1\ \mu{\rm s}\ \varepsilon_{0.1}\pi_{{\rm V},0.1}W_{0.1{\rm ms}}, \tag{5.34}$$

where $\varepsilon = \delta g/g$ is the fractional gain error, $\pi_{\rm V}$ is the degree of circular polarization, and W is the pulse width. Timing offsets from gain calibration errors will vary slowly with time and will be removed by the quadratic fit discussed in the next sub-section (see for example 5.9.1.3).

Systematic Deviations from the Quadratic Fit of Initial Timing Perturbations

1. Binary orbit parameter errors: For pulsars in short-period binary orbits, we will need to fit out higher order terms in t when the period is of order the integration time over the epoch and the binary parameter errors are large. The shortest period

binary in NG9 is PSR J0023+0923 with a period of 200 min, nearly seven times longer than the typical total integration time per epoch. The quadratic fit in Eq. 5.19 will approximate the sinusoidal variations in TOA offsets introduced by the orbit mis-estimation. The next dominant polynomial term is the cubic term, with error $\sim \sigma_{P_b}(T/P_b)^3$, where $(T/P_b)^3 \sim 0.15^3 \sim 3.4 \times 10^{-3}$ for PSR J0023+0923 and smaller for all other pulsars in the NANOGrav data set. Therefore, using Eq. 5.32, the error is negligible.

2. Ionospheric DM variations: Changes in DM over short timescales, such as from ionospheric variations, will cause $K(\nu)$ to have time-dependence. The ionospheric DM will vary over the time span of a day due to the changing incident solar flux on a position on the Earth's surface by an amount $\lesssim 3 \times 10^{-5}$ pc cm^{-3} (Lam et al. 2015). The timing error is approximately the error in the dispersive delay across a frequency channel, given by Eq. 5.33. For a maximum change in DM of 3×10^{-5} pc cm^{-3} over a 12 hr period, a 1 hr observing length, a 50 MHz channel bandwidth, and an observing frequency of 1 GHz, the timing perturbation is ≈ 1 ns. Therefore, over the observing span, the assumption that $K(\nu, t) \approx K(\nu)$ holds.

3. Cross-coupling errors: Instrumental self-polarization will cause a slow, secular variation in the initial timing residuals when unremoved (Cordes et al. 2004). Cross coupling in the feed will induce a measured false circular polarization $\pi_{\rm V} \simeq 2\eta^{1/2}\pi_{\rm L}$, where η is the voltage cross coupling coefficient and $\pi_{\rm L}$ is a pulsar's degree of linear polarization. While the associated timing errors can be large, errors introduced by the cross-coupling term will cause a slow, secular variation in the residuals as the feed rotates during an observation and will therefore be removed by our quadratic fit. Estimates of these parameters and the induced

timing uncertainties will be focused on in future papers.

4. Rotation Measure (RM) variations: Faraday rotation from magnetic fields along the pulse propagation path causes both a birefringent TOA delay and the pulse polarization position angle (PPA) to rotate. Changes in the rotation measure (RM $= \int dl \ n_e B_\parallel$, in units of rad m^{-2}) over short timescales can come from ionospheric variations as with DM. The birefringent delay is given as (Cordes 2002)

$$\delta t_{\rm RM} = 0.18 \text{ ns RM } \nu_{\rm GHz}^{-3} \tag{5.35}$$

and the change in PPA is (Lorimer & Kramer 2012)

$$\Delta\Psi_{\rm PPA} = \text{RM } \lambda^2 = 0.09 \text{ RM } \nu_{\rm GHz}^{-2}. \tag{5.36}$$

The RM through the ionosphere is ~ 1 rad m^{-2} with $\sim 10\%$ variations on the timescale of 1 hr (Sotomayor-Beltran et al. 2013) and the birefringent delay is therefore negligible over short timescales. The change in the PPA will cause errors in the polarization calibration that are slowly varying with time and therefore removed by the quadratic fit.

5. Intrinsic pulsar spin noise: Rotational instabilities in the pulsar cause deviations from the initial timing model with a steep, power-law noise spectrum over the timescale of years (Cordes 2013). Shannon & Cordes (2010) measured spin noise in radio pulsars to scale as $\sigma_{\rm spin} \propto T^{2.0\pm0.2}$. The pulsar with the largest measured rms spin noise in the NANOGrav data set is PSR B1937+21, with $\sigma_{\rm spin} \approx 1.5$ μs over 10 yr (Shannon & Cordes 2010; Arzoumanian et al. 2015b). The rms on the timescale of 1 hr is ~ 0.2 fs and is therefore negligible.

6. Stochastic GW background: Like intrinsic pulsar spin noise, GW perturbations will also induce long-term correlations in residuals. However, the rms timing

perturbation from a stochastic GW background of supermassive black hole binaries over 10 yr is on the order of 100 ns (Siemens 2013). The rms is expected to scale as $\sigma_{\rm GW} \propto T^{5/3}$, and therefore on the timescale of 1 hr the rms is ~ 0.6 fs and is also negligible.

Increases in Variance from Other Effects

1. Frequency-dependent DM: Cordes et al. (2016) describe differences in DM measured at different frequencies due to multipath scattering in the ISM and different volumes of electrons probed. The different DMs as a function of frequency cause differences in the frequency-dependent delays per channel, $K(\nu)$. However, the timescale of refractive variations are weeks or longer, and are therefore this effect is negligible on short timescales.

2. Mean PBF variations: As with frequency-dependent DM, the changes in PBFs will occur on a pulsar's refractive timescale and will therefore be negligible on timescale of an hour.

3. Pulsar mode changes: Any potential mode changes may cause timing parameter differences from the initial timing model. Pulse profile shapes in our MSPs have not been shown to deviate from the template over the timespan of single observations and any possible epoch-to-epoch mode changes are small and will be removed by our quadratic fit to obtain the short-term timing model (Eq. 5.19).

4. Transient events: Giant pulses have been seen in pulsars such as PSR B1937+21 and cause pulse shapes to deviate from the average template shape (Cognard et al. 1996; Jenet et al. 2001; Zhuravlev et al. 2013). For PSR B1937+21, giant pulses will appear at a rate of approximately 0.5 per 10 s pulse average, which

spans ≈ 6400 pulse periods. Therefore, the giant pulse S/N must be a factor of $\sim \sqrt{6400} \sim 80$ larger than the average single-pulse S/N in order to dominate the template matching fit and significantly alter the estimated TOA. The flux density of the strongest giant pulse in Zhuravlev et al. (2013) is a factor of ~ 3 smaller than the threshold needed to affect the TOA estimation.

5. Remaining RFI: Any remaining RFI in the pulse profiles will introduce unmodeled variance into our analysis. Broadband RFI can cause correlations between residuals that can increase estimates of jitter.

5.9.2 PDF of TOA Errors due to Combined Additive Noise and ISS Modulation

The template-fitting error (Eq. 5.5) can be written in the form

$$\sigma_{\mathrm{S/N}} = \sigma_0 \frac{S_0}{S}. \tag{5.37}$$

Again, S is the S/N, proportional to $(S_{\mathrm{PSR}}/\mathrm{SEFD})\sqrt{2BT}$, where S_{PSR} is the pulsar flux density, SEFD is the system equivalent flux density, B is the receiver bandwidth, and T is the total integration time. The subscript '0' is used to denote intrinsic values. We assume that S_0 is constant, meaning that both the pulsar flux density and system parameters are also constant (see §5.4.2).

We describe changes in S_0 with a multiplicative gain factor g such that $S = gS_0$. The PDF of the scintillation gains due to DISS with n_{ISS} scintles contributing to the measured profile is given by a chi-squared distribution with $2n_{\mathrm{ISS}}$ degrees of freedom (Cordes & Chernoff 1997, Appendix B):

$$f_g(g|n_{\mathrm{ISS}}) = \frac{(gn_{\mathrm{ISS}})^{n_{\mathrm{ISS}}}}{g\Gamma(n_{\mathrm{ISS}})} e^{-gn_{\mathrm{ISS}}} \Theta(g). \tag{5.38}$$

Unlike DISS, gains from RISS will vary slowly with both time and frequency. For media that follow a Kolmogorov-type electron density wavenumber spectrum with small refractive modulations, DISS and RISS are decoupled in the strong scattering regime. RISS will have a symmetric PDF if focusing is not important and can be approximated with a Gaussian distribution, $f_{g_{\rm RISS}}(g) = \mathcal{N}(0, \sigma^2_{\rm RISS})$ with some correlation time much greater than the observing duration T (Stinebring et al. 2000). The total gain can be written $g = g_{\rm DISS} g_{\rm RISS}$.

We can solve for the PDF of scintillated pulse S/Ns under a change of variables. Eq 5.38 becomes

$$\begin{aligned} f_S(S|n_{\rm ISS}) &= f_g(g|n_{\rm ISS})\frac{dg}{dS} && (5.39)\\ &= f_g\left(\frac{S}{S_0}\middle| n_{\rm ISS}\right)\frac{1}{S_0} && (5.40)\\ &= \frac{(Sn_{\rm ISS}/S_0)^{n_{\rm ISS}}}{S\Gamma(n_{\rm ISS})}e^{-Sn_{\rm ISS}/S_0}\Theta(S). && (5.41)\end{aligned}$$

We can also quantify the distribution of TOA errors, Δt, from scintillation. Errors solely from template fitting in the unscintillated case, Δt_0, will be normally-distributed, written as

$$f_{\Delta t_0}(\Delta t_0) = \mathcal{N}(0, \sigma^2_{S_0}). \quad (5.42)$$

As in Eq 5.5, we rewrite the rms error is

$$\begin{aligned} \sigma_{\rm S/N} &= \frac{W_{\rm eff}}{S\sqrt{N_\phi}} && (5.43)\\ &= \frac{W_{\rm eff}}{gS_0\sqrt{N_\phi}} && (5.44)\\ &= \frac{\sigma_{S_0}}{g} && (5.45)\end{aligned}$$

Again, under a change of variables, we can write

$$\begin{aligned} f_{\Delta t}(\Delta t|g) &= f_{\Delta t_0}(\Delta t_0)\frac{d\Delta t_0}{d\Delta t} && (5.46)\\ &= g f_{\Delta t_0}(g\Delta t) && (5.47)\end{aligned}$$

For brevity, we will write $Z = |\Delta t|/\sigma_{\Delta t_0}$. The marginal PDF is then

$$\begin{aligned} f_{\Delta t}(\Delta t) &= \int_{-\infty}^{\infty} dg\ f_g(g) f_{\Delta t}(\Delta t|g) && (5.48)\\ &= \int_{-\infty}^{\infty} dg\ g\ f_g(g) f_{\Delta t_0}(g\Delta t_0) && (5.49)\\ &= \int_{-\infty}^{\infty} dg\ g\ e^{-g}\ \Theta(g)\ \frac{1}{\sigma_{S_0}\sqrt{2\pi}}\ \exp\left(-\frac{1}{2}Z^2 g^2\right) && (5.50)\\ &= \frac{1}{\sigma_{S_0}\sqrt{2\pi}} \int_0^{\infty} dg\ g\ e^{-g}\ \exp\left(-\frac{1}{2}Z^2 g^2\right) && (5.51) \end{aligned}$$

From Gradshteyn et al. (2007), Eq. 3.462.1, we have

$$\int_0^{\infty} x^{\alpha-1} e^{-\beta x^2 - \gamma x} dx = (2\beta)^{-\alpha/2}\Gamma(\alpha) e^{\gamma^2/(8\beta)} D_{-\alpha}\left(\frac{\gamma}{\sqrt{2\beta}}\right), \mathrm{Re}\ \beta > 0, \mathrm{Re}\ \alpha > 0, \tag{5.52}$$

where $D_n(x) = 2^{-n/2} e^{-x^2/4} H_n(x/\sqrt{2})$ is the Parabolic Cylinder Function defined in terms of the Hermite Polynomial of order n, $H_n(x)$. For this calculation, we have $\alpha = n_{\mathrm{ISS}} + 1, \beta = \frac{1}{2}Z^2, \gamma = n_{\mathrm{ISS}}$. Thus, we can write

$$\begin{aligned} f_{\Delta t}(\Delta t|n_{\mathrm{ISS}}) &= \frac{1}{\sigma_{S_0}\sqrt{2\pi}} \frac{n_{\mathrm{ISS}}^{n_{\mathrm{ISS}}}}{\Gamma(n_{\mathrm{ISS}})} Z^{-(n_{\mathrm{ISS}}+1)} \Gamma(n_{\mathrm{ISS}}+1) \exp\left(\frac{n_{\mathrm{ISS}}^2}{4Z^2}\right) D_{-(n_{\mathrm{ISS}}+1)}\left(\frac{n_{\mathrm{ISS}}}{Z}\right)\\ &= \frac{1}{\sigma_{S_0}\sqrt{2\pi}} \left(\frac{n_{\mathrm{ISS}}}{Z}\right)^{n_{\mathrm{ISS}}+1} \exp\left(\frac{1}{4}\left(\frac{n_{\mathrm{ISS}}}{Z}\right)^2\right) D_{-(n_{\mathrm{ISS}}+1)}\left(\frac{n_{\mathrm{ISS}}}{Z}\right)\\ &= \frac{1}{\sigma_{S_0}\sqrt{2\pi}} \left(\frac{\sqrt{2}n_{\mathrm{ISS}}}{Z}\right)^{n_{\mathrm{ISS}}+1} H_{-(n_{\mathrm{ISS}}+1)}\left(\frac{n_{\mathrm{ISS}}}{\sqrt{2}Z}\right) && (5.53) \end{aligned}$$

In the case where $n_{\mathrm{ISS}} = 1$, this reduces to

$$f_{\Delta t}(\Delta t|n_{\mathrm{ISS}}) = \frac{1}{\sigma_{S_0}\sqrt{2\pi}} \left(Z^2 - \frac{\sqrt{\pi}\exp\left(\frac{1}{2Z^2}\right)\mathrm{erfc}\left(\frac{1}{\sqrt{2}Z}\right)}{\sqrt{2}Z^3}\right). \tag{5.54}$$

BIBLIOGRAPHY

Antoniadis, J. I. 2013, Ph.D. thesis, Univ. of Bonn

Armstrong, J. W. 1984, Nature, 307, 527

Arzoumanian, Z., Brazier, A., Burke-Spolaor, S., et al. 2015, ApJ, 810, 150

Arzoumanian, Z., Brazier, A., Burke-Spolaor, S., et al. 2015, ApJ, 813, 65

Arzoumanian, Z., Brazier, A., Burke-Spolaor, S., et al. 2015, ApJ, 821, 13

Backer, D. C., Rankin, J. M., & Campbell, D. B. 1975, ApJ, 197, 481

Blandford, R., Romani, R. W., & Narayan, R. 1984, Journal of Astrophysics and Astronomy, 5, 369

Cognard, I., Shrauner, J. A., Taylor, J. H., & Thorsett, S. E. 1996, ApJL, 457, L81

Coles, W. A., Kerr, M., Shannon, R. M., et al. 2015, ApJ, 808, 113

Cordes, J. M. 2002, Single-Dish Radio Astronomy: Techniques and Applications, 278, 227

Cordes, J. M. 2013, Classical and Quantum Gravity, 30, 224002

Cordes, J. M., & Chernoff, D. F. 1997, ApJ, 482, 971

Cordes, J. M., & Downs, G. S. 1985, ApJS, 59, 343

Cordes, J. M., & Lazio, T. J. W. 2002, arXiv:astro-ph/0207156

Cordes, J. M., & Rickett, B. J. 1998, ApJ, 507, 846

Cordes, J. M., & Shannon, R. M. 2010, arXiv:1010.3785

Cordes, J. M., Wolszczan, A., Dewey, R. J., Blaskiewicz, M., & Stinebring, D. R. 1990, ApJ, 349, 245

Cordes, J. M., Kramer, M., Lazio, T. J. W., et al. 2004, NewAR, 48, 1413

Cordes, J. M., Shannon, R. M., & Stinebring, D. R. 2016, ApJ, 817, 16

Craft, H. D., Jr. 1970, PhD thesis, Cornell Univ.

Demorest, P. B. 2007, Ph.D. thesis, Univ. California

Demorest, P. B., Pennucci, T., Ransom, S. M., Roberts, M. S. E., & Hessels, J. W. T. 2010, Nature, 467, 1081

Demorest, P. B., Ferdman, R. D., Gonzalez, M. E., et al. 2013, ApJ, 762, 94

Dolch, T., Lam, M. T., Cordes, J., et al. 2014, ApJ, 794, 21

DuPlain, R., Ransom, S., Demorest, P., et al. 2008, Proc. SPIE, 7019, 70191D

Ford, J. M., Demorest, P., & Ransom, S. 2010, Proc. SPIE, 7740, 77400A

Foster, R. S., & Cordes, J. M. 1990, ApJ, 364, 123

Gradshteyn, I. S., Ryzhik, I. M., Jeffrey, A., & Zwillinger, D. 2007, Table of Integrals, Series, and Products, Seventh Edition by I. S. Gradshteyn, I. M. Ryzhik, Alan Jeffrey, and Daniel Zwillinger. Elsevier Academic Press, 2007. ISBN 012-373637-4,

Hassall, T. E., Stappers, B. W., Hessels, J. W. T., et al. 2012, A&A, 543, A66

Hobbs, G., Lyne, A. G., & Kramer, M. 2010, MNRAS, 402, 1027

Hotan, A. W., van Straten, W., & Manchester, R. N. 2004, PASA, 21, 302

Jenet, F. A., Anderson, S. B., & Prince, T. A. 2001, ApJ, 546, 394

Keith, M. J., Coles, W., Shannon, R. M., et al. 2013, MNRAS, 429, 2161

Kramer, M. 1998, ApJ, 509, 856

Kramer, M., Xilouris, K. M., Lorimer, D. R., et al. 1998, ApJ, 501, 270

Lam, M. T., Cordes, J. M., Chatterjee, S., & Dolch, T. 2015, ApJ, 801, 130

Lambert, H. C., & Rickett, B. J. 1999, ApJ, 517, 299

Lazaridis, K., Wex, N., Jessner, A., et al. 2009, MNRAS, 400, 805

Lentati, L., Hobson, M. P., & Alexander, P. 2014, MNRAS, 444, 3863

Levin, L., McLaughlin, M. A., Jones, G., et al. 2016, ApJ, 818, 166

Liu, K., Verbiest, J. P. W., Kramer, M., et al. 2011, MNRAS, 417, 2916

Liu, K., Keane, E. F., Lee, K. J., et al. 2012, MNRAS, 420, 361

Lorimer, D. R., & Kramer, M. 2012, Handbook of Pulsar Astronomy, by D. R. Lorimer , M. Kramer, Cambridge, UK: Cambridge University Press, 2012,

Lyne, A., Graham-Smith, F., Weltevrede, P., et al. 2013, Science, 342, 598

McLaughlin, M. A. 2013, Classical and Quantum Gravity, 30, 224008

Pennucci, T. T., Demorest, P. B., & Ransom, S. M. 2014, ApJ, 790, 93

Perera, B. B. P., McLaughlin, M. A., Kramer, M., et al. 2010, ApJ, 721, 1193

Phillips, J. A., & Wolszczan, A. 1992, ApJ, 385, 273

Pilia, M., Hessels, J. W. T., Stappers, B. W., et al. 2015, arXiv:1509.06396

Rickett, B. J. 1990, ARA&A, 28, 56

Shannon, R. M., & Cordes, J. M. 2010, ApJ, 725, 1607

Shannon, R. M., & Cordes, J. M. 2012, ApJ, 761, 64

Shannon, R. M., Osłowski, S., Dai, S., et al. 2014, MNRAS, 443, 1463

Shao, L., & Wex, N. 2013, Classical and Quantum Gravity, 30, 1650

Siemens, X. 2013, Classical and Quantum Gravity, 30, 224015

Sotomayor-Beltran, C., Sobey, C., Hessels, J. W. T., et al. 2013, A&A, 552, A58

Stinebring, D. R., Smirnova, T. V., Hankins, T. H., et al. 2000, ApJ, 539, 300

Taylor, J. H. 1992, Royal Society of London Philosophical Transactions Series A, 341, 117

Turin, G. L. 1960, IRE Transactions on Information Theory, IT-6, 3, 311-329

van Haasteren, R., Levin, Y., McDonald, P., & Lu, T. 2009, MNRAS, 395, 1005

van Straten, W., Demorest, P., & Osłowski, S. 2012, Astronomical Research and Technology, 9, 237

Verbiest, J. P. W., Bailes, M., Coles, W. A., et al. 2009, MNRAS, 400, 951

Will, C. M. 2014, Living Reviews in Relativity, 17,

Yan, Z., Shen, Z.-Q., Wu, X.-J., et al. 2015, ApJ, 814, 5

Zhu, W. W., Stairs, I. H., Demorest, P. B., et al. 2015, ApJ, 809, 41

Zhuravlev, V. I., Popov, M. V., Soglasnov, V. A., et al. 2013, MNRAS, 430, 2815

CHAPTER 6

THE NANOGRAV NINE-YEAR DATA SET: EXCESS LONG-TERM CORRELATED NOISE IN PULSAR ARRIVAL TIMES

Gravitational wave experiments using a pulsar timing array require both high timing precision and high timing accuracy of recycled, millisecond pulsars. Pulse arrival times can vary by an amount inconsistent with measurement errors, implying irregularities in the astrophysical clock that must be properly characterized. The timing accuracy of pulsars is fundamentally limited by factors including rotational spin noise, interstellar propagation effects, and low-frequency gravitational waves. We assess the timing stability of 37 pulsars from the North American Nanohertz Observatory for Gravitational Waves by measuring the excess noise in pulsar timing residuals after taking into account the fully-measured white noise model. We find that 27 pulsars show inconsistencies with a white-noise-only model. Using the measurements of excess variance in our observed millisecond pulsars, we further constrain the "timing noise" scaling law of Shannon & Cordes (2010). We describe future strategies for determining the correlation properties of the timing residuals and discuss the implications for gravitational wave detection and observation.

6.1 Introduction

Pulsars are some of the most stable astrophysical clocks in the Universe; recycled millisecond pulsars (MSPs) are the most spin-stable. Such stability allows them to be used as tools in experiments of fundamental physics, including tests of gravitation (e.g., Zhu et al. 2015), constraints on general relativity (Will 2014), and detection of nHz-μHz-frequency gravitational waves (GWs; e.g., Arzoumanian et

al. 2015a, 2016).

GWs will appear as temporally-correlated stochastic deviations from a timing model that includes kinematic and astrometric terms that describe the pulsar-observatory line of sight. Detection of GWs is accomplished by measuring a specific, quadrupolar angular correlation in pulse time of arrival (TOA) deviations from many pulsars distributed over the sky. However, numerous other sources of temporally-correlated noise contaminate our timing models and reduce each pulsar's sensitivity to GWs.

Shannon & Cordes (2010, hereafter SC2010) investigated the strength and non-stationarity of long-term, correlated "red" noise in TOAs from pulsars in the literature. They attributed the red noise to rotational instabilities in individual pulsars, known as spin noise. Arguing that spin noise was the dominant source of red noise in the pulsars, they globally characterized and developed scaling relations of spin noise over all pulsar populations.

Other sources of red noise in TOAs are known. One such source is the interstellar medium (ISM), which causes frequency-dependent time delays in pulse arrival times. The largest effect comes from a dispersive delay proportional to the dispersion measure (DM), the electron density integral along the line of sight, and inverse radio frequency squared. DM is typically estimated using multi-frequency observations and removed by assuming some structure in time. Imperfect estimation of DM, from using incorrect temporal correlations, from combination of asynchronously observed multi-frequency data, or from frequency-dependent DMs due to interstellar scattering, will cause red noise in the timing residuals[1] (Lam et al. 2015; Cordes et al. 2016; Lam et al. 2016b). Other possible noise sources

[1]defined as TOAs minus timing model

that can be temporally correlated are possible, including variations in the pulse broadening function, polarization calibration (e.g., cross-coupling) errors, radio frequency interference (RFI), and pulsar mode changes (see Appendix A of Lam et al. 2016a, hereafter NG9WN).

The North American Nanohertz Observatory for Gravitational Waves (NANOGrav; McLaughlin 2013) is a collaboration that observes a pulsar timing array for the detection and long-term study of GWs. The goal is to correlate arrival time differences in pulses from individual pulsars after a timing model and noise model have been subtracted from each pulsar. Understanding the noise model is crucial for properly calibrating the array for optimal GW sensitivity. This work aims to characterize the timing accuracy of the NANOGrav MSPs, paralleling the results of NG9WN to characterize their timing precision. In §6.2, we describe the methodology for estimating a noise process in the presence of a second, known noise process. In §6.3, we describe the NANOGrav nine-year data set and the implementation of the measured white-noise model for producing residuals. We estimate the excess noise in our MSPs in §6.4. In §6.5, we insert our measurements into the SC2010 dataset and re-derive the scaling relations for excess noise in various pulsar class subsets. We lay out the methods for determining the spectral properties of our timing residuals and discuss other future work in §6.6, and we summarize our conclusions in §6.7.

6.2 Variance of a Stochastic Process with Additive Noise

We want to use pulsar timing residuals to determine the amount of excess variance over the white noise in our pulse arrival times. More generally, we want to measure

the posterior PDF of the variance of a stochastic process when combined with some other independent process, e.g., white noise. Let $y_i = x_i + n_i$ be the measured process that is the sum of two Gaussian processes, where x_i is the stochastic noise process of interest with variance we wish to characterize, n_i is additive white noise, and i will be used to label the individual measurements. We assume that both noise processes are zero mean; it therefore follows that y_i will be zero mean.

Since y_i is a zero mean Gaussian process then the PDF of y_i is simply $\mathcal{N}(0, \sigma_{y_i}^2)$, where $\sigma_{y_i}^2$ represents the variance of y_i. We can separate each $\sigma_{y_i}^2$ into the sum of two variances $\sigma_{x_i}^2 + \sigma_{n_i}^2$. We define the total excess variance over the white noise to be ${\sigma_{\rm ex}}^2 \equiv N^{-1} \sum \sigma_{x_i}^2$. Thus, for each measurement y_i with measurement error σ_{n_i}, we approximate the variance as $\sigma_{y_i}^2 = {\sigma_{\rm ex}}^2 + \sigma_{n_i}^2$. The likelihood function for $\sigma_{\rm ex}$ is then

$$\mathcal{L}(\sigma_{\rm ex}|\{y_i, \sigma_{n_i}\}) = \prod_i \frac{1}{\sqrt{2\pi({\sigma_{\rm ex}}^2 + \sigma_{n_i}^2)}} \exp\left[-\frac{y_i^2}{2({\sigma_{\rm ex}}^2 + \sigma_{n_i}^2)}\right]. \qquad (6.1)$$

The width of the likelihood function (how well we can estimate $\sigma_{\rm ex}$) will depend on the magnitude of the measurement errors σ_{n_i} and on the stationarity of $\sigma_{\rm ex}$. For example, any additional non-stationary noise processes, such as new short-term (i.e., much less than the total data span) RFI, will increase not only the estimated $\sigma_{\rm ex}$ but the error on $\sigma_{\rm ex}$ as well.

6.3 Observational Data: The NANOGrav Nine-Year Data Set

Here we will briefly summarize our data. We used TOAs and parameter files from the NANOGrav nine-year data set described in Arzoumanian et al. (2015b,

hereafter NG9) for our analysis. Multi-frequency observations of thirty-seven MSPs were carried out at the Green Bank Telescope (GBT) and Arecibo Observatory (AO). We used two generations of backends at each telescope, the GASP/GUPPI backends at GBT and the ASP/PUPPI backends at AO (Demorest 2007; DuPlain et al. 2008; Ford et al. 2010; Demorest et al. 2013), with later backends processing a much larger bandwidth for improved pulse sensitivity.

Pulse profiles were folded and de-dispersed using an initial timing model with sufficient accuracy to keep any timing noise from profile shape changes at negligible levels (NG9WN). Polarization calibration and RFI excision algorithms were applied to the raw data profiles using the PSRCHIVE[2] software package (Hotan et al. 2004; van Straten et al. 2012). Prior to every pulsar observation, a broadband noise source was introduced into the two polarization signal paths between the receiver and the backend systems, which allowed for differential gain and phase calibration. We assumed that the noise source power in the two hands of polarization was not constant with time. Therefore, we observed a bright, unpolarized quasar once per month per telescope per frequency to properly calibrate the noise source.

After calibration, known RFI signals were excised, followed by a filtering process that removed data frequency channels in which the off-pulse variation in a 20-channel wide frequency window was four times greater than the median variation value. Throughout the data reduction process, profiles were averaged together in time to reduce the data volume at each stage. The final pulse profiles used to generated TOAs were fully time averaged with some frequency averaging (the amount dependent on bandwidth) to build pulse S/N. The final frequency resolution was of

[2] `http://psrchive.sourceforge.net`, accessed via scripts available at `https://github.com/demorest/nanopipe`

order MHz per channel, sufficient so that timing errors from frequency-dependent pulse profile evolution were negligible across the channel (Pennucci et al. 2014; NG9WN). See NG9 for more details on the data processing.

Summing over both orthogonal polarization pulse profiles produced the intensity profiles used for timing. TOAs were generated from the multi-frequency pulse profiles using a single smoothed template waveform per pulsar per telescope per frequency band and a Fourier-domain estimation algorithm (Taylor 1992). Using the TOAs and an initial timing model as a starting point, we fit timing parameters describing the spin, astrometry, and environmental properties (e.g., binary) of each pulsar. We used the TEMPO[3] software package for all timing parameter estimation. Significance of new parameters was determined by use of an F-test.

On a given epoch, we observed each pulsar over at least two frequency bands to estimate the dispersive delay due to the changing dispersion measure (DM), the integral of electron density along the line of sight. We included one DMX parameter per epoch which described the difference from some fixed reference DM. In addition, between zero and five frequency-dependent terms (FD) modeling the time-independent pulse profile evolution were fit.

Lastly, NG9 used a parameterized noise model that includes both white and red noise terms correlated differently in time and frequency. The noise model estimation starts with the template-matching TOA measurement error and increases them with a scaling factor (EFAC) and adding additional variances in quadrature: one that characterizes the correlations between frequency bands due to processes such as pulse jitter or radio frequency interference (ECORR), and one that characterizes additional additive noise (EQUAD). Finally, red noise (RN) correlated in

[3] `http://tempo.sourceforge.net`

time was assumed to be a Gaussian process with a power-law spectrum. Complete definitions for the parameters are provided in NG9. The noise parameters were estimated with a Bayesian inference package[4] and fit for in a joint likelihood with the timing model parameters. Both parameter (par) and TOA (tim) files from the NG9 data release are available at `https://data.nanograv.org`.

6.4 Excess Variance Estimation

We now wish to estimate the amount excess variance in our timing residuals beyond the white-noise model described in NG9WN. Starting with the NG9 data release, we first remove all noise parameters from the par files to avoid biasing our results. We choose to keep all achromatic timing parameters for refitting. Parameters that are or are not introduced as significant by the F-test criterion as a result of the Bayesian noise model estimation will bias our variance estimation. However, the largest contributors to the timing fit are the spin and astrometric terms, all of which are fit. Introduction of higher-order binary terms, for example, will not significantly reduce the variance from a long-term, correlated process such as power law red noise but the spin frequency and spin frequency derivative parameters are linear and quadratic terms, respectively, and are highly covariant with the red noise; variance removed as a result of the fit for these two terms will be discussed later.

We fix the frequency-dependent FD and DMX parameters in our fit to the values estimated in NG9. In many cases, TEMPO will attempt to minimize the χ^2 of the overall timing fit by separating the TOAs from different frequency bands

[4] `https://github.com/jellis18/PAL2`

within a given epoch to produce residuals at different pulse phases as a function of frequency band. The splitting of residuals results from power preferentially being absorbed by the achromatic spin and astrometric terms, i.e., there is covariance between the the achromatic and chromatic parameters. In fixing the frequency-dependent terms, we assume that the TOAs previously fit over a given epoch are closely represented by the infinite-frequency value plus noise. Changes in the FD and DMX parameters from our fit should be non-zero but we assume them to be small in comparison to the total excess variance. DM mis-estimation error, as well as errors from other frequency-dependent effects ignored in the timing fit (e.g., temporal changes in interstellar scattering), will introduce excess noise into the timing residuals that will be included in the overall noise budget but again should not change greatly as a result of fixing the FD and DMX parameters.

We remove pulsar/backend combinations from our analysis where white-noise parameters could not estimated due to low pulse S/N. Otherwise, we add the jitter ($\sigma_{\rm J}$) and diffractive interstellar scintillation ($\sigma_{\rm DISS}$) errors from NG9WN in quadrature to the template-fitting errors after scaling them appropriately with time, such that

$$\sigma_{\rm S/N} \rightarrow \sqrt{\sigma^2_{\rm S/N} + \sigma^2_{\rm J}(t_{\rm obs}) + \sigma^2_{\rm DISS}(B_{\rm obs}, t_{\rm obs})}, \tag{6.2}$$

where $t_{\rm obs}$ is the total time span of the observation and $B_{\rm obs}$ is the channel bandwidth of each TOA (much less than the total of the observing band). The jitter noise $\sigma_{\rm J}$ is proportional to $t_{\rm obs}^{-1/2}$. The scintillation noise non-trivially scales with bandwidth and time according to the formula

$$\begin{aligned} \sigma_{\rm DISS} &\approx \frac{\tau_d}{\sqrt{n_{\rm ISS}}} \\ &\approx \tau_d \left[\left(1 + \eta_t \frac{T}{\Delta t_{\rm d}}\right) \left(1 + \eta_\nu \frac{B}{\Delta \nu_{\rm d}}\right) \right]^{-1/2}. \end{aligned} \tag{6.3}$$

Table 6.1. Variations in Noise Models

Model	$\sigma_{\rm S/N}$	EFAC	EQUAD	ECORR	RN	$\sigma_{\rm J}$	$\sigma_{\rm DISS}$	Fixed DMX/FD
A	×	×	×	×	×			
B	×							×
C	×					×	×	×

where τ_d is the scattering timescale, $n_{\rm ISS}$ is the number of scintles, $\Delta t_{\rm d}$ and $\Delta\nu_{\rm d}$ are the scintillation bandwidth and timescale respectively, T is the observation duration, and B is the observation bandwidth. The filling factors η_t, η_ν are typically in the range 0.1 to 0.3 (Cordes & Shannon 2010; Levin et al. 2016), we choose them to be 0.2 as in NG9WN. They also choose to scale jitter and scintillation noise to 30 minute observations and bandwidths equal to the that of the full band (rather than the channel banwidth), as provided in NG9. After we construct our new TOA errors, we use TEMPO to refit the timing model. For pulsars with upper limits on $\sigma_{\rm J}$, we set the value of $\sigma_{\rm J}$ we use equal to its 95% upper limit, providing us a conservative lower bound on the excess noise.

Table 6.1 provides a summary of three noise models we test in this section. Model A is directly from NG9. Model B removes all additional noise parameters except for the template-fitting errors on the TOAs. Note that in order to achieve a phase-connected solution between frequency bands, we must currently fix frequency-dependent timing parameters as discussed previously. Model C starts with Model B and adds in the jitter and scintillation noise parameters from NG9WN. It is the noise model we test most thoroughly in this paper.

We show a comparison of the timing residuals for PSR B1937+21 obtained from the three noise models in Figure 6.1. PSR B1937+21 has the smallest template-

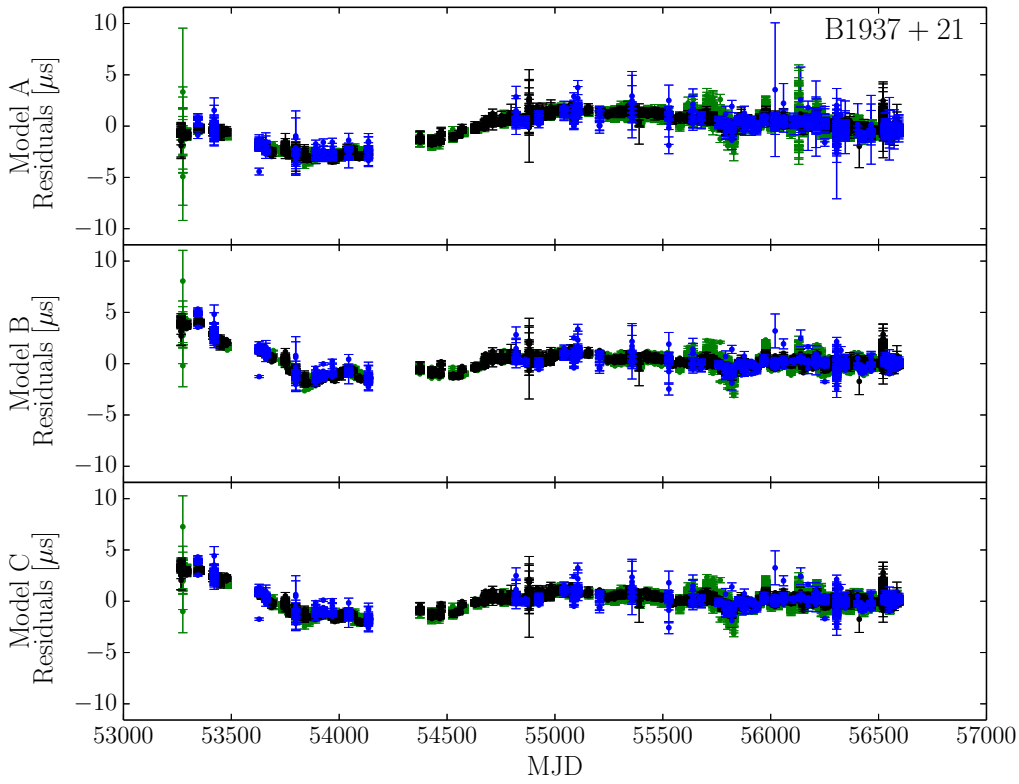

Figure 6.1: Comparison of residuals using the different noise models defined in Table 6.1. Colors indicate different bands, with green being 820 MHz, black being 1400 MHz, and blue being 2300 MHz.

fitting and jitter errors in NG9 within each given frequency band both at AO and GBT (NG9WN) while its scintillation noise is the largest of the three white-noise terms, which is atypical for pulsars in our data set. We show its residuals as an example to demonstrate the effect of the timing model refit because it is not dominated by template fitting errors and has known red noise residuals (e.g., Shannon & Cordes 2010; Arzoumanian et al. 2015b). As expected visually from Figure 6.1, we see PSR B1937+21 contains well-measured excess noise beyond the white-noise model.

Using the Model C residuals, we follow the methodology laid out in §6.2 for cal-

culating the excess noise. Figure 6.2 shows the results of the maximum likelihood analysis for measured excess noise in the NANOGrav pulsars using the Model C residuals. Detections are shown with the maximum likelihood value with ±34.1% errors. Non-detections are shown as 95% upper limits. All values are shown unnormalized to the length of the data span; we expect longer data sets to show increased excess noise, either from the presence of red noise or from increased probability of other noise sources (e.g., RFI) being introduced. We note that in SC2010, they consider the excess noise after a quadratic fit for spin frequency and frequency derivative over the timing residuals. Hereafter, we define the excess noise similarly to prevent the need for a prior model for the true excess noise and to keep our results consistent with theirs.

PSRs J1909−3744 and J1713+0747 are two of the best timers observed by NANOGrav, both high in S/N with very low white-noise parameters (NG9WN). We note that they also show the lowest amounts of excess noise of all of the NANOGrav pulsars. Many of the pulsars with the highest measured values are consistent with those that displayed "significant" red noise in NG9. Five of the top seven detections, PSRs J1643−1224, J1903+0327, J1910+1256, J1944+0907, and B1953+29, were all those in NG9 for which unmodeled ISM propagation effects were claimed to be the dominant cause of the the excess noise. For the other two, PSR J1012+5307 also showed measurable red noise in NG9. PSR J1923+2515 shows offset timing residuals at the lower frequency band (430 MHz) from the older ASP backend, suggesting an instrumental effect causing the large measured excess noise. The effect of instrumental biases are being explored in the next NANOGrav data release (Arzoumanian et al., in prep.).

In Figure 6.3, we explore the possible relationship between $\sigma_{\rm ex}$ and ISM noise

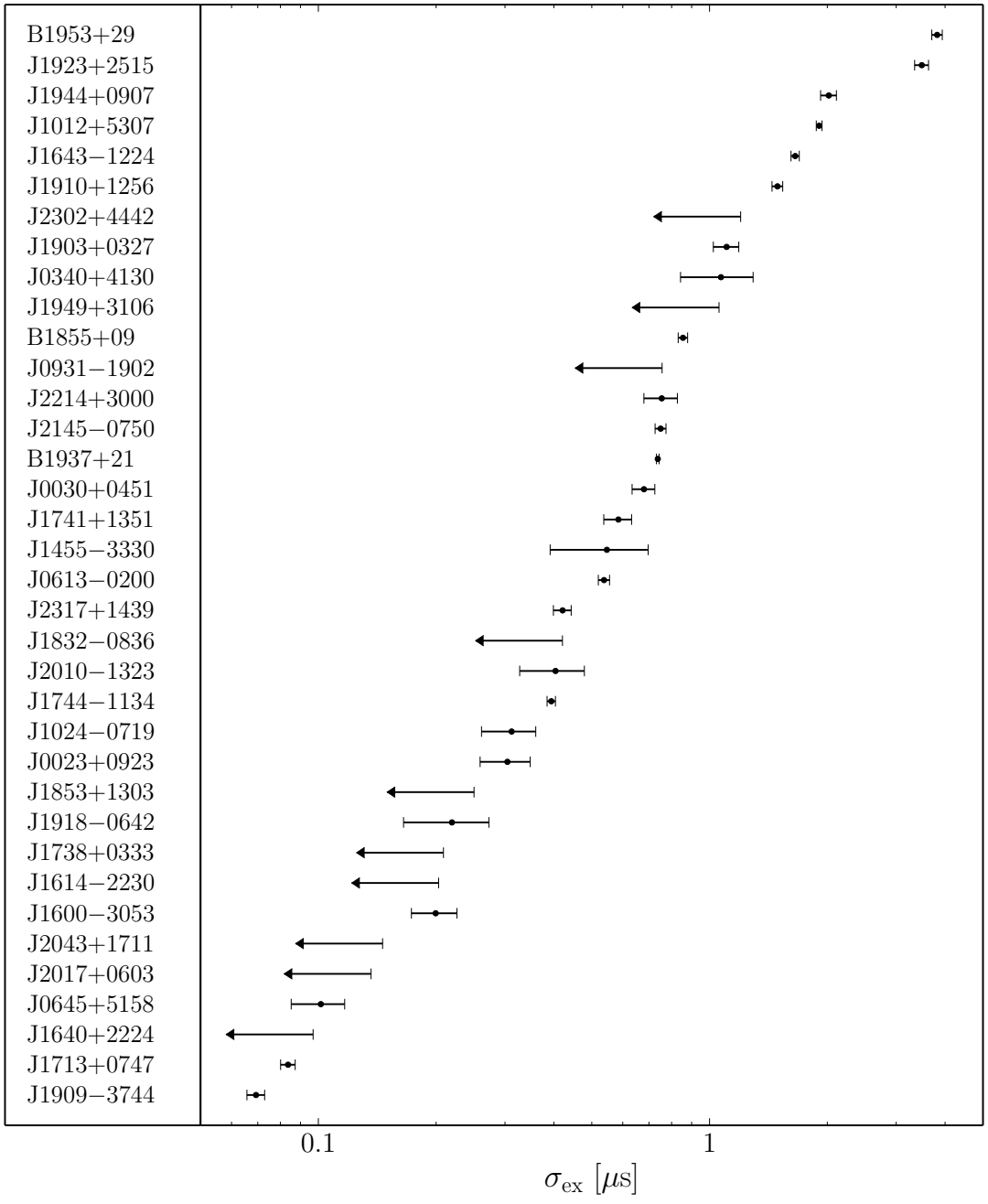

Figure 6.2: Measured excess noise for each of the NANOGrav pulsars ranked by decreasing value. Detections are shown with the maximum likelihood value and 34.1% errors. Upper limits are shown at the 95% level.

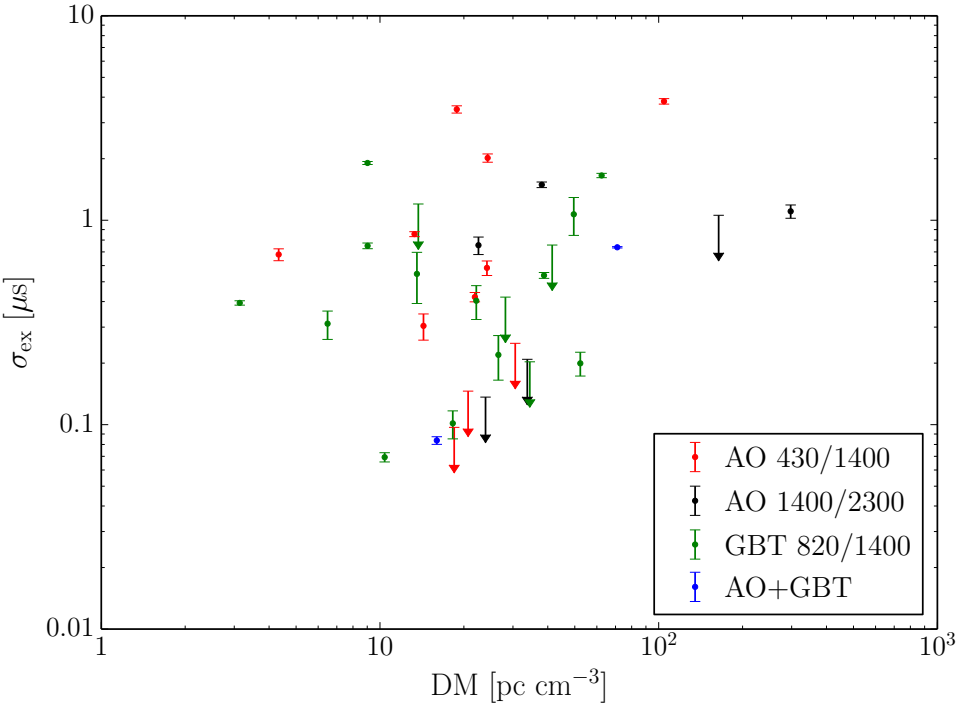

Figure 6.3: Excess noise in NANOGrav pulsars versus DM. Colors denote which telescope and frequency bands were used to observe a pulsar. The two blue points represent PSRs J1713+0747 (820/1400 at GBT and 1400/2300 at AO) and B1937+21 (820/1400 at GBT and 430/1400 at AO).

by plotting versus DM. Colors show which telescopes and frequency bands were used to observe each pulsar. No significant trend is found between the points.

6.5 Global Scaling Law Maximum Likelihood Analysis

We assume that the excess noise is a function of ν and $\dot{\nu}$, the spin frequency and spin frequency derivative, respectively, as well as a function of observing time span T. Figure 6.4 shows the excess noise as a function of these three observables. The different pulsar populations are displayed with differently shaped symbols and we explicitly separate the NANOGrav pulsars from the other MSPs provided in

SC2010. Detections of excess noise are given by the filled symbols and upper limits are given by the unfilled ones.

SC2010 attributes $\sigma_{\rm ex}$ to rotational spin noise alone and thus the excess noise would be a function of the two basic pulsar spin observables and time. They argue that for most pulsars, spin noise is the dominant source of excess noise. At the timing precision level of MSPs, it is not clear that spin noise should be the dominant term. In fact, we expect additional errors from sources previously listed (i.e., ISM, polarization calibration, GWs). However, while the MSP (including NANOGrav pulsars) spin noise values will be biased, the trends in overall excess noise as shown in Figure 6.4 remain the same. Therefore, we believe that using the three-observable formalism with parameters that only represent spin noise is adequate to describe the excess noise in general though more parameters may be required in the future. For example, if a trend is present in Figure 6.3, then a scaling in DM should be included in the fit.

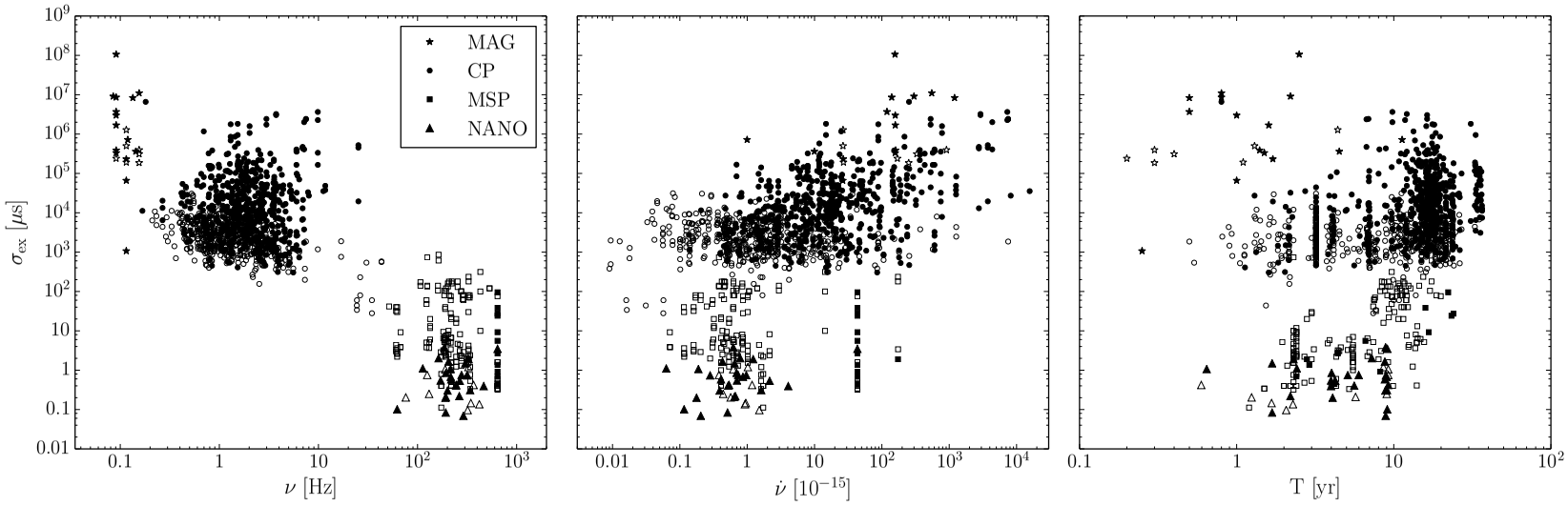

Figure 6.4: Measured excess noise versus spin frequency (left), spin frequency derivative (middle), and observing time span (right). Stars indicate magnetars (MAGs), circles indicate canonical pulsars (CPs), and squares indicate millisecond pulsars (MSPs), all from Shannon & Cordes (2010). Triangles indicate NANOGrav MSPs (NANO) with measurements derived from this work. Filled symbols indicate detections of excess noise while unfilled symbols indicate upper limits.

Following SC2010, we write the rms excess after a quadratic fit as

$$\hat{\sigma}_{\rm ex}(\nu, \dot{\nu}, T | C_2, \alpha, \beta, \gamma) = C_2 \nu_{\rm Hz}^{\alpha} |\dot{\nu}_{-15}|^{\beta} T_{\rm yr}^{\gamma} \ \mu{\rm s} \tag{6.4}$$

where $\mathrm{C}_2, \alpha, \beta,$ and γ are parameters to be estimated over each pulsar included in the analysis. For detections of excess noise, we assume that the variance is log-normally distributed, represented with a PDF

$$f_{\rm D}(\sigma_{\rm ex} | \{\nu, \dot{\nu}, T\}, \{C_2, \alpha, \beta, \gamma, \delta\}) = \\ \frac{1}{\sqrt{2\pi\delta^2}} \exp\left(-\frac{[\ln \sigma_{\rm ex} - \ln \hat{\sigma}_{\rm ex}(\nu, \dot{\nu}, T | C_2, \alpha, \beta, \gamma)]^2}{2\delta^2} \right). \tag{6.5}$$

For upper limit measurements on the excess noise, we use the survival function of the log-normal distribution (e.g., see Lawless 2005 for a review, noting that an upper limit likelihood is equivalent to a left-censored distribution, or 1 minus the survival function) to calculate the appropriate distribution for upper limits as

$$f_{\rm UL}(\sigma_{\rm ex} | \{\nu, \dot{\nu}, T\}, \{C_2, \alpha, \beta, \gamma, \delta\}) = \\ \frac{1}{2} \left(1 + {\rm erf} \left[\frac{\ln \sigma_{\rm ex} - \ln \hat{\sigma}_{\rm ex}(\nu, \dot{\nu}, T | C_2, \alpha, \beta, \gamma)}{\delta \sqrt{2}} \right] \right), \tag{6.6}$$

where erf is the error function. We note that the order of the argument to erf presented here corrects a typo in SC2010, which is reversed by a negative sign. Introduction of the typo into our likelihood code allowed us to recover parameters consistent with those reported in SC2010 for different pulsar population subsets except for the MSP-only case, in which we were unable to recover the parameters. Since only two pulsars (though many more measurements) were measured to have excess noise in SC2010, there are large covariance between the parameters because of the "steepness" of the fits (all but one measurement have the same ν and $\dot{n}u$). Therefore, we ignore the MSP-only case in our analysis.

We define our five-parameter likelihood function as

$$\mathcal{L}(C_2, \alpha, \beta, \gamma, \delta | \{\sigma_{\mathrm{ex},i}, \nu_i, \dot{\nu}_i, T_i\}) = \prod_j f_{\mathrm{D}}(\sigma_{\mathrm{ex},j} | \{\nu_j, \dot{\nu}_j, T_j\}, \{C_2, \alpha, \beta, \gamma, \delta\}) \times \prod_k f_{\mathrm{UL}}(\sigma_{\mathrm{ex},k} | \{\nu_k, \dot{\nu}_k, T_k\}, \{C_2, \alpha, \beta, \gamma, \delta\}) \quad (6.7)$$

where i labels all of the individual measurements, j labels the subset of measurements with detected excess variance, and k labels the subset of measurements with upper limits on the excess variance. We perform a linear grid search over the five parameters $\ln C_2, \alpha, \beta, \gamma, \delta$ with range and resolution to sufficiently sample the parameter space. For computational stability, we first compute the log-likelihood as the sum of the PDFs in Eq. 6.7.

Figure 6.5 shows the likelihood analysis run with all pulsars included. Parameters are estimated by taking the one-dimensional marginalized distributions, computing the CDF, and finding the 34.1% confidence regions. We perform a similar analysis over different subsets of the pulsar populations and provide out results in Table 6.2. Again, since the MSP-only case is not constraining, we do not report it.

Figure 6.6 shows the measured excess noise versus the model excess noise using the parameters when the maximum likelihood is computed for all pulsars. The addition of the NANOGrav pulsars to the fit helps constrain the power law relations at lower ν and $\dot{\nu}$ as compared with SC2010, which only contained (multiple estimates of) detected noise in two MSPs.

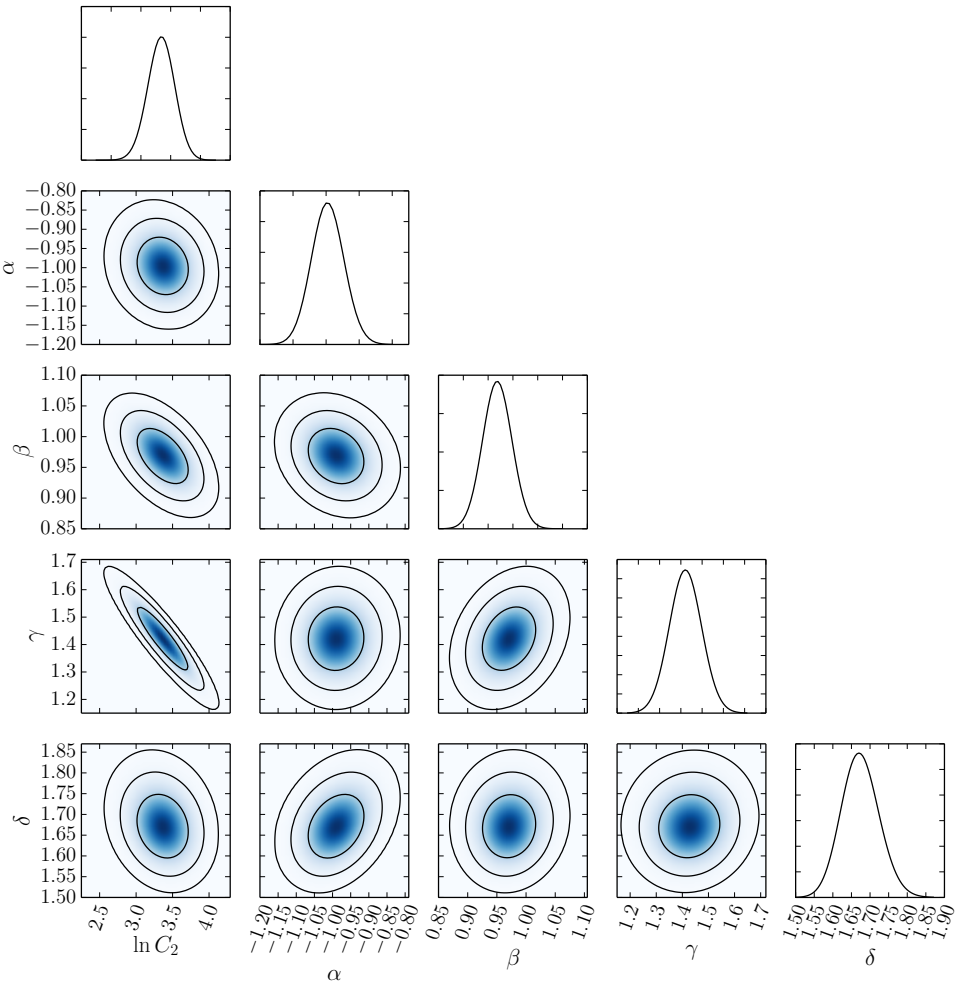

Figure 6.5: Global maximum likelihood analysis results when computed for all pulsars. The colored regions show the two-dimensional marginalized distributions, with the contours encapsulating the 68.3%, 95.5%, and 99.7% of the total probability. The line plots show the one-dimensional marginalized distributions from which the parameter estimates are calculated.

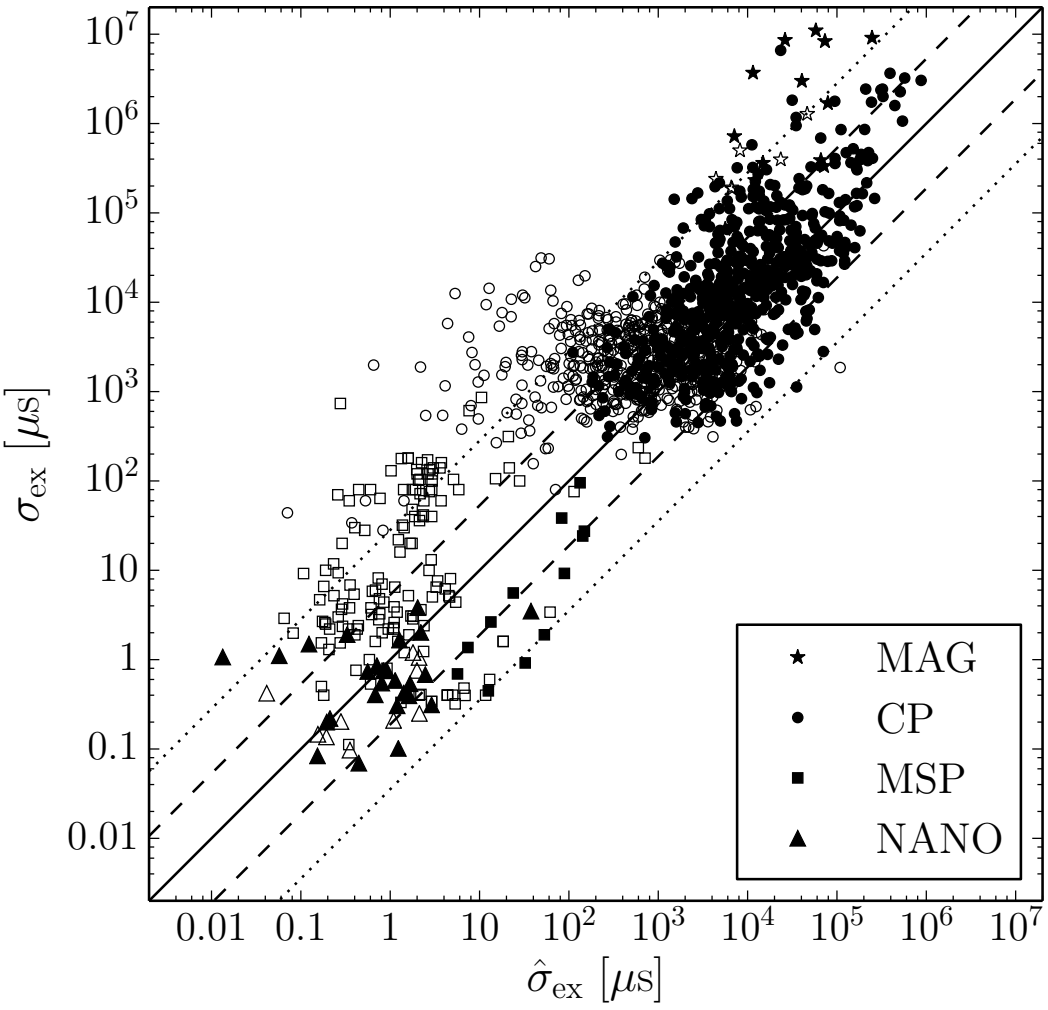

Figure 6.6: Measured excess noise versus model excess noise from Eq. 6.4 and using global parameters fit for over all pulsars as given in Table 6.2. Symbols are as defined in Figure 6.4, with filled symbols being detections and open symbols being upper limits. The solid line shows where the measured excess noise equals the model excess noise, and the dashed and dotted lines show the 1 and 2σ errors as estimated by δ, respectively.

Table 6.2. Best-fit Excess Noise Parameters

Fit	$\ln C_2$	α	β	γ	δ	$N_{\rm D}(N_{\rm UL})$[a]
CP	2.1 ± 0.3	-0.85 ± 0.09	0.99 ± 0.04	1.86 ± 0.09	1.54 ± 0.05	575(458)
MAG	9 ± 6	1 ± 3	1.4 ± 0.4	1.9 ± 0.7	1.9 ± 0.5	15(7)
NANO	2 ± 4	-0.4 ± 0.7	0.4 ± 0.3	-0.1 ± 0.3	1.0 ± 0.2	27(9)
CP+MAG	2.6 ± 0.3	-1.37 ± 0.08	1.11 ± 0.04	1.66 ± 0.08	1.64 ± 0.05	590(465)
CP+MSP	2.5 ± 0.3	-0.60 ± 0.07	0.86 ± 0.03	1.73 ± 0.09	1.63 ± 0.05	587(605)
MSP+NANO	18 ± 8	-3 ± 1	0.4 ± 0.4	1.3 ± 0.6	3.6 ± 0.6	39(156)
CP+MSP+NANO	2.5 ± 0.2	-0.83 ± 0.05	0.93 ± 0.03	1.72 ± 0.08	1.60 ± 0.05	614(614)
CP+MAG+MSP	3.2 ± 0.3	-0.99 ± 0.09	0.98 ± 0.04	1.48 ± 0.09	1.68 ± 0.05	602(612)
CP+MAG+MSP+NANO	3.3 ± 0.2	-1.00 ± 0.05	0.97 ± 0.03	1.42 ± 0.08	1.67 ± 0.05	629(621)

[a] $N_{\rm D}$ are the number of detected measurements of excess noise while $N_{\rm UL}$ are the number of upper limit measurements.

6.6 Future Work

Our first maximum likelihood analysis allowed us to characterize the total excess noise in the NANOGrav data set. Moving forward, we will break the total noise into its constituent components. For example, we can estimate two of the contributions of ISM noise: DM mis-estimation errors from non-simultaneous multi-frequency observations (Lam et al. 2015) and errors from improper fitting of frequency-dependent DM due to multipath propagation (Cordes et al. 2016). Limits on other sources of excess noise, such as from polarization calibration errors, can also be explored.

Besides measuring the total variance of individual pulsar residual time series, the spectral properties of each are also of interest. We can average together residuals within an epoch, which allows us to characterize the long-term correlated fluctuations with time rather than variations on a per-frequency-channel level largely associated with white noise. Epoch-averaged residuals can be constructed by calculating the covariance matrix from the white-noise model as described in Arzoumanian et al. (2015a).

One common method for estimating the spectral properties of a time series is with a Fourier-based method, such as a Lomb-Scargle periodogram for unequally sampled data (Lomb 1976; Scargle 1982). However, Fourier-based spectral estimators suffer from spectral leakage resulting from a finite time series data span. We can represent the data span as a window function $W(t)$ weighting an infinite data span such that the weights equal one within the time range and zero otherwise. The original spectrum of the infinite time series is then convolved with the spectral window function $|\tilde{W}(f)|^2$ to yield the measured power spectrum (e.g., see Coles et al. 2011). Since the sidelobes of the spectral window function fall of as

f^{-2}, power-law spectra with a spectral index steeper than 2 will be biased. Coles et al. (2011) suggest pre-whitening the time series via a Cholesky decomposition of the covariance matrix. The analysis is typically completed in stages since the spectral index is not known a priori. Each application of the pre-whitening filter reduces the observed spectral index by 2, allowing the unbiased spectral index to be recovered with a Fourier-based method.

Other methods exist for estimating a time series' spectral properties. A maximum entropy spectral estimator does not suffer from the effects of leakage described above though typically requires interpolation of the time series to an evenly sampled grid, which can cause artifacts in the resultant spectrum (especially interpolation at high polynomial order). A structure function analysis is useful for operating in the time domain while taking into account uneven sampling of the time series. Since low-order structure functions will saturate with increasing power laws in time lag τ, higher order structure functions can be used to estimate steeper spectra. However, higher orders require improved time sampling to adequately estimate the higher-order increments, which are a function of increased number of time series samples.

The quadratic fit for ν and $\dot{\nu}$ in the timing model will remove power from the noise spectrum and cause mis-estimation of the true spectral slope. Given the measured spectral slope, we can estimate the true spectral slope via two methods. First, we can simulate power-law noise, fit a quadratic polynomial, and calculate the variance loss over many realizations. The fractional variance loss will be greater for steeper power-law spectra. Second, we can more directly estimate the power loss by analytically calculating the transmission function and applying it to a given power spectrum (e.g., Madison et al. 2013). Either method will allow us to estimate

the true spectral index of the underlying noise process.

6.7 Conclusions

We examined the amount of excess noise in NANOGrav timing residuals beyond the measured white noise. After re-weighting our TOAs, we detect excess noise in 27 of our pulsars. The addition of measurements from the NANOGrav pulsars helps constrain the scaling relations first derived in SC2010 by anchoring the fit at lower ν and $\dot{\nu}$. Future work in splitting the excess noise into components can help further attribute the proper amount of noise to rotational instabilities and further bound the relations to spin noise.

For a Gaussian process with power spectrum $S(f) \propto f^{-\gamma_{\rm red}}$, the spectral index $\gamma_{\rm red}$ is related to the maximum likelihood parameter γ by $\gamma_{\rm red} = 2\gamma + 1$ (Arzoumanian et al. 2015b). Therefore, for $\gamma = 1.42 \pm 0.08$, a time series described with a power-law spectrum will have spectral index $\gamma_{\rm red} = 3.84 \pm 0.16$. The NANOGrav-pulsar-only fit with γ consistent with zero yields a shallower spectral index $\gamma_{\rm red} \approx 2$, and therefore our results are consistent with the overall finding in NG9 (note that our definition of $\gamma_{\rm red}$ differs by a minus sign.

As demonstrated by the Laser Interferometer Gravitational-Wave Observatory's recent detection of GWs, understanding the noise within the detector is imperative for the instrument's capability to detect GWs (Abbott et al. 2016)[5]. With NANOGrav and other collaborations moving towards the detection of low-frequency GWs, we require full noise characterization of the NANOGrav pulsar

[5]See also "Characterization of transient noise in Advanced LIGO relevant to gravitational wave signal GW150914", `https://dcc.ligo.org/public/0122/P1500238/022/P1500238_GW150914_noise_characterization.pdf`

timing array. Implementation of the full noise model we describe will help remove biases on timing parameter estimation and improve sensitivity towards the growing GW signal in our data.

BIBLIOGRAPHY

Abbott, B. P., Abbott, R., Abbott, T. D., et al. 2016, Physical Review Letters, 116, 061102

Arzoumanian, Z., Brazier, A., Burke-Spolaor, S., et al. 2015, ApJ, 810, 150

Arzoumanian, Z., Brazier, A., Burke-Spolaor, S., et al. 2015, ApJ, 813, 65

Arzoumanian, Z., Brazier, A., Burke-Spolaor, S., et al. 2015, ApJ, 821, 13

Coles, W., Hobbs, G., Champion, D. J., Manchester, R. N., & Verbiest, J. P. W. 2011, MNRAS, 418, 561

Cordes, J. M., & Shannon, R. M. 2010, arXiv:1010.3785

Cordes, J. M., Shannon, R. M., & Stinebring, D. R. 2016, ApJ, 817, 16

Demorest, P. B. 2007, Ph.D. thesis, Univ. California

Demorest, P. B., Ferdman, R. D., Gonzalez, M. E., et al. 2013, ApJ, 762, 94

Dewey, R. J., & Cordes, J. M. 1989, in Timing Neutron Stars, ed. H. Ögelman & E. P. J. van den Heuvel (New York, NY: Kluwer/Plenum), 119

DuPlain, R., Ransom, S., Demorest, P., et al. 2008, Proc. SPIE, 7019, 70191D

Ford, J. M., Demorest, P., & Ransom, S. 2010, Proc. SPIE, 7740, 77400A

Hotan, A. W., van Straten, W., & Manchester, R. N. 2004, PASA, 21, 302

Lam, M. T., Cordes, J. M., Chatterjee, S., & Dolch, T. 2015, ApJ, 801, 130

Lam, M. T., Cordes, J. M., Chatterjee, S., et al. 2016, ApJ, 819, 155

Lam, M. T., Cordes, J. M., Chatterjee, S., et al. 2016, ApJ, 821, 66

Lawless, J. F. 2005, Parametric Models in Survival Analysis, Encyclopedia of Biostatistics, 6

Levin, L., McLaughlin, M. A., Jones, G., et al. 2016, ApJ, 818, 166

Lomb, N. R. 1976, Ap&SS, 39, 447

Madison, D. R., Chatterjee, S., & Cordes, J. M. 2013, ApJ, 777, 104

McLaughlin, M. A. 2013, Classical and Quantum Gravity, 30, 224008

Pennucci, T. T., Demorest, P. B., & Ransom, S. M. 2014, ApJ, 790, 93

Scargle, J. D. 1982, ApJ, 263, 835

Shannon, R. M., & Cordes, J. M. 2010, ApJ, 725, 1607

Shannon, R. M., Cordes, J. M., Metcalfe, T. S., et al. 2013, ApJ, 766, 5

Taylor, J. H. 1992, Royal Society of London Philosophical Transactions Series A, 341, 117

van Straten, W., Demorest, P., & Osłowski, S. 2012, Astronomical Research and Technology, 9, 237

Will, C. M. 2014, Living Reviews in Relativity, 17,

Zhu, W. W., Stairs, I. H., Demorest, P. B., et al. 2015, ApJ, 809, 41

CHAPTER 7

FUTURE DIRECTIONS

In this chapter, we will briefly cover directions for future expansion on the work we have presented. We will continue with the characterization of pulsars and interstellar medium, leading to the eventual application of our work in timing and noise models for pulsar timing arrays.

7.1 Epoch-Dependent Refraction in the Interstellar Medium

Electron-density fluctuations in the interstellar medium (ISM) will alter the path of propagating radio waves as they pass through. Refraction of the source image causes a change in the position and shape (i.e., ellipticity) of the measured image, resulting in timing and intensity perturbations of observed pulses. We expect that pulsar timing observables, such as flux, scintillation bandwidth, scintillation timescale, etc., will be time-varying but correlated as refraction modulates the measured diffractive pattern. We observed PSR J2317+1439 at 327 MHz over six months at the Arecibo Observatory. We collected baseband data so that we could resolve the small scintles. With our data set, we can measure the different observables and test if the temporal variations in the observables can be described by changes in the image due to refraction. We can compare our results to those in the literature (e.g., Coles et al. 2015) for several other pulsars where various levels of correlation are observed, suggesting that refraction is a contributor to the time variability of the parameters along those lines of sight.

7.2 Constraining Spatial Anisotropies in Electron Density Wavenumber Spectra

Spatial variations in interstellar electron density are assumed to have a Kolmogorov-like wavenumber spectrum consistent with a large number of past measurements (see Chapter 4 for more information and references). The wavenumber spectrum is assumed to be a power law extending over a large range of wavenumbers q. The wavenumber range corresponds to electron-density length scales $l \equiv 2\pi/q$ probed in the ISM. The minimal length scale probed by pulsar observations comes from the scintillation timescale. For pulsars with a scintillation timescale $\Delta t_{\rm ISS} \sim 100$ s (on the shorter side for the typical pulsars we observe) traveling with velocity $v \sim 100$ km/s, the associated length scale probed is 10^4 km. Temporal variations in dispersion measure (DM) probe larger length scales; a pulsar moving with velocity $v \sim 100$ km/s over 10 years samples DM variations up to order mpc length scales. Using DM measurements from globular cluster pulsars (e.g., Ransom 2008), we can extend the range of length scales probed by measuring spatial variations in DM. For a globular cluster 10 kpc distant, pulsars separated by 1 arcsec will sample DM variations over a length scale of 0.05 pc, an order of magnitude larger than those sampled by temporal variations. Thus, we can further constrain the electron-density wavenumber spectra along those lines of sight over a greater range of wavenumbers.

Using DM measurements of globular cluster pulsars, we can also constrain anisotropies in the spatial variations, known from a number of past observations in the literature, such as scintillation arcs and ellipticity of scattered images (Cordes et al. 2006; Brisken et al. 2010). The anisotropic wavenumber spectrum can be written as a stretched version of the isotropic spectrum for simplicity, which pro-

vides an analytically tractable model with only a few additional parameters. Such power spectra are related to the spatial DM structure function, which can be sampled adequately if enough pulsar pairs can be observed. Therefore, we will target the globular clusters 47 Tucanae and Terzan 5, where each contain over 25 known millisecond pulsars. Combined with temporal DM measurements, we can directly probe anisotropies along both lines of sight.

7.3 Single Pulse Statistics and the Timing Noise Budget of PSR J1713+0747

In Chapter 2, we showed noise analyses of PSR J1713+0747 from timescales $\lesssim$ 1 day down to the timescale of seconds, the lower subintegration lengths from the telescopes used to observe the pulsars. The wealth of baseband data available from the campaign will allow for analyses to be performed directly on single pulses from one of the brightest and best-timed millisecond pulsars observed. We will be able to look for noise sources on the full 0-24 hour timescales that might limit our timing precision. We can employ a variety of techniques on single pulse data from a subset of the nine-telescope observation to constrain timing precision in current and future pulsar observations.

Such work has been mentioned in the list of follow-up projects in Chapter 2 (§5). The goals of this project include: (i) determining the types of pulse-to-pulse variations present; (ii) searching for the presence of or placing limits on state-change phenomena, such as mode changes; (iii) quantifying the amount of pulse phase and amplitude jitter; (iv) quantifying the frequency-dependent profile evolution of the pulse and the effect of its mis-estimation; and (v) quantifying

the rate of convergence of profiles and times of arrival versus the number of pulses averaged. We expect that an assessment of the three dominant white-noise terms in pulse arrival time errors (template fitting, jitter, and scintillation noise) will yield consistent results with those presented in Chapter 5 though we can verify that statement with these independent data. Any additional sources of noise found at the single pulse level can drastically alter our current prescription for a pulsar timing noise model. Placing limits on such noise sources is important for testing our assumptions of pulse profile stability in all pulsars used within a pulsar timing array.

7.4 Metrics for Pulsar Timing Quality

Using our current pulsar noise characterization, we can develop metrics for determining how well a pulsar will perform in a pulsar timing array. We can separate our metrics into two categories: those relying on pulsar-dependent parameters and those on observing parameters. Therefore, we can determine how intrinsically "good" a pulsar will perform and then how well it perform in the context of different observing setups (i.e., performance by new telescopes).

In Chapter 5, we discussed the three contributions to white noise in TOAs. The template fitting error depends on the effective width and the average signal-to-noise (S/N) ratio of the pulse. Scintillation can modulate the S/N, and so the scintillation bandwidth and timescale, which effect the number of scintles observed, must also be considered. The jitter noise can be parameterized as an rms timing perturbation at the single pulse level and will also depend on the pulse period (assuming constant observing times between pulsars). Scintillation noise will de-

pend on the two scintillation parameters. Spin noise has been shown to depend on the spin frequency and frequency derivative of the pulsars, as well as the total observing time span (Shannon & Cordes 2010; Chapter 6). Combining all of the parameters mentioned into suitable metrics will allow us to quantify how good of a timer a pulsar will be intrinsically.

Observatory-specific parameters, such as telescope area and system equivalent flux density, will directly affect the observed S/N and modify how well a given pulsar might perform. The choice of radio frequencies also alters the S/N since pulsar spectra are not flat. Different radio frequencies also change errors from interstellar propagation effects, e.g., asynchronous DM estimation (Chapter 3) or frequency-dependent DM (Cordes et al. 2016). Augmenting the intrinsic pulsar parameters with observatory parameters will allow us to quantify how good of a timer a pulsar will be observationally. By combining both and quantifying our metrics appropriately, we hope to be able to summarize any pulsar's performance in our pulsar timing array.

BIBLIOGRAPHY

Brisken, W. F., Macquart, J.-P., Gao, J. J., et al. 2010, ApJ, 708, 232

Coles, W. A., Kerr, M., Shannon, R. M., et al. 2015, ApJ, 808, 113

Cordes, J. M., Rickett, B. J., Stinebring, D. R., & Coles, W. A. 2006, ApJ, 637, 346

Cordes, J. M., Shannon, R. M., & Stinebring, D. R. 2016, ApJ, 817, 16

Ransom, S. M. 2008, Dynamical Evolution of Dense Stellar Systems, 246, 291

Shannon, R. M., & Cordes, J. M. 2010, ApJ, 725, 1607

CHAPTER 8

CONCLUSIONS

In this work, we have begun to characterize our pulsar timing array gravitational wave (GW) detector. We started with a targeted campaign of one of the best-timed pulsars and were able to demonstrate timing errors from frequency-dependent pulse profile evolution and intrinsic pulse jitter. We then quantified dispersion measure mis-estimation from asynchronous multi-frequency observations and its effect on timing precision. Systematic and stochastic causes of dispersion measure variations were explored in the following chapter, with contributions along the entire pulse propagation path between the observatory and the pulsar. Next, we analyzed pulsar observations on different epochs independently to develop a well-defined white noise budget for our millisecond pulsars. Finally, we were able to expand the scope of the pulsar noise model by quantifying additional contributions to pulse arrival time errors.

The North American Nanohertz Observatory for Gravitational Waves collaboration continues to observe many of the best-timed millisecond pulsars known. By implementing this work into the timing analyses, we hope to drastically gain sensitivity to GWs and further improve the timing quality of our pulsars. Equipped with our continuously advancing detector, we expect within the next few years to open a new window to the low-frequency GW Universe.

APPENDIX A

PYPULSE

Originally based on the PSRCHIVE[1] pulsar data processing package, PyPulse (`https://github.com/mtlam/PyPulse/`) is a pure Python implementation of PSRCHIVE's basic functionality in handling data in the PSRFITS format (Hotan et al. 2004; van Straten et al. 2012). It is designed to be easy to install, with a minimal number of standard Python packages used (e.g., numpy[2], scipy[3], matplotlib[4], astropy[5]). It is fully compatible with Python versions 2 and 3.

The code is object oriented in design, with the primary structures being class based. Constructed objects call their methods (functions) and change the internal stored state rather than have external functions called on the data products. The following sections will discuss each of the main classes of PyPulse.

A.1 Archive

The primary data array of profiles in a PSRFITS file is given by $\mathcal{I}(t, p, \nu, \phi)$, the pulse intensity as a function of time t, polarization p, frequency ν, phase ϕ, where the arguments are in the order of the array dimensions. To save memory, intensity data are stored in multiple arrays. The raw data array (DATA) d is the largest in dimensionality but for folded pulse data is typically stored as an array of 16-bit integers. To retrieve the raw data value for each pulse profile, the data array is then multiplied by a scale array (DAT_SCL) s and an offset array (DAT_OFFS) o

[1] `http://psrchive.sourceforge.net`
[2] `http://www.numpy.org/`
[3] `http://www.scipy.org/`
[4] `http://www.matplotlib.org/`
[5] `http://www.astropy.org/`

is added. An array of weights (DAT_WTS) w is also stored internally and typically modifies the raw data, e.g., when excising radio frequency interference. The three modifier arrays are of much smaller size than the data array and are typically stored as in 32-bit single-precision float format. Mathematically, the resultant array of pulse intensities can be written as

$$\mathcal{I}(t, p, \nu, \phi) = [s(t, p, \nu) \times d(t, p, \nu, \phi) + o(t, p, \nu)]\, w(t, \nu). \tag{A.1}$$

PSRFITS files also contain a wide range of additional information stored internally, including a history of all PSRCHIVE modifications to the file, a folding ephemeris, and a large global header of useful metadata. Besides the data array, PyPulse will unpack and store all extra information for retrieval via `get()` methods as desired.

The basic operation to reduce the size of the data array of intensities is known as "scrunching", which involves averaging over a specific window size over the array dimension. Averaging is possible in any of the four dimensions, invoked with the methods:

`tscrunch()` – time (subintegration) averaging
`pscrunch()` – polarization (channel) averaging
`fscrunch()` – frequency (channel) averaging
`bscrunch()` – phase (bin) averaging

Arguments can be provided to specify the window size or factor by which to reduce array dimension's size. All averaging actions can be undone by using the `reset()` method, which will replace the data array with a stored copy of the data if the `lowmem` flag is set to `True` (by default), or will reload the data from disk if `False`.

Pulse polarization information can be stored in a variety of states. The most common storage states are the coherence matrix (Coherence parameters) or Stokes

parameters. Given an electromagnetic wave's polarization represented by a Jones vector with orthogonal elements P and Q, the coherency matrix is defined as

$$\begin{pmatrix} PP^* & PQ^* \\ QP^* & QQ^* \end{pmatrix} \tag{A.2}$$

The four Coherence parameters are internally stored as $(PP^*, QQ^*, \mathrm{Re}[PQ^*], \mathrm{Im}[PQ^*])$. Assuming linear polarization, the Coherence parameters are related to the Stokes parameters as

$$\begin{aligned} I &= PP^* + QQ^* \\ Q &= PP^* - QQ^* \\ U &= 2\mathrm{Re}[PQ^*] \\ V &= 2\mathrm{Im}[PQ^*] \end{aligned} \tag{A.3}$$

By default, array data are polarization averaged as well as de-dispersed, in which a time delay is applied proportional to the dispersion measure (DM) in the PSRFITS header. This default array preparation can be turned off by supplying the `prepare=False` argument when creating the Archive constructor. Array data can be retrieved by `getData()`, which returns a numpy array with dimensions of length 1 removed. The `saveData()` method will write the primary data array $\mathcal{I}$ to either a numpy .npy file or an ASCII text file if specified.

Archive will create simple data products from the primary data array. The `getAxis()` method will calculate and return either the time or frequency axes depending on the argument supplied. All of the pulses in the data array (at its current state) can be wrapped in the SinglePulse class (see the next section) via the `getSinglePulses()` method, which allows bulk pulse properties to be applied to each single pulse. The helper method `fitPulses()` will return a requested subset

of the quantities of SinglePulses `fitPulse()` method (again, see the next section), rather than obtaining the SinglePulses and then running `fitPulse()` on each individually. A dynamic spectrum can be generated via `getDynamicSpectrum()`, which uses either the peak data intensity, or the best-fit intensity if a template waveform is supplied, as a function of time and frequency.

If the data have been averaged into a single dimension, typically such as phase, then `plot()` will display the pulse profile. `imshow()` produces a 2D plot in the style of matplotlib's imshow when the data have been averaged into two dimensions. `pavplot()` is a modification of `imshow()` that produces a 2D plot similar to PSRCHIVE's `pav` command, with either the `-GTpd` or `-YFpd` flags, depending on which dimensions are averaged over. `waterfall()` will produce a 2D series of line plots for easier pulse visibility. The `joyDivision()` method is a modification that produces a waterfall plot in the style of the famous album cover showing pulses from PSR B1919+21 (originally CP 1919, in Craft 1970).

The `time()` method will calculate pulse times of arrival (TOAs) given a template waveform. The TOAs returned will be phase values converted into time units (relative TOAs). However, if `MJD=True`, then true TOAs will be calculated with the appropriate time tags and delays computed (absolute TOAs).

A.2 SinglePulse

The SinglePulse class wraps a 1D data array containing pulse intensities as a function of phase. It stores the location of the main and off pulse (and interpulse, if provided) phase ranges of the profile, and can calculate one given the other. If no ranges are provided, it calculates the off pulse window given the method described

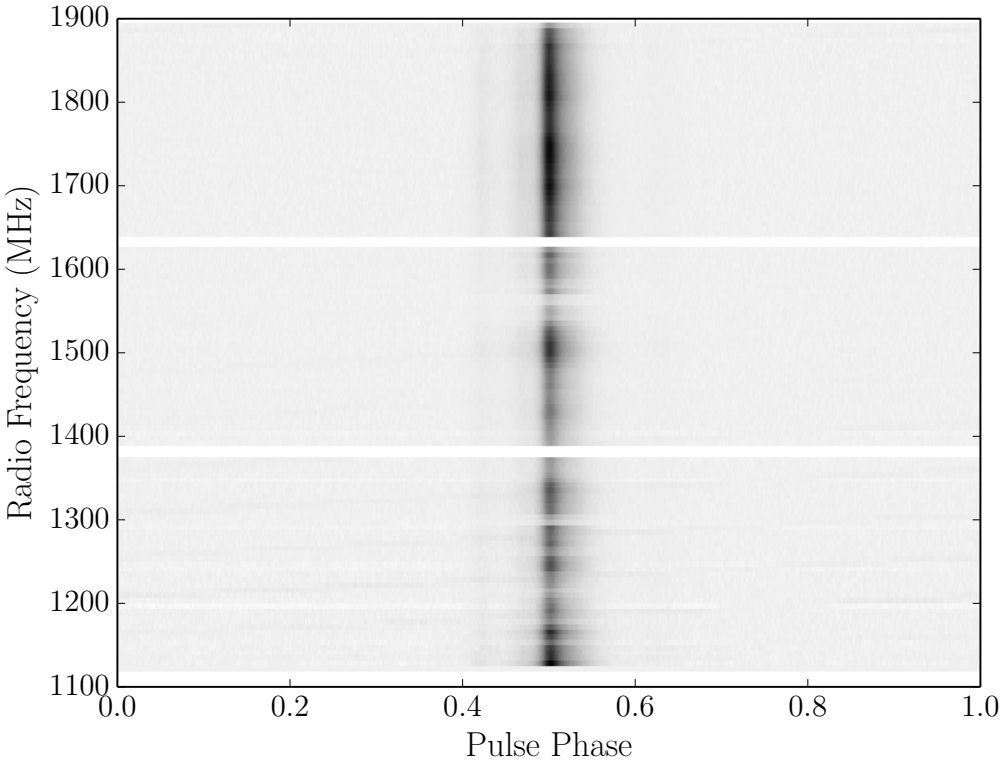

Figure A.1: Example of PyPulse's `imshow()` with data taken from the Green Bank Telescope for the 24-hour global campaign on PSR J1713+0747. This figure is identical to the top right panel of Figure 1.2. The code to produce this plot is provided in §A.5.

in Chapter 5, §3.1.

There are numerous operations that can be performed on the pulse, changing its saved state. The pulse can be rotated in phase by computing the Fourier transform of the profile, utilizing the shift theorem, and then computing the inverse Fourier transform of the final waveform. Note that rotating the pulse does not change the location of the three phase windows described above, which allows the pulse to be rotated into a pre-defined position without that position changing. Calling `remove_baseline()` will subtract the mean value from the off-pulse baseline. Normalizing the pulse to unit amplitude or area is accomplished with the

`normalize()` method.

The effective width ($W_{\rm eff}$) and full width at half maximum (FWHM) of a pulse can be calculated easily though it is recommended to do so only on noiseless data (i.e., a pulse template). The autocorrelation function (ACF) can also be calculated for each pulse window individually. One important aspect of proper calculation of an ACF is the removal of the baseline intensity level. Any constant offset added to a function will introduce a triangle function into an ACF and therefore the baseline must be removed for a proper width to be estimated.

The primary template matching algorithm of Taylor (1992) is performed through `fitPulse()`. The function takes a template waveform to fit to the stored data profile. It returns several quantities, including the estimated TOA with error, the scale factor with error, the pulse S/N, and the correlation coefficient ρ. See Chapter 5, Eq. 1.3 for the appropriate signal model. Normalizing the template waveform to unit amplitude is important for proper estimation of the scale factor and pulse S/N.

A.3 DynamicSpectrum

The DynamicSpectrum class is primarily a storage object for 2D dynamic spectra arrays. In addition to the data array of pulse intensities $\mathcal{I}(\nu, t)$, it can store the off-pulse dynamic spectrum, the errors on the estimated intensities, and a mask array, all of the same shape as the data array. It will also keep track of the two data axes in time and frequency.

The dynamic spectrum is used to calculate several data products which

can be done with the DynamicSpectrum class. The 2D ACF $R(\Delta\nu, \Delta t) = \langle \mathcal{I}(\nu, t)\mathcal{I}(\nu + \Delta\nu, t + \Delta t)\rangle$ is useful for estimating scintillation timescales $\Delta t_{\rm d}$ and bandwidths $\Delta\nu_{\rm d}$. It is computed with `acf2d()`, which uses a Fast Fourier Transform-based (FFT) convolution (scipy's `fftconvolve`). Similarly, we can compute the secondary spectrum (with `secondary_spectrum()`), $S(f_\nu, f_t) = |\tilde{A}(\nu, t)|^2$, which is useful for investigating scattering structure along the line of sight to a pulsar.

As with the 1D pulse ACF, the baseline intensity must be subtracted from the dynamic spectrum in order to properly calculate the scintillation parameters $\Delta\nu_{\rm d}$ and $\Delta t_{\rm d}$ from the widths of the central feature. We perform baseline removal by creating a histogram of the intensities and fitting either a Gaussian function or a more appropriate diffractive scintillation "gain" PDF (see Eq. 5.7) to the histogram and subtracting the intensity value that corresponds to the peak of the histogram. The scintillation parameters can then be estimated by fitting a 2D Gaussian function over the central ACF peak. The half width at half maximum in the frequency dimension is taken for $\Delta\nu_{\rm d}$ while the half width at $1/e$ is taken for $\Delta t_{\rm d}$ (Cordes 2002). The rotation of the 2D Gaussian $d\nu/dt$ is related to refraction and symmetries of the scattered pulsar image (Cordes et al. 1986).

DynamicSpectrum allows other dynamic spectra to be added to the stored array with the `add()` method. In addition, DynamicSpectrum allows for the data arrays to be saved to (via `save()`) and loaded from (via `load()`) a .npz (a numpy dictionary) file, such that any processing is retained in memory.

A.4 Other Utilities

PyPulse comes with a number of other classes and functions for use. The utils.py file contains generic mathematical and time series analysis routines. The functionfit.py file contains fitting routines for a number of functions used throughout PyPulse. The par.py file contains the Par class, useful for text manipulation of pulsar parameter (par) files. Similarly, the tim.py file contains the Tim class, which allows for quick text manipulation of pulsar TOA (tim) files.

A.5 Sample Code

Below is the code to produce Figure A.1.

```
# Import statements
import numpy as np
from matplotlib.pyplot import *
from matplotlib import rc,cm
from pypulse.archive import Archive

# Set LaTeX font
rc('text',usetex=True)
rc('font',**{'family':'serif','serif':['Times New Roman']})
rc('xtick',**{'labelsize':16})
rc('ytick',**{'labelsize':16})
rc('axes',**{'labelsize':18})

# Load archive
ar = Archive("GUPPI_J1713+0747_56466_10724_all.pzap")
ar.tscrunch()
F = ar.getAxis('F')
ar.imshow(cmap=cm.binary,show=False,
          extent=[0,1,F[0],F[-1]+(F[-1]-F[-2])])

# Label plots
xlabel("Pulse Phase")
ylabel("Radio Frequency (MHz)")
show()
```

BIBLIOGRAPHY

Cordes, J. M. 2002, Single-Dish Radio Astronomy: Techniques and Applications, 278, 227

Cordes, J. M., Pidwerbetsky, A., & Lovelace, R. V. E. 1986, ApJ, 310, 737

Craft, H. D., Jr. 1970, PhD thesis, Cornell Univ.

Hotan, A. W., van Straten, W., & Manchester, R. N. 2004, PASA, 21, 302

Taylor, J. H. 1992, Royal Society of London Philosophical Transactions Series A, 341, 117

van Straten, W., Demorest, P., & Oslowski, S. 2012, Astronomical Research and Technology, 9, 237

APPENDIX B

QUICKLOOK

Quicklook (`https://github.com/mtlam/Quicklook/`) is a pure Python program that allows for the rapid creation and viewing of pulsar data products. It uses the PyPulse package (Appendix A) for data access and processing. The main goals of Quicklook are to: (i) verify data quality, (ii) identify interesting features and variations in data products, and (iii) increase data accessibility. As with PyPulse, Quicklook is object oriented in design.

B.1 ArchiveHandler

The ArchiveHandler class builds upon PyPulse's Archive class (see Appendix A.1). It takes a filename and either creates an Archive in memory or loads data from a .npz (numpy dictionary) file. If it creates an Archive, then it will automatically create various data products from the pulse profiles (by calling internal `get()` methods) and store them internally. In addition, ArchiveHandler will store relevant metadata (e.g., axis information) from the PSRFITS file for plotting.

ArchiveHandler also produces the individual panel plots for each of the data products by calling internal `plot()` methods. Each plotting method can either draw a new matplotlib `figure` or can take an `axis` and draw to it directly, allowing for flexibility in where plot output is sent. All data products can be saved as a .npz file with the `save()` method to prevent future re-calculation.

B.2 Quicklook

The graphical interface is created within the Quicklook class. It contains a default set of `axis` objects drawn in specific positions on the `figure`. Future iterations of Quicklook will allow for increased flexibility in what is plotted and where. The Quicklook class contains a single ArchiveHandler object, which creates all of the data products and associated plots as described above. Quicklook simply provides the appropriate `axis` object to the corresponding ArchiveHandler method to retrieve the plots. In addition to the graphics management, all command-line argument parsing is handled within the quicklook.py file.

Figure B.1 shows a sample output plot using data taken from the Green Bank Telescope for the 24-hour global campaign on PSR J1713+0747. Useful header metadata information is provided at the top while the different panels show the various data products. See the figure caption for more details. The figure was produced by the following command:

```
$ ./quicklook.py -ext pdf -template J1713+0747.Rcvr1_2.GUPPI.9y.x.sum.sm
   GUPPI_J1713+0747_56466_10724_all.p.zap
```

Below we will describe the different panels as shown. The calculations are performed by PyPulse, and so explicit equations are provided in Appendix A.

B.2.1 Header

At the top, the text provides useful information from the PSRFITS file and observation, including the filename, telescope, MJD of the observation, pulsar observed,

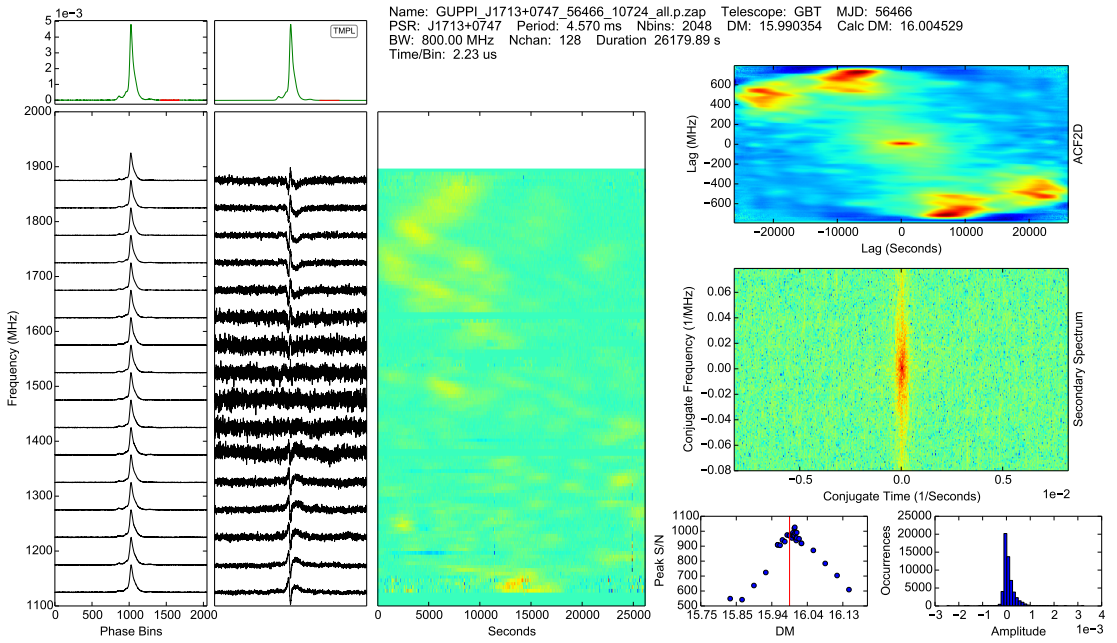

Figure B.1: Output from Quicklook with data taken from the Green Bank Telescope for the 24-hour global campaign on PSR J1713+0747. The two small panels in the top left show the average pulse profile and the pulse template (filename supplied as a command-line argument). Below are the pulse profiles and difference profiles (data − template) as a function of frequency. In the middle is the dynamic spectrum. The 2D autocorrelation function is shown at top right and below that is the secondary spectrum (see Appendix A for more information). Both plots are symmetric about the origin, a feature of the two data products. At bottom right, we show two diagnostic panels, the pulse S/N as a function of DM (left, DM in the PSRFITS header is shown by the vertical line) and the histogram of pulse amplitudes from the dynamic spectrum (right). Basic metadata about the observation are provided by the text at top.

pulsar period, number of phase bins, header dispersion measure (DM), best calculated dispersion measure, total observing bandwidth, number of frequency channels, observation duration, and amount of time per phase bin.

B.2.2 Average Profile

In the top left is the average profile, $\mathcal{I}(\phi) = \langle \mathcal{I}(\nu, p, t, \phi) \rangle_{\nu,p,t}$. The calculated off-pulse region is shown in red.

B.2.3 Template

If a template $\mathcal{U}(\phi)$ is provided, then we show the template shape with the calculated off-pulse region is shown in red. Otherwise, the panel is blank with the text displaying "NONE".

B.2.4 Intensity Profiles

In the lower left are the data profiles averaged in polarization and time, $\mathcal{I}(\nu, \phi) = \langle \mathcal{I}(\nu, p, t, \phi) \rangle_{p,t}$.

B.2.5 Difference Profiles

To the right of the intensity profiles, we show the difference profiles $\langle \mathcal{I}(\nu, p, t, \phi) \rangle_{p,t} - \mathcal{U}(\phi)$ as a function of frequency. If no template is provided, then the average profile is used as a template.

B.2.6 Dynamic Spectrum

The center panel shows the dynamic spectrum $\mathcal{I}(\nu, t)$. If a template is provided, then the template is fit to the data profile and the dynamic spectrum represents the best-fit pulse amplitudes. Otherwise, the dynamic spectrum is calculated from the intensity profiles as $\mathcal{I}(\nu, t) = \langle \mathcal{I}(\nu, p, t, \phi) \rangle_{p,\phi}$. At present, no color scaling has been implemented.

B.2.7 2D Autocorrelation Function

The top right panel shows the 2D autocorrelation function, computed from the dynamic spectrum as $R(\Delta\nu, \Delta t) = \langle \mathcal{I}(\nu, t)\mathcal{I}(\nu + \Delta\nu, t + \Delta t) \rangle$. The full range of lags is shown.

B.2.8 Secondary Spectrum

Below the 2D autocorrelation function, the secondary spectrum $S(f_\nu, f_t) = |\tilde{A}(\nu, t)|^2$ is shown. The full range in conjugate time and frequency is shown.

B.2.9 Dispersion Measure Estimate

Of the two bottom-right panels, the left shows the average pulse signal-to-noise (S/N) versus trial DM used to de-disperse the pulse. Note that frequency-dependent profile evolution is not accounted for here. The header DM is shown with the vertical line.

B.2.10 Pulse Amplitude Distribution

In the very bottom right, we show the amplitude distribution of our pulses $\mathcal{I}(\nu, t, \phi)$. This is simply a histogram of the amplitude values in the dynamic spectrum.